# University of Cambridge
## Institute of Astronomy

### A dissertation submitted to the University of Cambridge for the degree of Doctor of Philosophy

∽

# High Redshift Star-Forming Galaxies in Absorption and Emission

∽

## Anna Marie Quider
### Churchill College

*Submitted to the Board of Graduate Studies*
*June 2011*

### Under the Supervision of
### Professor Max Pettini

*Dedicated to:*
*G. Alec Stewart, William Stuckwisch, and Timothy Williamson*
*Inspirational educators and friends*

*"The teacher who is indeed wise does not bid you to enter the house of his wisdom but rather leads you to the threshold of your mind."*

– Khalil Gibran

# DECLARATION OF ORIGINALITY

I, Anna Marie Quider, declare that this thesis titled, 'High Redshift Star-Forming Galaxies in Absorption and Emission' and the work presented in it are my own. I confirm that:

- This work was done wholly while in candidature for a research degree at this University.

- This thesis has not previously been submitted for a degree or any other qualification at this University or any other institution.

- Where I have consulted the published work of others, this is always clearly attributed, especially in Chapter 1 which serves as an introduction and largely draws on work in the literature.

- Where I have quoted from the work of others, the source is always given. With the exception of quotations or figures that are credited to others, this thesis is entirely my own work.

- I have acknowledged all main sources of help in the Acknowledgements.

- Where the thesis is based on work done by myself jointly with others, I have made clear exactly what was done by others and what I have contributed myself. All writing has been put together by myself.

- The length of this thesis does not exceed the stated limit of the Degree Committee of Physics and Chemistry of 60,000 words.

_____
*Signed*

_____
*Date*

# Summary

## High Redshift Star-Forming Galaxies in Absorption and Emission

### Anna M. Quider

Galaxies in the redshift range $1 < z < 3$ existed during the most vigorous period of star formation in the history of the Universe. In the past 15 years, large rest-frame UV spectroscopic samples of $z \sim 3$ star-forming galaxies have been assembled. However, this particular redshift range, the so-called Redshift Desert, has only begun to be characterized. Most studies involve low resolution, low signal-to-noise spectra because the small angular size ($\delta \leq 1''$) and faintness ($R_{AB} = 24 - 25.5$) of high redshift galaxies limit what can be accomplished with a reasonable investment of observing time, even using the world's largest optical telescopes.

One way to circumvent these two issues is to study gravitationally lensed galaxies. The magnification boost (up to a factor of $30\times$) and morphological distortion of a high redshift galaxy by an intervening mass concentration allow for the study of the high redshift Universe in unprecedented detail. I present a detailed analysis of the rest-UV spectrum of two gravitationally lensed galaxies: the 'Cosmic Horseshoe' ($z_{\mathrm{sys}} = 2.38115$) and the 'Cosmic Eye' ($z_{\mathrm{sys}} = 3.07331$). The characterization of the stellar populations and the interstellar gas geometry, kinematics, and composition which I achieve is a preview of the type of information that will be available for unlensed high redshift galaxies with the next generation of optical telescopes.

I probe the lower redshift end of the Redshift Desert with a study of Fe II and Mg II features in the rest-frame near-UV spectrum of 96 star-forming galaxies in the redshift range $1 < z < 2$. Stacked spectra are used to explore average outflow and line profile trends with stellar mass and reddening. I also investigate the phenomenon of emission filling of absorption lines which has implications for the line strength and velocity offset of interstellar absorption lines. Individual galaxies are used to assess the range of outflow velocities as well as the prevalence of emission filling in galaxies from this epoch. This is the first large scale study of fine-structure emission from Fe II in high redshift galaxies, both in stacked and individual galaxy spectra.

An alternative to investigating galaxies by collecting their light is to study them as seen in absorption against a cosmic backlight, such as a quasar. The Sloan Digital Sky Survey, an imaging and spectroscopic survey which covers about one-quarter of the night sky, has collected many thousands of quasar spectra. I search $\sim 44\,600$ of these spectra, up through Data Release 4, for Mg II $\lambda\lambda 2796,2803$ absorption doublets. The final catalog includes $\sim 16\,700$ Mg II absorption line systems in the redshift range $0.36 \leq z \leq 2.28$. Measurements of the absorption redshift and rest equivalent widths of the Mg II doublet as well as select metal lines are available in the catalog. This is the largest publicly available catalog of its kind and its combination of large size and well understood statistics make it ideal for precision studies of the low-ionization and neutral gas regions of galaxies.

I conclude this thesis by suggesting several avenues for extending the studies of high redshift star-forming galaxies presented herein.

# ACKNOWLEDGMENTS

# Contents

# List of Figures

# List of Tables

*Great indeed are the things which in this brief treatise I propose for observation and consideration by all students of nature. I say great, because of the excellence of the subject itself, the entirely unexpected and novel character of these things, and finally because of the instrument by means of which they have been revealed to our senses.*

Galileo Galilei, *Sidereus Nuncius*

# 1

# Introduction

**T**HE historical record shows that humanity has been watching the sky for eons. For most of this time there has been little comprehension of the physical structures populating our Universe. As is often the case in science, this is an issue of instrumentation as well as an issue of theoretical framework. Galileo's decision to turn his telescope toward the sky in 1609 touched off instrument-driven observational astronomy. Suddenly more of the Universe was visible to humanity and within a hundred years objects beyond our own Galaxy were being observed. The nature of these objects was not realized until 1929 when Edwin Hubble proved their distance must put them beyond the bounds of our Galaxy. Since then there has been rapid progress in the study of galaxies throughout cosmic time. We are now at the point where we can begin to decipher the properties of galaxies from the young Universe to the present time.[1] In this introduction I will provide context on the significance of young galaxies for understanding the development of our Universe as well as briefly review the state of our knowledge regarding these galaxies.

## 1.1 Why Care About the Young Universe?

Observational astronomy hinges on the assumption that the speed of light has a constant velocity of $c = 299\,792$ km s$^{-1}$. It takes time for light from astronomical objects to reach the Earth. Indeed, even sunlight takes $\sim 8$ minutes to arrive at our planet. A major consequence of this is that astronomers are only able to see the Universe as it existed in the past. By analogy, this renders astronomers 'archaeologists' who piece together the history of the Universe using observations of cosmic structures as they have existed throughout time.

---

[1]In the context of this thesis, the phrase "young Universe" refers to the redshift range $1 < z < 3$. Current measurements put the age of the Universe at about 13.7 billion years. Therefore, this redshift interval correspond to $\sim 40\% - 15\%$ of the Universe's age when using the standard cosmology employed throughout this work ($\Omega_{\mathrm{M}} = 0.3$, $\Omega_\Lambda = 0.7$, and $H_0 = 70$ km s$^{-1}$ Mpc$^{-1}$).
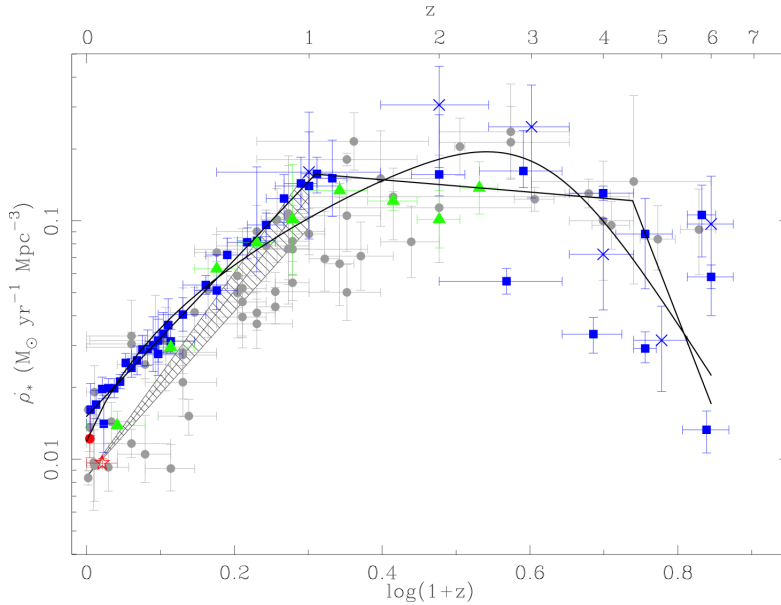
Figure 1.1 This is the cosmic star formation rate density and its evolution with redshift. The datasets represented by the symbols are explained in Hopkins & Beacom (2006), where this is Figure 1. Note that the peak of star formation in the Universe is at $z \sim 2$.

The story of the development and evolution of structure in the Universe is the story of the work of gravity. The currently accepted Big Bang paradigm says that the Universe started out as a nearly uniform distribution of energy. As the Universe expanded and cooled, tiny inhomogeneities in the distribution of baryonic and dark matter manifested themselves. These can be seen in the small temperature variations across the cosmic microwave background (CMB; Spergel et al. 2003). The force of gravity causes matter to self-attract; regions of slight matter overdensity become even more massive with time while the void grows in regions of matter underdensity (see Bullock et al. 2001). The small overdense regions seen in the CMB successfully accreted matter as the Universe aged. Dark matter is about $5\times$ more prevalent than baryonic matter in the Universe (Komatsu et al. 2011) so baryons can be thought of as migrating into the gravitational potential wells that form where dark matter accumulates. We track the build-up of structure by looking at baryonic matter because it interacts with light. Baryons cool, leading them to collapse into the centers of dark matter halos. Once a critical density of gas assembles in a dark matter halo, star formation commences. Small dark matter halos merge to form larger halos and this results in the formation of galaxies (Kauffmann et al. 1993). The process by which more massive galaxies are created by the successive merging of smaller galaxies is called hierarchical structure formation.

Measuring the rate of star formation is one way to study the evolution of the Universe. The young Universe was a period of vigorous star formation. Figure 1.1 (which is Figure 1 in Hopkins & Beacom 2006) is an updated Madau plot (Madau et al. 1998) which shows the evolution of the cosmic star formation rate volume density as a function of redshift. Star formation in galaxies peaked during the young Universe, at about $z \sim 2$. This period, often called the Golden Age of Galaxy Formation, happened when the Universe was small enough for large stores of gas to be readily accessible for making stars but old enough for galaxies to have had time to build up these gas reservoirs. Much of a

galaxy's stellar mass assembled during this period (Hopkins & Beacom 2006) and, due to hierarchical structure formation, galaxies from this epoch are the building blocks for the structures we see today.

Simulations have taught us about how star formation is regulated within galaxies. Models need observational constraints to provide the best match to galaxies in the physical Universe. A good example of this is feedback. Simulations tell us that feedback is necessary for the suppression of star formation, and that galactic winds driven by supernovae are a major component of mechanical feedback. Characterizing the velocity and extent of galactic winds can lead to better constrained, more insightful simulations (Davé, Oppenheimer & Finlator 2011). There are many more properties of a galaxy that are used to constrain models, including mass, metallicity, stellar populations, and gas geometry. All of these attributes can be measured and these observational limits are critical to constructing a picture of the young universe and to maximizing the usefulness of simulations.

There are two mains ways to approach the observational study of galaxies. The first is directly observing galaxies by collecting and analyzing their light. The second approach is to study structures which are seen in absorption against a cosmic backlight, such as a quasar. Each technique has its own merits and limitations. Direct study can tell you about all of its constituents (stars, gas, and dust) but requires that the galaxy be bright enough for spectroscopy. Analyzing absorption lines from a galaxy which appear in the spectrum of a background object is valuable in that faint galaxies can be easily studied. However, galaxies seen in absorption often have poorly constrained physical parameters because of their faintness. I employ both techniques for studying galaxies. In the next few sections, I review both techniques, putting more emphasis on direct study as the bulk of this thesis employs this approach.

## 1.2 LBG Photometric Selection Technique

Unfortunately, it is difficult to find and observe galaxies from the young Universe. The average star-forming galaxy from $z \sim 2$ has a small angular size ($\delta \leq 1''$) and is faint ($R_{AB} = 24 - 25.5$). This means that the significant light collecting power of the world's largest optical telescopes is required for studying these galaxies with a reasonable observing time commitment.

The first searches for high redshift galaxies focused on the Lyman-$\alpha$ (Ly$\alpha$) emission feature from neutral hydrogen. In the hydrogen atom, the transition of an electron from the $n = 2$ orbital to the $n = 1$ orbital results in the emission of a photon with $\lambda = 1215.67\,\text{Å}$. This transition is known as Lyman-$\alpha$ as it is first in the Lyman series. It was speculated by Partridge & Peebles (1967) that Ly$\alpha$ emission from young galaxies could be much stronger than their continuum emission and that it may even be strong enough for the detection of individual sources. Conveniently, redshifted Ly$\alpha$ from young galaxies falls into the optical wavelength band, making it a good target for ground-based observations. Motivated by these factors, blind imaging and spectroscopic surveys for Ly$\alpha$ emission commenced. Unfortunately, they were not particularly fruitful (e.g. Djorgovski, Thompson, and Smith 1992).

Steidel et al. (1996) demonstrated the effectiveness of the Lyman break photometric

selection technique for identifying statistically significant samples of high redshift galaxies using 10-m class telescopes. This technique relies on a distinct, easily detected brightness drop in the blue color compared to the red color of a galaxy. This flux change is caused by the hydrogen atoms absorption of all light shortward of the Lyman limit at 912 Å and the depression of flux between 912 Å and 1216 Å due to the Lyα forest. Galaxies found using this photometric selection technique have been dubbed "Lyman Break Galaxies" (LBGs).
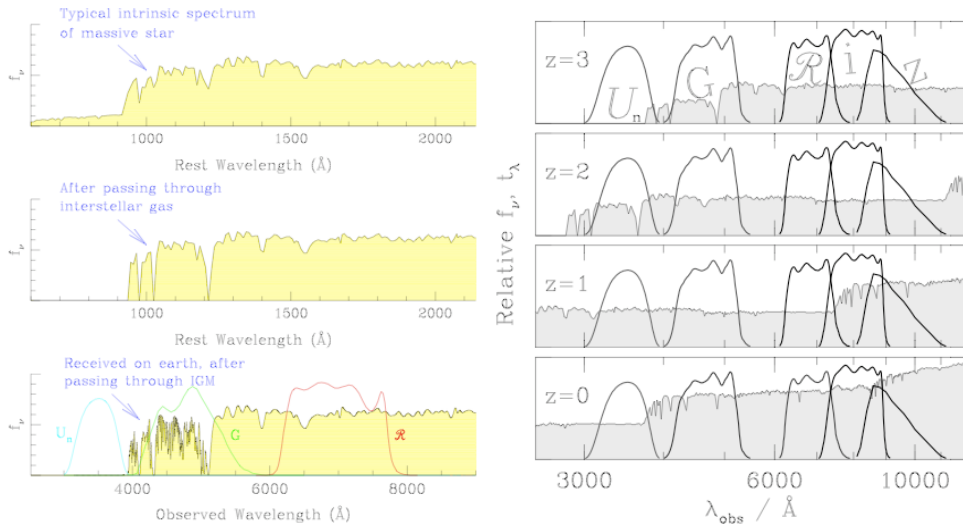


Figure 1.2 Left: (top) The spectrum of a massive star (middle) which exhibits absorption by interstellar gas and (bottom) absorption from H I intergalactic gas with the three LBG photometric selection filters superimposed on the observed spectrum (Pettini 2004) Right: An illustration of the characteristic spectral features for each of a $z = 0, 1, 2, 3$ galaxy spectrum with an overlay of the filters for selecting galaxies with $1 < z < 3$ (Adelberger et al. 2004)

Figure 1.2 illustrates the way in which photometric filters are used to isolate high-$z$ galaxies. The majority of the flux in a galaxy's rest frame ultraviolet (UV) spectrum comes from hot, massive OB stars and has a flat spectral shape in $f_\nu$ (Steidel et al. 1996). Galactic light travels through the interstellar medium (ISM) and intergalactic medium (IGM) on its way to Earth. The cumulative effect of the constituents of the ISM and IGM on the galactic light received on Earth is illustrated in the left bottom panel. This selection technique is well suited to ground-based searches for LBG candidates because the rest-frame UV flux of a $z \sim 3$ galaxy falls within the wavelength range that is accessible from the ground, as illustrated by the overlay of the $U_n$, G, and R filters in the left bottom panel and right panel. Steidel et al. (2003) define the general color criteria used to select LBGs as

$$R \leq 25.5; G - R \leq 1.2; (U_n - G) \geq (G - R) + 1.0 \qquad (1.1)$$

Adelberger et al. (2004) showed that the same filter set, with appropriate color cuts, can be used to isolate the population of galaxies in well defined redshift intervals from $z = 1$ to 3. The color selection criteria need to be adjusted in accordance with the spectral

features present in the observed optical spectrum of a high-$z$ galaxy, as illustrated in the right panel of Figure 1.2. Beyond the LBG population, the two main high redshift galaxy populations selected for using the principles of the LBG photometric selection technique are called BX and BM galaxies (Steidel et al. 2004). These galaxies have intrinsic properties very similar to LBGs but their average redshift is different: $<z> = 1.70$ and 2.2 for BM and BX galaxies, respectively. The left panel of Figure 1.3 shows the region of color-space populated by LBG, BX, and BM galaxies. The three histograms on the right trace the redshift distribution of these three galaxy subsets.
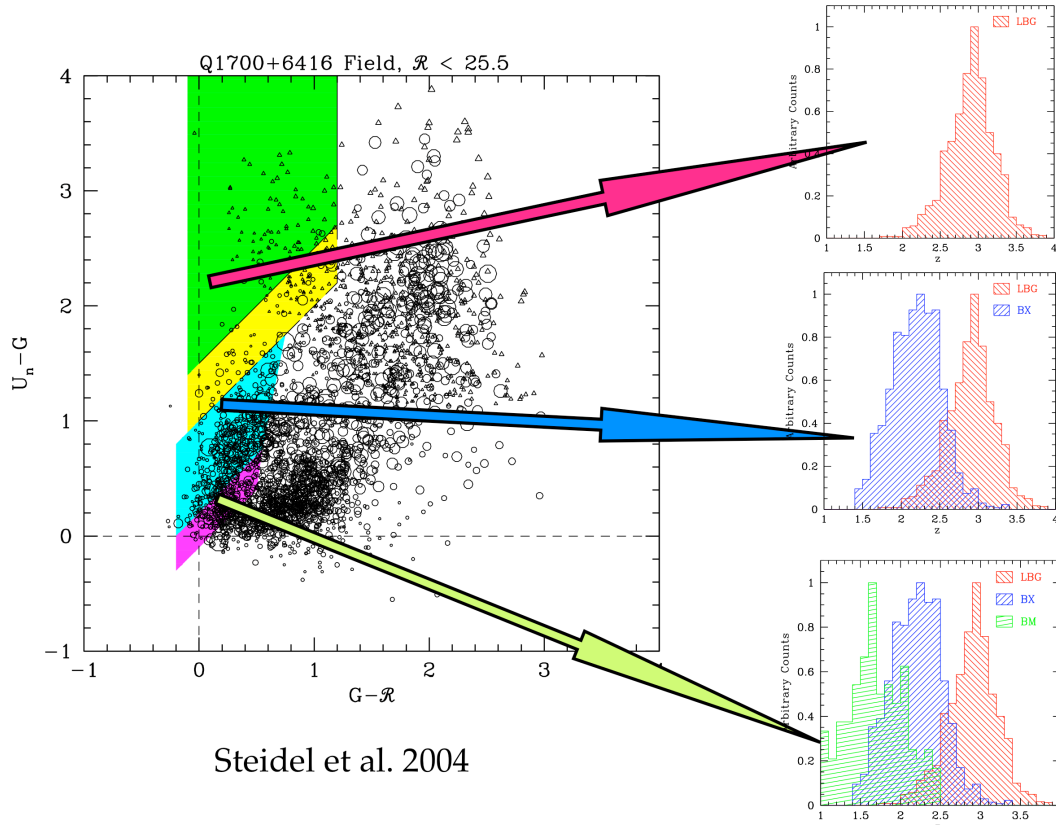


Figure 1.3 High redshift star-forming galaxies populate different regions of the color-color diagram depending upon their redshift. This compilation of figures is from Pettini et al. (2007).

The LBG photometric selection technique has been successful in identifying numerous high-$z$ sources. Indeed, Steidel et al. (2003) estimate that this technique has increased the efficiency of studying the $z \sim 3$ galaxy population by a factor of 30 as compared to traditional surveys. Indeed, the sample of galaxies at $1.7 \leq z \leq 2.3$ and at $2.7 \leq z \leq 3.3$ is over 2000 galaxies per interval and growing.

It should be pointed out that there are ways other than the LBG technique to identify high-$z$ star-forming galaxies. Using multiple sets of selection criteria is necessary to compare the effectiveness of different methods and to quantify the completeness of each method. One alternative to LBG selection is BzK selection (Daddi et al. 2004). The z-K and B-z colors find and distinguish between star-forming and passively evolving galaxies

in the redshift range $1.4 < z < 2.5$. Another way to select star-forming galaxies is using submillimeter (sub-mm) wavelength radio emission (Blain et al. 1999, 2002). Those which are most actively star-forming will appear more red than usual because their blue light is dust-extincted; however, they will appear radio-bright due to re-radiation by dust. Since optical selection criteria are tuned to look for blue colors, sub-mm sources can be missed in these searches (Chapman et al. 2000). Reddy et al. (2005) compared the effectiveness of several selection techniques using multiwavelength data for the GOODS-North field. They conclude that LBG and BzK selected star-forming galaxy populations overlap at the level of 70%-80%. Further, $> 80\%$ of sub-mm sources were identified as either star-forming or red by at least one of the LBG or BzK criteria. While a limitation of the LBG technique is that it does not pick out the extreme red end of the population, it is still selecting a significant portion of the typical star-forming galaxies at this epoch.

## 1.3 Low Resolution UV Spectra

### 1.3.1 Individual spectra

Due to the faintness of typical LBGs, it is only possible to obtain a low resolution, low signal-to-noise ratio (SNR) spectrum for an individual galaxy within the limits of reasonable observing time. Steidel et al. (1996) confirmed 16 LBGs with $z > 3$ and instructively compared these spectra to the spectrum of a local starburst galaxy, which is shown in Figure 1.4. These spectra show that LBGs and local starburst galaxies have similar UV spectral features:

1. a flat continuum

2. weak or absent Ly$\alpha$ emission

3. prominent high-ionization stellar lines of He II, C IV, Si IV, and N V

4. strong interstellar absorption lines due to different ionization stages of C, O, Si, and Al

The Ly$\alpha$ properties of LBGs are similar to those of local starburst galaxies. From a study of local starburst galaxies, Kunth et al. (1998) suggest that the geometry of the interstellar medium is the controlling factor in the transport of Ly$\alpha$ photons out from the star-forming regions. Recent models by Verhamme et al. (2006) do indeed confirm that the geometry of the gas in the star-forming regions contributes to how the Ly$\alpha$ transition manifests itself in a spectrum: as absorption, emission, or a combination of both, as well as the line strength.

The strongest interstellar absorption lines are visible in the low resolution spectra of LBGs. Local starbursts have been shown to have galactic winds driven by star formation activity (Heckman et al. 2000). These galactic winds can be traced by strong interstellar absorption features. Only the bulk motion of the gas can be determined from low resolution spectroscopy, measured as the offset between the interstellar absorption lines or the Ly$\alpha$ emission feature and the systemic redshift, as defined by the redshift of the stars or H II regions. Figure 1.5 shows the kinematic offsets for the interstellar and Ly$\alpha$ features
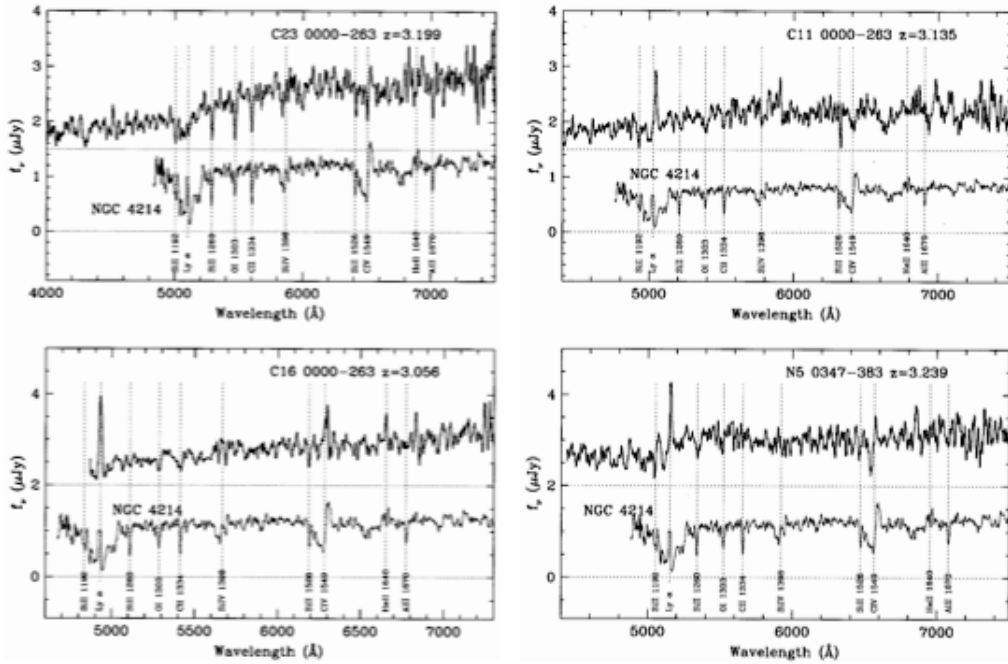
Figure 1.4 A comparison of four LBG rest-frame UV spectra with the rest-frame UV spectrum of a local starburst galaxy which has been shifted to be at the redshift of the LBG (Steidel et al. 1996).

of a set of $z \sim 2$ and $z \sim 3$ galaxies. This is evidence for large-scale outflows that are powered by supernovae and the winds from massive, hot stars (Pettini et al. 2001).

A simple physical model that is successful at explaining the observed kinematic profile of the interstellar gas and the Ly$\alpha$ transition is illustrated in Figure 1.6. The hot OB stars are surrounded by an outwardly expanding shell of gas and are taken to define the systemic redshift, or rest-frame, for the LBG. The stellar continuum photons pass through the frontside of the shell that is expanding toward the observer (colored blue in the Figure). This imparts to the interstellar absorption lines a bulk velocity offset, which happens to be 250 km s$^{-1}$ for this example. The H I gas in the shell is nearly opaque to Ly$\alpha$ photons. As a result, the Ly$\alpha$ photons which travel directly toward the observer are absorbed by the shell. Nevertheless, there is a way for Ly$\alpha$ photons to make it to the observer. Photons which are absorbed by the backside of the outflow (the portion moving away from the observer, colored red in the Figure) are re-emitted at a wavelength slightly longer than the rest wavelength of Ly$\alpha$. When these re-emitted photons encounter the frontside of the outflow they see a much lower optical depth for neutral hydrogen which permits them to pass through the shell. As a result, Ly$\alpha$ emission is often seen at a positive velocity with respect to the galactic rest frame, as seen in Figure 1.5. The photons re-emitted by the backside of the shell are redistributed in both wavelength-space and physical-space. The wavelength redistribution is clearly seen in the asymmetric shape of the Ly$\alpha$ emission line in the bottom-right corner of Figure 1.6. High-$z$ star-forming galaxies have also been shown to have spatially extended ($\sim 100$ kpc) Ly$\alpha$ halos due to the scattering and re-emission of Ly$\alpha$ photons by the outflow (Steidel et al. 2011).
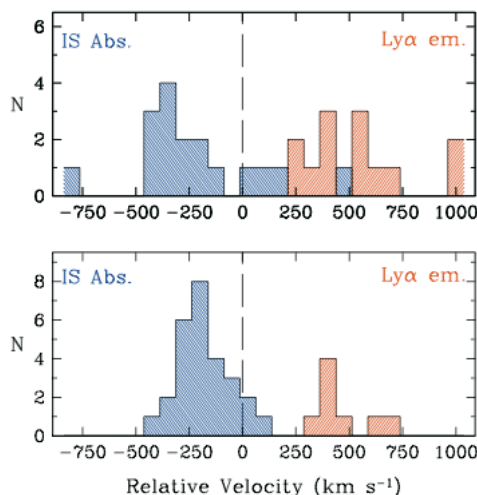
Figure 1.5 Velocity offsets between the interstellar absorption lines and Ly$\alpha$ emission. Top: Results for $z \sim 3$ galaxies. Bottom: Results for $z \sim 2$ galaxies (Steidel et al. 2004).

### 1.3.2 Composite spectra

The individual rest-frame UV spectra of LBGs are not well suited to studying LBG properties in detail because of their low SNR and low resolution. Combining the individual spectra into composites can improve the SNR (Shapley et al. 2003). Spectral features that are not visible in individual spectra become apparent and measurable. The spectrum in Figure 1.7 is a composite of 811 LBGs. Its stellar and interstellar features were measured in order to gain insight into the stellar populations and outflow dynamics of LBGs. Shapley et al. (2003) is the definitive study of LBG properties so it is worthwhile spending some time outlining the results of this study.

Outflows are a major aspect of LBGs that this composite UV spectrum has illuminated. There are two components to the outflowing gas: neutral gas, which is traced by neutral hydrogen and neutral or singly ionized metals, and ionized gas, which is traced by highly ionized metals. The low ionization gas is determined to have an average velocity of $\Delta$v $= -150 \pm 60$ km s$^{-1}$ while the high ionization gas has an average velocity of $\Delta$v $= -180$ km s$^{-1}$ as measured from the Si IV $\lambda\lambda$ 1393,1402 doublet. These velocity measurements refer to the gas of highest optical depth and do not shed light on the velocity extent of the outflow. Nevertheless, they show that the average LBG has a multiphase bulk outflow of considerable velocity.

As mentioned in Section 1.3.1, the shape and strength of the Ly$\alpha$ transition in a spectrum encodes information about the geometry of the gas in a galaxy. In order to better understand the Ly$\alpha$ properties of LBGs, Shapley et al. (2003) binned the 794 LBGs with measurable Ly$\alpha$ profiles into four equal groups based on the strength of their Ly$\alpha$ transition. These spectra are shown in Figure 1.8. One of the most significant trends is that as Ly$\alpha$ emission strength decreases, the strength of the low-ionization absorption lines increases by a factor of $\sim 3$. Further, the kinematic offset between Ly$\alpha$ emission and low-ionization absorption varies from $\Delta$v$_{em-abs} = 800$ km s$^{-1}$ to $\Delta$v$_{em-abs} = 480$ km s$^{-1}$ as Ly$\alpha$ emission increases. The properties of the high-ionization absorption lines remain fairly constant across all four bins.

**GALACTIC SCALE OUTFLOW**

$M_{out} \gtrsim 80 M_\odot yr^{-1} \gtrsim M_{in} \approx 40 M_\odot yr^{-1}$

$2.5 \times 10^5$ stars

$v_- \approx 250$ km s$^{-1}$

$v_+ \approx 300$ km s$^{-1}$

IS abs. lines

Ly$\alpha$ Em. line

Lyman Cont. photons?
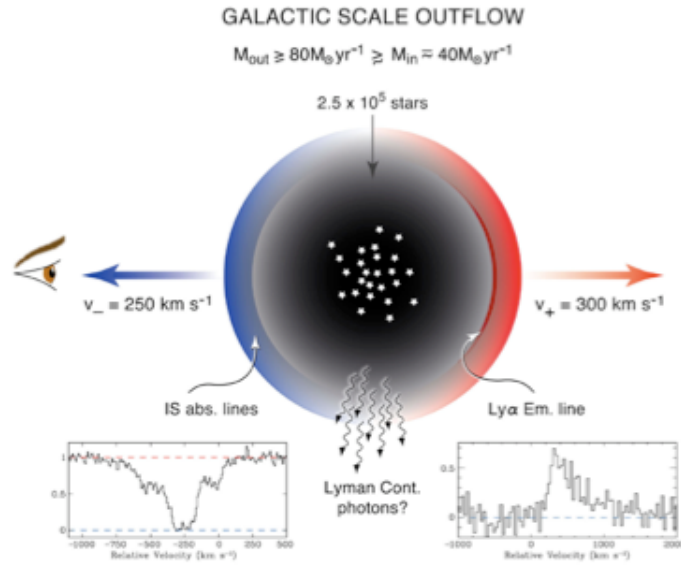
Figure 1.6 Schematic of the the geometric orientation of the stars and gas in a LBG (Pettini 2007).

A physical picture that is suggested by the results of Shapley et al. (2003), which have been partly summarized here, invokes gaseous shells and patches. The results of the varying line strengths of the low-ionization lines compared to the constant strength of the high-ionization lines indicates that perhaps the neutral gas in the outflow varies in its coverage of the stars but the high-ionization gas is stable in its coverage. This could happen if the neutral gas existed in patches that are embedded in a continuous shell of high-ionization gas. This model retains the same elements of the physical model in Figure 1.6 but adds in a patchy distribution of neutral gas. Recent work has started to flesh out this more realistic view of gas distribution (for example Chapter 3 of this work; Martin & Bouché 2009; Steidel et al. 2010).

## 1.4 High Resolution Rest-UV Spectroscopy

While composite spectra have a higher SNR than the typical LBG galaxy spectrum, they do not improve the spectral resolution. The only way to see a LBG with higher resolution, and therefore more detail, is to take a higher resolution spectrum of the galaxy at the outset. The faintness of most LBGs makes this unrealistic. However, a few rare high redshift galaxies which have been magnified by gravitational lensing and are suitable for high resolution spectroscopy have been identified. Prior to this thesis, the only one of these galaxies to be studied was MS1512-cB58 (cB58; Pettini et al. 2000, 2002). Because of its significant import to this work, it is worthwhile to review the use of gravitational lensing as a tool for studying the high redshift Universe as well as summarize the study of cB58.
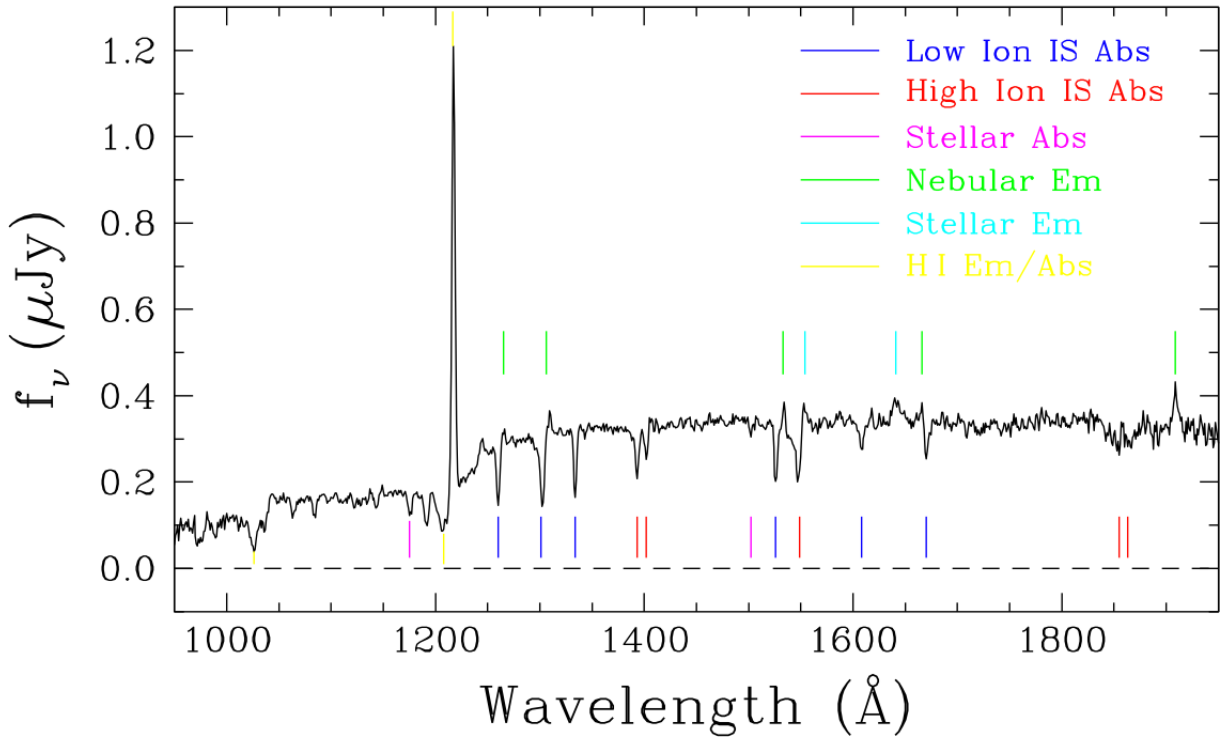
Figure 1.7 The rest-frame UV composite spectrum of 811 individual LBGs. Relevant spectral features are marked on the plot (Shapley et al. 2003).

### 1.4.1 Gravitational lensing: nature's telescope

It has been well established over the past hundred years or so that light is deflected by gravitational fields. When light from objects in the Universe travels towards us, it can pass in the vicinity of massive structures that exist along the path to Earth. The gravitational field of the intervening object, called the lens, distorts and magnifies the light from the original object, called the source. From the perspective of the Earth-bound observer, an image, or multiple images, of the more distant object is seen. In this image, the source is distorted and magnified from its original state. A good analogy for this phenomenon is the familiar bending of light by a lens; therefore, the bending of light by gravity is called gravitational lensing.

Figure 1.9 illustrates gravitational lensing using basic ray tracing. The light from the distant galaxy (the source) travels towards our telescope. The light, represented by the thin white lines, is deflected and refocused by an intervening galaxy cluster (the lens). We see along straight lines, represented by the diverging thin dashed lines, so it appears to the telescope as though there are two spatially-separated, distorted galaxies (the images). There are different regimes of gravitational lensing–strong, weak, and micro–depending on the degree of distortion and magnification present in the image. The lensing represented in this Figure (as well as the lensing discussed throughout this thesis) is of the strong variety.
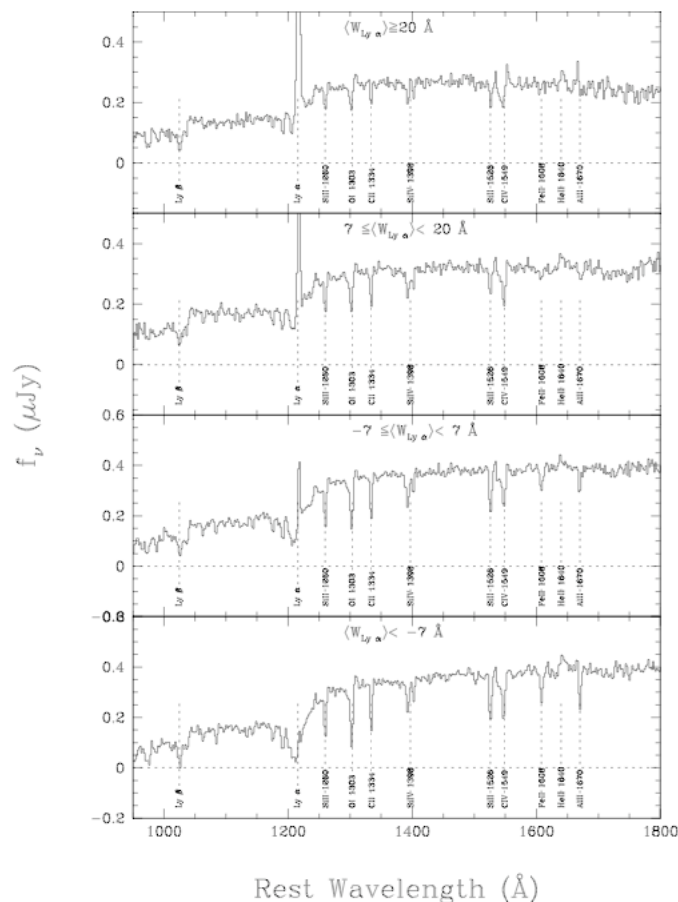
Figure 1.8 The rest-frame UV composite spectrum of 793 individual LBGs, binned by Lyα strength. Relevant spectral features and bin sizes are marked on the plot (Shapley et al. 2003).

For simplicity, Figure 1.9 depicts two distinct images of the source galaxy being created through gravitational lensing. In reality, images come in a wide variety of shapes and sizes. Figure 1.10 shows numerous images of lensed galaxies with redshifts between 1.5 and 5 from Richard et al. (2011). Note that the Cosmic Eye, which I will discuss in Chapter 4, is included in this compilation.

It is only recently that we have begun amassing sizable samples of young, gravitationally lensed galaxies. This progress is thanks to efforts like the CAmbridge Sloan Survey Of Wide ARcs in the skY (CASSOWARY) which searches the Sloan Digital Sky Survey (SDSS; see Chapter 2) for large separation gravitational lens systems (Belokurov et al. 2009). CASSOWARY targets galaxy-galaxy lenses where a single massive foreground galaxy is responsible for lensing a background galaxy. The Cosmic Horseshoe, to be discussed in Chapter 3, was discovered by this group (Belokurov et al. 2007) and their catalog currently contains 43 objects (http://www.ast.cam.ac.uk/ioa/research/cassowary). This is just one of nearly a dozen recent methodical searches for lensed galaxies in SDSS (e.g. Bolton et al. 2006; Willis et al. 2006; Estrada et al. 2007; Ofek et al. 2008; Shin et al. 2008; Belokurov et al. 2009; Kubo et al. 2009, 2010; Lin et al. 2009; Wen et al. 2009).
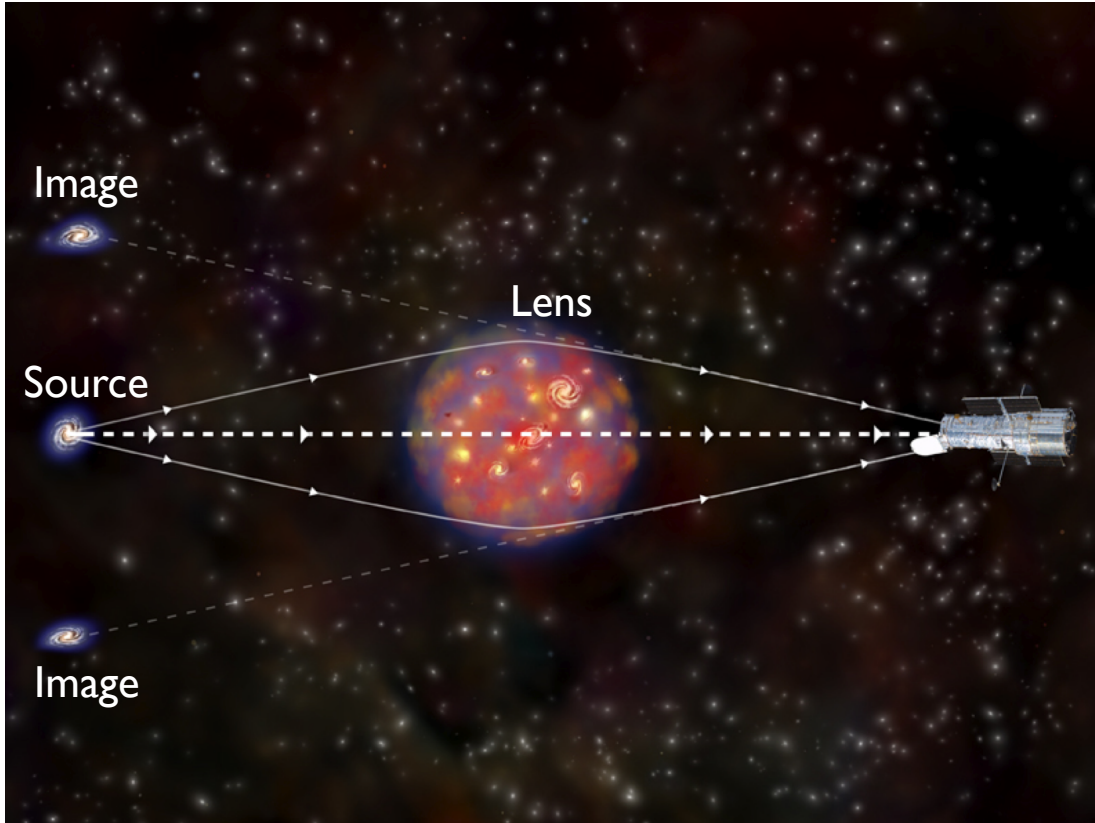
Figure 1.9 A schematic of strong gravitational lensing. The gravitational field of intervening objects (the lens) can distort and magnify the light from more distant objects (the source) into at least one image.

Apart from using SDSS, other efforts have included targeted searches of galaxy cluster images to find lensed young galaxies. Clusters are very massive structures so they are a good place to look for lensed high redshift galaxies. Searching Hubble Space Telescope archival images of clusters has yielded numerous confirmed systems (e.g. Jones et al. 2009, Richard et al. 2011). In particular, the Cosmic Eye, discussed in Chapter 4, was found by Smail et al. (2007) using this method.

Despite recent success at finding lensed high redshift galaxies, most are not bright enough for detailed study of the kind presented in Chapters 3 and 4 of this work. Further, of the handful of known systems that are most suitable, two were found serendipitously (Yee et al. 1996; Allam et al. 2007). The only galaxy to be studied in detail comparable to the lensed galaxies in this thesis is MS 1512−cB58 (Yee et al. 1996; Pettini et al. 2000, 2002); therefore, I will briefly review this work.

## 1.4.2   The galaxy MS 1512−cB58

The galaxy cB58 is a typical $\sim L^*$ LBG with redshift $z = 2.7276$ which has been magnified by $\sim 30$ times through gravitational lensing (Seitz et al. 1998). Echellette Spectrograph and Imager (ESI) spectroscopy of cB58 has provided a wealth of information about its stellar populations, composition, and structure (Pettini et al. 2002). This spectrum has
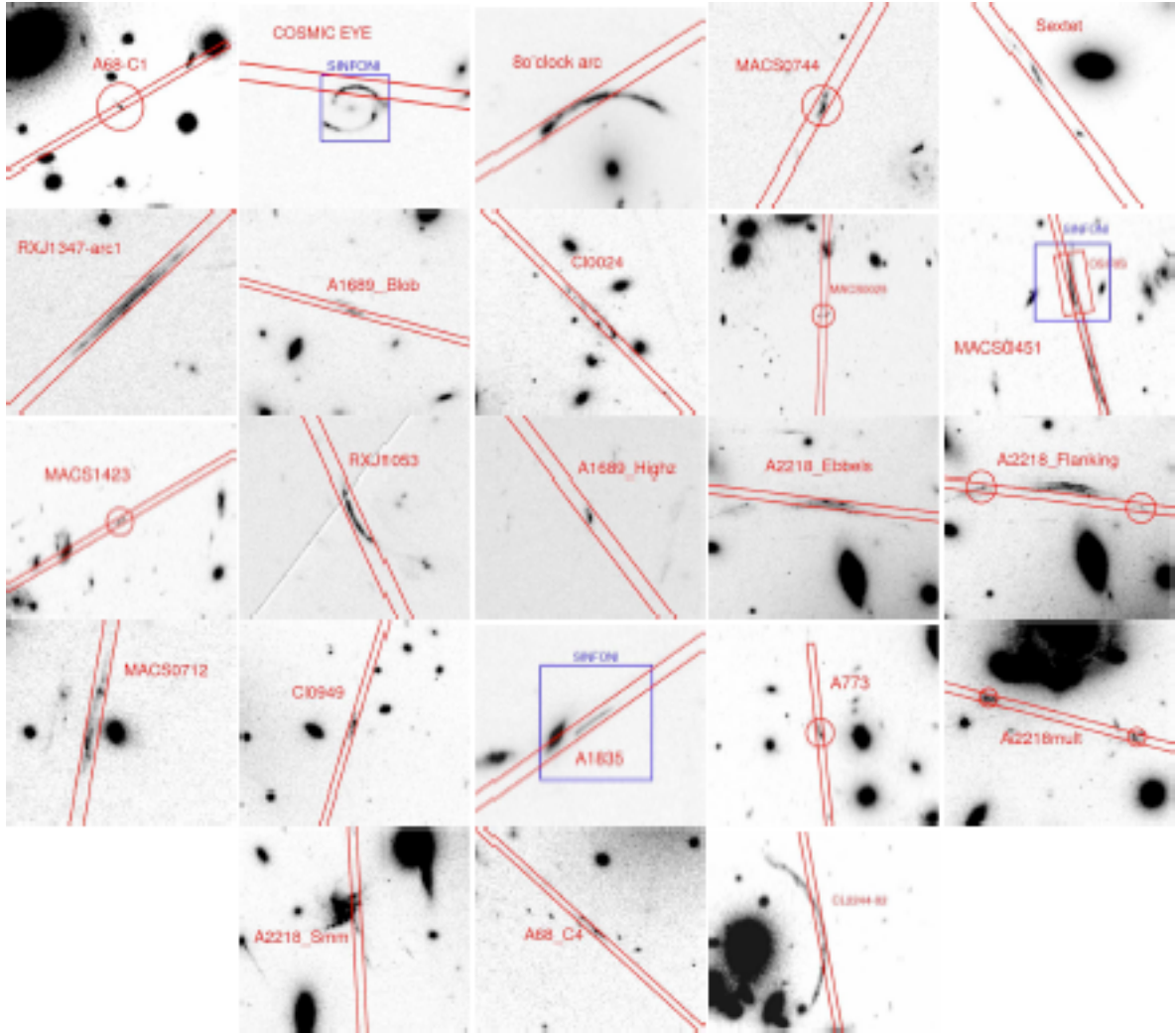
Figure 1.10 A collection of gravitationally lensed galaxies with $1.5 < z < 5$ from Richard et al. (2011). The red lines delineate the spectroscopic slit used in their study and lensed galaxies are named and encircled where unclear. There are a wide array of galaxy images created by gravitational lensing, ranging from small knots to extended arcs.

a resolution of 58 km s$^{-1}$ FWHM and a signal-to-noise ratio between 30 and 55, making it the best rest-frame UV spectrum to date of a LBG.

One of the critical uses of the high resolution rest-frame UV spectrum of cB58 is determining chemical abundances from the interstellar absorption lines. The conclusion for cB58 is that the metallicity of the ISM is 0.4 Z$_\odot$ for the products of Type II supernovae, such as O, Mg, Si, P, and S, as seen in Figure 1.11. However, cB58 is deficient in the products of intermediate mass stars such as N and Fe-peak elements. This lends itself to the interpretation that the burst which enriched cB58 has an age $t \leq 300$ Myr. This picture is consistent with that presented by Pettini et al. (2000). They used the *Starburst99* population synthesis code to fit the stellar wind P Cygni profiles of C IV and N V with a continuous star formation model having a Salpeter IMF (Salpeter 1955). From the discrepancies between the model spectra and cB58, the authors concluded that the metallicity of the stars in cB58 is subsolar by a factor of a few and closer to that of
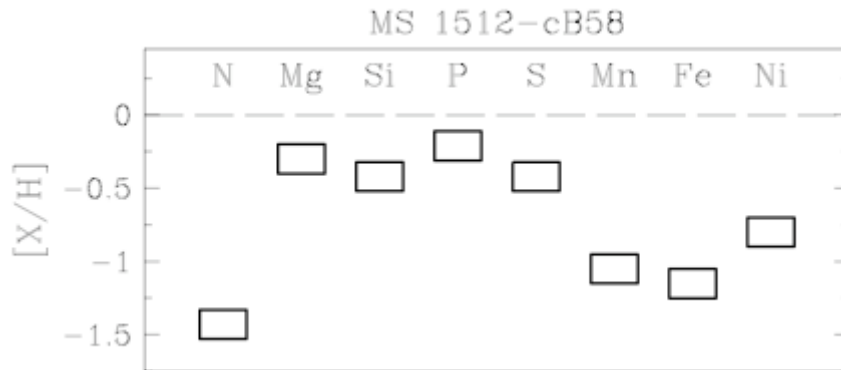
Figure 1.11 Measurements of the elemental abundances in the interstellar medium of cB58. This illustrates the detail with which we can study gravitationally lensed LBGs. The height of the boxes reflects the $\pm 0.1$ dex statistical uncertainty in the ion column densities and systematic errors are expected to be less than 0.2 dex (Pettini et al. 2002).

the Large Magellanic Cloud rather than the local Milky Way.

The most obvious and striking features of cB58 are its interstellar absorption lines. The gas with greatest optical depth is outflowing at a velocity of $v = -255$ km s$^{-1}$ with respect to the stars. These absorption lines have a velocity spread of $\sim \Delta v = 1000$ km s$^{-1}$, within a range of $-775$ to $+225$ km s$^{-1}$. Both the low-ionization and high-ionization species have nearly the same bulk outflow velocity and velocity spread. This reveals that there must be gas in front of the stars which has a wide range of velocities with respect to the majority of the outflow. Further, the fact that the metallicity is so high indicates that cB58 must have been able to retain many of its stellar products. This puts an empirical limit of how much gas has been stripped from cB58. Such restrictions are important for constraining galaxy evolution models which rely on outflows as feedback mechanisms for halting star formation. Beyond constraining galaxy models, outflows have been shown to have a significant impact on the intergalactic medium and a strong connection to the stellar mass-metallicity relation (Adelberger et al. 2003, Finlator & Davé 2008, Steidel et al. 2010).

Another critical component of LBG galaxies that was studied in detail in cB58 was the Ly$\alpha$ transition, which is shown in Figure 1.12. From Shapley et al. (2003) we know that cB58 is in the top quartile of LBGs with strong Ly$\alpha$ and interstellar absorption. As can be seen in Figure 1.8, even the strongest Ly$\alpha$ absorption composite spectrum has some Ly$\alpha$ emission; however, Shapley et al. stated that Ly$\alpha$ emission cannot be seen in the individual rest-frame UV spectra in their sample. This is a clear case where having a high resolution rest-frame UV spectrum of a LBG provides us with previously inaccessible information for studying the characteristics of LBGs. The Ly$\alpha$ transition of cB58 was modeled in detail by Schaerer & Verhamme (2008) where it was shown that cB58 has an intrinsically strong Ly$\alpha$ emission peak which is converted into a modest emission feature by radiation transfer effects and dust. This leads these authors to postulate that most LBGs have intrinsically strong Ly$\alpha$ emission but it is usually suppressed.

The essential information outlined above is inaccessible to traditional studies of high-$z$ galaxies. Only through the study of high resolution rest-frame UV spectra of LBGs can
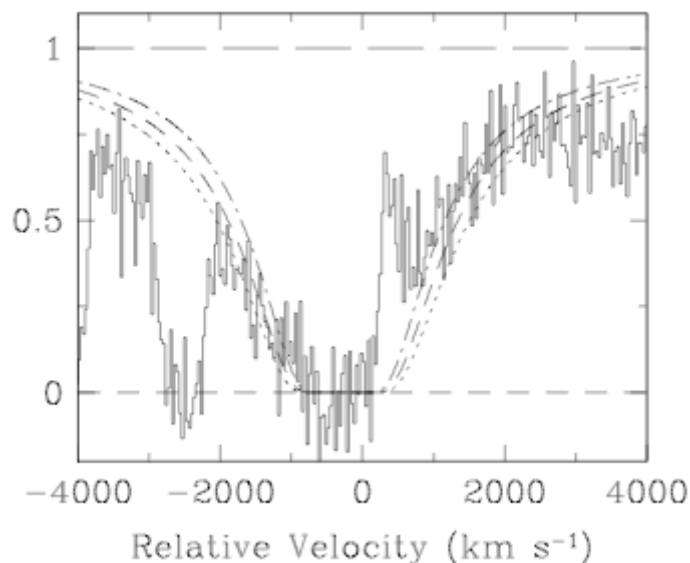
Figure 1.12 The Lyα transition of cB58. The velocity scale is with respect to the stellar redshift. The theoretical profiles superimposed on the observed spectrum are for $N(\text{H I})$ = 5.5, 7.0, and 8.5 x $10^{20}$ cm$^{-2}$ for the dash-dot, dashed, and dotted lines respectively (Pettini et al. 2002).

we gain insight into the specific structural orientation of the gas and stars, the dynamics of galaxy-wide outflows, and the composition of the stars and interstellar medium for LBGs. It is also important to extend our sample to include as many high resolution rest-frame UV spectra as possible so that we can begin to quantify the range of LBG properties. All of this information is critical to understanding the properties of the high-$z$ Universe, how those properties translate into today's galaxies, and using these properties to constrain galaxy formation models.

The work done by Schaerer & Verhamme (2008) on modeling the Lyα transition of cB58 has already been extended to 11 LBGs with strong Lyα emission and it will be interesting to see how these models hold up as more detailed information regarding Lyα spectral features in LBGs becomes available. The similarity between local starburst galaxies and LBGs is an active area of research which is being pursued by many authors (Rix et al. 2004; Haliday et al. 2008; Leitherer et al. 2001; Heckman et al. 2005) but we will only be able to take full advantage of the known properties of local starburst galaxies once we have detailed multi-wavelength information on LBGs that is of comparable quality to that available for local starburst galaxies (Heckman et al. 2001).

In the spirit of the study of cB58, this thesis includes an analysis of high resolution rest-frame UV spectra of two more highly magnified gravitationally lensed LBGs: the 'Cosmic Horseshoe' (Belokurov et al. 2007) in Chapter 3 and the 'Cosmic Eye' (Smail et al. 2007) in Chapter 4. These studies are helping to bridge the gap between understanding a single object and characterizing the properties of a whole population of galaxies.
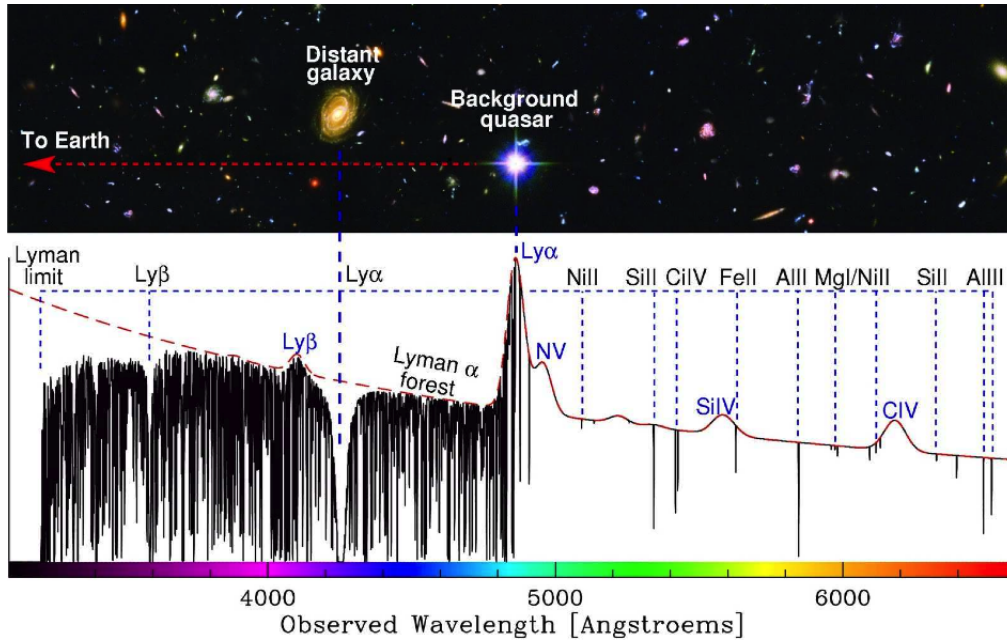
Figure 1.13 An example of a quasar absorption line system. The quasar emits a broad band continuum which is represented by the red line in the bottom panel. Quasar light is intercepted by the cold gas in a galaxy between the Earth and the quasar, as seen in the top panel. The cold gas in the intervening galaxy can be seen in the spectrum of the quasar as narrow absorption lines indicated by vertical dashed lines in the bottom panel. Image Credit: Michael Murphy, Swinburne University of Technology, Melbourne, Australia. Hubble Ultra Deep Field: NASA, ESA, S. Beckwith (STScI) and the HUDF Team.

## 1.5 Quasar Absorption Lines

A complementary technique for studying galaxies is to use quasar absorption line spectroscopy. A quasar is a supermassive black hole with an accretion disk of in-falling matter which releases a huge amount of radiation across a broad swath of the electromagnetic spectrum. Quasars have distinct emission spectra: a power law slope rising into the blue with broad emission lines. The red line in the bottom panel of Figure 1.13 represents a quasar's continuum spectrum.

A quasar illuminates other objects between it and the Earth. The top panel of Figure 1.13 illustrates the path a quasar's light takes on its journey towards the Earth. In this case, the quasar's light passes through the extended gas halo of a spiral galaxy. The galaxy causes narrow absorption lines to appear in the quasar's spectrum at the redshift of the galaxy. These absorption lines are due to numerous elements and ionization states as seen in the bottom panel of Figure 1.13. The galaxy's absorption can be distinguished from the quasar's spectrum because the quasar's continuum emission is smooth, consists of features much broader than those of the galaxy, and the two objects are offset from each other in redshift.

There are two principles which combine to make quasar absorption line studies a powerful tool for studying the Universe. The first is that a quasar's light encounters a

random sample of objects in the Universe between the quasar and the Earth. Therefore, quasar absorption lines take representative slices through the structure of the Universe as a function of time. This makes quasar absorption lines useful for studying bound structures, such as galaxies, as well as more diffuse structures like the intergalactic medium. Secondly, quasar light intercepts structures in the Universe according to their gas cross-section. Low surface brightness objects can still be identified and studied because they are illuminated by a quasar irrespective of their apparent magnitude. This is not the case with more traditional galaxy studies which select targets for spectroscopic follow-up based on their imaging properties.

A longstanding challenge has been linking specific objects to the absorption lines seen in quasar spectra. This is difficult for several reasons. Quasars themselves are bright so their light can make identifying faint galaxies in their vicinity difficult using optical imaging. Galaxies have gaseous halos that are several times more extended than their stellar component. Only the stellar component of a high redshift galaxy is seen in optical imaging so the galaxy causing the intervening absorption lines will be offset from the quasar, complicating linking a galaxy to a quasar absorption line system.

Despite these challenges, much work has been done linking galaxies to quasar absorption line systems. The Mg II $\lambda\lambda\,2796, 2803$ doublet is regularly used to find galaxies through their quasar absorption lines. There are several reasons that this doublet is particularly suited to this. As it is a doublet, this transition is easily identified in quasar spectra. The oscillator strength of this transition is high so it is detectable even in low column densities of gas. Its wavelength makes it accessible to ground-based optical spectroscopy for a wide range of redshifts ($z \sim 0.4 - 2.2$) which covers about 6 billion years of cosmic development. Figure 1.14 demonstrates the wide array of Mg II absorption profiles found along sightlines to quasars and the galaxies associated with the absorption.

The strength of Mg II absorption in quasar spectra has been shown to be correlated with different types of galaxies. The strongest Mg II absorption systems, those which are saturated over several hundred km s$^{-1}$, select for galaxies with the highest neutral hydrogen column density, N(HI) $> 2 \times 10^{20}$ cm$^{-2}$: damped Ly$\alpha$ systems (DLAs). DLAs have been shown to be faint ($\sim 0.1$ L$^*$) and to have a wide range of galaxy morphologies (Churchill et al. 2000; Rao & Turnshek 2000; Rao et al. 2011). These galaxies are the neutral hydrogen storehouses of the Universe with very little star formation activity. Mg II absorption systems which have more complex kinematics with multiple saturated absorption components have been linked to Lyman limit systems (N(HI) $> 2 \times 10^{17}$ cm$^{-2}$). These galaxies are normal galaxies with luminosities between 0.1 L$^*$ and 3 L$^*$ (Steidel, Dickinson & Persson 1994; Churchill & Vogt 2001; Rao et al. 2011). Finally, the weakest, least kinematically complex Mg II absorbers are associated with sub-Lyman limit systems (N(HI) $< 6 \times 10^{16}$ cm$^{-2}$). Galaxies such as these range from regular bright galaxies to dwarf galaxies (Churchill & Charlton 1999; Rigby, Charlton & Churchill 2001). Selecting for galaxies based on Mg II absorption in quasar spectra results in galaxies covering a wide range of neutral hydrogen column density and kinematic properties. Galaxy properties, such as inclination angle, distance from the background quasar (the impact parameter), and complex gas structures (both in geometry as well as in ionisation), and their relationship to the observed Mg II absorption profiles are also active areas of research (Rao et al. 2011; Kacprzak et al. 2011 and references therein).

Figure 1.15, reproduced from Steidel et al. 2002, is an excellent illustration of the
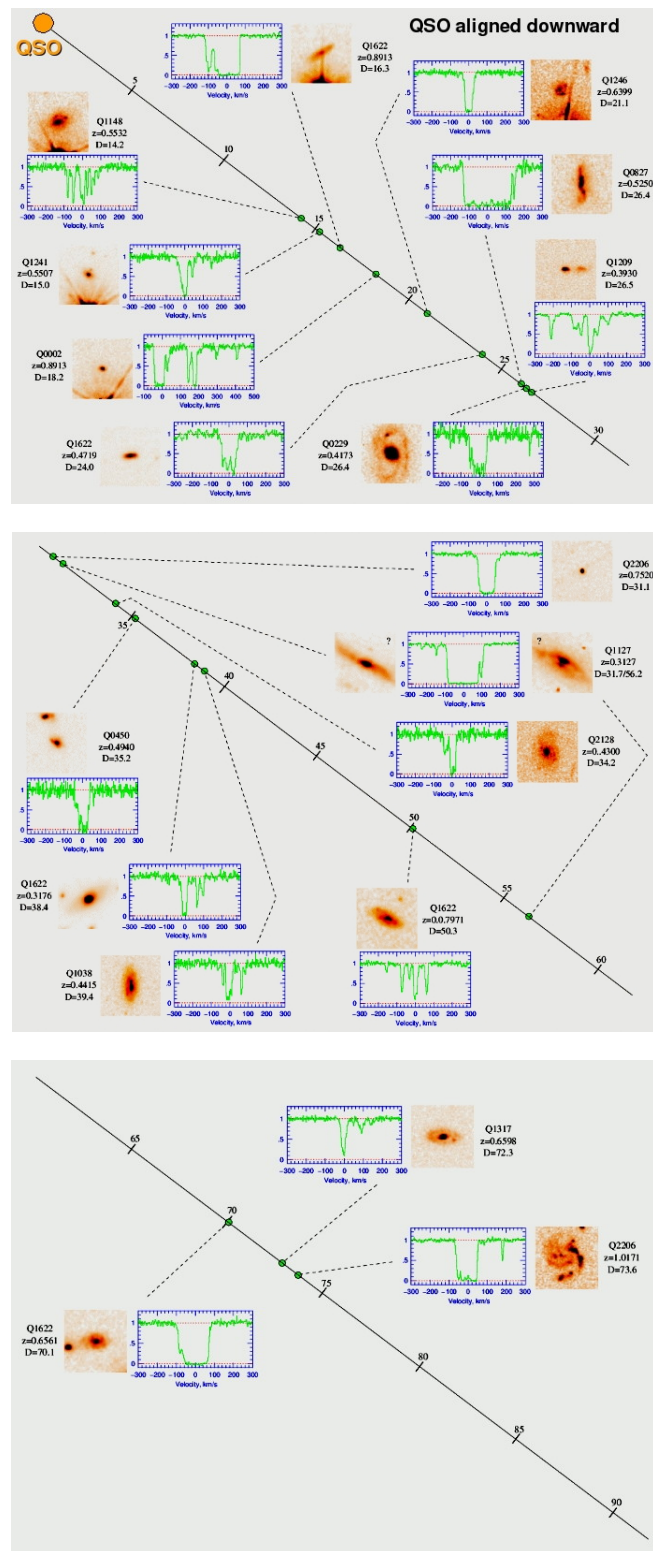
Figure 1.14 This illustrates the wide variety of Mg II absorption profiles and galaxy morphologies found along quasar sightlines. The diagonal line in the middle of each panel represents the quasar's sightline. Numbers along the sightline are distances from the quasar in kiloparsecs. Image source: Chris Churchill talk "MgII Absorption Through Galaxies at Intermediate Redshift"

link between quasar absorption lines and galaxies. The right middle panel plots the Mg II absorption seen in the spectrum of Q1038+0625, the quasar labeled in the top left panel. Note that this absorption is strong and easily detected. Spectroscopic follow-up confirmed that the galaxy labeled G1 in the bottom left panel is at the same redshift as the quasar absorption lines.

In Chapter 6 I present a catalog of Mg II absorption lines found in the spectra of quasars. This catalog has been used to study the properties of galaxies, including those with extreme outflows (Nestor et al. 2009) and their star formation activity (Ménard et al. 2011), among other uses.
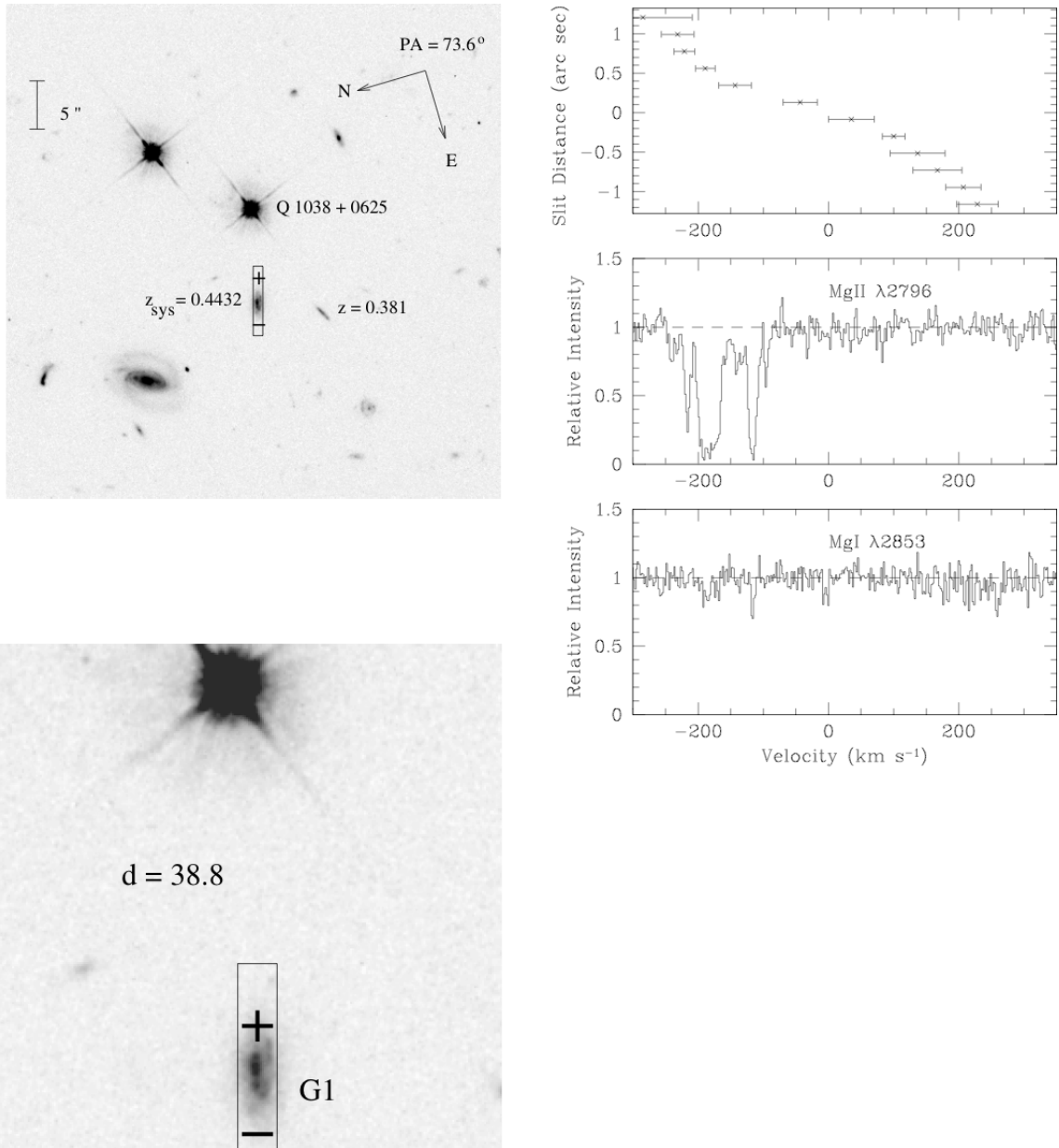
Figure 1.15 Figure 1 from Steidel et al. (2002). This illustrates the link between a galaxy and absorption seen in the spectrum of a quasar. The two images on the left show the galaxy causing the absorption lines plotted in the bottom two figures on the right. The plot in the upper right illustrates the rotation curve for the galaxy indicated in the images.

## 1.6 Organisational Notes

This thesis seeks to build upon the studies outlined above by adding to our understanding of galaxies from the young Universe. In the spirit of the study of cB58, this thesis includes an analysis of high resolution rest-frame UV spectra of two more highly magnified gravitationally lensed LBGs: the 'Cosmic Horseshoe' (Belokurov et al. 2007) and the 'Cosmic Eye' (Smail et al. 2007). Low resolution spectroscopy of a statistically significant sample of BX/BM galaxies is analyzed to assess the spread of galaxy properties. Finally, the largest publicly available catalog of Mg II quasar absorption lines is created for the study of structures spanning nearly half the age of the Universe.

**Chapter Two:** *Instruments and Data Processing*
This chapter describes the instruments and data processing techniques I have used for the observations described in this thesis.

**Chapter Three:** *The Ultraviolet Spectrum of the Gravitationally Lensed Galaxy 'The Cosmic Horseshoe': A Close-up of a Star-forming Galaxy at $z \sim 2$*
This work is published as Quider et al. 2009, MNRAS 398, 1263, and was carried out in collaboration with the paper co-authors: Alice Shapley, Max Pettini, and Charles Steidel.

**Chapter Four:** *A Study of Interstellar Gas and Stars in the Gravitationally Lensed Galaxy 'The Cosmic Eye' from Rest-Frame Ultraviolet Spectroscopy*
This work is published as Quider et al. 2010, MNRAS 402, 1467.
It was carried out in collaboration with the paper co-authors: Alice Shapley, Max Pettini, Charles Steidel, Daniel Stark.

**Chapter Five:** *Absorption and Emission from Galaxies at $1 < z < 2$*
This work is in preparation for publication.

**Chapter Six:** *The Pittsburgh SDSS Mg II Quasar Absorption-Line Survey Catalog*
This work is published as Quider et al. 2011, AJ 141, 137.
It was carried out in collaboration with the paper co-authors: Daniel Nestor, David Turnshek, Sandhya Rao, Anja Weyant, Eric Monier, and Joseph Busche.

**Chapter Seven:** *Discussion and Conclusion*
This chapter reflects upon the discoveries presented in this thesis and suggests some avenues for future work, including projects that are already underway.

For the remainder of this thesis, unless otherwise, noted, all wavelengths are reported in Angstroms (Å) and the cosmology used is $\Omega_M = 0.3$, $\Omega_\Lambda = 0.7$, and $H_0 = 70 \, \mathrm{km \, s^{-1} \, Mpc^{-1}}$.

# 2

# Instruments and Data Processing

O BSERVATIONAL astronomy necessarily requires the use of telescopes to record signals from the Universe. The work in this thesis solely explores spectroscopy of electromagnetic radiation in the optical band ($\lambda \sim 4\,000\,\text{Å} - 10\,000\,\text{Å}$, observed). In this chapter I will discuss the telescopes and instruments I have used for the observations described in this thesis. Further, I describe the data processing techniques used on these data.

## 2.1 Keck Telescopes

The W. M. Keck Observatory sits atop Mauna Kea at 13,796 feet above sea level in Hawai'i, USA (http://keckobservatory.org/). This observatory, which saw first light in 1993, is home to two twin telescopes aptly named the Keck telescopes, shown in Figure 2.1. Each telescope has a 36-segment primary mirror that is a total of 10 meters in diameter, making them the largest of their kind in the world. This amazing light-collecting capacity means that they can observe fainter, and therefore more distant, objects in the Universe.

Telescopes are used in conjunction with specialized instruments which manipulate and record the light collected by a telescope. For the work in Chapters 3 and 4 on the Cosmic Horseshoe and the Cosmic Eye, respectively, I have used the Keck II telescope in conjunction with the Echellette Spectrograph and Imager (ESI; Sheinis et al. 2000, 2002) instrument. The observations reported in Chapter 5 were made using the DEep Imaging Multi-Object Spectrograph (DEIMOS; http://www2.keck.hawaii.edu/inst/deimos/) instrument which is also on the Keck II telescope. In the next two sections I will discuss these two instruments and my use of them for the work reported in this thesis.

### 2.1.1 Echellette Spectrograph and Imager (ESI)

As implied by its name, ESI can be used for either direct imaging or spectroscopy. I have used ESI in echellette spectroscopy mode. In this mode the spectroscopic slit is 20-arcsec long. There are a few features which make ESI's echellette spectroscopy mode
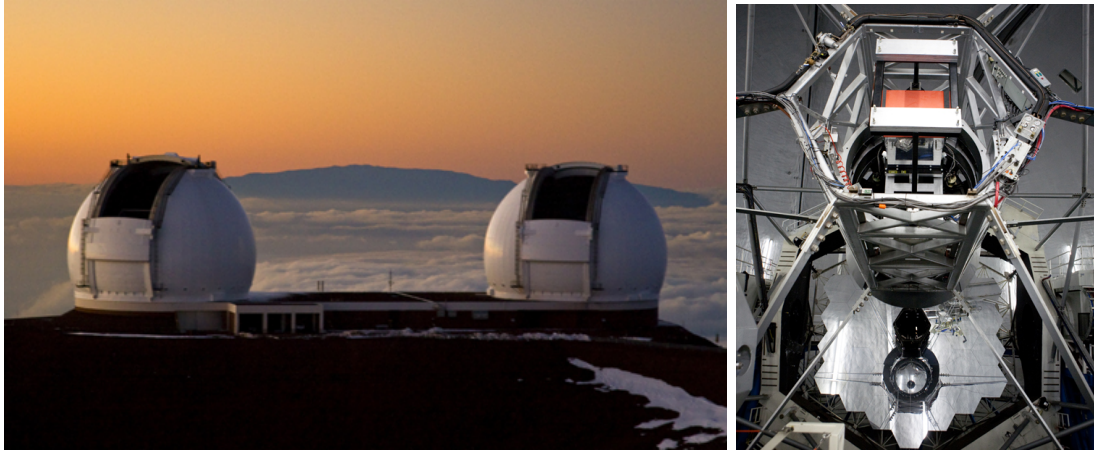
Figure 2.1 *left*: These are the iconic domes of the twin Keck telescopes atop Mauna Kea in Hawai'i, USA. Note how these telescopes are above the cloud line, indicating the altitude of the observatory. *right*: This is the Keck II telescope. The segmented 10 meter primary mirror is clearly visible in the bottom-center of the image. Source: http://keckobservatory.org.

ideally suited to detailed rest-UV spectroscopy of $z \sim 2 - 3$ galaxies. ESI's wide spectral coverage of $\sim 4\,000$ to $10\,000\,\text{Å}$, with spectral orders running from 15 to 6, respectively, is well-matched to the rest-frame UV wavelengths of galaxies at $z \sim 2 - 3$. ESI has a design optimized for efficiency. Figure 2.2 illustrates that there are few opportunities for light loss within the instrument, a contributing factor to its high performance. This is an instrument with high efficiency across many spectral orders, with a peak efficiency of nearly 40% at $\lambda \sim 6\,000\,\text{Å}$, as seen in Figure 2.3 (Sheinis et al. 2002). Therefore, ESI is a good instrument for observing faint objects as a fair amount of the collected light is actually output as a spectrum. Finally, a resolution of $R = \lambda/\Delta\lambda = 4\,000$ can be obtained with a $1\,\text{arcsec}$ slit. This results in some of the most detailed spectra of high redshift galaxies to date.

There are several shortcomings of this instrument within the context of my observations. ESI's CCD has a defective column which slices through parts of orders 13 and 14, as seen in Figure 2.4. This renders a $\sim 70$ Å wide portion of the spectrum unusable within the wavelength range $\sim 4\,450 - 4\,600$ Å depending on where the object falls in the slit. While this instrument has wavelength coverage out to $10\,000\,\text{Å}$, the instrument efficiency drops precipitously after $\sim 9\,000\,\text{Å}$ (see Figure 2.3). Combining this drop in efficiency with the prevalence of night sky emission in the reddest spectral orders, these spectra become unreliable after $\sim 9\,000\,\text{Å}$.

There are also instrumental shortcomings that specifically relate to the extended nature of my objects of interest. The length of the spectroscopic slit influenced my slit placement. It was important to include sufficient sky around my objects so that adequate background subtraction could be executed. This proved particularly challenging for the Cosmic Horseshoe, a 10-arcsec diameter nearly-complete Einstein ring (see below for further details of the data reduction for this spectrum). The lack of an integral field spectrograph was also limiting for my observations. Being constrained to a straight slit meant that I was unable to collect the maximum amount of light from the curved galaxy
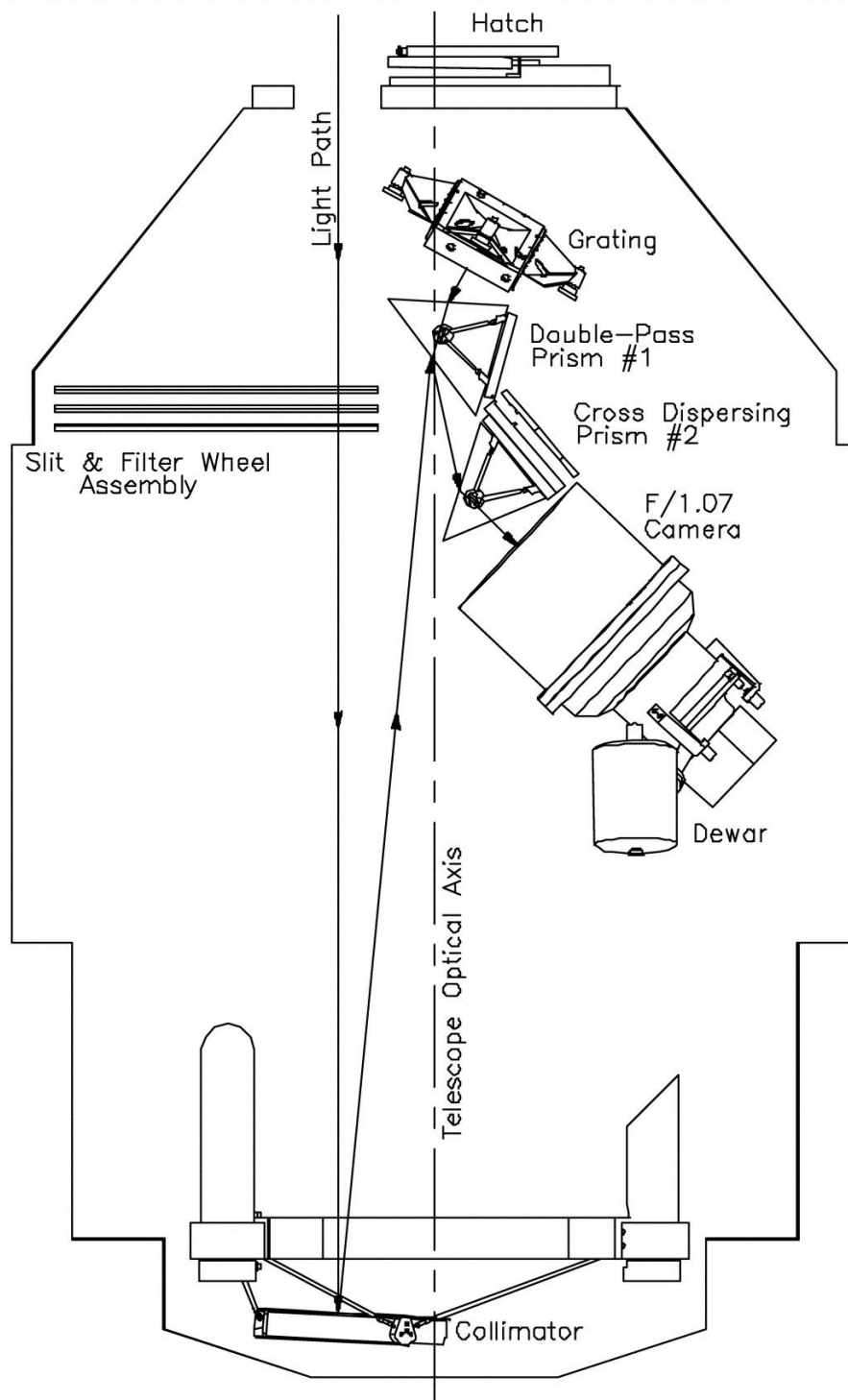
Figure 2.2 ESI was designed with efficiency in mind, as evidenced by this schematic of the instrument (Fig. 1 of Sheinis et al. 2002). Manipulation of the light was intentionally kept to a minimum to reduce light loss.
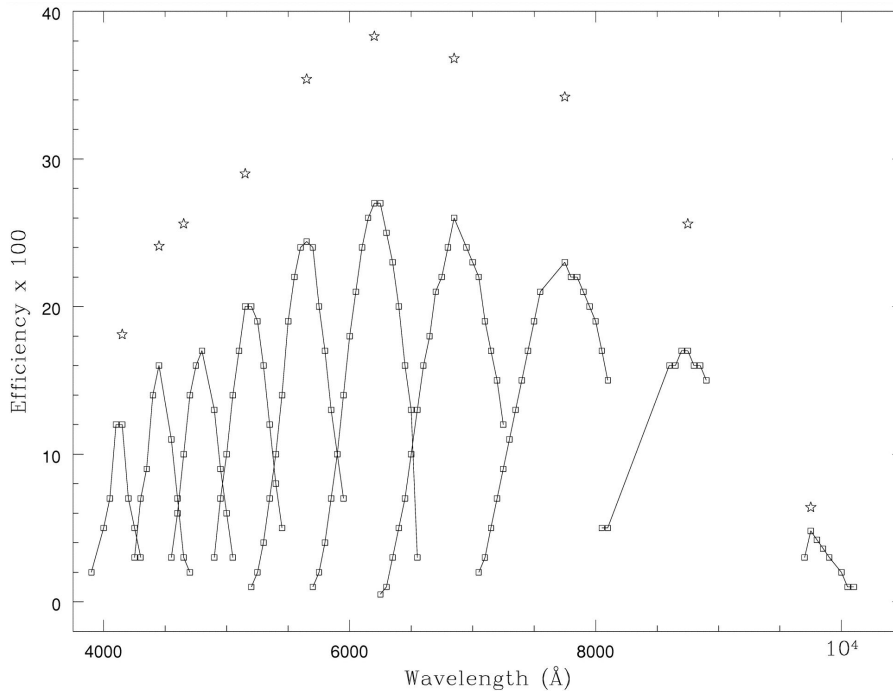
Figure 2.3 The efficiency of ESI in echellette mode can be seen from the measured through-put for each order (Fig. 13 of Sheinis et al. 2002). This figure shows the efficiency of ESI before (star symbols) and after (boxes) accounting for telescope light loss. This instrument remains remarkably efficient across many orders.

arcs. Not only did this reduce the potential S/N of my spectra, it did not allow me to take full advantage of the galaxies' gravitationally lensed nature, where different portions of the arcs can correspond to different regions of the source galaxy. Collecting spectra along the arcs may have given me some insight into the small-scale (down to $\sim 100$ pc) variations within these galaxies.

In the following two sections I will describe the observations and data reduction procedures executed for the two lensed galaxies I analyzed for this thesis: the Cosmic Horseshoe and the Cosmic Eye. The data reduction methods used for the two galaxies were very similar. Therefore, in the interest of avoiding duplication, I have chosen to provide a detailed account of the data reduction process for the Cosmic Horseshoe and only to point out deviations from this procedure when discussing the Cosmic Eye.

**Cosmic Horseshoe: Observations and Data Reduction**

The data were collected over two nights (2008 March 6 and 7 UT) in mostly sub-arcsecond seeing; the total exposure time was $36100\,\mathrm{s}$, made up of a number of $1800\,\mathrm{s}$ or $2000\,\mathrm{s}$-long individual integrations. The ESI slit was oriented at sky P.A. = 10.8 degrees East of North, and positioned so as to encompass the two brightest knots in the Einstein ring, as shown in Figure 2.5. The northern knot, labelled 'Aperture 1' in the Figure, is knot 'A' in the labelling of the features by Belokurov et al. (2007), while 'Aperture 2' corresponds to their knot 'D'. Both knots are due to the same object in the source plane, although 'Aperture 1' may include a small contribution from the fainter component $\sim 0.7\,\mathrm{arcsec}$
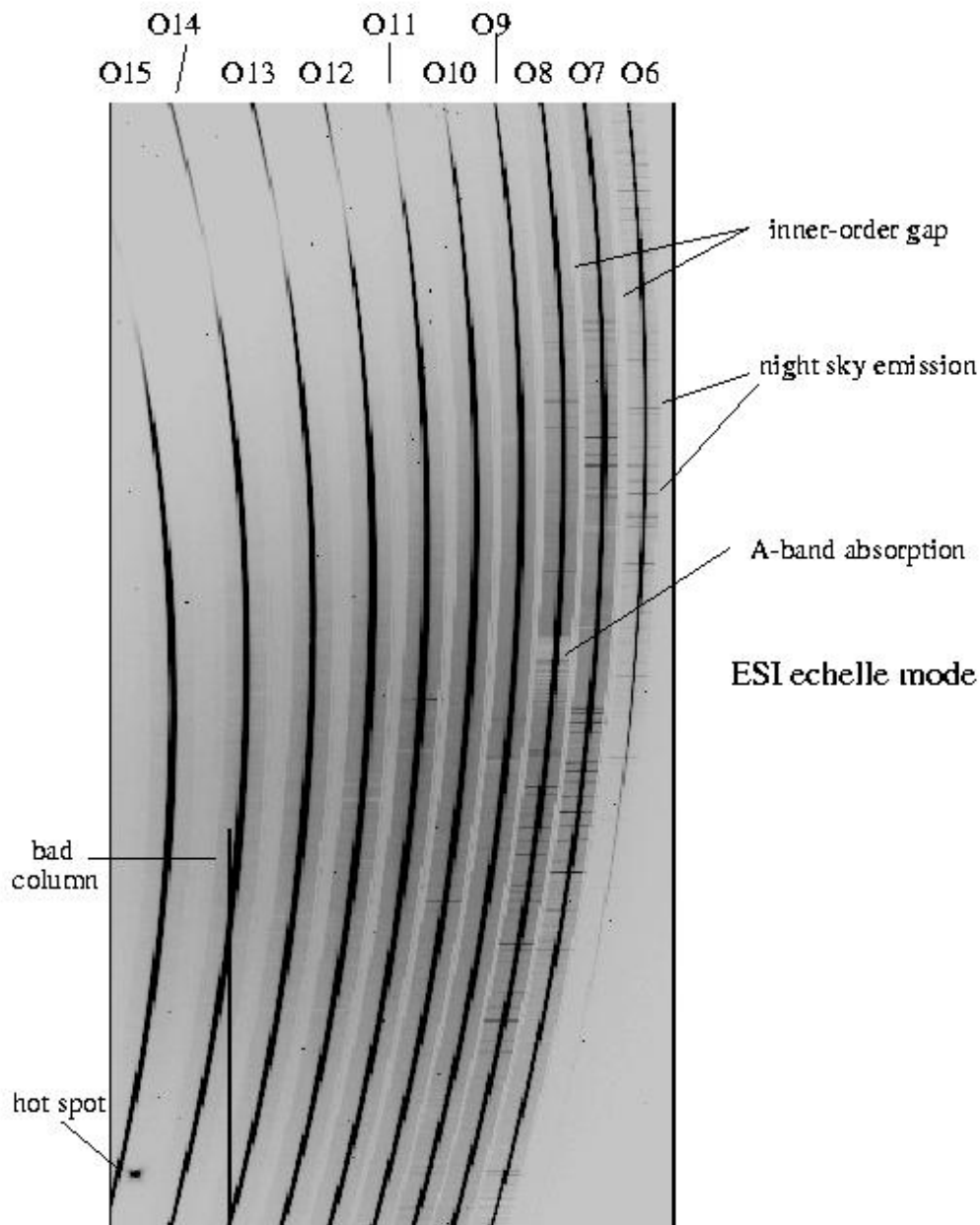
Figure 2.4 This is an example ESI two-dimensional spectrum. Relevant features are labeled. The long black curved lines are the science spectrum. The short dark horizontal lines are night sky emission lines. The order numbers are increasing from the right, starting with order 6, and the wavelength scale increases from bottom to top. Numerous of the challenges inherent in processing these data are apparent, including curved spectral orders, CCD defects, and the presence of night sky emission. Source: http://www2.keck.hawaii.edu/inst/esi/echmode.html.
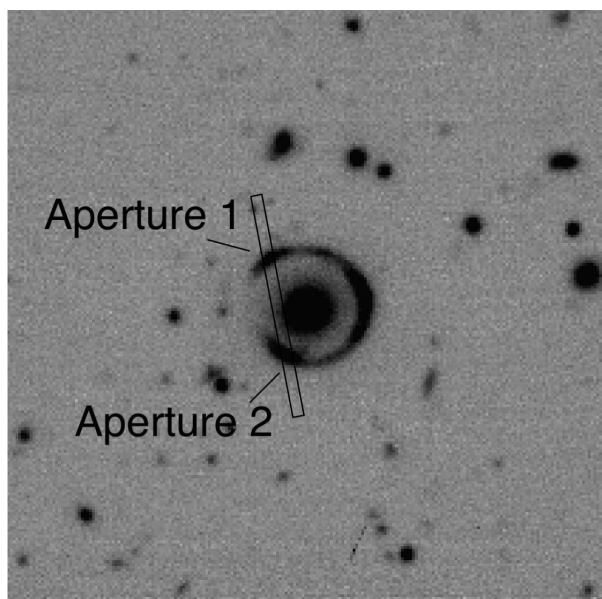
Figure 2.5 *R*-band image of the Cosmic Horseshoe obtained with FORS2 on the Very Large Telescope of the European Southern Observatory (courtesy of L. J. King). North is up and East is to the left. Superposed on the image is the $1.0 \times 20$ arcsec entrance slit of ESI used for the observations reported here.

to the North of the main source of the ring (Dye et al. 2008). The location of the ESI slit is the same as that of the NIRSPEC observations by Hainline et al. (2009).

The data were processed with standard tasks from the Image Reduction and Analysis Facility (IRAF) software package. For the remainder of this section, italicized words refer to IRAF tasks. The complete two-dimensional (2-D) spectrum was recorded on a single CCD chip. The ratio of the gain on the left side of the chip to the gain on the right side of the chip is 0.93451. The gain was equalized across the chip and the overscan regions were removed using *ccdproc*. Each individual 2-D spectrum was geometrically corrected (to correct for the spectral curvature of each echellette order). This was done by fitting a function to the curvature of each order and determining the lateral shift necessary to align the pixels into a straight line. For ease of further processing, each 2-D spectrum was isolated into its own file. Flat-fielding was done using a response-corrected flatfield and *ccdproc*. The spectra were corrected for cosmetic defects and cosmic-ray affected pixels using *fixpix*. In the next step, all of the images thus processed were co-added using *imarith* into a total 2-D frame which was then background subtracted using *background*. A 2-D variance image was created for each order using the individual exposures.

The background subtraction process was non-trivial for this object. The first hurdle, as mentioned earlier, is that the spectrograph slit was 20 arcsec long and the object subtended 10 arcsec. This left little sky beyond the edge of the object which could be used for background subtraction. The necessity of maintaining a usable amount of sky on either side of the object reduced my ability to offset the object in the spectrograph slit. The second, and more significant, complication with the background subtraction is that the slit placement, shown in Figure 2.5, resulted in some light from the lensing luminous red galaxy (LRG) entering the slit. The light from the LRG is clearly visible
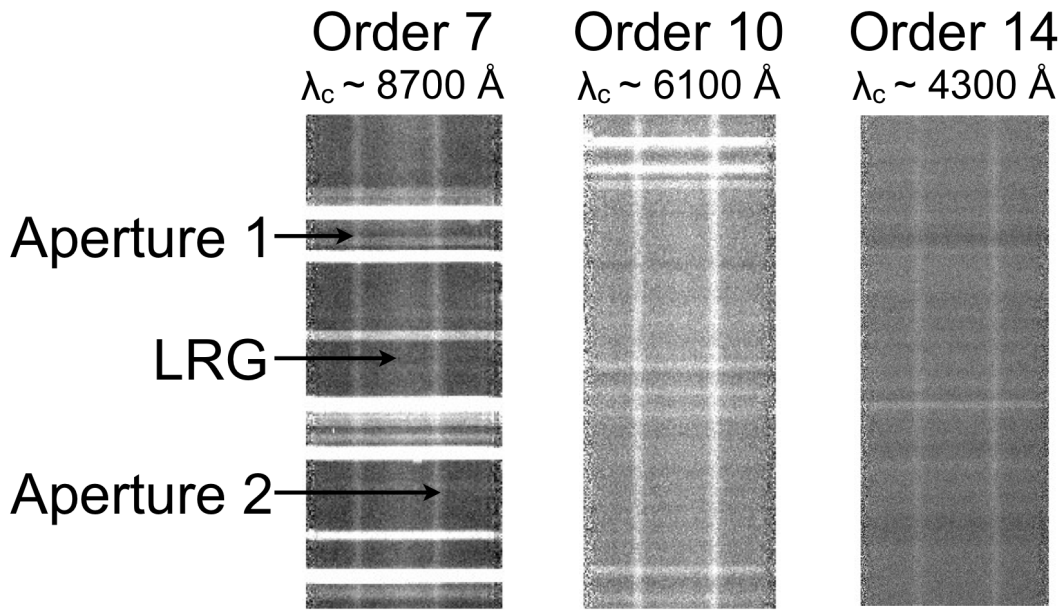
Figure 2.6 The three panels are portions of the 2-D spectrum of the Cosmic Horseshoe for three orders spanning ESI's wavelength coverage. The central wavelength of the order is given above each spectrum. This figure illustrates the contribution to the background due to the LRG. The vertical white lines are spectra of Apertures 1 and 2 of the Cosmic Horseshoe with the LRG's spectrum in between. Refer to Figure 2.5 for the spectroscopic slit alignment. The LRG's light is most prominent in the reddest orders and it negligibly contributes to the background in the bluest orders. The horizontal white lines are night sky emission lines.

above the sky at the longer wavelengths of the ESI range. Figure 2.6 shows segments of the 2-D spectra of orders 7, 10, and 14 which span the wavelength range of ESI. The LRG can be clearly identified in order 7 (which has a central wavelength of $\lambda_c \sim 8\,700\,\text{Å}$) and it loses prominence by order 14 ($\lambda_c \sim 4\,300\,\text{Å}$). We used a higher order spline function fit to carefully selected regions of the background, both beyond and within the arc, to remove the LRG light during background subtraction. To check whether the background subtraction properly accounted for the LRG light, I compared the profiles of the strongest, saturated absorption lines from the interstellar gas within the Cosmic Horseshoe source galaxy which can be found throughout the spectrum. I reasoned that the longer wavelength absorption lines will be most affected by the LRG light because the LRG is most apparent in the redder orders. If the background is undersubtracted, the strongest ISM absorption lines will have a peak depth that is shallower than that of the shorter wavelength absorption lines; an oversubtracted background will cause the longer wavelength ISM absorption lines to have a peak depth that is greater than the saturated absorption lines at the shorter wavelengths. I found that the strongest absorption lines throughout the spectrum were consistently at a similar depth, giving me confidence in the background subtraction.

Finally, two 1-D galaxy spectra were extracted, one for each 'Aperture', using *apall*. *Scombine* merged the 10 echellette orders of ESI into one continuous spectrum, with

weighted addition of portions of adjacent orders which overlap in wavelength. Two 1-D variance spectra were extracted for each 'Aperture' using the same extraction width and trace as was used for the galaxy spectrum extraction. The square root of each variance spectrum was taken, resulting in a 1-D root mean square spectrum for each 'Aperture'. The galaxy and error spectra were calibrated using the spectra of Cu-Ar and Hg-Ne-Xe hollow-cathode lamps which were processed in the same way as that of the Horseshoe. The wavelength solution is accurate to at least one-fifth of a pixel. We applied a heliocentric correction to account for the Earth's motion around the Sun and we also converted our wavelength scale from air wavelengths to vacuum wavelengths.

I compared carefully the 1-D spectra of Aperture 1 and Aperture 2 to look for differences which one may expect to be revealed by the gravitational magnification of any spatial structure in the source, but found none. Neither dividing one spectrum by the other nor subtracting one from the other revealed features more significant than the noise. As discussed in Chapter 3, this is also the case for the Ly$\alpha$ emission line which (a) has the highest signal-to-noise ratio (S/N), and (b) is most sensitive to geometrical effects, being resonantly scattered. The only difference between the two apertures is in the total flux: emission line and continuum are uniformly higher by a factor of 1.19 in Aperture 2 than in Aperture 1, as seen in Figure 3.9. Thus, in order to improve the S/N, the two spectra were averaged and the resulting spectrum mapped onto 0.5 Å bins.

This final spectrum has a resolution (full width at half maximum) FWHM = 75 km s$^{-1}$, sampled with three wavelength bins at 6000 Å, as determined from the widths of narrow emission lines from the Cu-Ar and Hg-Ne-Xe hollow-cathode lamps used for wavelength calibration, whose spectrum was processed in the same way as that of the Horseshoe. From the rms deviation of the data from the mean, I measured an average S/N $\simeq$ 8 per 0.5 Å wavelength bin between $\sim$ 4000 and $\sim$ 7500 Å ($\sim$ 1200 and $\sim$ 2200 Å in the rest frame), with a factor of $\sim$ 50% variation in S/N across each echellette order. At the wavelengths of the Ly$\alpha$ emission line the S/N rises to a maximum S/N = 44 per 0.5 Å bin.

I attempted to put our spectrum on an absolute flux scale by reference to those of three flux-standard stars recorded during the two nights of observation, but found a scatter of $\pm20\%$ in the flux calibration among the three stars. Adopting the mean value of the three flux scales, I deduced a mean $\langle f_\nu \rangle = 8.3 \times 10^{-29}$ erg s$^{-1}$ cm$^{-2}$ Hz$^{-1}$ between 4200–5485 Å. This wavelength interval corresponds to the FWHM of the transmission curve of the Gunn $g$ filter through which Belokurov et al. (2007) measured $g = 20.1$ (corresponding to $\langle f_\nu \rangle = 3.3 \times 10^{-28}$ erg s$^{-1}$ cm$^{-2}$ Hz$^{-1}$) for the entire Einstein ring. Thus, if the flux calibration is correct, the ESI slit captured a fraction $0.25 \pm 0.05$ of the light of the Cosmic Horseshoe, corresponding to an effective magnitude within the two Apertures of $g = 21.6 \pm 0.2$. Being able to record the spectrum of an object this faint, with the S/N and resolution we obtained, is a demonstration of the power of combining the Keck II telescope and ESI.

## The Cosmic Eye: Observations and Data Reduction

ESI was used to record the rest-frame UV spectrum of the Cosmic Eye on the nights of 2007 September 13 and 14 UT. On the first night, the 1″ wide slit of ESI was positioned on the northern arc of the Cosmic Eye at position angle P.A. = 86.44° (see Figure 2.7); on
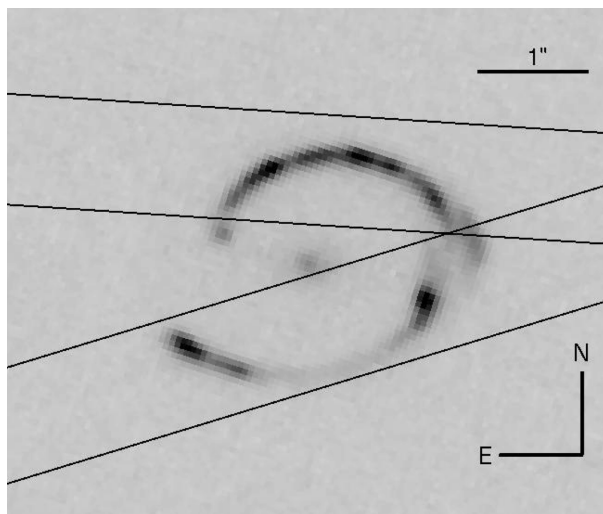
Figure 2.7 HST/ACS F606W image of the Cosmic Eye. The straight lines indicate the two placements of the $1.0 \times 20''$ entrance slit of ESI used for the observations reported here.

the second night the light of the southern arc at P.A. $= 287.12°$ was recorded. The total exposure time *for each arc* was $16\,000\,\text{s}$, broken up into eight $2000\,\text{s}$ long integrations on the ESI detector. The seeing was sub-arcsecond on both nights.

Inspection of the 2-D spectra shows that only the light from the main ring structure was recorded; the fainter extensions to the East and the West of the northern ring which, as explained in Chapter 4, are due to the secondary component of the source in the lensing model of Dye et al. (2007), were only partially covered by the slit placements (see Figure 4.1) and are in any case much fainter than the main ring structures.

The data were processed with standard IRAF tasks following the steps outlined above for the Cosmic Horseshoe; compared to that work, subtraction of the background was considerably more straightforward because in the present case light from the lensing galaxy did not fall within the ESI slit (see Figure 2.7). Nevertheless, once the data were fully reduced, I found residual flux in the core of the damped Ly$\alpha$ absorption line (see Chapter 4), amounting to $\sim 5\%$ of the continuum level. I cannot determine whether the effect is real, indicating that the damped Ly$\alpha$ line only covers 95% of the OB stars producing the continuum near $1216\,\text{Å}$, or is an artifact of errors in the determination of the background level to be subtracted. Indeed, a 5% error in the background subtraction is not an unreasonable level of error. Unfortunately, I do not have any other 'markers' in the spectrum as definitive as the damped Ly$\alpha$ line to help me assess whether this background correction, whatever its origin, is constant along the spectrum or varies with wavelength. In the circumstances, I limited myself to applying to the final one-dimensional (1D) spectrum a uniform background correction of 5% of the continuum flux.

At the S/N ratio of the present data, I could not find any significant differences between the extracted 1D spectra of the northern and southern arcs; their similarity is consistent with the lensing model of Dye et al. (2007) which shows them to be images of the same source, mostly contained within the caustic (see Figure 4 of Dye et al. 2007).[1]

---

[1] Note, however, that Smail et al. (2007) did report differences in the profiles of the interstellar

Therefore, I averaged the spectra of the two arcs and rebinned the resulting spectrum to $0.5\,\text{Å}$ bins to maximise the S/N ratio. The final composite 1D spectrum (reproduced in Figure 4.3) has an average S/N $\simeq 14$ per $0.5\,\text{Å}$ bin between 5200 and $7500\,\text{Å}$ ($1275$–$1840\,\text{Å}$ in the rest-frame of the source), and a resolution FWHM $= 75\,\text{km s}^{-1}$, sampled with $\sim 3$ wavelength bins.

## 2.1.2  DEep Imaging Multi-Object Spectrograph (DEIMOS)

DEIMOS is a medium resolution optical spectrometer with long-slit, multi-slit, and direct imaging modes. Figure 2.8 illustrates the components of the instrument. I used the multi-slit spectroscopy mode where up to 130 slitlets can be put on a single mask and observed at the same time. The spectral coverage, from $\sim 4\,100 - 11\,000\,\text{Å}$, covers the rest-frame near-UV features of galaxies with $1 \le z \le 2$, from $\text{Fe\,II}\,\lambda\,2260$ to $[\text{O\,II}]\,\lambda\lambda\,3727, 3729$. This instrument allows for a reasonable degree of flexibility in observing parameters. The main parameters that can be modified are the slitlet width, dispersion grating, and blocking filter. The width of the slitlets affects the amount of light that enters the spectrograph as well as the spectral resolution. The grating determines the pixel dispersion. Blocking filters are used to avoid order overlap. DEIMOS has filters which allow the spectrum to begin at four intervals between $4\,000\,\text{Å}$ and $5\,500\,\text{Å}$, inclusive. This flexibility in selecting the slit width, grating, and blocking filter allowed us to maximize our spectral S/N and resolution. The 29% throughput of this instrument-telescope combination makes it appropriate for observing faint objects.

DEIMOS has a few limitations which influenced my observations. The spectra are taken across two rows of four CCD chips: one row captures the blue portion of a spectrum while the other row captures the red. There is a $\sim 20\,\text{Å}$ gap in the observed frame wavelength coverage when transitioning from one chip to the next along a spectrum. There are several locations in the instrument's field of view where spectra cannot be obtained. The upper right corner suffers from severe vignetting and a central portion is blocked by the camera's shadow. These regions were avoided when making the slit mask.

The work in Chapter 5 uses DEIMOS spectra of BX/BM photometrically selected galaxies. Spectra of 147 BX-BM galaxy candidates were recorded. These spectra were drawn from the spectroscopic sample of Steidel et al. (2004). We observed one slit mask in each of three quasar fields. Not all of the BX-BM galaxy candidates for each field were observed because they all cannot fit on a single mask. Objects were given highest priority to be placed on the mask if they were bright ($R <\sim 24$, ideally) and had a known redshift in our target range ($1 < z < 2$). The remainder of the mask was completed using objects without previously known redshifts. These were preferentially brighter and selected by the BM rather than BX criteria because BM galaxies are more likely to be in the target redshift range (see Figure 1.3 for the redshift distribution of galaxies which meet the BM and BX criteria). Ultimately, the galaxies in our sample are likely to be somewhat brighter than the UV-selected sample as a whole (the mean $R$ magnitude of BM galaxies is $R \sim 24.5$, including those both with and without known redshifts).

As will be discussed in Chapter 5, only those 96 galaxies with a spectroscopic $z >$

---

absorption lines between the northern and southern arcs. The fact that I do not confirm such differences could be due either to the higher S/N ratio and resolution of our spectra, or to the different slit positions employed in the two studies.
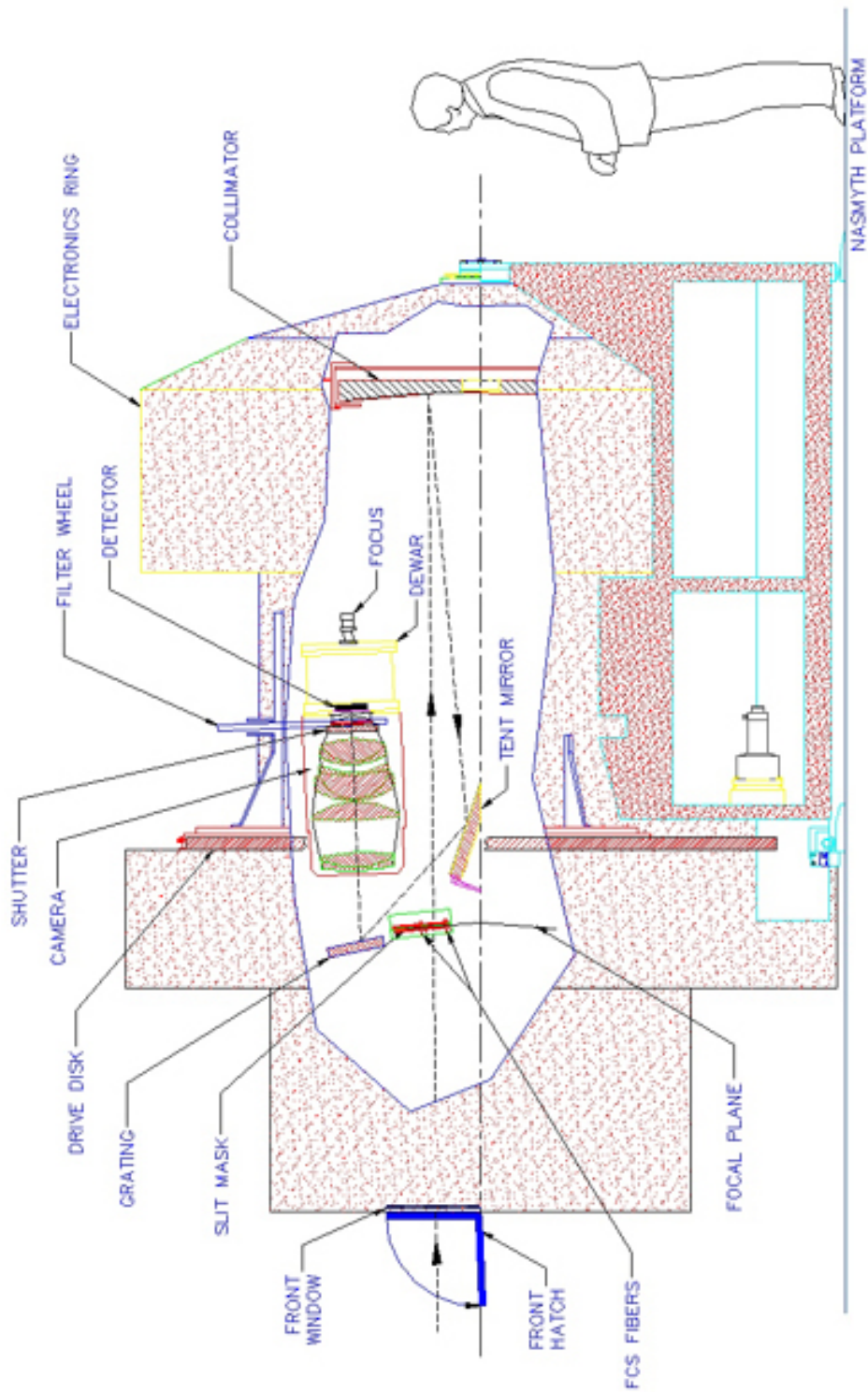
Figure 2.8 A schematic of the DEIMOS instrument that operates on the Keck II telescope. Here the light path through the instrument as well as the components of the instrument are shown. Image source: http://loen.ucolick.org/Deimos/mechanical_manual.htm.

Table 2.1 BX/BM Galaxies Observation Parameters

| Quasar Field ..................... | Q1623 | Q1700 | Q2343 |
|---|---|---|---|
| Observation Date (UT) ... | 01, 03-04 Aug 2008 | 22-24 Aug 2009 | 01 Aug 2008; 21-24 Aug 2009 |
| Exposure Time (s) ........... | 34 200 | 27 000 | 39 600 |
| Grating (lines mm$^{-1}$) ...... | 600 | 600 | 600 |
| $\lambda_{central}$ (Å) ....................... | 7500 | 7200 | 7500 |
| Blocking Filter ................. | OG550 | GG495 | OG550 |
| Slit Width ($''$) ................. | 1.0 | 1.2 | 1.2 |

1 were used for my thesis work. These galaxies were distributed among three quasar fields: Q1623, Q1700, and Q2343. The observing conditions and instrument setup varied between the fields and are detailed in Table 2.1. The seeing was sub-arcsecond for nearly all of these observations and all of these observations were taken during the first half of the night listed for the Observation Date in Table 2.1.

The spectra were processed primarily using the DEEP2 data processing pipeline (http://www2.keck.hawaii.edu/inst/deimos/pipeline.html). The pipeline is written in Interactive Data Language (IDL) and it was developed at UC Berkeley. It is based on the Sloan Digital Sky Survey spectral reduction pipeline (see next section) so it is well-tested and highly automated. Emergent from the pipeline were 1-D air wavelength-calibrated galaxy, 1$\sigma$ error, and sky spectra. The galaxy and error spectra were put on a relative flux scale using the IRAF software package. The calibration was done using standard stars observed in the same manner as the galaxies. This step was done solely to remove the instrument signature from the data, thereby facilitating continuum normalization.

The telluric absorption bands due to molecular oxygen at $\sim 6\,800$ Å and $\sim 7\,500$ Å needed to be removed to simplify continuum normalization. Telluric correction is a delicate and labor-intensive process, particularly if the intention is to measure galaxy features that fall within the telluric absorption bands. As my intention was to improve continuum fitting, it was not critical that my spectra be precisely corrected for telluric absorption, only that the general shape of the telluric features be removed from the individual galaxy spectra. Telluric features are sensitive to the amount of atmosphere through which the light of an object is being observed. Usually telluric correction is done by scaling the strength of the telluric absorption seen in a standard star spectrum to the absorption strength seen in an object's spectrum. In this case, the galaxies were observed over a range of air masses so a single standard star observation taken at a single air mass was not a good match to the telluric feature strength in our individual galaxy spectra. We found that a composite observed-frame galaxy spectrum for each field gave a better measurement of the shape of the telluric features. Using these composite spectra, we created a template telluric feature for the galaxies in each of the three fields and corrected individual galaxy spectra using these templates.

It is unusual to correct for telluric features in this manner so a more in-depth discussion of this procedure is warranted. I used IRAF to create a composite, observed frame galaxy spectrum of all the galaxies in each quasar field, resulting in one high SNR composite

Table 2.2 SDSS Filters

| SDSS Filter | $u$ | $g$ | $r$ | $i$ | $z$ |
|---|---|---|---|---|---|
| $\lambda_{ave}$ (Å) | 3551 | 4686 | 6165 | 7481 | 8931 |
| $m_{limit}$ | 22.0 | 22.2 | 22.2 | 21.3 | 20.5 |

galaxy spectrum per quasar field. The telluric absorption features seen in this composite spectrum represented the average telluric features for the galaxies in a given quasar field. In principle the telluric features in each galaxy spectrum, for a given quasar field, should be very similar because all of the galaxies on a mask are observed at the same time, through the same atmospheric conditions. Each composite galaxy spectrum was normalized and smoothed. Portions of the spectrum which were outside of the telluric bands were forced to have a normalized flux value of 1, leaving the telluric bands as the only deviations from continuum. The resulting spectrum served as the template telluric spectrum for each quasar field. The template was then divided into each of the galaxy and error spectra. This method for removing the general shape of the telluric absorption features from each galaxy's spectrum was sufficient for improving the continuum fit to an individual galaxy spectrum (see Chapter 5 for a discussion of the continuum fitting procedure).

Finally, the individual spectra were put onto a vacuum wavelength scale and rebinned. The night sky lines were oversampled so we rebinned by a factor of two to increase the S/N. The final pixel scale is 1.25 Å per pixel in the observed frame.

## 2.2 Sloan Digital Sky Survey (SDSS)

The Sloan Digital Sky Survey (SDSS) is an imaging and spectroscopic survey covering more than one quarter of the night sky (York et al. 2000). It began in 2000 and is still ongoing. The survey uses a 2.5-meter diameter telescope, seen in Figure 2.9, at Apache Point Observatory in New Mexico, USA (Gunn et al. 2006). SDSS releases the survey data to the public through scheduled data releases. For my work in Chapter 6, I used Data Release Four (Adelman-McCarthy et al. 2006). Therefore, the following discussion will relate to SDSS DR4, which may include information that is not accurate for other data releases.

Images of the survey area were taken in five bands (SDSS filters $u$, $g$, $r$, $i$, $z$) with a short effective exposure time of 54 seconds for each filter. The SDSS identifies an object if the peak flux is at least 5-sigma above the sky level. Table 2.2 presents the average wavelength and 95% completeness limiting apparent magnitude for each filter. 180 million unique objects within 6670 square degrees were imaged.

Objects were algorithmically selected for spectroscopic follow-up based primarily on their imaging colors and morphology. This is done using a pipeline named "target" within the suite of spectroscopy pipelines. SDSS has two multi-object fiber spectrographs which can take a total of 640 spectra at once. The resulting spectra have a wavelength range of 3 800 to 9 200 Å which is recorded across a blue and a red chip. Each pixel in a spectrum
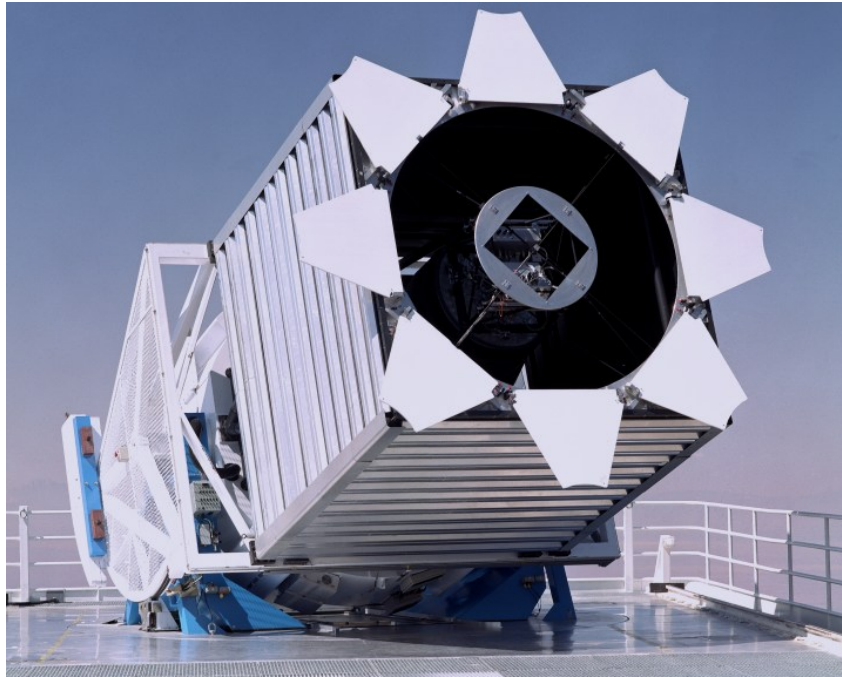
Figure 2.9 The main survey telescope of the Sloan Digital Sky Survey (SDSS), located at Apache Point Observatory in New Mexico, USA. It has a mirror that is 2.5-meter in diameter. The metallic box surrounding the telescope's main shaft is a protective wind screen because the telescope is not housed within a dome during observations. Image source: http://www.sdss.org.

is $69\,\mathrm{km\,s^{-1}}$ and the wavelength solution is accurate to at least $10\,\mathrm{km\,s^{-1}}$. The spectral resolution is $R = 1800$. The S/N $> 4$ pixel$^{-1}$ for $g = 20.2$. SDSS DR4 spectroscopy includes 76 483 quasars which formed the basis of my sample in Chapter 6.

SDSS quasar spectra are processed by two additional pipelines before they are released to the public. The first is called "spectro2d". This does standard spectral processing, such as spectrum extraction, wavelength and flux calibration, sky subtraction, and combination of multiple exposures (http://www.sdss.org/dr4/dataflow/index.html). In addition to removing the expected instrumental effects (scattered light, pixel-to-pixel variation on the CCD) and night sky effects, this pipeline also removes fiber-to-fiber variations. It also stitches together the blue and red halves of the spectrum to make one continuous spectrum. The second SDSS spectrum processing pipeline is called "spectro1d". Properties of the object, such as its classification and redshift, as well as spectrum quality flags are assigned at this stage. All of the spectra and spectroscopy-based selection criteria I use in Chapter 6 are generated by these two pipelines. Figure 2.10 shows the final pipeline output for six quasars from my sample. They were randomly chosen from the beginning, peak, and tail of my sample's redshift distribution as shown in Figure 6.2.
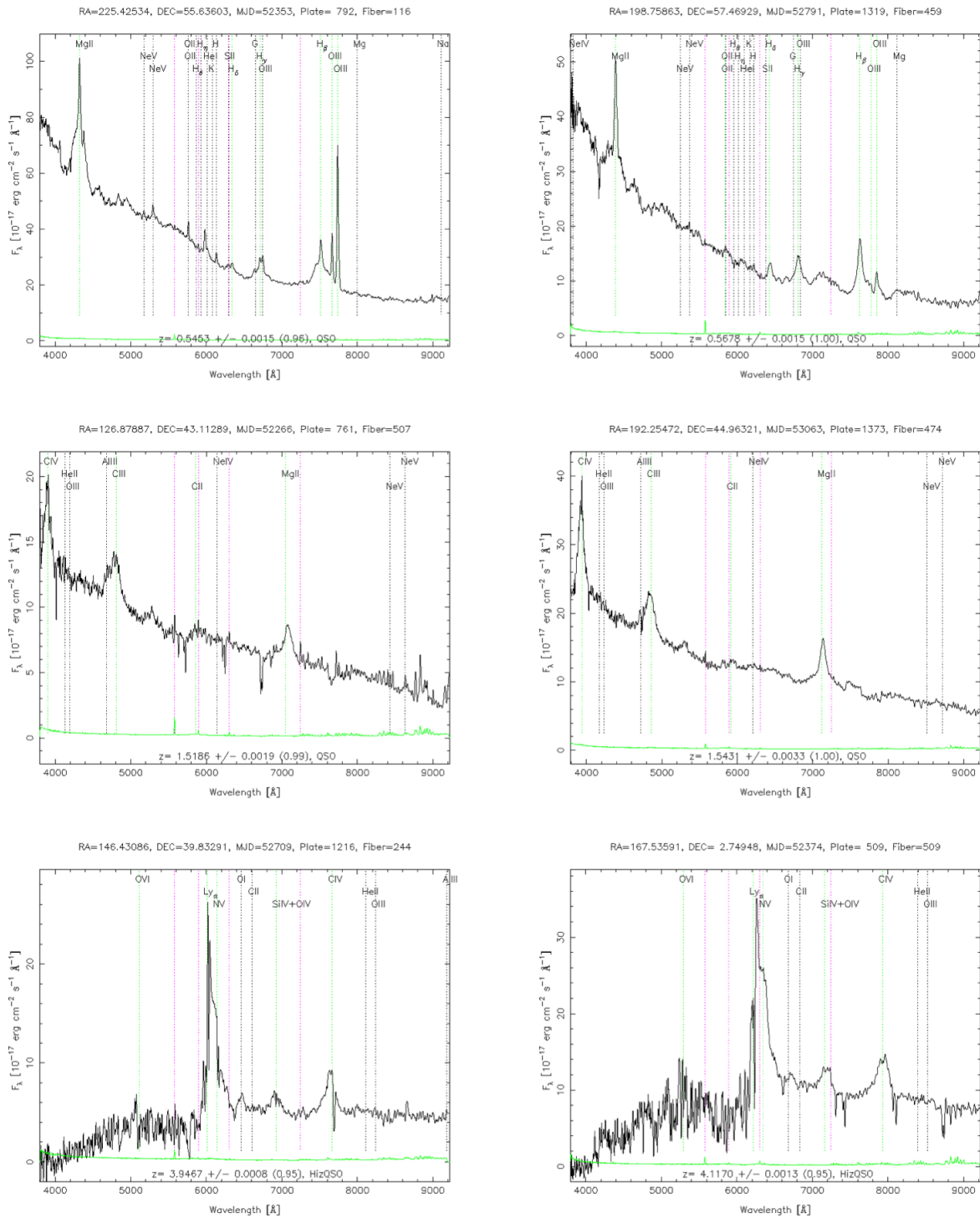
Figure 2.10 A sampling of SDSS quasars used in Chapter 6. They were randomly pulled from the tails and peak of my sample's quasar emission redshift distribution. The quasar spectrum is in black and the error spectrum is in green. Labeled on each spectrum are the possible features visible at a given wavelength, the spectroscopic redshift, coordinates, and SDSS observation date along with spectroscopic plate and fiber. Image source: http://www.sdss.org/dr7.

<div align="right">

# 3

</div>

# The Ultraviolet Spectrum of the Gravitationally Lensed Galaxy 'The Cosmic Horseshoe': A Close-up of a Star-forming Galaxy at $z \sim 2$

## 3.1 Introduction

In the fifteen years that have elapsed since the term "Lyman break galaxy" (or LBG) was coined, samples of galaxies at $z = 2$–4 have increased a thousand-fold. Large surveys, selecting galaxies not only via the break at 912 Å (due mostly to intergalactic H I absorption), but also via Ly$\alpha$ emission, a variety of colour criteria, and sub-mm emission, have given us a broad view of the galaxy population during the epoch when star-formation activity was at its peak in the history of our Universe (see Pettini et al. 2008 for a brief review).

However, typical galaxies at $z \simeq 3$ are faint, with fiducial $\mathcal{R}$-band magnitude $m_{\mathcal{R}}^* = 24.4$ (Steidel et al. 1999; Reddy et al. 2008), so that, even with the most efficient optical and infrared (IR) telescopes and spectrographs currently available, it is only possible to record their spectra with limited resolution and signal-to-noise ratio. Until the next generation of 30+ m optical/IR telescopes comes into operation, the only strategy at our disposal for studying *in detail* the internal properties of normal galaxies at these redshifts is to take advantage of fortuitous alignments with foreground mass concentrations (massive galaxies or galaxy clusters) which can provide an order-of-magnitude boost of the flux reaching the Earth through gravitational lensing.

For several years, the archetypal object for this kind of study has been the Lyman break galaxy MS 1512-cB58 (or cB58 for short; Yee et al. 1996). The magnification by a factor of $\sim 30$ (Seitz et al. 1998) provided by an intervening galaxy cluster at $z = 0.37$

<div align="center">

39

</div>

brings this $L^*$, $z = 2.7276$, galaxy within reach of high resolution spectroscopy from the ground and has made it the target of extensive observations at wavelengths from the visible to the mm range (Pettini et al. 2000, 2002; Savaglio, Panagia, & Padovani 2002; Teplitz et al. 2000; Siana et al. 2008; Baker et al. 2001, 2004; Sawicki 2001). These studies provided unprecedented clear views of the interstellar medium, young stars, star-formation history, dust, metallicity, kinematics, and many other physical properties of a 'typical' LBG at $z \sim 3$.

But how typical is cB58? We know from the work of Shapley et al. (2003) that its ultraviolet (UV) continuum is more reddened, and its interstellar absorption lines are stronger, than in an 'average' LBG. Furthermore, its young age of only 10–20 Myr (Ellingson et al. 1996; Siana et al. 2008) is at the lower end of the wide range of values deduced by fitting the spectral energy distributions of galaxies at $z = 2$–3 (Papovich, Dickinson, & Ferguson 2001; Shapley et al. 2001; Erb et al. 2006b), although it is likely that an older stellar population is present too. Clearly, it is important to study in detail several other similarly bright sources and establish the *range* of properties of galaxies at a given cosmic epoch, rather than naively assuming that any particular galaxy is representative of a whole population. Fortunately, the large area of sky surveyed by the *Sloan Digital Sky Survey (SDSS)* has led to the recent identification of many other examples of highly magnified galaxies (see, for instance, Belokurov et al. 2009; Kubo et al. 2009,2010, and references therein). These and other discoveries have spurred a number of follow-up studies (e.g. Smail et al. 2007; Stark et al. 2008; Finkelstein et al. 2009; Hainline et al. 2009; Yuan & Kewley 2009).

With these new samples of objects, including the work in this Chapter and Chapter 4, it will be possible to make progress on a variety of outstanding questions which cannot be satisfactorily addressed with lower resolution data. In particular:

(i) To what extent do different metallicity indicators, based on stellar photospheric lines, wind lines from the most massive stars, interstellar absorption lines, and emission lines from H II regions, give consistent answers? This is an important issue, not only to explore the degree of chemical homogeneity of galaxies undergoing rapid star-formation, but also to clarify the sources of the systematic offsets between different H II region metallicity calibrators, and possibly bring them into better internal agreement (see, for example, the discussions by Pettini 2006, and Kewley & Ellison 2008).

(ii) What do the profiles of the interstellar absorption lines tell us about large-scale outflows in actively star-forming galaxies and about the inflow of gas fueling star formation? Can we see any evidence of the leakage of hydrogen ionizing photons from the sites of star formation into the intergalactic medium (IGM) which has proved so difficult to detect directly (e.g. Shapley et al. 2006; Iwata et al. 2009) and yet seems to be required by a number of indirect lines of evidence (e.g. Faucher-Giguère et al. 2008)?

(iii) Can we place limits on possible variations of the stellar initial mass function (IMF) at $z = 2$–3? Claims to this effect have certainly been put forward (e.g. Wilkins et al. 2008 and references therein), but the evidence is still controversial (e.g. Reddy & Steidel 2009).

(iv) What are the factors affecting the wide variety of spectral morphologies of the Ly$\alpha$ line, from strong narrow emission to damped absorption (e.g. Mas-Hesse et al. 2003; Verhamme, Schaerer, & Maselli 2006), and what can we learn about the relationship of the so called 'Ly$\alpha$ emitters' to the more general LBG population?

Figure 3.1 $R$-band image of the Cosmic Horseshoe obtained with FORS2 on the Very Large Telescope of the European Southern Observatory (courtesy of L. J. King). North is up and East is to the left. Superposed on the image is the $1.0 \times 20$ arcsec entrance slit of ESI used for the observations reported here.

## 3.2 The Cosmic Horseshoe

The Cosmic Horseshoe, or J1148+1930, is a nearly complete blue Einstein ring of $10$ arcsec diameter encircling a red galaxy (Figure 3.1; see also http://www.ast.cam.ac.uk/research/cassowary/). Low resolution spectroscopy by Belokurov et al. (2007) revealed the lens to be a massive luminous red galaxy ($M \sim 6 \times 10^{12} M_\odot$) at $z = 0.444$ and the ring to be the gravitationally lensed image of a star-forming galaxy at $z = 2.379$. From the extent of the ring, Belokurov et al. estimated an approximate magnification factor of $\sim 35$, while the detailed lensing models constructed by Dye et al. (2008) give overall magnification factors of $24 \pm 2$. Adopting the latter value, and interpolating between the total integrated magnitudes of the ring $g = 20.1$, $i = 19.7$ reported by Belokurov et al. (2007), we deduce a luminosity $L \simeq 2.4 L^*$ for the source, relative to $M^*_{\rm AB}(1700\,\text{Å}) = -21.0$ from the luminosity function of UV-selected $z \simeq 2$ galaxies by Reddy et al. (2008). The image

reconstruction in the source plane with the best fitting lensing model by Dye et al. (2008) shows that the major contributor to this luminosity is a compact source with half-light radius $r_{1/2} \sim 0.3$ arcsec, or $\sim 2.5$ kpc at $z = 2.379$; there is also evidence for a second, fainter, source $\sim 0.7$ arcsec to the North.

We briefly review the information currently available on the lensed galaxy. Its rest-frame UV spectrum is essentially flat in $F_\nu$, reflecting a recent star-formation episode and modest reddening [$E(B - V) \simeq 0.1$–$0.2$; Belokurov et al. 2007], but a more extensive characterization of its stellar population(s) awaits longer wavelength photometry to build-up the spectral energy distribution from the UV to the near-IR (e.g. Shapley et al. 2005; Erb et al. 2006b). Recently, Hainline et al. (2009) reported observations of several rest-frame optical emission lines formed in the H II regions of the Cosmic Horseshoe, from which they were able to measure a number of parameters of interest. The light from multiple H II regions within the Cosmic Horseshoe source galaxy has been recorded as a single emission spectrum. Therefore, these emission features represent the aggregate properties of the star-forming regions within this galaxy. Note that the emission spectrum from an individual H II region may deviate from the composite emission spectrum discussed by Hainline et al. As a result, the physical parameters that one would derive from the emission spectrum of a single star-forming region may differ from the parameters that have been measured and reported in Hainline et al. and that we quote in this section. The H$\alpha$ luminosity implies a star formation rate of $113\,M_\odot$ yr$^{-1}$, after correcting for reddening and a lensing magnification factor of 24. The emission line widths indicate a velocity dispersion $\sigma \simeq 65$ km s$^{-1}$ and a corresponding virial mass $M_{\mathrm{vir}} \simeq 1.0 \times 10^{10} M_\odot$. The oxygen abundance deduced from the ratios of the strongest emission lines is in the range $(\mathrm{O/H})_{\mathrm{H\,II}} \simeq 0.5$–$1.5\,(\mathrm{O/H})_\odot$. These parameters are typical of UV-bright galaxies at $z \sim 2$ (Erb et al. 2006a,b,c), although the star formation rate is at the upper end of the distribution of values found by Erb et al. (2006c). It is of interest now to compare such estimates with those provided by the rest-frame UV spectrum.

## 3.3 Observations and Data Reduction

The observations and data reduction for this object were described in detail in Chapter 2. For your immediate reference, however, the final spectrum of the Cosmic Horseshoe has a resolution (full width at half maximum) FWHM $= 75$ km s$^{-1}$, sampled with three wavelength bins at 6000 Å, an average S/N $\simeq 8$ per 0.5 Å wavelength bin between $\sim 4000$ and $\sim 7500$ Å ($\sim 1200$ and $\sim 2200$ Å in the rest frame), with a factor of $\sim 50\%$ variation in S/N across each echellette order. At the wavelengths of the Ly$\alpha$ emission line the S/N rises to a maximum S/N $= 44$ per 0.5 Å bin. The Cosmic Horseshoe spectrum is reproduced in Figure 3.2. For display purposes, it has been rebinned to 2 Å pixel$^{-1}$ and the Ly$\alpha$ emission feature has been excluded. Refer to Figure 3.9 for the Ly$\alpha$ emission profile.

## 3.4 The Stellar Spectrum

The rest-frame UV spectra of star-forming galaxies are complex blends of interstellar absorption lines, nebular emission lines, and absorption/emission lines formed in the
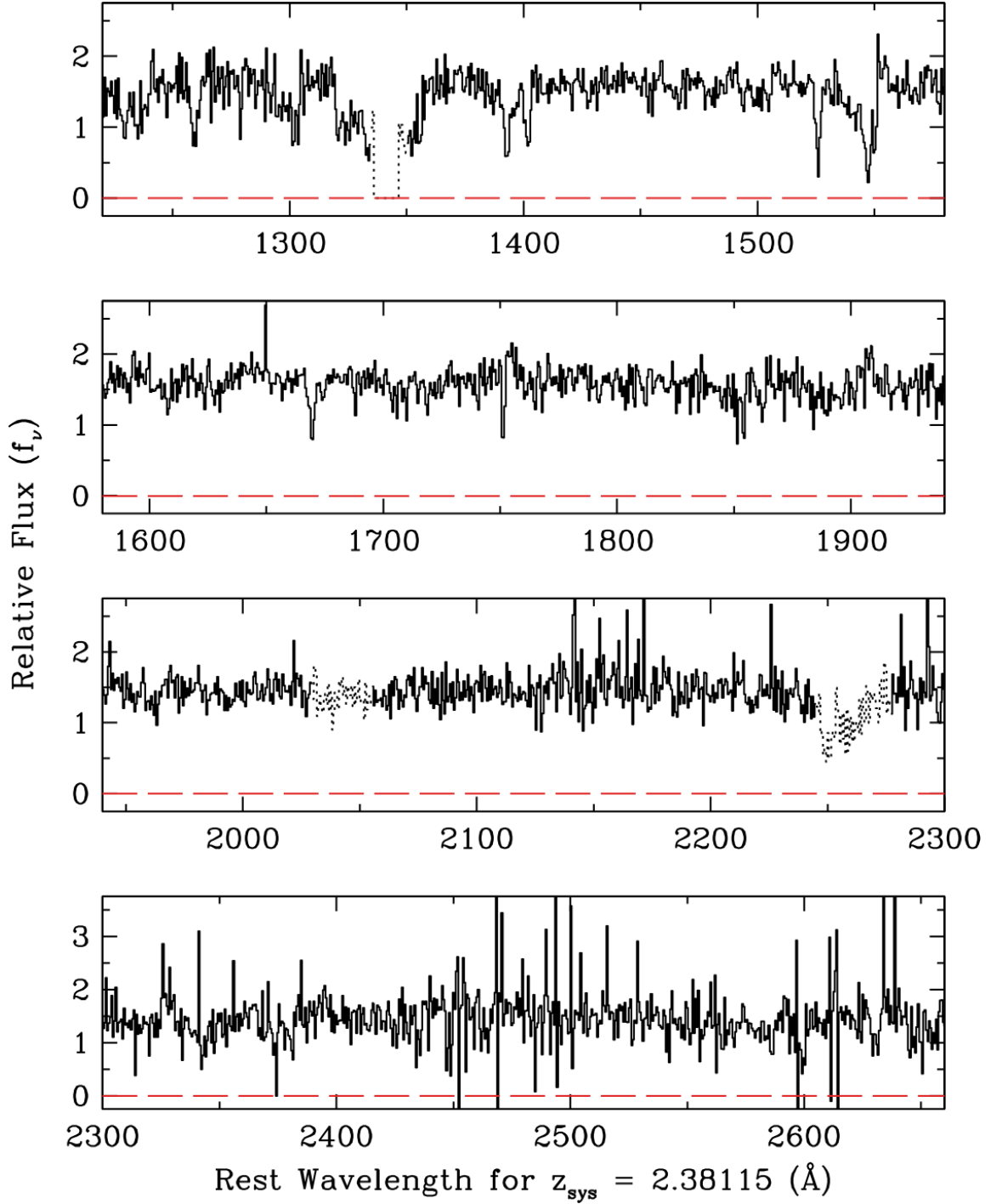
Figure 3.2 The UV spectrum of the Cosmic Horseshoe between rest-frame wavelengths 1220 Å and 2660 Å. The flux from both Aperture 1 and Aperture 2 was summed to produce this composite, which was rebinned to 2 Å (to facilitate reproduction) before reducing to the rest-frame at $z_{\mathrm{sys}} = 2.38115$. Regions of the spectrum affected by the bad column (top panel) or affected by atmospheric absorption (third panel from top) are plotted with a dotted line. The Ly$\alpha$ profile has been omitted from the first panel for ease of scaling. Refer to Figure 3.9 for the Ly$\alpha$ emission profile.

Table 3.1 SYSTEMIC REDSHIFT

| Ion | $\lambda_{\mathrm{lab}}^{\mathrm{a}}$ (Å) | $z_{\mathrm{abs}}$ | Origin |
|---|---|---|---|
| S V | 1501.763 | 2.38107 | Stars |
| N IV | 1718.551 | 2.38119 | Stars |
| C III] | 1906.683 | 2.38103 | H II Regions |
| C III] | 1908.734 | 2.38127 | H II Regions |
| C III | 2297.579 | 2.38118 | Stars |
| H$\alpha^{\mathrm{b}}$ | 6564.614 | 2.38123 | H II Regions |

[a] Vacuum wavelengths
[b] As reported by Hainline et al. (2009)

atmospheres of OB stars. This wealth of spectral features, properly interpreted, is a rich source of information on the physical properties of the gas and stars in these galaxies. In this section, we consider photospheric absorption lines which have been shown to be useful abundance diagnostics, and P-Cygni profiles formed in the expanding atmospheres of the most luminous early-type stars whose strength is also sensitive to the upper end of the initial mass function.

## 3.4.1 The systemic redshift of the Cosmic Horseshoe

The first step in the analysis is the determination of the systemic redshift of the galaxy. While most photospheric features are unresolved blends of multiple lines, a few exceptions allow the redshift of the hot stars to be determined. Within the wavelength range covered by our data, we identified the following unblended photospheric absorption lines: S V $\lambda 1501.763$, N IV $\lambda 1718.551$, and C III $\lambda 2297.579$ [$\lambda_{\mathrm{air}} = 2296.871$—all three vacuum wavelengths from the National Institute of Standards and Technology (NIST) database available at http://physics.nist.gov/PhysRefData/ASD/].

The redshifts of these three lines are in good mutual agreement (see Table 3.1), and define an average $z_{\mathrm{stars}} = 2.38115 \pm 0.00006$. The $1\sigma$ error corresponds to an uncertainty of $\pm 5\,\mathrm{km\,s^{-1}}$, or 1/5 of a wavelength bin in our final spectrum. Also included in Table 3.1 are values of $z_{\mathrm{H\,II}}$ from the C III] $\lambda\lambda 1906.683, 1908.734$ doublet lines which are resolved in our ESI spectrum (see Section 3.7), and from H$\alpha$ measured from the NIRSPEC spectrum of Hainline et al. (2009). The mean $z_{\mathrm{C\,III]}} = 2.38115 \pm 0.00012$ is in excellent agreement with $z_{\mathrm{stars}}$; $z_{\mathrm{H\alpha}}$ differs by only $7\,\mathrm{km\,s^{-1}}$ which may include a small systematic offset between the wavelength calibrations of the ESI and NIRSPEC spectra. Thus, we conclude that the systemic redshift of the Cosmic Horseshoe is $z_{\mathrm{sys}} = 2.38115$ and we adopt this value throughout the paper.

## 3.4.2 Photospheric lines

In this and the following subsection, we analyse photospheric and wind lines in the spectrum of the Cosmic Horseshoe by comparing our data with model spectra computed with the population synthesis code *Starburst99* which couples libraries of either empirical

(Leitherer et al. 1999, 2001) or theoretical (Rix et al. 2004) ultraviolet OB stellar spectra with stellar evolutionary tracks. The input set of parameters to *Starburst99* can be adjusted to simulate a variety of star formation histories, ages, IMF parameters, and metallicities so as to determine the combination that best fits the observations under scrutiny.

In the absence of more detailed information on the previous history of star formation in the Cosmic Horseshoe, we shall adopt the simplest case of continuous star formation— with a Salpeter slope of the upper end of the IMF—which has been proceeding at a steady rate (as opposed to a declining rate, or a series of bursts) for 100 Myr (this being a safe lower limit beyond which the spectrum no longer changes with time because the stars that contribute to the UV light are born and die at the same rate). While this scenario is undoubtedly an over-simplification, it may not be too different from reality when considering the spectrum of a whole galaxy, rather than individual regions of star formation.

Continuous star formation is a likely scenario for many galaxies like the Cosmic Horseshoe from considering the star formation rates obtained from different indicators. H$\alpha$ emission is sensitive to the presence of the most massive and shortest lived ($\sim 10$ Myr) stars while the UV continuum is primarily due to the longer lived ($\sim 50$ Myr) UV-bright stars. Erb et al. (2006b) has shown that the star formation rates obtained from these two indicators are consistent, once corrected for reddening, for tens of high redshift star-forming galaxies. This is evidence against a single burst of star formation because a burst scenario would result in a small fraction of UV-selected galaxies having emission from H$\alpha$. Further, Erb et al. (2006b) find that SED fits with a continuous star formation history generally provide better fits than those assuming an exponentially declining burst of star formation activity.

An age of more than 100 Myr is typical of most $z = 2$ UV-bright galaxies in the 'BX' sample of Erb et al. (2006b) and seems plausible given the near-solar metallicity of the H II regions of the Horseshoe (Hainline et al. 2009). The stellar wind features stabilise after $\sim 10 - 20$ Myr, the lifetime of the most massive stars which are primarily contributing to the stellar wind features (particularly the C IV wind feature to be discussed later in this chapter). Ages of much less than tens of Myr are not likely for regions of star formation as the dynamical timescale of galaxies such as the Cosmic Horseshoe is of that order.

Leitherer et al. (2001) and Rix et al. (2004) pointed out the existence of some blends of UV photospheric lines whose strengths, under the above assumptions, depend on metallicity (see also Halliday et al. 2008). The "1425" index of Rix et al. (2004) measures the equivalent width of a blend of Si III $\lambda 1417$, C III $\lambda 1427$, and Fe V $\lambda 1430$ absorption lines spanning the wavelength interval 1415–1435 Å; at longer wavelengths, the "1978" index measures the strengths of several Fe III absorption lines from B stars between 1935 and 2020 Å. Both indices stabilise after $\sim 50$ Myr from the onset of star formation, and increase monotonically with metallicity. In the left-hand portion of Figure 3.3, we compare the ESI spectrum of the Cosmic Horseshoe with the model spectra of Rix et al. (2004) for five values of metallicity, from 1/20 of solar to twice solar, in the regions of the 1425 and 1978 indices. For this comparison, we smoothed our spectrum to the 2.5 Å resolution of the Rix et al. models, and normalized it using the psuedo-continuum windows suggested by those authors. Thus, the observed and model spectra should be directly comparable.

Figure 3.3 shows a generally good agreement in the detailed features of the synthetic
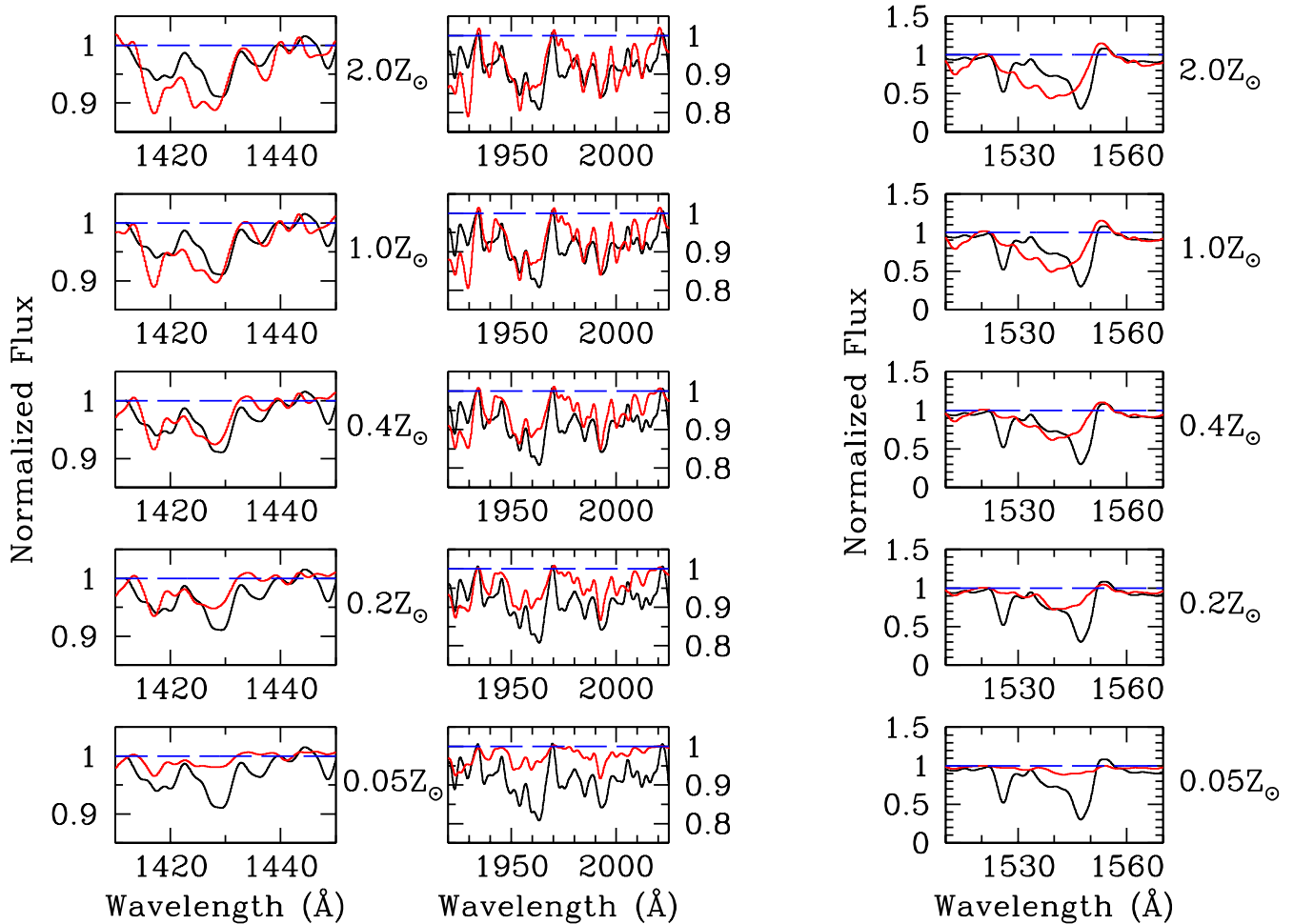
Figure 3.3 *Left-hand pair of panels:* Portions of the UV spectrum of the Cosmic Horse-shoe (black) in the regions encompassing the 1425 and 1978 indices compared with model spectra (red) from the work by Rix et al. (2004) for five different metallicities, as indicated. The ESI spectrum has been smoothed to the 2.5 Å resolution of the model spectra. See text for further details of the models. *Right-hand panel:* Comparison of the Rix et al. models with the smoothed and normalized spectrum of the Cosmic Horseshoe in the region of the C IV $\lambda\lambda 1548.204, 1550.781$ doublet. This region also includes C IV and Si II $\lambda 1526.7070$ *interstellar* absorption which is unaccounted for in the Rix et al. models. Note the difference in the $y$-axis scales between the C IV panels and those for the weaker photospheric 1425 and 1978 features to the left.

and real spectra in the two wavelength regions considered here, attesting to the sophistication reached by current hot-star atmosphere and stellar population synthesis models. Referring to the 1425 Å region (left-most panel in Figure 3.3), it can be seen that the strength of the photospheric lines in this region of the Cosmic Horseshoe spectrum is intermediate between those computed with metallicities $Z = 0.4Z_\odot$ and $Z = 1.0Z_\odot$ respectively. Using the relationship between metallicity and the 1425 index proposed by Rix et al. (2004):

$$\log(Z/Z_\odot) = A \times \mathrm{EW}(1425) + B \tag{3.1}$$

with $A = 1.14$ and $B = -1.75$ appropriate to the value $\mathrm{EW}(1425) = 0.95$ Å we measure here, we derive $Z_{\mathrm{OBstars}} = 0.5Z_\odot$.

Qualitatively, the observed spectrum seems to be intermediate between the 0.4 solar and solar metallicity cases in the 1978 region too (see middle panel of Figure 3.3). However, there appears to be excess absorption between 1960 and 1980 Å over that expected from the models for *any* metallicity; the presence of these additional features does not allow us to deduce a value of $Z_{\mathrm{Bstars}}$ from $\mathrm{EW}(1978)$ using the Rix et al. (2004) calibration of this index. We considered the possibilities that the excess absorption may be noise, or an intervening absorption system unrelated to the Cosmic Horseshoe, but could find no evidence to support either interpretation. It also seems unlikely that the excess is due to a different mix of stellar spectral types or chemical elements, since all of the photospheric absorption in this region is thought to be due to Fe III lines, and the rest of the spectral features between 1920 and 2025 Å match the data well. No such discrepancies were found by Rix et al. (2004) in the two galaxies they considered (MS 1512-cB58 and Q1307-BM1163, the latter at $z = 1.411$), nor by Halliday et al. (2008) in their composite spectrum of $z \sim 2$ galaxies. However, the cases where these photospheric indices have been measured are still very few, and it is important to continue to look critically at the match between model and real spectra as more data of suitable quality become available.

### 3.4.3 Wind lines

The model spectra by Rix et al. (2004) show that the spectral features most sensitive to metallicity are the P-Cygni lines formed in the expanding winds of the most luminous OB stars whose mass-loss rates are thought to be lower at lower metallicities (e.g. Kudritzki & Puls 2000). Among the P-Cygni lines covered by our spectrum, the C IV $\lambda\lambda1548.204, 1550.781$ (unresolved at the coarse 2.5 Å pixel$^{-1}$ resolution of the Rix et al. models) doublet is the strongest. Referring to the rightmost panel in Figure 3.3, we find that its strength in the Cosmic Horseshoe is intermediate between those of the models with metallicities $Z = 0.2Z_\odot$ and $Z = 0.4Z_\odot$. However, as emphasised by Crowther et al. (2006), the interpretation of this feature is complicated by its blending with interstellar C IV (and to a lesser extent Si II $\lambda1526.7070$) absorption, at least at the coarse resolution of most spectra of distant galaxies. Similar problems affect the generally weaker Si IV $\lambda\lambda1393.7602, 1402.7729$ and N V $\lambda1238.821, 1242.804$ wind lines.

At the high resolution of our ESI spectrum, interstellar and stellar components are easily separated, as can be appreciated from Figure 3.4. The top panel compares the observed spectrum of the Cosmic Horseshoe in the C IV region with those generated by *Starburst99* now using libraries of *empirical* stellar spectra, assembled from UV observations of stars
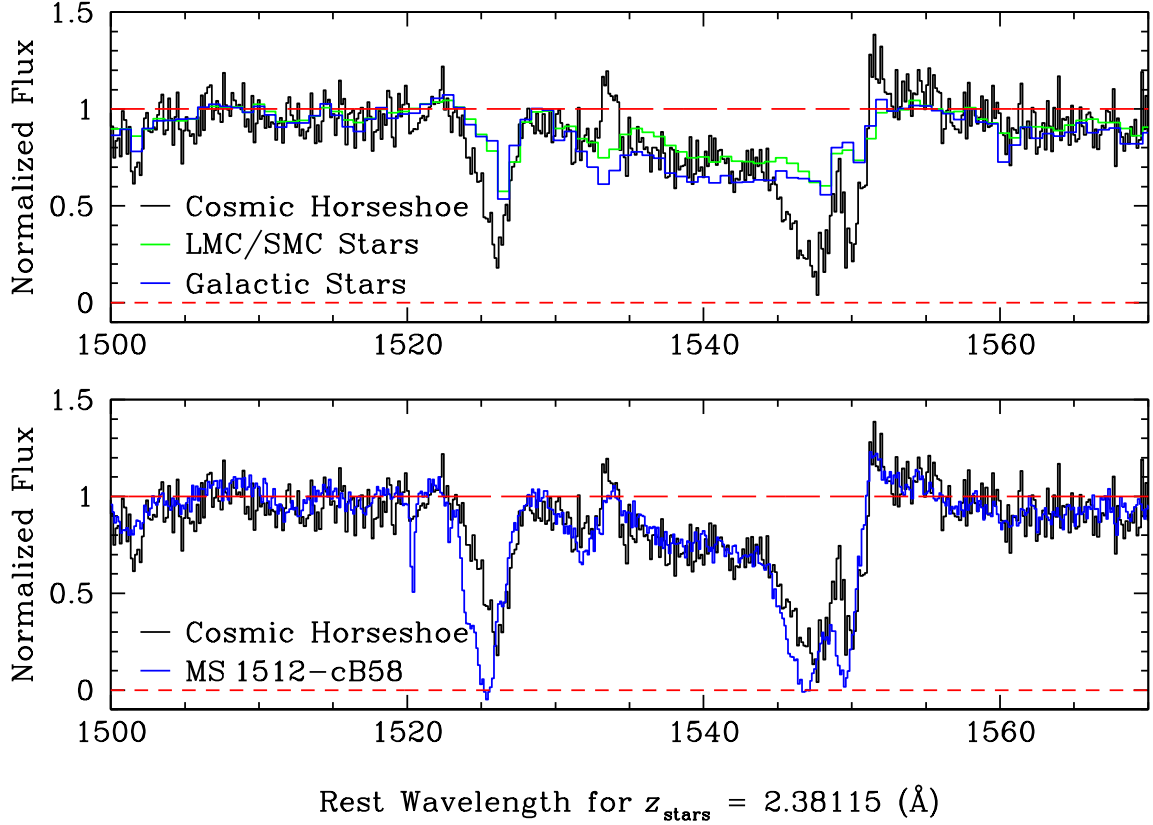
Figure 3.4 *Upper panel:* Comparison between the ESI spectrum of the Cosmic Horseshoe in the region encompassing the C IV line and model spectra computed with *Starburst99* and empirical libraries of Galactic and Magellanic Clouds stars, as indicated. The model spectra were generated assuming a 100 Myr old continuous star formation episode with a Salpeter IMF. *Lower panel:* The stellar spectra of the Cosmic Horseshoe and of MS 1512-cB58 are remarkably similar in the wavelength region shown. The ESI spectrum of cB58 is reproduced from Pettini et al. (2002), and has been reduced to its rest wavelengths at $z_{stars} = 2.7276$.

in either the Galaxy or the Magellanic Clouds. Both models are for 100 Myr old continuous star formation with Salpeter IMF and stellar masses in the range $5 \leq M \leq 100\,M_\odot$. Apart from the narrow interstellar Si II $\lambda1526.7070$ and C IV $\lambda\lambda1548.204, 1550.781$ absorption lines, which are stronger in the distant galaxy than in the spectra of the stars that make up the *Starburst99* libraries, the agreement between models and observations is clearly very good. The broad blue absorption wing of the P-Cygni profile reaches similar terminal velocities in the models and the data, and its depth is roughly intermediate between those of the Galactic and Magellanic Clouds models. The latter library of stellar spectra was built-up by Leitherer et al. (2001) with *Hubble Space Telescope* (*HST*) observations of stars in *both* the Large and Small Magellanic Clouds (LMC/SMC) and may thus correspond to an approximate metallicity $Z_{\mathrm{MC}} \sim 0.4Z_\odot$, given that in the LMC $(\mathrm{O/H}) \simeq 0.5\,(\mathrm{O/H})_\odot$ and in the SMC $(\mathrm{O/H}) \simeq 0.25\,(\mathrm{O/H})_\odot$ (e.g Pagel 2003). By linearly interpolating between the Galactic and LMC models and minimising the difference from the observed spectrum, we find $Z_{\mathrm{Ostars}} \approx 0.6Z_\odot$, in good agreement with $Z_{\mathrm{OBstars}} = 0.5Z_\odot$ deduced above from consideration of the 1425 photospheric index.

It is interesting that both Galactic and Magellanic Clouds models seem to *under-predict* the emission component of the P-Cygni profile. However, the narrow emission feature centred near 1551.6 Å may be partly of nebular origin (Leitherer, Calzetti, & Martins 2002). Similarly, the narrow emission centred near 1533.7 Å is probably nebular Si II* $\lambda1533.4312$; both features are missing from the synthetic spectra which were designed to reproduce only the stellar component of the galaxy spectrum. The superposition of P-Cygni broad emission/absorption, photospheric broad absorption, narrow interstellar absorption and narrow nebular emission attests to the complex nature of this portion of the UV spectrum of star-forming galaxies.

In the lower panel of Figure 3.4 we compare the ESI spectra of MS 1512-cB58 (from Pettini et al. 2002) and the Cosmic Horseshoe in the wavelength region 1500–1570 Å. There is a startling similarity in this spectral region between these two galaxies which are at different redshifts (cB58 is at $z_{\mathrm{stars}} = 2.7276$) and were selected randomly, only by virtue of the fact that they are highly lensed as seen from Earth (although they are both more luminous than the 'average' galaxy at these redshifts, even after correcting for the lensing magnifications). Presumably, not only the chemical abundances, but also the young stellar populations of these two galaxies are remarkably similar. Only the interstellar absorption lines are different, with those in cB58 apparently stronger than in the Cosmic Horseshoe (but see the discussion in Section 3.5).

The P-Cygni component of the C IV complex is due to the most massive (and luminous) O stars, which drive the strongest winds. On the other hand, a wider range of stellar spectral types, including all stars with masses greater than about $5M_\odot$, are thought to make up the integrated continuum light near 1550 Å (e.g. Rix et al. 2004). Thus, the contrast of the P-Cygni features relative to the continuum is sensitive not only to metallicity, but also to the slope and upper end cut-off of the IMF, as well as to more subtle effects, such as differential dust extinction among stars at the upper end of the IMF (the most massive and short-lived stars may in principle be more reddened than longer lived ones—Leitherer et al. 2002), and the relative proportions of OB stars in star clusters and in the field (Chandar et al. 2005). Pettini et al. (2000) showed how even relatively minor changes to the IMF slope (or alternatively the upper mass cut-off) result in noticeable alterations to the integrated spectrum of a star-forming galaxy in the C IV

region. On that basis, those authors concluded that a standard Salpeter IMF extending to $M_{\rm up} > 50 M_\odot$ provides the best match to the spectrum of cB58, without the need to invoke a different IMF at high redshift, as claimed by some. Clearly, the same conclusion applies here to the massive stellar population in the Cosmic Horseshoe. More generally, the similarity evident in the lower panel of Figure 3.4 suggests that the minor effects discussed above (differential dust extinction and the balance between cluster and field stars) presumably average out in at least a subset of star-forming galaxies at $z = 2 - 3$, when their integrated spectra are considered.

Summarising the conclusions of this section, we find that the metallicity of the early-type stars in the Cosmic Horseshoe is approximately half-solar, from consideration of photospheric and wind absorption lines. A continuous mode of star formation with a Salpeter slope for stars more massive than $5 \, M_\odot$ gives a good representation of the UV spectrum. The 1978 index introduced by Rix et al. (2004) appears to be contaminated by additional features of uncertain origin in the spectrum of the Horseshoe. The C IV region is a complex blend of stellar, interstellar and nebular features, but the stellar component in the Cosmic Horseshoe is surprisingly similar to that in cB58, the only other high redshift star-forming galaxy studied in comparable detail so far. This may of course be a coincidence, but it may also point to the fact that many of the parameters which can affect the appearance of this spectral region average out to a large extent in the integrated UV spectrum of a whole galaxy.

## 3.5 The Interstellar Spectrum

### 3.5.1 Kinematics of the absorbing gas

In the wavelength interval from 1200 to 2600 Å, we identified 21 interstellar absorption lines from six chemical elements in a variety of ionization stages, from O I to C IV. Relevant measurements are collected in Table 3.2, while Figure 3.5 shows selected transitions chosen to illustrate the range of elements and ion stages covered. The interstellar lines in the Cosmic Horseshoe are broad, with absorption extending smoothly from $-800$ to $+250 \, {\rm km \ s^{-1}}$ with respect to $z_{\rm sys} = z_{\rm stars} = 2.38115$. Within the limits of the noise, we find no convincing differences between the profiles of different ions, although the maximum velocities measured depend on the strength of the transition, as is the case in local starbursts (e.g. Grimes et al. 2009). The values of $z_{\rm abs}$ listed in column (4) of Table 3.2 are those derived from the centroids of the lines (that is, the mean wavelength of the line weighted by the absorption in each wavelength bin); their mean value is $\langle z \rangle = 2.3788 \pm 0.0009$ which corresponds to a velocity offset $\Delta v = -208 \, {\rm km \ s^{-1}}$ with respect to the stars. We also measured the redshift at the peak optical depth in the most clearly defined line profiles and found a mean $z_{\rm ISM} = 2.3795 \pm 0.0002$ ($\Delta v = -146 \, {\rm km \ s^{-1}}$).

This net blueshift of the interstellar lines is a common feature of star-forming galaxies at low (e.g. Heckman et al. 2000; Martin 2005) as well as high (e.g. Pettini et al. 2001; Shapley et al. 2003; Steidel et al. 2009; Vanzella et al. 2009) redshifts. It is generally interpreted as empirical evidence for the existence of large-scale outflows of the interstellar medium driven by the kinetic energy deposited by supernovae and the winds of massive
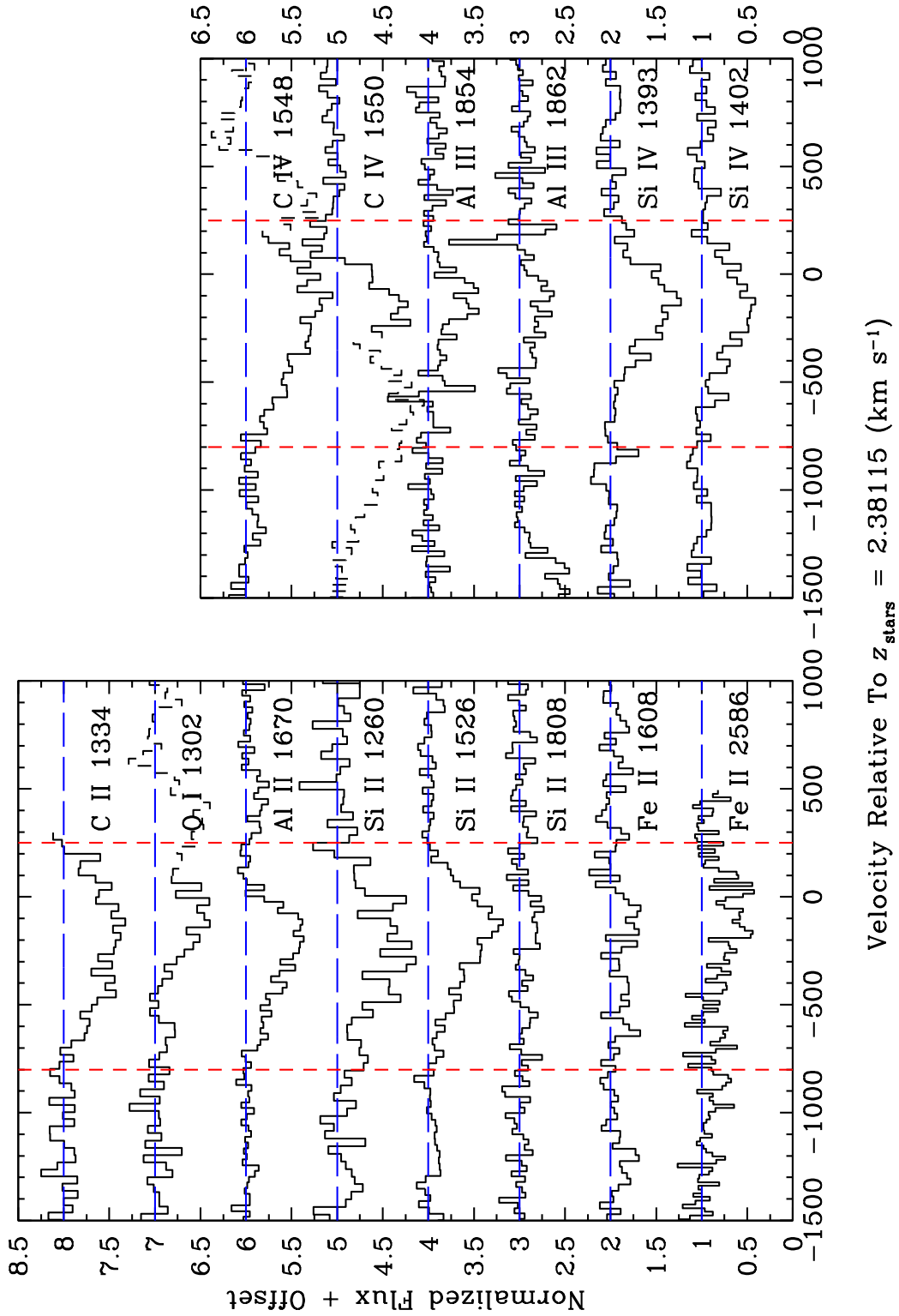
Figure 3.5 Normalized profiles of selected interstellar absorption lines. *Left panel:* Transitions of ions which are the dominant species of the corresponding elements in H I regions. *Right panel:* Higher ionization stages. In both panels the vertical red dash lines indicate the velocity range over which the values of equivalent width listed in Table 3.2 were generally measured.

stars. The values of $\Delta v$ we deduce here, irrespective of whether one considers the mean redshift of the line centroids or of the gas with the highest optical depth, are typical of $z = 3$ galaxies for which Shapley et al. (2003) derive a mean $\langle \Delta v \rangle = -150 \pm 60 \, \mathrm{km \, s^{-1}}$. Similarly, the widths of the strongest lines ($FWHM \simeq 400\text{–}600 \, \mathrm{km \, s^{-1}}$) are within the range $\langle FWHM \rangle = 575 \pm 150 \, \mathrm{km \, s^{-1}}$ measured by Shapley et al. (2003) from their composite spectrum of 811 LBGs.

Although with the higher resolution of our data (compared to that normally employed to record the spectra of unlensed $z = 2-3$ galaxies) the interstellar lines are fully resolved, we are still unable to recognize clear clues in the line profiles as to the location of the absorbing gas. The profiles are smooth and relatively featureless, and we see no trends between, for example, velocity and degree of ionization, which could be used to construct a kinematical model. While the blueshifted absorption is presumably due to outflowing material, the location and nature of the gas moving at *positive* velocities relative to the stars remain unexplained. It is interesting to note that the absorption lines in the ESI spectrum of MS 1512-cB58 analysed by Pettini et al. (2002) also extend over the same velocity range, from $\sim -800$ to $\sim +250 \, \mathrm{km \, s^{-1}}$ relative to the systemic redshift of the stars, although in cB58 the gas with the highest optical depth is moving at a higher velocity $\Delta v = -255 \, \mathrm{km \, s^{-1}}$. The two galaxies have similar star formation rates, $\mathrm{SFR} \approx 50 \, M_\odot \, \mathrm{yr^{-1}}$, as estimated from their UV continua (see Section 3.6.3). Overall, the profiles of the interstellar absorption lines from the first ions appear smoother in the Horseshoe than in cB58, but the lower S/N of the present data makes it more difficult to recognize distinct velocity components than is the case in cB58.

### 3.5.2  Partial coverage and column densities

One noticeable difference between the Cosmic Horseshoe and cB58 is in the optical depth of the interstellar absorption lines (see Figure 3.4). Whereas in cB58 the strongest interstellar lines have saturated cores of zero residual intensity (at the spectral resolution of ESI—see Figures 1 and 2 of Pettini et al. 2002), the same transitions never seem to reach below an optical depth $\tau \sim 1$ in the Cosmic Horseshoe, as can be appreciated from inspection of Figure 3.5.

One possibility is that the column densities of even the most abundant ions are genuinely lower in the Horseshoe compared to cB58. An alternative explanation is that the interstellar gas does not completely cover the early-type stars producing the UV continuum against which the absorption is seen. The latter interpretation is not unlikely in general—given the composite nature of the UV spectra of star-forming galaxies which are the superposition of hundreds of thousands of individual stellar spectra—and is suggested by the similarity in the residual intensity in the cores of all the strongest absorption lines in Figure 3.5.

We can assess quantitatively the partial coverage hypothesis using the apparent optical depth method of Savage & Sembach (1991). If the absorption lines are resolved, as seems to be the case here, the column density of an ion in each velocity bin, $N_a(v)$ [in units $\mathrm{cm^{-2} \, (km \, s^{-1})^{-1}}$], can be deduced directly from the optical depth in each velocity bin,

$$\tau_a(v) = -\ln \left[ I_{\mathrm{obs}}(v) / I_0(v) \right] \tag{3.2}$$

Table 3.2 INTERSTELLAR ABSORPTION LINES

| Ion | $\lambda_{\mathrm{lab}}$[a] (Å) | $f$[a] | $z_{\mathrm{abs}}$ | $W_0$[b] (Å) | $\delta W_0$[b] (Å) | Comments |
|---|---|---|---|---|---|---|
| C II | 1334.5323 | 0.1278 | 2.3786 | 1.62 | 0.16 | Blended with C II* $\lambda$1335.6627 |
| C IV | 1548.204 | 0.1899 | 2.3783 | 2.36 | 0.08 | Blended with stellar C IV $\lambda$1549.1; $W_0$ measured from $-800$ to $+100\,\mathrm{km\,s^{-1}}$ |
| | 1550.781 | 0.09475 | 2.3798 | 0.85 | 0.04 | Blended with stellar C IV $\lambda$1549.1; $W_0$ measured from $-250$ to $+60\,\mathrm{km\,s^{-1}}$ |
| O I | 1302.1685 | 0.04887 | 2.3791 | 0.90 | 0.09 | $W_0$ measured from $-800$ to $+100\,\mathrm{km\,s^{-1}}$ |
| Al II | 1670.7886 | 1.74 | 2.3779 | 1.48 | 0.07 | |
| Al III | 1854.7184 | 0.559 | 2.3792 | 0.93 | 0.10 | |
| | 1862.7910 | 0.278 | 2.3782 | 0.61 | 0.13 | |
| Si II | 1260.4221 | 1.18 | 2.3778 | 1.71 | 0.18 | Blended with S II $\lambda$1259.519 |
| | 1304.3702 | 0.0863 | 2.3792 | 0.71 | 0.06 | $W_0$ measured from $-400$ to $+25\,\mathrm{km\,s^{-1}}$ |
| | 1526.7070 | 0.133 | 2.3788 | 1.81 | 0.06 | |
| | 1808.0129 | 0.00208 | 2.3778 | 0.40 | 0.08 | |
| Si IV | 1393.7602 | 0.513 | 2.3795 | 1.36 | 0.09 | |
| | 1402.7729 | 0.254 | 2.3791 | 1.13 | 0.08 | |
| Fe II | 1608.4511 | 0.0577 | 2.3774 | 0.51 | 0.12 | |
| | 2344.2139 | 0.114 | 2.3807 | 0.40 | 0.23 | |
| | 2374.4612 | 0.0313 | 2.3795 | 1.47 | 0.23 | |
| | 2382.7652 | 0.320 | 2.3767 | 1.25 | 0.18 | $W_0$ measured from $-700$ to $+250\,\mathrm{km\,s^{-1}}$ |
| | 2586.6500 | 0.0691 | 2.3791 | 1.85 | 0.13 | |
| | 2600.1729 | 0.239 | 2.3793 | 2.25 | 0.28 | |
| Ni II | 1317.217 | 0.0571 | 2.3786 | 0.12 | 0.05 | $W_0$ measured from $-350$ to $-80\,\mathrm{km\,s^{-1}}$ |
| | 1741.5531 | 0.0427 | 2.3799 | 0.14 | 0.05 | $W_0$ measured from $-180$ to $-20\,\mathrm{km\,s^{-1}}$ |

[a] Vacuum wavelength and $f$-values are from Morton (2003) with updates by Jenkins & Tripp (2006).

[b] Rest-frame equivalent width and $1\sigma$ random error on the rest-frame equivalent width measured over the velocity range $-800$ to $+250\,\mathrm{km\,s^{-1}}$ with respect to $z_{\mathrm{stars}}$, unless otherwise noted.
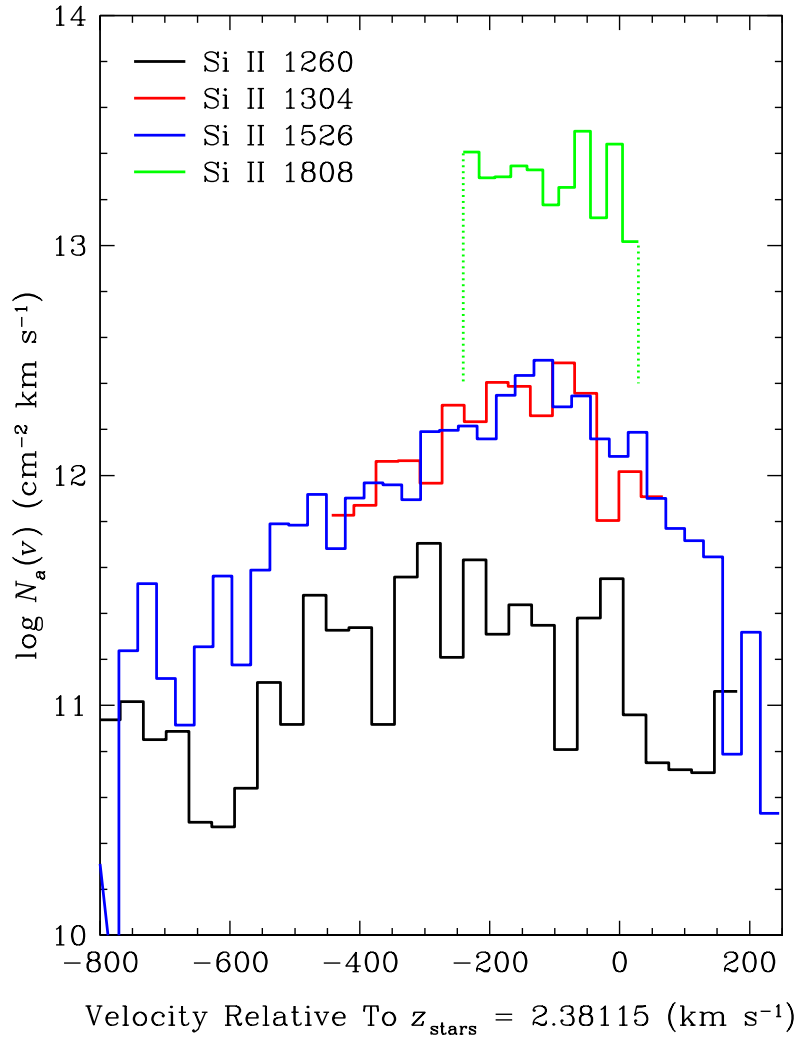
Figure 3.6 When analysed with the Apparent Optical Depth method, the four Si II transitions recorded in our ESI spectrum of the Cosmic Horseshoe yield values of column density which differ systematically, in the sense expected if the interstellar gas does not completely cover the stellar UV continuum (see Section 3.5.2 for further details).

from the relation

$$N_a(v) = 3.768 \times 10^{14} \cdot \frac{\tau_a(v)}{f\lambda} \tag{3.3}$$

where $f$ measures the strength of the transition at wavelength $\lambda$ (Å), and $I_{\rm obs}$ and $I_0$ denote the relative intensities in the line and in the continuum respectively. If multiple absorption lines arising from the same ground state of an ion but with different values of the product $f\lambda$ are available, partial coverage would manifest itself as a mismatch between the values of column density deduced from each transition, the lines with smaller values of $f\lambda$ giving systematically higher values of $N_a(v)$.

Among the ions covered by the ESI spectrum of the Horseshoe, Si II is the one best suited to this analysis, with four transitions spanning a range of $\sim 400$ in $f\lambda$ (see Table 3.2) and falling at wavelengths where the S/N of the data is highest. As can be seen from Figure 3.6, the run of $N_a(v)$ vs. $v$ for the four Si II lines does indeed show the systematic differences expected if the absorbing gas does not completely cover the background stellar continuum. In the line core, the apparent optical depth of the weakest absorption line, Si II $\lambda 1808.0129$, implies values of column density *two orders of magnitude* higher than those deduced from the strongest transition, Si II $\lambda 1260.4221$. The profiles of Si II $\lambda 1304.3702$ and $\lambda 1526.7070$, with very similar values of $f\lambda$ intermediate between those of the other two lines, indicate that partial coverage extends well beyond the line cores and probably applies to the full velocity range spanned by the absorption.

We also cover several Fe II transitions (see Table 3.2), but their $f\lambda$ values range over a factor of only $\sim 10$ and most of them are redshifted to far-red wavelengths, where the S/N of our data is lower. Nevertheless, the profiles of the Fe II lines are consistent with the conclusions drawn from Figure 3.6, in showing a systematic trend of increasing $N_a(v)$ with decreasing $f\lambda$. Turning to the high ionization lines in the right-hand panel of Figure 3.5, we found that the weaker member of the Si IV doublet, $\lambda 1402.7729$, also gives systematically higher values of $N_a(v)$ than $\lambda 1393.7602$, even though the $f\lambda$ values of the two lines differ by only a factor of 2, while the evidence is less clear-cut in the case of the Al III doublet which is recorded at lower S/N. The C IV lines are difficult to interpret in this context because they are blended with each other and with the stellar P-Cygni profile, as discussed above (Section 3.4.3).

Given our lack of knowledge of the relative configuration of interstellar gas and stars, it is quite possible, or even likely (e.g. Martin & Bouché 2009), that the covering factor varies with velocity and degree of ionization of the gas. However, the S/N of our data is insufficient to establish the magnitude of such variations. Instead, we adopted the simplest assumption that "one size fits all" and corrected the absorption line profiles by re-adjusting the zero level by the same fractional amount of the continuum at all wavelengths. Inspection of the spectrum shows that even the strongest absorption lines, which are normally saturated in the spectra of Galactic stars and of nearby starbursts, all seem to have a minimum residual intensity $I_\lambda/I_0 \sim 0.4$ (see Figure 3.5). With the simplistic assumption that the interstellar gas only covers 60% of the stellar light, and that the remaining 40% of the UV continuum sees no absorption in our direction, the adjusted profiles of the four Si II lines become internally consistent, as shown in Figure 3.7.

Specifically, after subtracting 40% of the stellar continuum and renormalizing the line profiles, we deduced the column density of Si II, $\log N(\text{Si II})/\text{cm}^{-2} = 16.00$, by integrating eq. (3.3) over the velocity range spanned by the weakest Si II line, $\lambda 1808.0129$, which is
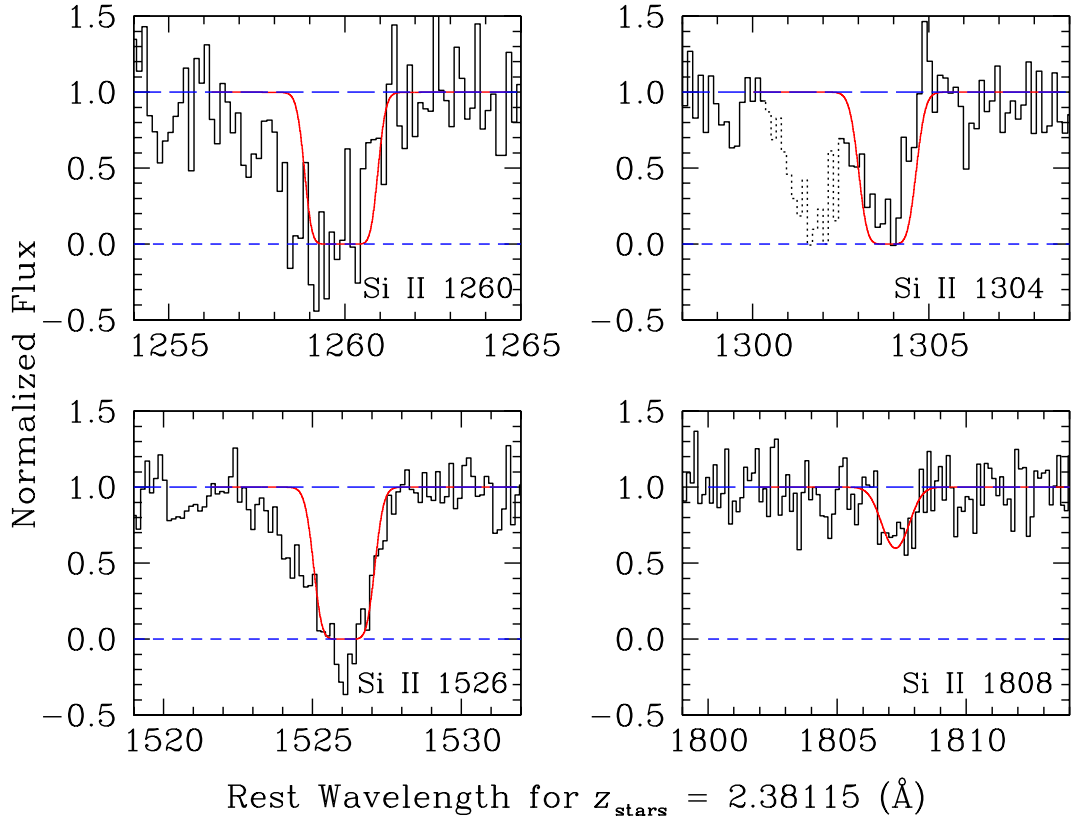
Figure 3.7 *Black histograms:* Normalized profiles of the four Si II absorption lines after subtracting 40% of the continuum level, under the assumption that the gas only covers 60% of the stellar light. *Red continuous lines:* Theoretical absorption line profiles generated with the values of $N(\text{Si\,II})$ and velocity dispersion parameter $b$ implied by the weakest transition, $\lambda 1808.0129$, which is unsaturated. The absorption line shown by the short-dash histogram in the top right-hand panel is O I $\lambda 1302.1685$.

unsaturated even after the readjustment of the zero level. We then used the absorption line fitting software XVOIGT (Mar & Bailey 1995) to fit the profile of Si II $\lambda 1808.0129$ with this column density and deduced the value of the velocity dispersion parameter, $b = 105\,\text{km s}^{-1}$, which best reproduces the width of this line. In the next step, we used this pair of values of $N(\text{Si\,II})$ and $b$ to generate XVOIGT profiles of the other three Si II absorption lines. As can be seen fom Figure 3.7, these computed profiles provide satisfactory fits to the main absorption component of the three stronger Si II transitions, given the noise in the data. (We have not attempted to fit the blue wing of the three lines because this absorption is too weak to be detected in Si II $\lambda 1808.0129$, but its contribution to the value of $N_{\text{TOT}}(\text{Si\,II})$ is only a small fraction of the total, unless the covering factor of the high velocity gas is much smaller than 60%).

Table 3.3 lists the values of ion column density deduced by integrating eq. (3.3) over the velocities spanned by those absorption lines that remain unsaturated after the 40% adjustment of the zero level. Errors in the column density, $\delta N$, were determined by

Table 3.3 Ion Column Densities

| Ion | $\lambda_{\mathrm{lab}}$ (Å) | $f$ | $\log N/\mathrm{cm}^{-2\mathrm{a}}$ | $\log \delta N/\mathrm{cm}^{-2\mathrm{a}}$ |
|---|---|---|---|---|
| Al III | 1854.7184 | 0.559 | 14.22 | $-0.06$, ... |
|  | 1862.7910 | 0.278 | 14.26 | $-0.07$, $+0.14$ |
| Si II | 1808.0129 | 0.00208 | 16.00 | $-0.06$, $+0.07$ |
| Si IV | 1402.7729 | 0.254 | 14.92 | $-0.06$, ... |
| Fe II | 1608.4511 | 0.0577 | 14.94 | $-0.10$, $+0.11$ |
|  | 2586.6500 | 0.0691 | 15.12 | $-0.06$, ... |
| Ni II | 1317.217 | 0.0571 | 14.22 | $-0.24$, $+0.20$ |
|  | 1741.5531 | 0.0427 | 14.40 | $-0.21$, $+0.19$ |

[a] Values of the ion column density $N$ were deduced by integrating eq. (3.3) over the velocities spanned by those absorption lines that remain unsaturated after the 40% adjustment of the zero level. Errors in the column density, $\delta N$, were determined by adding/subtracting the $1\sigma$ error spectrum to/from the line profiles and recalculating the column density; in cases where the addition of the noise spectrum results in the line becoming saturated an error of "..." is given.

adding/subtracting the $1\sigma$ error spectrum to/from the line profiles and recalculating the column density; in cases where the addition of the noise spectrum results in the line becoming saturated no corresponding error is given in Table 3.3. Again, we see from the Table that there is good internal agreement between the values of $N$ implied by different transitions of the same ion, after correcting for the 40% unabsorbed stellar continuum.

The interstellar column densities of the first ions in the Cosmic Horseshoe are surprisingly similar to those measured in cB58 by Pettini et al. (2002). For the transitions in common between the two studies, we have: $\log N/\mathrm{cm}^{-2}$ (Horseshoe/cB58) $= 16.00/15.99$ for Si II $\lambda1808.0129$; $14.94/15.17$ for Fe II $\lambda1608.4511$; $14.22/14.32$ for Ni II $\lambda1317.217$; and $14.40/ \leq 14.45$ for Ni II $\lambda1741.5531$. Although the metallicities reached by the two galaxies are similar, as discussed above (Section 3.4), there was no reason to expect that the column densities of interstellar gas entrained by the outflows—nor the ionization of this gas—should be so similar. Furthermore, even the ratios of elements that are depleted onto dust by different degrees, or are synthesised by stars of different masses, are similar between these two galaxies. Thus, the iron-peak and easily depleted elements Fe and Ni are underabundant (in their first ions) compared with the undepleted alpha-capture element Si by about one order of magnitude, as is the case in cB58 (see Figure 8 of Pettini et al. 2002). All of this may just be a coincidence, of course, or may point to a more fundamental uniformity in the conditions of the gas outflowing from high-redshift star-forming galaxies, or at least a subset of such galaxies.

Given the similarity in the column densities of the first ions and in the metallicity of the two galaxies, it follows that we also expect similar values of the column density of hydrogen $N(\mathrm{H})$. Indeed, if the majority of the first ions arises from H I regions, we can deduce values of $N(\mathrm{H\,I})$ from the column densities in Table 3.3 and the assumption that $Z_{\mathrm{ISM}} = Z_{\mathrm{OBstars}} = 0.5Z_{\odot}$. This leads to $\log N(\mathrm{H\,I})/\mathrm{cm}^{-2} = 20.79$ using Si II as the

reference ion, indeed very close to $\log N(\text{H I})/\text{cm}^{-2} = 20.85$ deduced by Pettini et al. (2002) from the damped profile of the Ly$\alpha$ line in cB58. As we shall see in a moment, however, there are striking differences between the profiles of the Ly$\alpha$ line observed in the two galaxies. Whereas in the case of cB58 we see a clear damped absorption profile with a weak superposed emission component, Ly$\alpha$ is in emission in the Cosmic Horseshoe.

## 3.6 The Ly$\alpha$ Line

### 3.6.1 Ly$\alpha$ line morphology

The top panel of Figure 3.8 shows the spectral region encompassing the Ly$\alpha$ line in the Cosmic Horseshoe, plotted in arbitrary flux-density units vs. velocity relative to the systemic redshift of the galaxy. We interpret the complex morphology as consisting of two main emission components: a narrow, symmetric component which is barely resolved (FWHM $\lesssim 50\,\text{km s}^{-1}$ after deconvolution with the ESI spectral resolution of FWHM $= 75\,\text{km s}^{-1}$) centred at $v = +115\,\text{km s}^{-1}$, and a broader, asymmetric component which peaks at $v = +275\,\text{km s}^{-1}$ but extends to $v \simeq +700\,\text{km s}^{-1}$. The first, narrow component has a peak flux $\sim 1.5$ times higher than that of the second. There may be a third, weak component at negative velocities, centred near $v \sim -80\,\text{km s}^{-1}$, but its identification is uncertain, given the blending with absorption from the Ly$\alpha$ forest. The total flux in the line, without correcting for gravitational lensing and reddening (these corrections will be applied later—see Section 3.6.3) is $F(\text{Ly}\alpha) = (4.5 \pm 0.2) \times 10^{-16}\,\text{erg s}^{-1}\,\text{cm}^{-2}$ where the error reflects both the random noise in the data and the uncertainty in the stellar continuum (measured redward of Ly$\alpha$), combined in quadrature. In our assumed cosmology, the measured flux corresponds to a Ly$\alpha$ luminosity $L(\text{Ly}\alpha) = (2.0 \pm 0.1) \times 10^{43}\,\text{erg s}^{-1}$. The line equivalent width is $W_0(\text{Ly}\alpha) = (11 \pm 0.2 \pm 2.5)\,\text{Å}$, (switching sign convention, compared to Table 3.2, to indicate equivalent widths of emission lines as positive and those of absorption lines as negative); here we have quoted separately the random and systematic errors respectively to emphasize that the main uncertainty in the value of $W_0(\text{Ly}\alpha)$ arises from the placement of the underlying stellar continuum. Although the net profile is in emission, the value of $W_0(\text{Ly}\alpha)$ we measure is below the threshold $W_0(\text{Ly}\alpha) \geq 20\,\text{Å}$ generally adopted to define the so-called Ly$\alpha$ emitters (e.g. Hu et al. 1998; Rhoads et al. 2000; Shapley et al. 2003). Nevertheless, the profile exhibits the broad characteristics that are typical of Ly$\alpha$ emission from high-$z$ galaxies: an abrupt blue edge and an extended red wing (e.g. Tapken et al. 2007); with the high resolution and S/N of our data we can now examine its characteristics in greater detail than is normally possible.

### 3.6.2 Comparison to radiative transfer models

The Ly$\alpha$ emission line emerging from star-forming galaxies has been the subject of many studies over the last forty years, since the seminal paper by Partridge & Peebles (1967). Among more recent investigations, those by the Geneva group (see, for example, Schaerer 2007 which also includes a comprehensive set of references to earlier work) have focussed in particular on the radiation transfer of Ly$\alpha$ photons in an expanding medium, in an attempt to reproduce the variety of Ly$\alpha$ profiles seen in high-redshift galaxies, where

large-scale outflows are the norm. Having established the existence of such outflows in the Cosmic Horseshoe (Section 3.5.1), we can use the models by Verhamme et al. (2006) to interpret the Ly$\alpha$ profile in Figure 3.8.

The basic idea is that the Ly$\alpha$ photons emitted from a central region of star-formation, where the early-type stars and their H II regions are located, suffer multiple scatterings before they can escape the nebula. Such scatterings not only redistribute the photons in frequency, but also convert a fraction of them into infrared photons if any dust is present. If the scattering medium is expanding, the net effect is a reduction of the Ly$\alpha$ luminosity (measured by the fraction, $f_{\rm esc}$, of photons which manage to escape) and an overall shift of the wavelength distribution of the escaping photons to longer wavelengths, as blue-shifted photons are absorbed by the H I gas in front of the stars. The profile of the emergent Ly$\alpha$ line (for a given star formation rate which determines the intrinsic Ly$\alpha$ luminosity) depends on a combination of parameters, principally the expansion velocity of the medium, $v_{\rm exp}$; its internal velocity dispersion, normally measured by the parameter $b = \sqrt{2}\sigma$; the column density of neutral hydrogen, $N(\text{H I})$; and the column of dust, as measured by the colour excess $E(B-V)$.

The Ly$\alpha$ line in the Cosmic Horseshoe matches well some of the characteristics of the theoretical profiles generated by the Verhamme et al. (2006) models for the simplest geometrical configuration: a spherical shell expanding with uniform velocity. Indeed, as can be appreciated from Figure 3.8 where the Ly$\alpha$ emission line and the Si II $\lambda1526.7070$ absorption line are plotted on a common velocity scale, the red wing of the former almost mirrors the blue wing of the latter, both extending to $|v| \simeq 700$–$800\,\text{km s}^{-1}$. A prediction of the models is that there should be a maximum in the Ly$\alpha$ emission at a positive velocity (relative to the stars) $v = -2v_{\rm exp}$. In our case, the velocity of the longer-wavelength peak, $v = +275\,\text{km s}^{-1}$ is indeed at about twice $|v| = 146$ km s$^{-1}$ which we measured in Section 3.5.1 for the gas with the highest optical depth in absorption. Referring to Figure 12 of Verhamme et al. (2006), these are photons which have undergone just one backscattering from the receding portion of the expanding shell into our line of sight—with this frequency shift they can travel unabsorbed through the approaching (i.e. blue-shifted) part of the shell. The long tail to $v \simeq 700\,\text{km s}^{-1}$ is made up of photons which have undergone two or more backscatterings, while the narrow component centred at $v = +115\,\text{km s}^{-1}$ consists of photons which have been multiply scattered from the approaching part of the shell.

The balance between the photons escaping from the approaching and receding portions of the shell—reflected in the relative flux of the two emission peaks—is a function of the column density of neutral hydrogen through the shell: as $N(\text{H I})$ increases, the more redshifted peak of emission dominates over the lower redshift one. Out of the illustrative examples considered by Verhamme et al. (2006) in their Figure 16, the case with $N(\text{H I}) = 7 \times 10^{19}\,\text{cm}^{-2}$ matches our observed profile closely.

While this correspondence between simulated and observed profiles is impressive, other aspects of the models are less satisfactory. One of the difficulties in relating the Verhamme et al. (2006) models to our observations of the Cosmic Horseshoe stems from the fact that the absorption profiles of the interstellar lines do not fit the simple picture of an expanding shell with a well-defined velocity. With absorption extending over a thousand km s$^{-1}$, and without any information which would allow us to relate the velocity of the gas to its location within the galaxy, there is no obvious justification for equating the velocity

of the gas with the highest optical depth, $v = -146$ km s$^{-1}$, to the expansion velocity of the idealised shell. A further difficulty is that in the Verhamme et al. (2006) models there is also a strong dependence of the line profile on the velocity dispersion of the gas within the expanding shell. The clear distinction between the two redshifted peaks of emission requires not only low column densities of neutral gas [$N(\mathrm{H\,I}) \lesssim 5 \times 10^{20}\,\mathrm{cm}^{-2}$], but also relatively quiescent gas within the expanding shell ($|v_{\mathrm{exp}}|/b \gtrsim 5$). With the values we measure from the interstellar lines in the Horseshoe, $|v_{\mathrm{exp}}|/b = 145/105 \sim 1$, the profiles predicted by Verhamme et al. (2006) would look drastically different (see their Figure 15) and the two emission components would merge into one. The problem is exacerbated by the presence of gas at velocities as high as $v \simeq -800\,\mathrm{km\ s}^{-1}$ (see Figure 3.5) which is not included in the models. A final point is that the models considered by Verhamme et al. (2006) generally assume unity covering factor of the central source of Ly$\alpha$ photons by the outflowing gas, whereas in the Cosmic Horseshoe the interstellar absorption lines appear to cover only $\sim 60\%$ of the stellar UV continuum (Section 3.5.2).

Presumably, the real geometrical configuration of stars, H\,II regions (which recall are at the same velocity as the stars—see Table 3.1), and outflowing ISM is more complicated than in the simple picture considered (for general illustrative purposes) by Verhamme et al. (2006). Treatments of Ly$\alpha$ radiation transfer in more complex situations have been examined in the literature, but generally with fewer specific realizations that can be compared directly to our observations of the Ly$\alpha$ line in the Cosmic Horseshoe. For example, Hansen & Oh (2006) considered the effects of a multiphase gas outflow, either in a shell with holes or in an ensemble of gas clumps. It is interesting that in their simulations the former scenario can still give a double-peak Ly$\alpha$ emission line, whereas the latter tends to generate more amorphous profiles. A further point of note is that in such multiphase outflows Ly$\alpha$ photons can escape even when the intervening column density of neutral hydrogen is high. It would obviously be of considerable interest to test whether a model tailored to the observed properties of the Cosmic Horseshoe can reproduce its Ly$\alpha$ profile.

### 3.6.3 Escape fraction of Ly$\alpha$ photons

Before concluding this section, we calculate the escape fraction of Ly$\alpha$ photons by comparing the observed Ly$\alpha$ luminosity with that of the UV continuum. In carrying out such a comparison, we convert the luminosities to star formation rates (SFR) using the conversions proposed by Kennicutt (1998), divided by a factor of 1.8 to account for the lower proportion of low mass stars in the Chabrier (2003) IMF relative to the standard Salpeter (1955) IMF adopted by Kennicutt. [1] We also correct for gravitational lensing magnification, although our conclusion is not sensitive to this factor, as we are comparing luminosities over the same regions of the Cosmic Horseshoe. In the lensing model by Dye et al. (2008), the magnification factor of the whole Einstein ring is 24; in Section 3.3

---

[1]Earlier in this work, for our comparison between the stellar wind profiles and *Starburst99* models, we used a Salpeter IMF. For our calculation of SFRs we use a Chabrier IMF. This is merely for ease of comparison with the work of previous authors, whose IMF choices we are emulating. As noted in the text, the Chabrier and Salpeter IMFs are the same at the very high mass end but differ at the low mass end of the function. As we are concerned with the light from the massive OB stars, these two IMFs are very similar for our purposes.
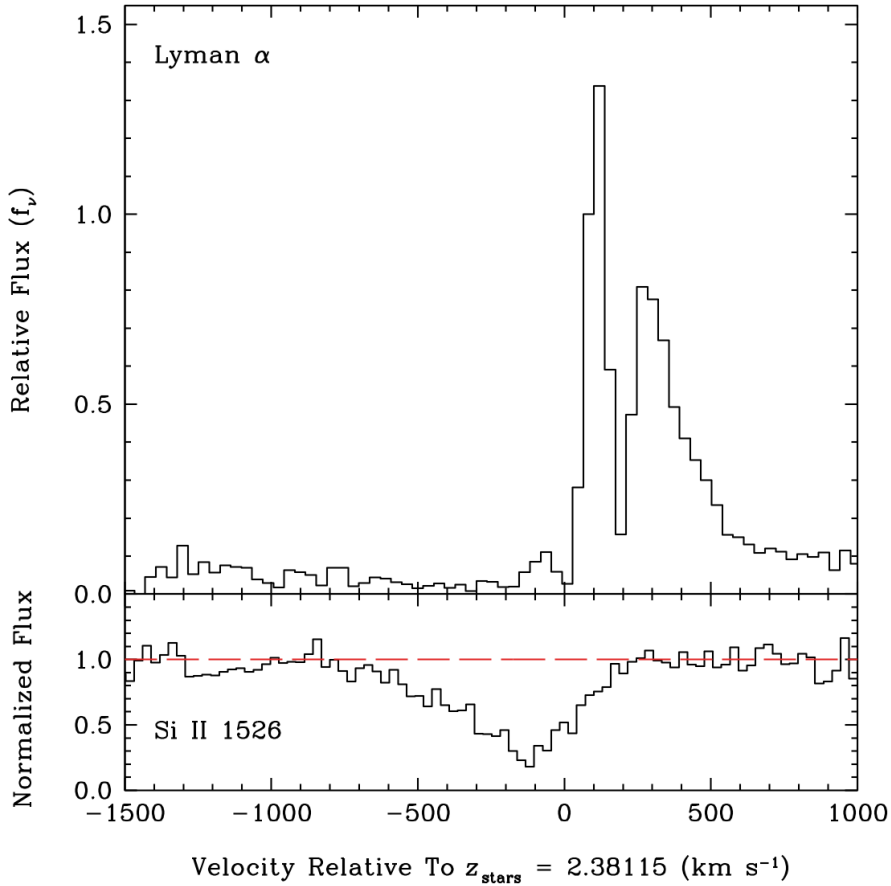
Figure 3.8 Lyα emission and Si II absorption lines plotted on a common velocity scale. The former mirrors the latter in velocity space.

we calculated that the ESI slit captured a fraction $0.25 \pm 0.05$ of the total light. In the following, we do not carry the uncertainty in this estimate through the calculation, as it is the same for the Lyα line and the UV continuum, and we adopt a magnification factor of $24 \times 0.25 = 6$ for the portion of the Cosmic Horseshoe recorded with ESI. The comparison between SFR(Lyα) and SFR(UV) is sensitive to the reddening correction, since the two estimates are based on features at different wavelengths. We adopt $E(B - V) = 0.15$, as determined for the same two knots of the Horseshoe by Hainline et al. (2009—see their discussion of the derivation of this value), together with the reddening curve of Calzetti et al. (2000).

From our ESI spectrum we measure a UV continuum luminosity at 1700 Å $L_\nu(1700\,\text{Å}) = 1.1 \times 10^{30}$ erg s$^{-1}$ Hz$^{-1}$ which, using Kennicutt's (1998) conversion

$$\text{SFR(UV)}(M_\odot \text{ yr}^{-1}) = 1.4 \times 10^{-28} L_\nu \text{ (erg s}^{-1}\text{ Hz}^{-1}), \tag{3.4}$$

gives

$$\text{SFR(UV)} = 159 \times 1/1.8 \times 3.8 \times 1/6 = 56 M_\odot \text{ yr}^{-1} \tag{3.5}$$

with correction factors for the IMF, reddening, and magnification respectively.[2]

---

[2]Recently, Leitherer (2008) re-examined Kennicutt's calibrations as given here in eqs. (3.4) and (3.6) in the light of new *Starburst99* models which include the effects of stellar rotation. While these models are still at an exploratory stage, the indications are that, at solar metallicities, they may result in $\sim 20\%$ reductions of the values of SFR deduced from both the UV continuum and Hα. At sub-solar metallicities, however, SFR(Hα) is further reduced relative to SFR(UV), reflecting the harder ionizing spectrum of

For comparison, Hainline et al. (2009) deduced SFR(H$\alpha$) = 113 $\pm$ 17$M_\odot$ yr$^{-1}$ from the H$\alpha$ luminosity measured with NIRSPEC, but the comparison is complicated by the uncertainties in the respective flux calibrations. In any case, in galaxies at $z = 2-3$, there is an inherent dispersion (of about this magnitude) in star formation measurements from H$\alpha$ emission and UV continuum (e.g. Pettini et al. 2001; Erb et al. 2006c) which can have a number of causes, apart from random errors. First, emission lines and UV continuum do not sample the same stellar populations: the luminosity of H$\alpha$ is due primarily to the most massive stars, with shorter lifetimes than the wider range of stellar masses ($M \gtrsim 5M_\odot$) whose integrated light makes up the continuum at 1700 Å. Second, the conversion from H$\alpha$ (and Ly$\alpha$) luminosity to SFR implicitly assumes that all the Lyman continuum (LyC) photons are absorbed within the H II region and reprocessed into emission lines—a situation which is often referred to as a 'radiation-bounded nebula'. Of course, if a fraction of LyC photons escape unabsorbed from the H II region, SFR(H$\alpha$) and SFR(Ly$\alpha$) will be systematically lower than SFR(UV).

Turning to Ly$\alpha$, we can use Kennicutt's (1998) calibration of SFR(H$\alpha$) and case B recombination to deduce

$$\text{SFR(Ly}\alpha)(M_\odot \text{ yr}^{-1}) = 9.1 \times 10^{-43} L(\text{Ly}\alpha) \text{ (erg s}^{-1}) \qquad (3.6)$$

which, together with our measured $L(\text{Ly}\alpha) = 2.0 \times 10^{43}$ erg s$^{-1}$, gives

$$\text{SFR(Ly}\alpha) = 18 \times 1/1.8 \times 5.3 \times 1/6 = 8.9 M_\odot \text{ yr}^{-1} \qquad (3.7)$$

where, as in eq. (3.5), the correction factors account for the IMF, dust extinction, and magnification respectively.

By comparing the three estimates of SFR, we deduce $f_{\text{esc}}^{\text{Ly}\alpha} \simeq 0.16$–0.08, depending on whether we compare SFR(Ly$\alpha$) to SFR(UV) or SFR(H$\alpha$), respectively. The former value is independent of the absolute flux calibration but assumes that, intrinsically (i.e. before the Ly$\alpha$ line is quenched by resonant scattering), SFR(UV) $\equiv$ SFR(Ly$\alpha$). Conversely, the latter value assumes no errors in the relative flux calibrations of the NIRSPEC and ESI data, and in the calculation of the fractions of the total light from the Horseshoe captured by the two spectrographs. However, either estimate of $f_{\text{esc}}^{\text{Ly}\alpha}$ is plausible, given the wide range found in other Ly$\alpha$ emitters (e.g. Verhamme et al. 2008; Pentericci et al. 2009). It must also be remembered that these values of $f_{\text{esc}}^{\text{Ly}\alpha}$ apply to our viewing angle and to the area of the galaxy covered by the entrance slit of the spectrographs; the escape fraction could be higher in other directions (Neufeld 1991) and over larger areas (Saito et al. 2006).

Concluding this section, models of Ly$\alpha$ emission resonantly scattered by an expanding medium need further improvement in order to reproduce simultaneously the observed properties of the Ly$\alpha$ emission line and of the interstellar absorption lines in the Cosmic Horseshoe. Nevertheless, interpreting the Ly$\alpha$ line in terms of these models has given us some insight into the physical conditions of the gas. The main inference one would draw from the models of Verhamme et al. (2006) is that the column densities of neutral hydrogen and dust need to be relatively low—$N(\text{H I}) \simeq 7 \times 10^{19}$ cm$^{-2}$ and $E(B-V) \simeq$ 0.1—in order for the line to exhibit two distinct emission peaks at the velocities observed.

---

metal-poor massive stars. Such effects may partly explain why we deduce SFR(H$\alpha$) > SFR(UV) in the Cosmic Horseshoe.

Rest-Frame UV Spectrum of 'The Cosmic Horseshoe'
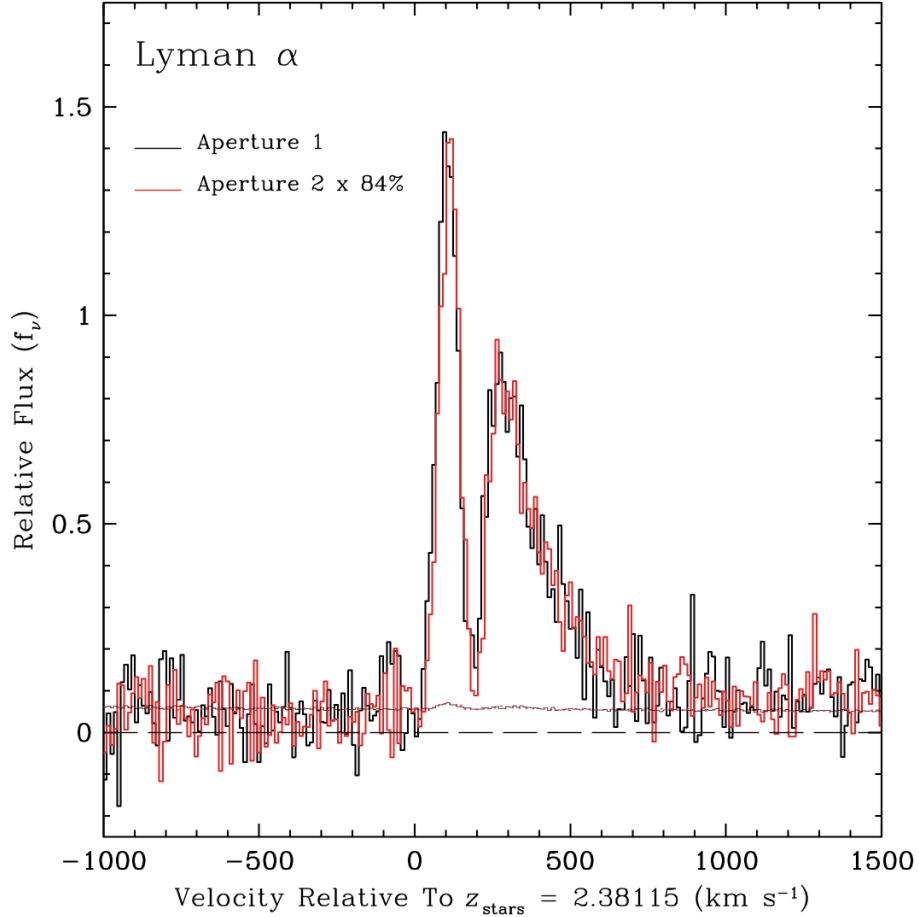
Figure 3.9 After scaling the flux in Aperture 2 (see Figure 3.1) by a factor of 0.84, the Lyα profiles recorded from the two bright knots of emission in the Cosmic Horseshoe are indistinguishable from each other at the S/N of the present observations. The corresponding error spectra are also plotted (thin line near the zero level).

On the other hand, recall that in Section 3.5.2 we concluded that $\log N(\text{H\,I})/\text{cm}^{-2} \simeq 20.8$ *if* the first ions arise primarily in H I gas, as is the case in the Milky Way, damped Lyα systems, and the gravitationally lensed LBG cB58. The order of magnitude difference between these two estimates of the column density of gas can be reconciled if most of the gas in front of the stars in the Cosmic Horseshoe is ionized, with a neutral fraction of only about 10%. The profile of the O I $\lambda 1302.1685$ absorption line, which traces exclusively neutral gas, is consistent with this conclusion.

Given the sensitivity of the profile of the Lyα line to the geometrical and physical properties of the ambient interstellar medium, one may expect to see variations between even slightly different sightlines through the galaxy. In principle, the lensing magnification of the source offers a good opportunity to recognize such small-scale inhomogeneities. And yet no such variations are seen in the Cosmic Horseshoe. Recall (Section 3.3 and Figure 3.1) that we obtained separate spectra for the two brightest knots in the Einstein ring, which we labelled 'Aperture 1' and 'Aperture 2'. After scaling the latter by a factor of 0.84 (derived empirically and found to be the same for the Lyα line and the UV continuum), the profiles of the Lyα line in the two apertures are identical within the limits of the noise, as can be appreciated from inspection of Figure 3.9. Evidently, the same region of the source is lensed into the two knots of the Cosmic Horseshoe. This is all the more puzzling, given that Hainline et al. (2009) found that the ratio [N II] $\lambda 6584/\text{H}\alpha$

Table 3.4 C III] Emission Lines

| Line | $z$ | $\sigma^{\mathrm{a}}$ $(\mathrm{km\ s^{-1}})$ | $F^{\mathrm{b}}$ $(10^{-18}\mathrm{erg\ s^{-1}\ cm^{-2}})$ | $L^{\mathrm{b}}$ $(10^{41}\,\mathrm{erg\ s^{-1}})$ |
|---|---|---|---|---|
| 1906.683 | $2.38103 \pm 0.00014$ | $62 \pm 7$ | $9.9 \pm 1.3$ | $1.29 \pm 0.16$ |
| 1908.734 | $2.38127 \pm 0.00017$ | $62 \pm 7$ | $8.8 \pm 1.3$ | $1.14 \pm 0.16$ |

[a] After correcting for the instrumental resolution ($\sigma_{\mathrm{instr}} = 32\,\mathrm{km\ s^{-1}}$), and constrained to be the same for both lines.
[b] Corrected for reddening and lensing magnification.

differs by almost a factor of 2 (at the $\sim 4\sigma$ significance level) between the two Apertures. The [N II]/H$\alpha$ ratio responds to changes in metallicity and ionization parameter (e.g. Pettini & Pagel 2004; Kobulnicky & Kewley 2004) which presumably are not the same in the regions of the galaxy lensed into Apertures 1 and 2 within the Einstein ring (knots 'A' and 'D' of Belokurov et al. 2007). Evidently, such variations do not have an impact on the Ly$\alpha$ emission morphology.

## 3.7 Other Emission Lines

The nebular C III] $\lambda\lambda 1906.683, 1908.734$ doublet is clearly resolved in our ESI spectrum of the Cosmic Horseshoe (see Figure 3.10). By fitting Gaussian profiles to the two lines, we deduced the parameters listed in Table 3.4. The mean redshift, $z_{\mathrm{C\,III]}} = 2.38115$, is in excellent agreement with the redshift of the OB stars, as expected (Section 3.4.1), and differs by only $-7\,\mathrm{km\ s^{-1}}$ from the weighted mean $\langle z_{\mathrm{H\alpha}} \rangle = 2.38123$ of the two apertures (see Figure 3.1) measured separately by Hainline et al. (2009) from their NIRSPEC spectra. The good match attests to the mutual consistency of the ESI and NIRSPEC wavelength scales. The line widths are rather uncertain due to the limited S/N; with the prior condition that the width should be the same for both lines, we obtain $\sigma_{\mathrm{C\,III]}} = 62 \pm 7\,\mathrm{km\ s^{-1}}$ (this is the value used in the fits shown in Figure 3.10), in very good agreement—again, as expected—with the weighted mean $\langle \sigma_{\mathrm{H\alpha}} \rangle = 65\,\mathrm{km\ s^{-1}}$ of the two apertures reported by Hainline et al. (2009).[3]

As is well known, the ratio of these two C III] lines is a function of the electron density, varying from $F(1906)/F(1908) = 1.5$ to $\sim 0.8$ in the range $n(e) = 100$–$30\,000\,\mathrm{cm^{-3}}$. Our measured $F(1906)/F(1908) = 1.1 \pm 0.2$ implies very high densities, in the range $n(e) \simeq 5\,000$–$25\,000\,\mathrm{cm^{-3}}$, which however may not be unusual for starbursts at $z = 2 - 3$ (Brinchmann et al. 2008; Liu et al. 2008; Hainline et al. 2009).

We searched for nebular O III] $\lambda\lambda 1660.809, 1666.150$ emission, but these lines are below the detection limit of our data. This is not surprising, given that the O III] doublet is weaker than C III] by a factor of $\sim 7$ in the LBG composite spectrum of Shapley et

---

[3]Our ESI observations are comparable to the NIRSPEC observations of Hainline et al. because the spectroscopic slits used in each study were aligned in the same way, covering the same part of the lensed ring.
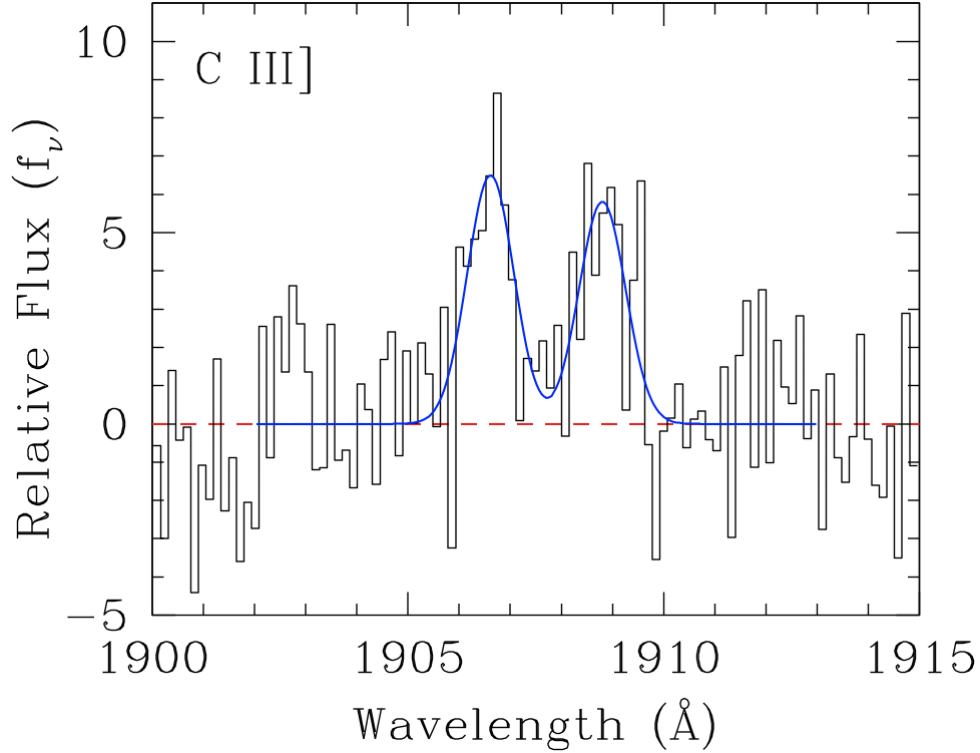
Figure 3.10 *Histogram:* Portion of the ESI spectrum of the Cosmic Horseshoe in the region of the C III] $\lambda\lambda 1906.683, 1908.734$ nebular emission lines, after subtracting the stellar continuum. *Blue continuous line:* Gaussian fits to the emission lines; see Table 3.4 and Section 3.7 for details.

al. (2003), and the C III] lines in the Cosmic Horseshoe are only detected at the $\sim 7\sigma$ significance level (Table 3.4). Any He II $\lambda 1640.418$ emission from Wolf-Rayet stars is also too weak to be identified with certainty in our spectrum.

## 3.8 Discussion

We now consider the results of the previous sections in the light of some of the questions raised in the Introduction.

### 3.8.1 Metallicity estimates

With available instrumentation, only strongly lensed galaxies offer the means to cross-check at high redshift the metallicity of early-type stars with that of the H II regions that surround them. We naturally expect the two measures to be the same, since the stars presumably formed very recently out of the gas which they now ionize; thus, this is essentially a consistency check between different metallicity indicators, all the more important given the known systematic offsets between different emission line measures of chemical abundance in H II regions (see, for example, Kewley & Ellison 2008). Such offsets in turn impact on the interpretation of chemical patterns and of trends, such as the mass-metallicity relation and its evolution with redshift, which can give us insights

into galactic chemical evolution.

In Table 3.5 we have collected available determinations of element abundances in the Cosmic Horseshoe, bringing together the stellar data from Section 3.4 with the nebular measurements by Hainline et al. (2009). The first three entries in the Table give the oxygen abundance deduced from strong emission line indices, respectively the $R23$ index of Pagel et al. (1979), for which Hainline et al. (2009) used the calibration by Tremonti et al. (2004) based on observations of tens of thousands of nearby galaxies in the *SDSS*, and the $N2$ and $O3N2$ indices of Pettini & Pagel (2004). The last three entries in the Table are from our analysis in this paper of UV spectral features from OB stars in the Horseshoe.

It is difficult to quote an error for each of the entries in Table 3.5; a realistic estimate should take into account the S/N of the data, the scatter in the adopted index calibration and the systematic bias which may affect it. However, most estimates evidently converge towards a metallicity of about a half solar (which, incidentally, is quite typical of star-forming galaxies at these redshifts—see Erb et al. 2006a). It is reassuring that stellar and nebular abundances are generally in good mutual agreement. The only deviant measure appears to be from the $R23$ method which is known, however, to overestimate the oxygen abundance in the near-solar regime, particularly when the calibration by Tremonti et al. (2004) is used (e.g. Kennicutt, Bresolin & Garnett 2003; Kewley & Ellison 2008).

Less satisfactory aspects of the comparison in Table 3.5 are: (i) the poorly understood failure of the 1978 index of Rix et al. (2004) to provide a meaningful estimate of metallicity in this particular case; and (ii) the current limitations in the use of the wind lines as accurate abundance diagnostics. Point (i) can only be addressed with a larger set of high quality UV spectra of high redshift galaxies. Until it is resolved, however, it may be unwise to use this index to investigate the possibility of a differential enrichment of Fe-peak elements compared to the products of Type-II supernovae (Pettini et al. 2002; Halliday et al. 2008). Concerning point (ii), it is frustrating that while the strong wind lines are in principle one of the most easily measured abundance diagnostics—at least in data of sufficient resolution to resolve stellar and interstellar components—we still lack a comprehensive library of empirical ultraviolet spectra of OB stars of different metallicities to realise their full potential. The *HST* survey of the Magellanic Clouds by Leitherer et al. (2001) went some way towards remedying this situation, but their sampling of the upper H-R diagram is still too sparse to assemble separate sets of Large and Small Magellanic Cloud stars. The resulting hybrid library, obtained by combining all the available spectra into one set, can only give an approximate measure of metallicity, given the factor of $\sim 2$ difference in the oxygen abundance of the two Clouds.

## 3.8.2   Escape of ionizing photons

It is still unclear what determines $f_{\rm esc}^{\rm LyC}$, the fraction of hydrogen ionizing photons which escape from star-forming galaxies into the intergalactic medium. Direct detection of these Lyman continuum photons has proved problematic until recently (e.g. Shapley et al. 2006; Iwata et al. 2009), and yet $f_{\rm esc}^{\rm LyC}$ must have been large at very high redshifts for the Universe to be reionized by the star-formation activity thought to have taken place at $z > 6$ (e.g. Bolton & Haehnelt 2007; Ryan-Weber et al. 2009).

Observations of gravitationally lensed galaxies may offer insights into the factors that

Table 3.5 Metallicity Comparison

| Method | Element(s) | $Z/Z_\odot$[a] | Comments |
|--------|-----------|-------------|----------|
| $R23$ | O | 1.5 | H II regions[b] |
| $N2$ | O | 0.5 | H II regions[b] |
| $O3N2$ | O | 0.5 | H II regions[b] |
| 1425 | C, Si, Fe | 0.5 | Photospheric, OB stars[c] |
| 1978 | Fe | ... | Photospheric, B stars[c] |
| C IV | C, N, O, Fe | $\sim 0.6$ | Stellar wind, O stars[d] |

[a] Abundance relative to solar (on a linear scale), using the compilation of solar abundances by Asplund et al. (2005).
[b] As reported by Hainline et al. (2009).
[c] This work (Section 3.4.2).
[d] This work (Section 3.4.3).

control $f_{\rm esc}^{\rm LyC}$. By fully resolving the interstellar absorption lines in our ESI spectrum of the Cosmic Horseshoe, we reached the conclusion that the interstellar gas only covers $\sim 60\%$ of the stellar UV light, as viewed from Earth. This is a promising prerequisite for large values of $f_{\rm esc}^{\rm LyC}$, making the Horseshoe a high priority candidate in searches for LyC emission from high-$z$ galaxies. On the other hand, if $\sim 40\%$ of the photons from the stars and surrounding H II regions really had a clear path out of the galaxy, we may have expected to see a strong and narrow Ly$\alpha$ emission line centred at $z_{\rm H\,II}$, whereas no such feature is present in our spectrum. Possibly, some 40% of the stars are located behind neutral gas of too low a column density to give discernible absorption in the metal lines, and yet capable of scattering most of the Ly$\alpha$ photons out of the line of sight (Hansen & Oh 2006). Whether such gas would be optically thick to LyC photons remains to be established.

Another necessary condition for the escape of LyC photons is a weaker H$\alpha$ emission line than expected on the basis of the UV continuum luminosity and reddening (admittedly in the idealised case of continuous star formation at a constant rate). Such a disparity would arise from a 'matter-bounded nebula', where not all of the LyC photons emitted by the stars are absorbed and reprocessed within the H II region. As discussed in Section 3.6.3, in the Cosmic Horseshoe SFR(H$\alpha$) $>$ SFR(UV), although a number of different factors, apart from leakage of LyC photons, can affect this comparison. In conclusion, it would definitely be worthwhile to search for LyC emission in the Cosmic Horseshoe at wavelengths below 3085 Å (the redshifted value of the Lyman limit at $z = 2.38115$). Furthermore, it would be of interest to check for partial covering of the stars by the foreground interstellar medium in more galaxies among the newly discovered strongly lensed sources, ideally including galaxies with a range of Ly$\alpha$ equivalent widths. With such data in hand, we should be in a better position to understand the conditions that determine the escape fraction of LyC photons and the morphology of the Ly$\alpha$ line.

### 3.8.3 Comparison with MS 1512-cB58

One of the motivations for the present study was to establish how typical are the properties of the galaxy MS 1512-cB58, the only previous case where the gravitational lensing boost was sufficient to allow a detailed look at the spectrum of a high-redshift star-forming galaxy. While we have now doubled the 'sample' of high-$z$ galaxies with good-quality ESI spectra, it would clearly be premature to draw general conclusions on the basis of just two objects. Nevertheless, one cannot help but being struck by how closely these two galaxies resemble each other in many of their properties. They are very similar in their overall metallicity and probably in their detailed chemical composition, indicating that they have reached comparable stages in the conversion of their gas reservoirs into stars. Their young stellar populations are largely indistinguishable in their UV spectral features, especially the P-Cygni lines which are sensitive indicators of the mode of massive star formation and of differential reddening among stars at the upper end of the IMF. Most remarkable perhaps is the unexpected similarity in the properties of their outflowing interstellar media, with velocities spanning in both cases $\sim 1000\,\mathrm{km\ s^{-1}}$, from $-800$ to $+250\,\mathrm{km\ s^{-1}}$ relative to the stars, and involving comparable column densities of gas.

Presumably, it is just a coincidence that the first two galaxies at $z = 2$–$3$ whose UV spectra have been put under the 'microscope' of gravitational lensing have also turned out to be similar in so many respects. After all, we now know that the Cosmic Horseshoe and MS 1512-cB58 are also forming stars at comparable rates of $\sim 50$–$100\,M_\odot\ \mathrm{yr^{-1}}$, and have similar dynamical masses of $M_{\mathrm{vir}} \sim 1 \times 10^{10} M_\odot$ (Hainline et al. 2009 for these measurements in the Cosmic Horseshoe and Teplitz et al. 2000 for cB58). Future studies of other gravitationally lensed objects will arguably show a wider range of properties of star-forming galaxies at these redshifts.

What is interesting then, given the underlying similarity of the Horseshoe and cB58, is to consider the aspects in which they *differ*: the incomplete coverage of the stellar light by the interstellar absorption lines and the strikingly different Ly$\alpha$ morphologies. It is these two factors alone that would lead an observer to 'classify' the two galaxies differently. For example, in the rough breakdown of LBGs by Shapley et al. (2003) according to their UV spectral properties, cB58 would fall in the quartile with the highest interstellar absorption line equivalent widths and reddening, while the Cosmic Horseshoe would be in the quartile with the second highest Ly$\alpha$ *emission* equivalent width. And yet, from what we have uncovered in the present study, it may be the case that these differences are perhaps simply due to orientation effects—viewing two intrinsically similar galaxies along differing sightlines through their interstellar media, one (the Horseshoe) more rarefied and highly ionized than the other (cB58). With future studies of other strongly lensed galaxies we shall hopefully learn how to distinguish intrinsic differences from those caused by second-order effects, of which the direction from which we view the central starburst may be one example. For the moment, however, we must remain cautious of overinterpreting differences between different 'classes' of high-redshift galaxies, especially if such distinctions are based on the morphology and strength of the Ly$\alpha$ line, whose appearance is so sensitive to a variety of different parameters (e.g. Pentericci et al. 2009).

# 3.9 Summary and Conclusions

We have presented ESI observations of the rest-frame ultraviolet spectrum of a star-forming galaxy at $z = 2.38115$, lensed by a massive foreground galaxy into a nearly complete Einstein ring dubbed the 'Cosmic Horseshoe'. The high gravitational magnification affords the rare opportunity of recording the spectrum of this member of the $z = 2$–$3$ galaxy population at higher resolution and S/N than otherwise achievable, and thereby provides us with a close-up look of a galaxy during the epoch when cosmic star-formation activity was at its peak. Our main findings are as follows.

(i) The Cosmic Horseshoe shares many of its properties with the population of 'BX' galaxies selected with the colour criteria of Steidel et al. (2004). Its metallicity $Z \simeq 0.5 Z_{\odot}$, dynamical mass $M_{\rm vir} \simeq 1 \times 10^{10} M_{\odot}$, and reddening $E(B-V) = 0.15$ are all typical of those galaxies (Erb et al. 2006a,b,c). With a star-formation rate SFR $\simeq 100 M_{\odot}$ yr$^{-1}$, the Horseshoe is among the most luminous galaxies in the BX sample.

(ii) Generally, there is good agreement between different metallicity indicators based, respectively, on ratios of strong nebular emission lines, on blends of stellar photospheric lines, and on P-Cygni lines from the most luminous OB stars. The $R23$ index of Pagel et al. (1979) seems to overpredict the oxygen abundance by a factor of $\sim 3$, when calibrated with the prescription by Tremonti et al. (2004). Of the stellar measures, the 1978 index of Rix et al. (2004) does not fit the data well due to excess absorption not present in the models and whose identity remains unclear.

(iii) A continuous mode of star formation with a Salpeter slope for stars with masses $5 \le M \le 100 \, M_{\odot}$ and $100$ Myr age is consistent with the UV spectrum. Within the S/N limits of our spectrum, we see no evidence for a departure from a Salpeter IMF, nor differential reddening among massive stars, in the contrast of the P-Cygni lines over the underlying UV continuum.

(iv) The interstellar absorption lines are broad, extending over a velocity interval of $\sim 1000$ km s$^{-1}$, from $-800$ to $+250$ km s$^{-1}$ relative to the redshift of the stars and H II regions. The gas with the highest optical depths is outflowing from the regions of star formation with a speed of $\sim 150$ km s$^{-1}$, and only covers $\sim 60\%$ of the stellar continuum light.

(v) The Ly$\alpha$ line is in emission and shares many of the properties of the so-called Ly$\alpha$ emitters, although its equivalent width is a factor of $\sim 2$ smaller than the lower limit $W_0({\rm Ly}\alpha) \ge 20$ Å commonly adopted to define this subset of galaxies. The resolved line profile matches well those computed with models of resonantly scattered Ly$\alpha$ photons in an expanding medium, although such models find it difficult to account for the fact that the velocity dispersion of the gas is comparable to its bulk expansion velocity, and for the existence of gas extending over hundreds of km s$^{-1}$ in velocity space. Some $\sim 10$–$15\%$ of the Ly$\alpha$ photons produced escape the galaxy, the remainder presumably being absorbed by dust and recycled into infrared photons, or scattered over a larger area than that covered by our narrow-slit observations. It remains to be established what fraction of the Lyman *continuum* photons emitted by the stars leak into the IGM.

(vi) Overall, many of the physical properties of the stars and interstellar medium of the Cosmic Horseshoe are similar to those of the only other galaxy previously studied at comparable resolution and S/N, MS 1512-cB58 at $z = 2.7276$. This may not be surprising, given that both galaxies are fairly typical examples of the star-forming galaxy population

at these redshifts. The fundamental similarities between the two objects highlight the fact that the aspects in which they differ, particularly the very different morphologies of their Lyα lines, may be due to superficial reasons, such as differing viewing angles, rather than to more deeply rooted causes.

In the near future it should be possible to make further progress on all of these topics with the increasing numbers of strongly lensed high-redshift galaxies being discovered by the *SDSS* and other lensing surveys.

# 4

# A Study of Interstellar Gas and Stars in the Gravitationally Lensed Galaxy 'The Cosmic Eye' from Rest-Frame Ultraviolet Spectroscopy

$T$HE specific scientific context of studying the rest-UV spectrum of gravitationally lensed high redshift galaxies was presented in the Introduction to Chapter 3. So as to avoid redundancy, I refer the reader there for the background information necessary to appreciate the role of this chapter in the greater scientific discourse.

## 4.1 The Cosmic Eye

Among the bright, strongly lensed, high redshift galaxies, the Cosmic Eye is the most well-studied to date after cB58. Here we summarize available information which is relevant to our analysis.

The Cosmic Eye, also known as LBG J213512.73−010143, was so named because it consists of two bright arcs extending $\sim 3''$ which nearly fully surround a compact galaxy (Figure 4.1). From low resolution spectroscopy, the central galaxy was classified as a massive early-type spiral, or S0, galaxy at $z = 0.73$, and from rest-frame optical spectroscopy the source redshift was estimated to be $z = 3.0743$ (Smail et al. 2007). The detailed lensing model by Dye et al. (2007) concluded that the lensing of the Cosmic Eye is attributable to both the galaxy at $z = 0.73$ and a foreground cluster, MACS J2135.2-0102, at $z = 0.33$. Their models require two source components at similar redshifts: a main component which creates the Eye's ringed structure, and a secondary component, offset $\sim 0.3''$ to the west, responsible for producing faint extensions at either end of the northern arc. The total magnification of the system is estimated to be $\sim 25$; when
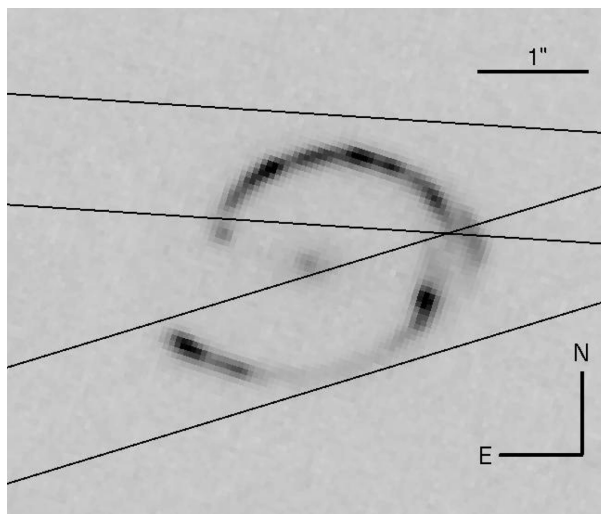
Figure 4.1 HST/ACS F606W image of the Cosmic Eye. The straight lines indicate the two placements of the $1.0 \times 20''$ entrance slit of ESI used for the observations reported here.

this is taken into account, the observed magnitude $r = 20.3$ corresponds to an intrinsic luminosity $L_{1700} \sim 1.5$–$2L^*_{1700}$ compared to the luminosity function of $z = 3$ galaxies estimated by Steidel et al. (1999) and more recently Reddy et al. (2008).

The geometry and kinematics of the Cosmic Eye have begun to be explored. Most recently, Siana et al. (2009) used the galaxy's far-infrared luminosity, which they found to be $\sim 8$ times lower than expected from its rest-frame UV luminosity (measured from both broadband *HST* photometry as well as the rest-UV spectrum of the Eye), to argue that a reddening curve similar to those determined from observations of stars in the Large and Small Magellanic Clouds (LMC/SMC) is more appropriate for the dust in the Cosmic Eye than the Calzetti et al. (2000) attenuation curve normally adopted for starbursts. The difference between the two reddening laws is one of geometry: the Calzetti et al. (2000) curve is thought to arise from a configuration where stars and dust are mixed together, whereas the LMC/SMC (or, for that matter, Milky Way) extinction curves are more appropriate to the reddening produced by a 'screen of dust' which is in the foreground of the sources of UV light.

Integral field spectroscopy of H$\beta$ and [O III] $\lambda\lambda 4959, 5007$ nebular emission lines with the OH-Suppressing Infrared Integral Field Spectrograph (OSIRIS) on the Keck II telescope (Stark et al. 2008) showed a regular rotation pattern $v_{\rm rot} \sin i = 55 \, {\rm km \, s^{-1}}$ on which are superimposed random motions with a comparable velocity dispersion of $\sigma = 54 \, {\rm km \, s^{-1}}$. Coppin et al. (2007) detected CO emission from the Cosmic Eye and found the signal to peak at the location of the secondary component of the source, suggesting that this component may be the remaining reservoir of gas available to fuel star formation.

The star formation rate of the galaxy has been estimated from its luminosity in the UV stellar continuum, H$\beta$ emission line, and infrared dust emission to be SFR $\sim 900$ (assuming a Calzetti reddening law), $\sim 100$, and $\sim 140 \, M_\odot \, {\rm yr^{-1}}$, respectively (Stark et al. 2008; Coppin et al. 2007; Siana et al. 2009).[1] The metallicity determined from

[1] All of these estimates are based on the conversion factors between luminosity and SFR given by

Table 4.1 SYSTEMIC REDSHIFT

| Ion | $\lambda_{\mathrm{lab}}^{\mathrm{a}}$ (Å) | $z$ | Origin |
|-----|------|------|--------|
| C II+N III | 1324.1418[b] | 3.0731 | Stars |
| O IV | 1343.354 | 3.0730 | Stars |
| S V | 1501.763 | 3.0732 | Stars |
| H$\beta$[c] | 4862.721 | 3.0737 | H II Regions |
| [O III][c] | 4960.295 | 3.0734 | H II Regions |
| [O III][c] | 5008.239 | 3.0735 | H II Regions |

[a] Vacuum wavelengths.
[b] Central wavelength of the blend.
[c] Measured from OSIRIS data reported by Stark et al. (2008).

the ratio of strong emission lines (the $R_{23}$ method of Pagel et al. 1979), is $Z \sim 0.9\,Z_\odot$ (Stark et al. 2008). At the current rate of star formation, it would have taken the galaxy $\sim 100\,\mathrm{Myr}$ to build its stellar mass of $\sim 6 \times 10^9\,M_\odot$ (Coppin et al. 2007).

To this growing body of data we now add a high resolution study of the rest-frame UV spectrum of the Cosmic Eye. At UV wavelengths the spectrum is dominated by the combined emission from early-type stars and absorption from interstellar gas. Such data can shed new light on the kinematics, chemical composition and stellar populations of this galaxy, complementing the information gleaned from other wavelengths.

## 4.2 Observations and Data Reduction

The observations and data reduction for this object were described in detail in Chapter 2. For your immediate reference, however, the final spectrum of the Cosmic Eye has a S/N $\simeq 14$ per $0.5\,\text{Å}$ bin between 5200 and $7500\,\text{Å}$ ($1275$–$1840\,\text{Å}$ in the rest-frame of the source), and a resolution FWHM $= 75\,\mathrm{km\,s^{-1}}$, sampled with $\sim 3$ wavelength bins.

## 4.3 The Interstellar Spectrum

### 4.3.1 The systemic redshift of the Cosmic Eye

An accurate determination of the systemic redshift of the lensed galaxy in the Cosmic Eye is critical to the rest of our analysis. Our rest-frame UV spectrum includes several absorption features from the photospheres of hot stars which can be used for this purpose. The cleanest among these are O IV $\lambda 1343.354$, S V $\lambda 1501.763$, and a close blend of C II and N III lines centred at $\lambda 1324.1418$ (all vacuum wavelengths); see Figure 4.2. Table 4.1 lists the redshifts deduced from each of these stellar lines, as well as the values of redshift we measured from the H$\beta$ and [O III] $\lambda\lambda 4959, 5007$ emission lines in the OSIRIS spectrum

---

Kennicutt (1998) and are appropriate for a Salpeter (1955) IMF. Adoption of a more realistic formulation of the IMF, such as that proposed by Chabrier (2003), would result in smaller values of SFR by a factor of 1.8 .
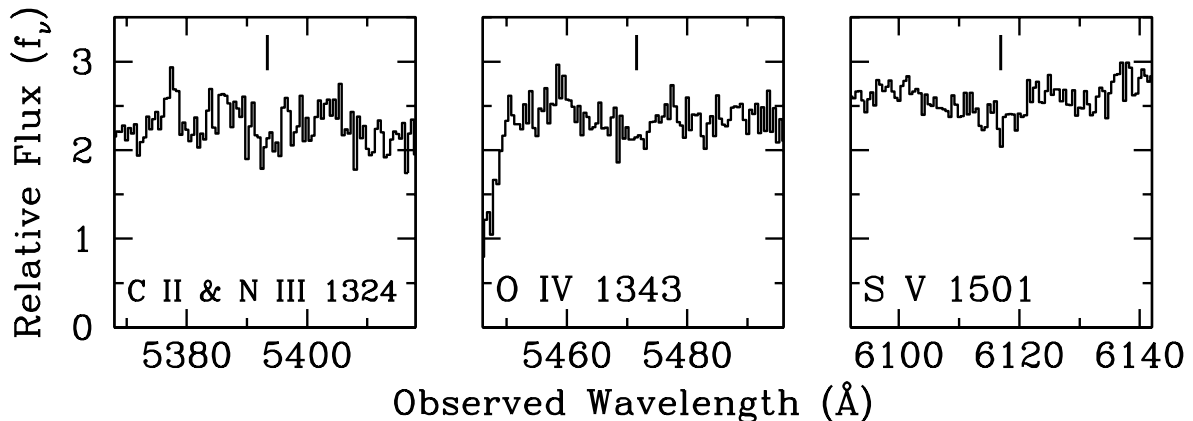
Figure 4.2 Portions of the spectrum of the Cosmic Eye encompassing stellar photospheric absorption lines used for the determination of the systemic redshift of the galaxy (see Table 4.1).

of Stark et al. (2008). As can be seen from Table 4.1, the mean redshift of the UV stellar lines, $\langle z_{\mathrm{OB\ stars}} \rangle = 3.0731$, differs by $-29\,\mathrm{km\ s^{-1}}$ from the mean $\langle z_{\mathrm{H\,II}} \rangle = 3.0735$ of the three nebular lines.[2] This small difference may reflect a small offset between the wavelength calibrations of ESI and OSIRIS, or may be simply due to noise in the spectra. It could also be real but, as we have no other reason to suspect that the massive stars in this galaxy and the nebulae they ionize should be at systematically different redshifts, we decided to average together all the values of redshift in Table 4.1 to deduce a mean systemic redshift for the galaxy $z_{\mathrm{sys}} = 3.07331 \pm 0.00024$ $(1\sigma)$. The standard deviation corresponds to a velocity uncertainty $\delta v = 18\,\mathrm{km\ s^{-1}}$, or just over one half of a wavelength bin in the final 1D ESI spectrum.

The 1-D rest-UV spectrum of the Cosmic Eye is presented in Figure 4.3. It was rebinned to $2\,\text{Å}\ \mathrm{pixel}^{-1}$ in the observed frame (for display purposes) before shifting to the rest-frame at $z_{\mathrm{sys}} = 3.07331$.

## 4.3.2 Kinematics of the absorbing gas

We closely inspected the spectrum of the Cosmic Eye for interstellar absorption lines and identified 20 transitions from eight elements in different ionization states, from O I to C IV. The absorption lines are listed in Table 4.2 and all but two (for clarity purposes) are reproduced in the montage in Figure 4.4.[3]

The most striking aspect of the Cosmic Eye's interstellar absorption lines is that they consist of two distinct components: a (mostly) blueshifted component centred at $v_{\mathrm{blue}} \simeq$

---

[2]Note that this differs from $\langle z_{\mathrm{H\,II}} \rangle = 3.0743$ reported by Smail et al. (2007), but the latter was not on a vacuum heliocentric scale (M. Swinbank, private communication).

[3]The two transitions omitted from Figure 4.4 are Si II $\lambda1304$, which is actually visible in the plot for the nearby O I $\lambda1302$ where it is indicated by a dotted line, and Ni II $\lambda1709$ which is of similar strength to the other two Ni II lines reproduced in the middle panel of Figure 4.4.

Table 4.2 Interstellar Absorption Lines

| Ion | $\lambda_{\mathrm{lab}}^{\mathrm{a}}$ (Å) | $f^{\mathrm{a}}$ | $\Delta v_{\mathrm{blue}}^{\mathrm{b}}$ (km s$^{-1}$) | $z_{\mathrm{blue}}^{\mathrm{c}}$ | $W_{\mathrm{blue}}^{\mathrm{d}}$ (Å) | $\delta W_{\mathrm{blue}}^{\mathrm{e}}$ (Å) | $\Delta v_{\mathrm{red}}^{\mathrm{f}}$ (km s$^{-1}$) | $z_{\mathrm{red}}^{\mathrm{g}}$ | $W_{\mathrm{red}}^{\mathrm{h}}$ (Å) | $\delta W_{\mathrm{red}}^{\mathrm{i}}$ (Å) | Comments |
|---|---|---|---|---|---|---|---|---|---|---|---|
| (1) | (2) | (3) | (4) | (5) | (6) | (7) | (8) | (9) | (10) | (11) | (12) |
| C II | 1334.5323 | 0.1278 | $-600,+600^{\mathrm{j}}$ | $3.0752^{\mathrm{j}}$ | $3.15^{\mathrm{j}}$ | $0.06^{\mathrm{j}}$ | ... | ... | ... | ... | Blended with C II* λ1335.6627 |
| C IV | 1548.204 | 0.1899 | $-400,+100$ | 3.0719 | 0.68 | 0.06 | ... | ... | ... | ... | Blended with stellar C IV λ1549.1 |
| | 1550.781 | 0.09475 | $-400,+100$ | 3.0718 | 0.74 | 0.04 | ... | ... | ... | ... | Blended with stellar C IV λ1549.1 |
| O I | 1302.1685 | 0.04887 | $-500,+75$ | 3.0711 | 1.12 | 0.04 | ... | ... | ... | ... | Redshifted component blended with Si II λ1304.3702 |
| Al II | 1670.7886 | 1.74 | $-400,+150$ | 3.0722 | 1.19 | 0.02 | $+150,+600$ | 3.0777 | 1.40 | 0.02 | |
| Al III | 1854.7184 | 0.559 | $-400,+200$ | 3.0725 | 0.84 | 0.02 | $+200,+450$ | 3.0779 | 0.23 | 0.01 | |
| | 1862.7910 | 0.278 | $-400,+180$ | 3.0722 | 0.68 | 0.02 | ... | ... | ... | ... | |
| Si II | 1260.4221 | 1.18 | $-600,+600^{\mathrm{j}}$ | $3.0740^{\mathrm{j}}$ | $3.20^{\mathrm{j}}$ | $0.05^{\mathrm{j}}$ | ... | ... | ... | ... | Blended with S II λ1259.519 |
| | 1304.3702 | 0.0863 | ... | ... | ... | ... | $+85,+500$ | 3.0772 | 1.20 | 0.03 | Blueshifted component blended with O I λ1302.1685 |
| | 1526.7070 | 0.133 | $-600,+100$ | 3.0716 | 1.22 | 0.03 | $+100,+600$ | 3.0772 | 1.30 | 0.02 | |
| | 1808.0129 | 0.00208 | $-300,+150$ | 3.0723 | 0.48 | 0.03 | $+150,+500$ | 3.0782 | 0.24 | 0.03 | |
| Si IV | 1393.7602 | 0.513 | $-500,+120$ | 3.0711 | 1.83 | 0.03 | ... | ... | ... | ... | |
| | 1402.7729 | 0.254 | $-400,+200$ | 3.0722 | 0.94 | 0.03 | ... | ... | ... | ... | |
| S II | 1250.578 | 0.00543 | $-300,+150$ | 3.0727 | 0.45 | 0.03 | $+150,+500$ | 3.0780 | 0.40 | 0.03 | |
| | 1253.805 | 0.0109 | $-300,+150$ | 3.0726 | 0.69 | 0.03 | $+150,+500$ | 3.0774 | 0.28 | 0.03 | |
| Fe II | 1608.4511 | 0.0577 | $-300,+150$ | 3.0724 | 0.69 | 0.03 | $+150,+500$ | 3.0779 | 1.03 | 0.03 | |
| Ni II | 1709.6042 | 0.0324 | $-300,+150$ | 3.0727 | 0.17 | 0.02 | $+150,+500$ | 3.0775 | 0.15 | 0.02 | |
| | 1741.5531 | 0.0427 | $-300,+150$ | 3.0724 | 0.31 | 0.03 | $+150,+500$ | 3.0777 | 0.18 | 0.02 | |
| | 1751.9157 | 0.0277 | $-300,+150$ | 3.0726 | 0.31 | 0.03 | $+150,+500$ | 3.0769 | 0.12 | 0.02 | |
| Zn II | 2026.137 | 0.501 | $-300,+150$ | 3.0729 | 0.27 | 0.03 | $+150,+500$ | 3.0783 | 0.12 | 0.02 | |

[a] Vacuum wavelength and $f$-values are from Morton (2003) with updates by Jenkins & Tripp (2006).
[b] Velocity range for measurements of blueshifted absorption component.
[c] Redshift of the centroid of blueshifted absorption component.
[d] Rest-frame equivalent width of blueshifted absorption component.
[e] $1\sigma$ random error on the rest-frame equivalent width of blueshifted absorption component.
[f] Velocity range for measurements of redshifted absorption component.
[g] Redshift of the centroid of redshifted absorption component.
[h] Rest-frame equivalent width of redshifted absorption component.
[i] $1\sigma$ random error on the rest-frame equivalent width of redshifted absorption component.
[j] These values refer to the blend of blueshifted and redshifted absorption components.
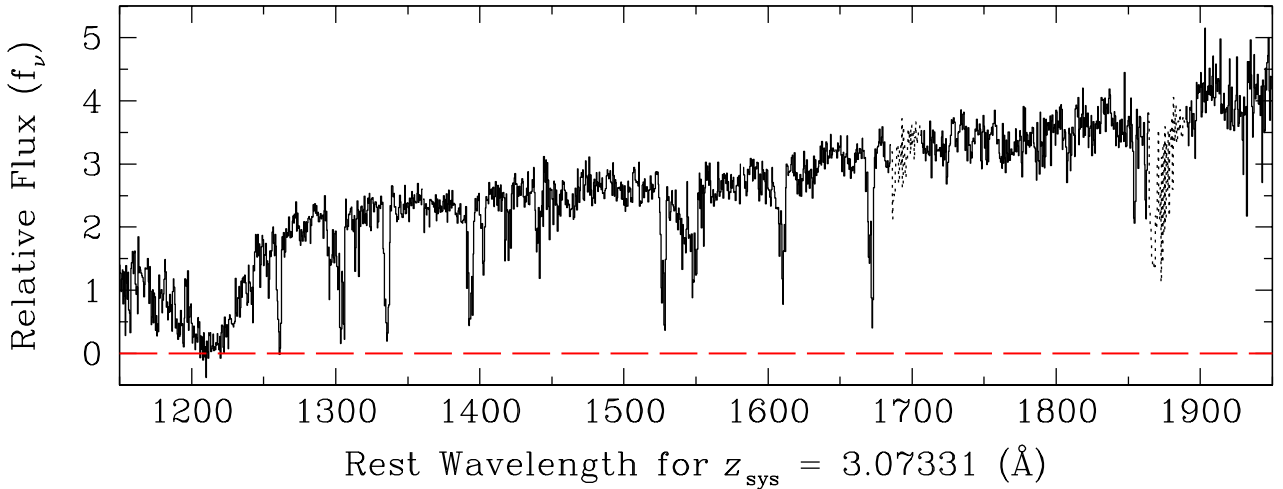
Figure 4.3 The UV spectrum of the Cosmic Eye between rest-frame wavelengths 1150 Å
and 1950 Å. The flux from both northern an southern arcs was summed to produce this
composite, which was rebinned to 2 Å bins (to facilitate reproduction) before reducing
to the rest-frame at $z_{sys} = 3.07331$. Regions of the spectrum affected by atmospheric
absorption are plotted with a dotted line.

$-70\,\mathrm{km\,s^{-1}}$ relative to $z_{sys} = 3.07331$, and a redshifted component centred at $v_{red} \simeq$
$+350\,\mathrm{km\,s^{-1}}$ (these velocities refer to the wavelength bins with the highest apparent
optical depth in the line profiles).

As we shall see below (Section 4.5), the sightline to the Cosmic Eye intersects sev-
eral lower redshift absorbers that produce a multitude of intervening absorption lines
unrelated to the lensed galaxy at $z = 3.07331$. These features do complicate the in-
terpretation of the interstellar absorption due to the Cosmic Eye itself; in Figure 4.4
we have indicated with downward pointing arrows instances where the absorption lines
due to the interstellar medium in the Cosmic Eye are contaminated by intervening ab-
sorbers at lower redshifts. The two-component structure of the interstellar lines in the
Cosmic Eye is most clearly seen in Figure 4.4 in unblended transitions recorded at high
S/N, such as Si II $\lambda1526.7070$ and Al II $\lambda1670.7886$. From these absorption lines it ap-
pears that the blueshifted component extends over a velocity range $\Delta v \sim 700\,\mathrm{km\,s^{-1}}$,
from $\sim -600\,\mathrm{km\,s^{-1}}$ to $\sim +100\,\mathrm{km\,s^{-1}}$ relative to the systemic redshift $z_{sys} = 3.07331$,
while the redshifted component is somewhat narrower with $\Delta v \sim 500\,\mathrm{km\,s^{-1}}$ (from
$\sim +100\,\mathrm{km\,s^{-1}}$ to $\sim +600\,\mathrm{km\,s^{-1}}$ relative to $z_{sys}$). Furthermore, it can be seen from
Figure 4.4 that the redshifted component is absent in the absorption lines of the most
highly ionized gas, C IV and Si IV, and is relatively weak in the intermediate ionization
stage Al III. Whenever possible, we have listed measurements of absorption redshift and
equivalent width separately for the two components in Table 4.2. Note, however, that
the values of equivalent width given in the table may include blends with intervening
absorption features, as explained above; in this respect, the purely random errors quoted
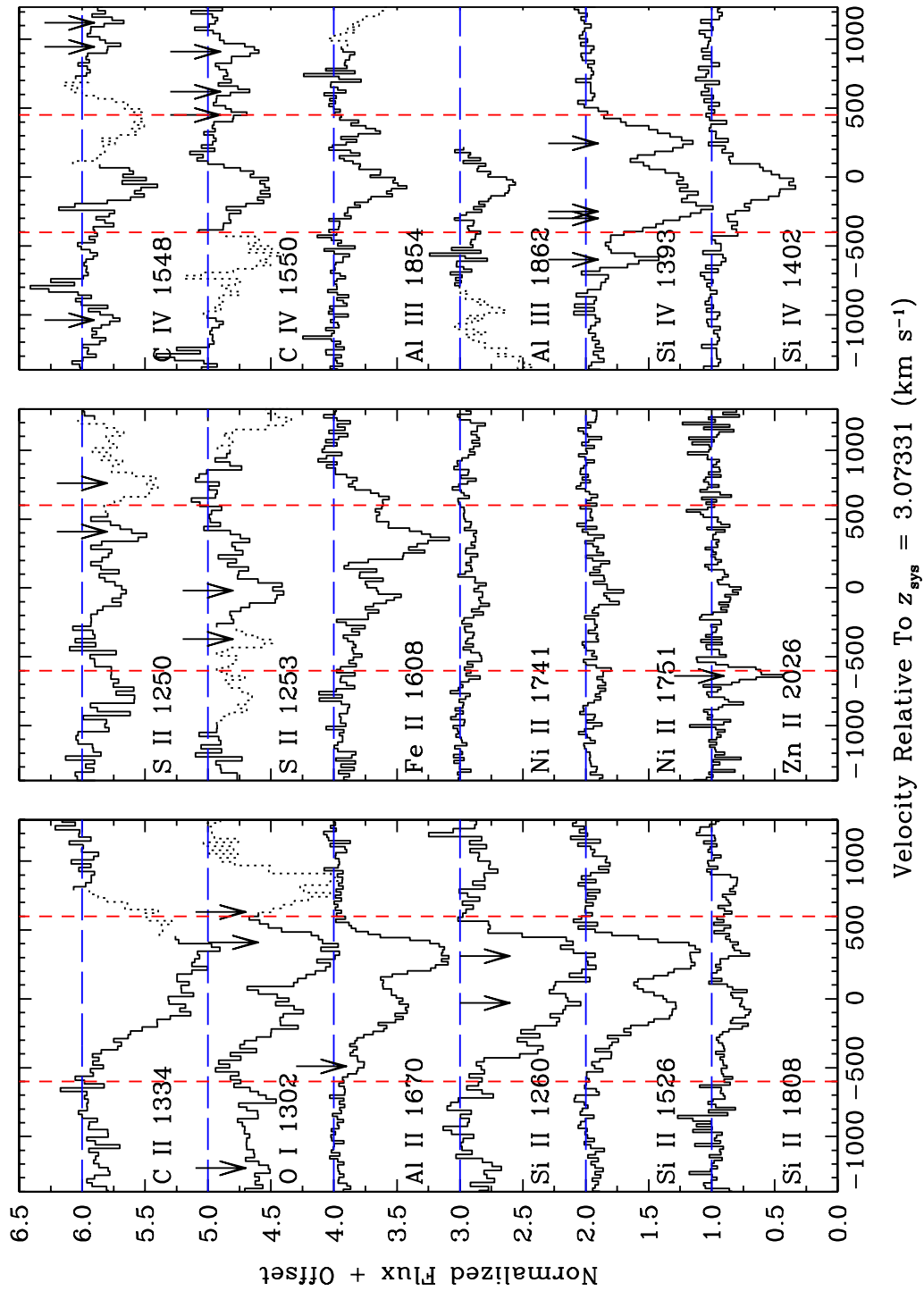
Figure 4.4 Normalized profiles of selected interstellar absorption lines. *Left and middle panels*: Transitions of ions which are dominant in H I regions. *Right panel*: Transitions of ions which are ionized beyond the species dominant in H I regions. The vertical red dash lines indicate the velocity range over which we measured the equivalent widths of the strongest absorption lines (see Table 4.2). Arrows mark the locations of intervening absorption lines unrelated to the Cosmic Eye; these are sometimes resolved as individual features (e.g. see panel for Zn II λ2026), while in other cases they add to absorption from the Cosmic Eye (e.g. see panel for Si II λ1260). Section 4.5 and Table 4.3 give a full account of these intervening absorption systems. Dotted lines have been used to indicate spectral features in the Cosmic Eye other than those to which the label in each plot refers. Thus, for example, C IV λ1550 is shown with a dotted line in the C IV λ1548 plot (top plot in the right-hand panel), and C IV λ1548 is shown with a dotted line in the C IV λ1550 plot (second plot from the top of right-hand panel).

in columns (7) and (11) underestimate the true uncertainties (random and systematic) affecting these measurements.

The kinematic pattern revealed by Figure 4.4 is unexpected for star-forming galaxies at all redshifts, where the interstellar medium seen in absorption against the starburst is primarily moving with *negative* velocities, commonly interpreted as large-scale outflows. For example, in the stack of more than 800 low resolution spectra of galaxies at $z \simeq 3$ constructed by Shapley et al. (2003), the interstellar lines have a net blueshift of $\sim -150 \, \mathrm{km \, s^{-1}}$, and an analogous result is found in stacked spectra of galaxies at $z = 2$ (Law et al. 2007), and $z = 4$, 5 and 6 (Vanzella et al. 2009). Similarly, in her ESI study of the interstellar Na I D lines in 18 local ultraluminous infrared galaxies, Martin (2005) found signatures of outflows in 15 cases and of inflow in only one case. Our earlier high-resolution work on other strongly lensed galaxies at $z = 2 - 3$ (Pettini et al. 2002; Quider et al. 2009) did show a tail of absorption extending to positive velocities, but what we see in the Cosmic Eye is qualitatively different, with the redshifted component being of comparable strength to the blueshifted absorption. When observed at the low resolutions of most spectra of high-$z$ galaxies ($R < 1000$), the stronger interstellar lines in the Cosmic Eye would have a net redshift of $\sim +150 \, \mathrm{km \, s^{-1}}$, which is highly unusual (e.g. Steidel et al. in preparation). We discuss possible interpretations in Section 4.6.2.

### 4.3.3   Partial coverage

The profiles of the interstellar lines in the Cosmic Eye hold clues to the geometry of gas, dust, and stars in this galaxy. An inspection of Figure 4.4 reveals that the cores of the strongest lines which are not contaminated by intervening absorption at lower redshifts (that is, lines not marked by a downward pointing arrow) do not reach zero flux in either of the two kinematic components. We consider the implications of this residual intensity in the line cores for each component in turn.

First we consider the redshifted component. Si II $\lambda$1526, Al II $\lambda$1670 and Fe II $\lambda$1608 all exhibit flat cores at a residual intensity of $I_\lambda/I_0 \simeq 0.15$ (where $I_\lambda$ is the measured intensity in the line at wavelength $\lambda$ and $I_0$ is intensity in the continuum). The most straightforward interpretation is that we are seeing the superposition within the spectrum of saturated absorption lines and escaping continuum photons. Such a scenario would apply if the absorbing material only covers $\sim 85\%$ of the continuum source.

The analysis of the blueshifted component is less clear-cut. It appears to be covering even less of the stellar light than the redshifted component, with the saturated cores of Si II $\lambda$1526 and O I $\lambda$1302 levelling at a residual intensity $I_\lambda/I_0 \simeq 0.3$, corresponding to an apparent optical depth $\tau_\mathrm{a} \sim 1$ [with the usual definition of the optical depth $\tau$ given by $I_\lambda/I_0 = \exp(-\tau)$]. Al II $\lambda$1670 and Fe II $\lambda$1608 may not be fully saturated in this component, since their minimum residual intensities (in the blue component) are higher: $I_\lambda/I_0 \simeq 0.45$, and $\simeq 0.55$ respectively. On the other hand, we do not have a satisfactory explanation for the higher apparent optical depth of C II $\lambda$1334, unless this transition is blended with other unrecognized absorption (in addition to the fine structure line C II* $\lambda$1335 which would fall $\sim 250 \, \mathrm{km \, s^{-1}}$ to the red in the top left-hand panel of Figure 4.4).

In any case, a lower covering factor of the blueshifted gas compared to the redshifted absorption is required in order to make sense of the apparent contradiction between
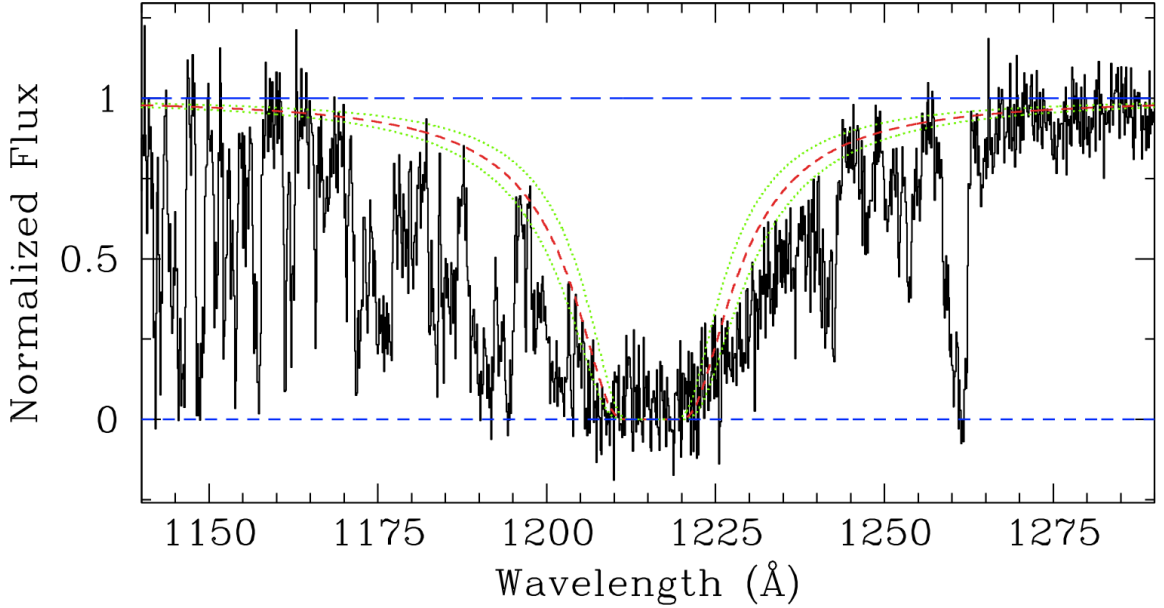
Figure 4.5 Portion of the ESI spectrum of the lensed galaxy in the Cosmic Eye encompassing the region of the Lyα line. Overlaid on the spectrum are three theoretical damped profiles, centred at $z_{\mathrm{sys}} = 3.07331$, produced by column densities of neutral hydrogen $N(\mathrm{H\,I}) = (3.0 \pm 0.8) \times 10^{21}\,\mathrm{cm}^{-2}$.

the relative strengths of the red and blue components in absorption lines of differing $f$-values. For example, the two components are observed to have comparable values of $\tau_{\mathrm{a}}$ in Si II λ1808 but different values in Si II λ1526, with the blue component being weaker than the red one (see lower two panels in the left-hand column of Figure 4.4). Such an arrangement would at first sight appear to be unphysical. These two Si II transitions have widely different $f$-values (see Table 4.2); since they both arise from the same ground state of $\mathrm{Si}^{+}$, their *intrinsic* optical depths must be in the same ratio as their $\lambda \times f$ products, or $\tau(1526)/\tau(1808) = 54$. This expectation can only be reconciled with the measured values of *apparent* optical depth, $\tau_{\mathrm{a}}$, if we assume that the covering factor of the blue component is lower than that of the red one, and that both components are in fact saturated in Si II λ1526. Once that is taken into account, and the zero level adjusted accordingly, the intrinsic (rather than apparent) optical depth is actually higher in the blue component than in the red one.

The combination of: (a) partial coverage by differing factors for the blue and red components, and possibly even varying as a function of velocity within each component (see Martin & Bouché 2009); (b) contamination by unrelated absorption features due to lower redshift systems; and (c) limited S/N ratio, makes it very difficult in our view to deduce reliable ion column densities from the analysis of the line profiles. Accordingly, we have refrained from attempting to do so.

## 4.3.4 The Lyα line

The Lyα line in the Cosmic Eye shows a strong damped absorption profile, from which we deduce a neutral hydrogen column density $N(\mathrm{H\,I}) = (3.0 \pm 0.8) \times 10^{21}\,\mathrm{cm}^{-2}$ (see

Figure 4.5). This is a high value of $N(\mathrm{H\,I})$, near the upper end of the column density distribution of QSO-DLAs (Noterdaeme et al. 2009) and more typical of the DLAs seen in the spectra of the afterglows of high redshift gamma-ray bursts (Pontzen et al. 2010). The corresponding line width is FWHM $= 27.4\,\text{Å}$ or $\sim 6750\,\mathrm{km\,s^{-1}}$ (Jenkins 1971). On kinematic grounds it is therefore impossible, with the S/N ratio of the present data, to assign the DLA absorption to one or other of the two main components visible in the metal absorption lines, which are separated by only $\approx 400\,\mathrm{km\,s^{-1}}$ (Section 4.3.2).

Nevertheless, we suspect that most of the DLA absorption may be due to the red-shifted component, which has the larger covering fraction of the two and consists primarily of neutral gas. The $\sim 70\%$ covering factor we surmised for the outflowing, blueshifted, component may lead to the escape of a substantial fraction of the Ly$\alpha$ photons produced by the H II regions surrounding the OB stars, as found by Quider et al. (2009) in the case of the Cosmic Horseshoe. And yet no Ly$\alpha$ emission line is seen here, not even as residual emission when the damped profile is divided out, as is the case in cB58 (Pettini et al. 2000, 2002) and in the lensed $z = 3.77$ LBG FORJ0332$-$3557 observed by Cabanac et al. (2008). It is possible that any Ly$\alpha$ photons that escape from the star-forming regions in the Cosmic Eye are absorbed by the foreground neutral gas giving rise to the redshifted component of the metal absorption lines.

It is interesting that the damped Ly$\alpha$ line has a larger covering factor than any other absorption feature in the spectrum. Recall that at the outset we subtracted off 5% of the continuum flux from the entire spectrum (Section 4.2), in order to bring the core of the damped Ly$\alpha$ line to zero. At this small level, we cannot be sure whether this residual flux in the core of the line is due to inaccurate background estimation, or is the true level of unobscured continuum flux. In any case, the correction we have applied to our data translates to a lower limit of 95% to the covering factor of the OB star continuum by foreground H I gas. The fact that this is larger than the values we deduced in Section 4.3.3 for the metal lines is not surprising, given that for solar abundances the optical depth in the Ly$\alpha$ line will exceed that of even the strongest metal lines from H I regions by factors of $> 10^4$. In other words, low column densities of gas, undetectable even in the strongest metal absorption lines, could be adding to the apparent optical depth in Ly$\alpha$ to give a higher overall covering fraction.

Bringing together the points discussed in this Section, our high resolution ESI observations have revealed that the interstellar spectrum of the Cosmic Eye is unusual in showing two absorption components, of approximately equal strengths, one blueshifted by $-70\,\mathrm{km\,s^{-1}}$ and the other redshifted by $+350\,\mathrm{km\,s^{-1}}$ relative to the systemic redshift $z_{\mathrm{sys}} = 3.07331$ defined by the OB stars and their H II regions. The redshifted component is mostly of low ionization. The interpretation of the interstellar spectrum is complicated by the fact that the metal lines appear to only partially cover the starburst, with differing covering factors for blueshifted and redshifted absorption. There is a very large column of foreground neutral gas, $N(\mathrm{H\,I}) = 3 \times 10^{21}\,\mathrm{cm^{-2}}$, giving rise to a strong damped Ly$\alpha$ line which covers at least 95% of the stellar continuum.
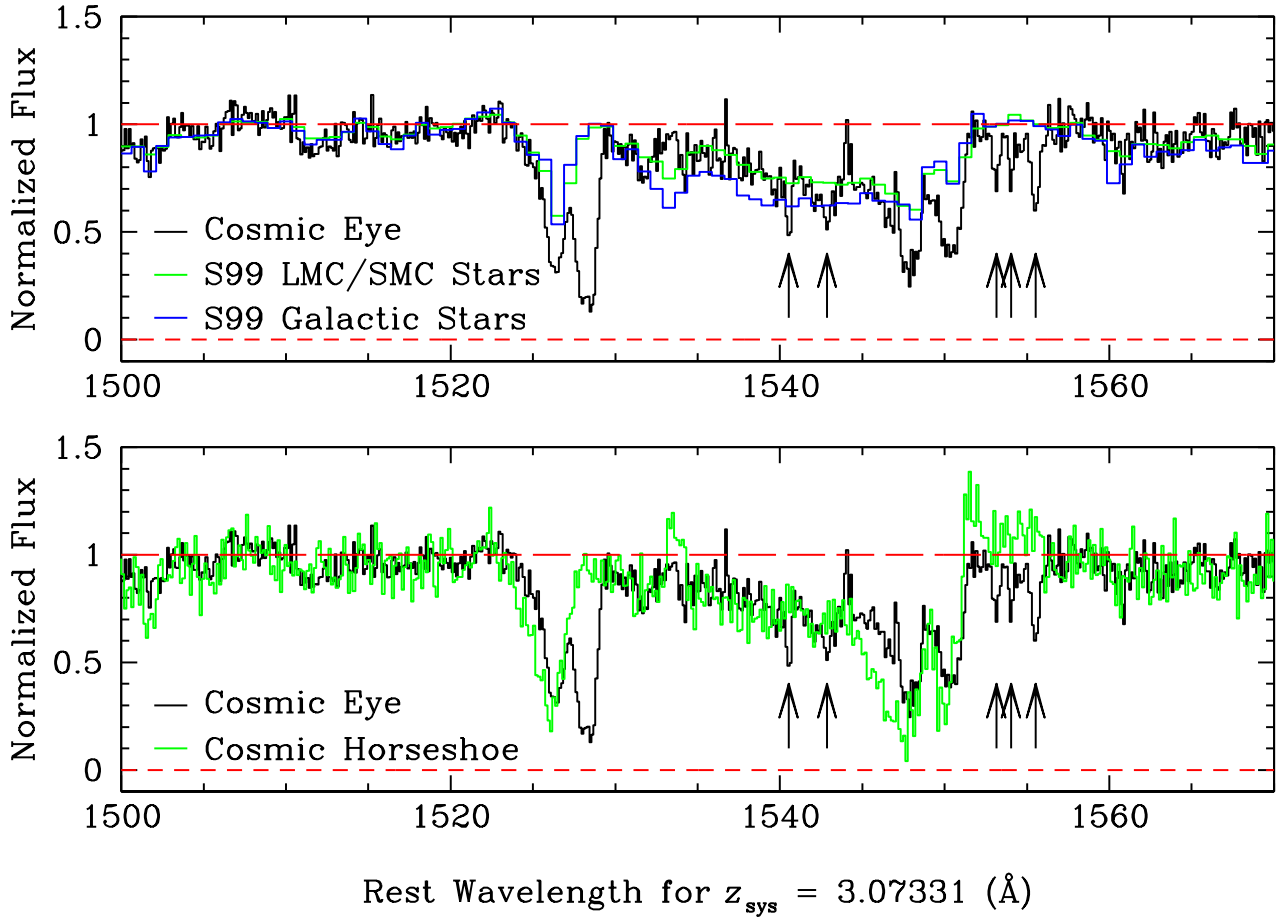
Figure 4.6 *Upper panel:* Comparison between the ESI spectrum of the Cosmic Eye in the region encompassing the C IV line and two model spectra computed with *Starburst99* and empirical libraries of, respectively, Magellanic Clouds and Galactic stars, as indicated. The model spectra were generated assuming a 100 Myr old continuous star formation episode with a Salpeter IMF with an upper mass limit $M_{up} = 100 M_\odot$. *Lower panel:* The stellar spectra of the Cosmic Eye and of the Cosmic Horseshoe are remarkably similar in the wavelength region shown. The ESI spectrum of the Cosmic Horseshoe is reproduced from Quider et al. (2009), and has been reduced to its rest wavelengths at $z_{stars} = 2.38115$. Upward pointing arrows indicate the positions of narrow, intervening absorption lines unrelated to the Cosmic Eye itself (see Section 4.5): a possible C IV doublet and three closely spaced Al II $\lambda 1670$ lines.

## 4.4 The Stellar Spectrum

The stars which provide the rest-frame UV continuum light in a high redshift galaxy leave their imprint on the galaxy's spectrum. The stellar wind features are a clear signature from the most massive O stars which have the strongest stellar winds (Kudritzki & Puls 2000). Rix et al. (2004) have shown that the P Cygni profile of the stellar wind features is sensitive to the metallicity of the stars, as well as to the slope and upper mass cut-off of the IMF. While stellar and interstellar features are usually blended at the low resolution of typical high redshift galaxy spectra (Crowther et al. 2006), the high resolution of our spectrum allows us to easily separate them and focus on the stellar component.

We used model spectra computed with the spectral synthesis code *Starburst99* to exploit the metallicity and IMF sensitivities of the P Cygni profiles evident in the spectrum of the Cosmic Eye. The two model spectra considered here were generated using libraries of empirical UV spectra from stars either within the Galaxy ($Z \sim 1.0\,Z_\odot$), or within the Large and Small Magellanic Clouds ($Z \sim 0.4\,Z_\odot$; Leitherer et al. 1999, 2001). Both models are for 100 Myr old continuous star formation with a Salpeter IMF with upper mass limit $M_{\rm up} = 100 M_\odot$, which are reasonable parameters for the current star formation episode (Coppin et al. 2007; Pettini et al. 2000; Quider et al. 2009).

The strongest stellar wind feature present in the Cosmic Eye is the C IV $\lambda\lambda 1548, 1550$ P Cygni profile shown in Figure 4.6. Also plotted in the top panel are the two *Starburst99* model spectra for comparison. Clearly there is a good agreement between the models and the data. The main deviations from the models are due to *interstellar* Si II $\lambda 1526$ and C IV $\lambda\lambda 1548, 1550$ (see Section 4.3), which are evident in the blue absorption trough, and narrower intervening Al II $\lambda 1670$ and C IV $\lambda\lambda 1548, 1550$ absorption (see Section 4.5) which can be seen in the P Cygni emission and absorption respectively (the intervening absorptions are highlighted with upward pointing arrows in Figure 4.6). Of the two model spectra shown, the one computed with libraries of Magellanic Cloud stars is the better match, while Milky Way metallicities overpredict the strength of the absorption. This conclusion is also consistent with the P Cygni profile of N V $\lambda\lambda 1238, 1242$, although the analysis of the latter is complicated by blending with the red wing of the damped Ly$\alpha$ line and some intervening absorption. Thus, we infer that $Z_{\rm O\,stars} \approx 0.4\,Z_\odot$. We also investigated the effects on the emergent P Cygni profile of varying the slope and upper mass cut-off of the IMF. As found in previous studies, (e.g. Pettini et al. 2000), there are no indications of a departure from the 'standard' Salpeter IMF for stars with masses $M > 5 M_\odot$.

The lower panel of Figure 4.6 compares the P Cygni region of the Cosmic Eye with that of the Cosmic Horseshoe, also recorded with ESI (reproduced from Quider et al. 2009). The P Cygni profiles of these two galaxies are very similar, and both are similar to that seen in cB58 (see Quider et al. 2009 for comparison of this spectral region in the Cosmic Horseshoe and cB58). The most striking difference between the Cosmic Horseshoe and the Cosmic Eye is in their interstellar absorption profiles: the Horseshoe's interstellar absorption extends to higher outflow velocities, while in the Cosmic Eye there is strong absorption at positive velocities in Si II $\lambda 1526$ (and other ions dominant in neutral gas), as discussed above (Section 4.3.2). The emission component of the C IV P Cygni profile, which can be clearly seen in the Cosmic Horseshoe and cB58, seems to be absent from the Cosmic Eye. Smail et al. (2007) interpreted this as evidence that the massive stellar

population of the galaxy is deficient in O-type stars; with our higher spectral resolution we can now see that the lack of emission is partly due to the presence of foreground absorption by an intervening triplet of Al II $\lambda1670$ lines at $z_{abs} = 2.7865, 2.7891, 2.7925$ (see Table 4.3). Finally, nebular Si II $\lambda1533.4312$ emission, which is evident in the Horseshoe and cB58, is weak in the Cosmic Eye.

Several blends of stellar photospheric absorption lines in the integrated spectra of star-forming galaxies have been shown to be sensitive to the metallicity of early-type stars (Leitherer et al. 2001; Rix et al. 2004). Two of these regions are a blend of Si III $\lambda1417$, C III $\lambda1427$, and Fe V $\lambda1430$ absorption lines spanning the wavelength interval 1415–1435 Å (the "1425" index of Rix et al. 2004), and a blend of several Fe III absorption lines from B stars between 1935 and 2020 Å (the "1978" index). The 1425 index has been shown to yield an estimate of the stellar metallicity which is consistent with other metallicity measures for the same galaxies (Rix et al. 2004; Halliday et al. 2008; Quider et al. 2009), but these same studies are divided on the effectiveness of the 1978 index.

In the case of the Cosmic Eye, we cannot use the 1425 index because it is heavily contaminated by intervening absorption lines at lower redshifts (Section 4.5). While these features are significantly narrower than the broad blend of stellar absorption, they nevertheless compromise the placement of the continuum in this region of the spectrum, rendering the measurement of the 1425 index too uncertain to be useful. The 1978 index region appears to be 'clean', but we found it to be a generally poor match to the model spectra by Rix et al. (2004), in particular being stronger than any of the metallicities considered by those authors between 1985 and 2015 Å. Quider et al. (2009) also found the 1978 index to be problematic for the Cosmic Horseshoe (although in that case the index failed between 1960 and 1980 Å), so we reiterate their cautionary note that the 1978 index needs to be tested on more galaxies to establish its usefulness as an abundance indicator.

To sum up this section, from a consideration of the C IV stellar wind profile, the population of early-type stars in the lensed galaxy of the Cosmic Eye was found to be very similar to those of the Cosmic Horseshoe and cB58. In all three cases, *Starburst99* models with metallicity $Z \simeq 0.4\, Z_\odot$, continuous star formation, and Salpeter IMF in the mass range $100 M_\odot \geq M \geq 5 M_\odot$ provide satisfactory fits to the UV spectra. The 1978 index is not well-matched by the spectrum of the Cosmic Eye at any of the model metallicities, indicating that further testing of this index is necessary before it can be reliably used as a metallicity measure.

## 4.5 Intervening Absorption Systems

Possibly because of its high redshift, and the high resolution and S/N ratio of our data, the spectrum of the Cosmic Eye shows numerous narrow absorption lines at redshifts $z < z_{sys}$ due to intervening absorbers along the line of sight. Limiting ourselves to the wavelength interval longwards of the Ly$\alpha$ line (so as to avoid the Ly$\alpha$ forest), we identified 41 such absorption lines associated with seven definite and one possible systems at redshifts from $z_{abs} = 2.4563$ to $z_{abs} = 3.0528$. Every system has a C IV $\lambda\lambda1548, 1550$ doublet associated with it and six systems have additional low or high ionization species present. Table 4.3 lists the identified intervening absorption lines with their redshifts and observed equivalent widths.

Table 4.3 Intervening Absorption Line Systems

| $\lambda_{obs}$ (Å) | Identification | $z_{abs}$ | $W_{obs}$ (Å) | Comments |
|---|---|---|---|---|
| | | | | System 1: $z_{abs} = 2.4563$ |
| 5277.15 | Si II 1526.7070 | 2.4567 | 1.31 | Blended with Si IV 1393.7602 in System 4 and stellar absorption features |
| 5351.27 | C IV 1548.204 | 2.4564 | 1.80 | |
| 5360.11 | C IV 1550.781 | 2.4564 | 1.26 | Blended with N III 1317 in Cosmic Eye |
| 5559.42 | Fe II 1608.4511 | 2.4563 | 0.44 | |
| 5774.69 | Al II 1670.7886 | 2.4563 | 1.88 | |
| 6409.68 | Al III 1854.7184 | 2.4563 | 0.69 | |
| 6438.52 | Al III 1862.7910 | 2.4559 | 0.48 | |
| 8102.21 | Fe II 2344.2139 | 2.4564 | 0.85 | |
| 8235.86 | Fe II 2382.7652 | 2.4564 | 1.37 | |
| | | | | System 2: $z_{abs} = 2.6597$ |
| 5100.64 | Si IV 1393.7602 | 2.6596 | 1.08 | |
| ... | Si IV 1402.7729 | ... | ... | Blended with Si II 1260 in Cosmic Eye |
| 5665.89 | C IV 1548.204 | 2.6597 | 1.07 | |
| ... | C IV 1550.781 | ... | ... | Blended with Si IV 1393 in Cosmic Eye and C IV 1548 in System 3 |
| | | | | System 3: $z_{abs} = 2.6639$ |
| 5106.67 | Si IV 1393.7602 | 2.6640 | 2.61 | Blended with S II 1253 in Cosmic Eye |
| ... | Si IV 1402.7729 | ... | ... | Blended with Si II 1260 in Cosmic Eye |
| 5672.94 | C IV 1548.204 | 2.6642 | 5.42 | Blended with Si IV 1393 in Cosmic Eye |
| 5682.19 | C IV 1550.781 | 2.6641 | 3.64 | Blended with Si IV 1393 in Cosmic Eye and C IV 1550 in System 2 |
| 6794.61 | Al II 1854.7184 | 2.6634 | 1.06 | Blended with Al II 1670 in Cosmic Eye |
| | | | | System 4: $z_{abs} = 2.7865$ |
| 5053.73 | C II 1334.5323 | 2.7869 | 0.67 | |
| 5277.15 | Si IV 1393.7602 | 2.7864 | 1.31 | Blended with Si II 1526 in System 1 and stellar absorption features |
| ... | Si IV 1402.7729 | ... | ... | Blended with O I 1302 in Cosmic Eye |
| 5780.88 | Si II 1526.7070 | 2.7865 | 0.69 | |
| 5862.35 | C IV 1548.204 | 2.7865 | 1.93 | |
| 5871.72 | C IV 1550.781 | 2.7863 | 2.12 | Blended with C IV 1548 in System 6 |
| 6090.54 | Fe II 1608.4511 | 2.7866 | 0.78 | |
| 6326.42 | Al II 1670.7886 | 2.7865 | 0.57 | Blended with C IV P Cygni emission in Cosmic Eye |
| 7023.16 | Al III 1854.7184 | 2.7866 | 0.60 | |
| 7053.51 | Al III 1862.7910 | 2.7865 | 0.34 | |

| $\lambda_{\mathrm{obs}}$ (Å) | Identification | $z_{\mathrm{abs}}$ | $W_{\mathrm{obs}}$ (Å) | Comments |
|---|---|---|---|---|
| | | | System 5: $z_{\mathrm{abs}} = 2.7891$ | |
| 5057: | C II 1334.5323 | 2.79: | . . . | Blended |
| 5281.97 | Si IV 1393.7602 | 2.7896 | 0.61 | Blended with stellar absorption features |
| . . . | Si IV 1402.7729 | . . . | . . . | Blended with Si II 1304 in Cosmic Eye |
| 5784.63 | Si II 1526.7070 | 2.7890 | 0.83 | |
| 5866.87 | C IV 1548.204 | 2.7895 | 1.45 | |
| 5876.32 | C IV 1550.781 | 2.7893 | 1.00 | |
| 6330.05 | Al II 1670.7886 | 2.7887 | 0.41 | Blended with C IV P Cygni emission in Cosmic Eye |
| 7026.91 | Al III 1854.7184 | 2.7887 | 0.24 | |
| 7058.23 | Al III 1862.7910 | 2.7891 | 0.30 | |
| | | | System 6: $z_{\mathrm{abs}} = 2.7925$ | |
| 5061.13 | C II 1334.5323 | 2.7924 | 1.91 | |
| 5789.76 | Si II 1526.7070 | 2.7923 | 0.84 | |
| 5871.72 | C IV 1548.204 | 2.7926 | 2.12 | Blended with C IV 1550 in System 4 |
| 5881.45 | C IV 1550.781 | 2.7926 | 0.86 | |
| 6336.16 | Al II 1670.7886 | 2.7923 | 1.06 | Blended with C IV P Cygni emission in Cosmic Eye |
| | | | System 7: $z_{\mathrm{abs}} = 2.8106$ | |
| 5899.50 | C IV 1548.204 | 2.8105 | 1.49 | |
| 5909.52 | C IV 1550.781 | 2.8107 | 1.25 | |
| | | | (Possible) System 8: $z_{\mathrm{abs}} = 3.0528$ | |
| 6275.06 | C IV 1548.204 | 3.0531 | 0.60 | Blended with C IV P Cygni absorption in Cosmic Eye |
| 6284.55 | C IV 1550.781 | 3.0525 | 0.58 | Blended with C IV P Cygni absorption in Cosmic Eye |

Although for clarity we have labelled each resolved set of absorption lines as an 'absorption system', some of the absorbers are separated by redshift differences which correspond to relative velocities of only a few hundred km s$^{-1}$. If, for ease of comparison with earlier absorption line statistics from lower resolution work, we group together into one 'absorption system' lines which fall within a velocity interval $\Delta v = 1000$ km s$^{-1}$, we have four such (definite) systems within a redshift interval $\Delta z = 0.81$ between $z_{\mathrm{abs}} = 2.25$ and $z_{\mathrm{abs}} = 3.06$, considering that we could have detected C IV doublets between $\lambda_{\mathrm{obs}} = 5030$ Å and $\lambda_{\mathrm{obs}} = 6293$ Å (approximately the redshifted wavelengths of Ly$\alpha$ and C IV in the Cosmic Eye). All four systems thus defined have $W_0(1548) \geq 0.40$ Å, where $W_0(1548)$ is the rest-frame equivalent width of the stronger member of the C IV doublet. Thus, in the Cosmic Eye the number of such systems per unit redshift is $N(z) = 4/0.81 \simeq 5$, or $\sim 5$ times higher than the mean $\langle N(z) \rangle \simeq 1$ for absorbers of this strength and in the same redshift interval in QSO spectra (Steidel 1990). It is hard to conclude, without a more detailed analysis which is beyond the scope of this paper, whether this is just a statistical fluctuation, or whether the excess number of strong C IV absorbers in front of the Cosmic Eye is at least partly due to the extension of the image on the plane of the sky (two arcs, each $\sim 3''$ long).

As can be seen in Figure 4.4, the intervening absorption lines are scattered throughout the spectrum of the Cosmic Eye, inconveniently falling within several features of interest. Column (5) of Table 4.3 details the blending of the intervening absorbers with interstellar lines in the Cosmic Eye as well as each other. There is no doubt that the presence of so many intervening absorption lines complicates the interpretation of the Cosmic Eye spectrum. This is a clear case where a high resolution spectrum reveals a more complex situation than was inferred from lower resolution observations. Thus, the Cosmic Eye serves as a cautionary tale for the interpretation of high redshift galaxy spectra which, without the boost provided by gravitational lensing, generally can only be recorded at low resolution with available instrumentation.

We also searched for Mg II $\lambda\lambda 2796, 2803$ absorption near $z = 0.73$, the redshift of the lensing galaxy of the Cosmic Eye and of at least two other galaxies in the field (Smail et al. 2007). However, these lines would fall in the Ly$\alpha$ forest and, if present, are difficult to disentangle from the intergalactic medium absorption at the S/N ratio of our data.

## 4.6 Discussion

One of the advantages offered by strongly lensed LBGs is that they can be observed in numerous wavebands allowing us to put together a more extensive picture of their properties than is normally possible in the absence of lensing. In this respect, the Cosmic Eye is among the better studied galaxies at $z = 3$ (see Section 4.1); in this section we discuss our findings from the analysis of its rest-frame UV spectrum in the light of previous work carried out at other wavelengths.

### 4.6.1 Geometry and reddening

When Siana et al. (2009) compared the far-infrared (at wavelengths $\lambda = 40$–$120\,\mu$m, $L_{\mathrm{FIR}}$) and UV (1600 Å, $L_{1600}$) luminosities of the Cosmic Eye, they found the ratio $L_{\mathrm{FIR}}/L_{1600}$

to be $\sim 8$ times lower than the value predicted with the relationship by Meurer, Heckman, & Calzetti (1999), which relates $L_{\mathrm{FIR}}/L_{1600}$ to the slope $\beta$ of the UV stellar continuum in local starburst galaxies (assumed to be a power law of the form $F_\lambda \propto \lambda^\beta$). In general, lower values of this luminosity ratio correspond to smaller values of $\beta$. This relationship between luminosity ratio and spectral slope is referred to as the Meurer et al. (1999) relation. An analogous discrepancy, albeit by a smaller factor, was found by Siana et al. (2008) for MS 1512-cB58. These two studies attributed such departures to a steeper extinction curve for the dust in the Cosmic Eye and cB58 than that applicable to dust in local starbursts (Calzetti et al. 2000): a faster rise in the extinction $A_\lambda$ with decreasing $\lambda$ would have the net effect of increasing $\beta$ (i.e. making the UV spectral slope redder) for a lower overall degree of dust extinction, as measured by the $L_{\mathrm{FIR}}/L_{1600}$ ratio. Siana et al. (2009) showed that a UV extinction curve similar to those measured in the Large and Small Magellanic Clouds could account for the observed values of $L_{\mathrm{FIR}}/L_{1600}$ and $\beta$ in the Cosmic Eye and cB58.

The difference between the Calzetti and LMC/SMC extinction curves is thought to be one of geometry, depending on whether the bulk of the dust is mixed with, or lies in front of, the OB stars whose light is being attenuated. The implication that in cB58 and the Cosmic Eye most of the dust may be located in a 'foreground screen' is consistent with the finding that in both cases the UV spectra of the galaxies exhibit a damped Ly$\alpha$ line with near 100% covering factor (Pettini et al. 2002 for cB58, and Section 4.3.4 of the present paper for the Cosmic Eye). The ubiquitous presence of galaxy-scale outflows in star-forming galaxies at $z = 2 - 3$ may lead to a geometrical configuration of dust and stars more analogous to that described by the LMC/SMC curves in many LBGs, as considered by Pettini et al. (1998a). Another factor may be age: in their recent study, Reddy et al. (2010) find that it is the galaxies that are younger than $\sim 100\,\mathrm{Myr}$ that exhibit a tendency to lie below the Meurer et al. (1999) relation (which, as defined above, relates $L_{\mathrm{FIR}}/L_{1600}$ to the slope $\beta$ of the UV stellar continuum in local starburst galaxies; see Figure 5 of Siana et al. 2009).

Looking ahead, with a larger sample of high resolution spectra of strongly lensed LBGs it may be possible to disentangle the effects of geometry and age on the emergent UV flux of star-forming galaxies. An immediately obvious test is to measure the $L_{\mathrm{FIR}}/L_{1600}$ ratio in LBGs where the Ly$\alpha$ line is predominantly in emission, such as the Cosmic Horseshoe where our earlier work also showed that the insterstellar medium only covers $\sim 60\%$ of the UV stellar continuum (Quider et al. 2009). In the physical picture put forward by Shapley et al. (2003) and more recently Kornei et al. (2009), the three parameters (age, Ly$\alpha$ luminosity, and covering factor) are related, in that galaxies with strong Ly$\alpha$ emission represent a later evolutionary stage, in which supernova-induced outflows have reduced the dust covering fraction.

## 4.6.2 Kinematics

The interstellar absorption lines provide information on the kinematics of the interstellar gas along our line of sight to the OB stars of the Cosmic Eye. This only allows us to make a one dimensional assessment of the gas motions in the galaxy, given that the UV light is dominated by a single source with a half-light radius of $\sim 1\,\mathrm{kpc}$ in the lensing model of Dye et al. (2007—see Section 4.1). However, using laser-guided adaptive optics, Stark

et al. (2008) were able to probe the two-dimensional distribution of velocities of nebular emission lines ([O III] and H$\beta$) across the face of the galaxy on unprecedented small scales of $\sim 100\,$pc. They found a regular pattern (see Figure 2 of Stark et al. 2008) from which they constructed a rotation curve extending to $\pm 2\,$kpc from the dynamical centre with an amplitude of $v_{\rm rot} \sin i = 55 \pm 7\,{\rm km\ s}^{-1}$, where $i$ is the inclination angle. Superposed on this regular pattern are chaotic motions with a dispersion $\sigma_0 = 54 \pm 4\,{\rm km\ s}^{-1}$. Such a low ratio of ordered to random motions, $v_{\rm rot}/\sigma_0 \sim 1$, is commonly found in star-forming galaxies at $z = 2$–3 (e.g. Law et al. 2009; Förster Schreiber et al. 2009).[4]

To these kinematic data we now add measurements of outflowing gas seen in absorption. As discussed in Section 4.3.2, the blueshifted component of the absorption lines has maximum apparent optical depth at a velocity $v_{\rm blue} \simeq -70\,{\rm km\ s}^{-1}$, relative to $z_{\rm sys} = 3.07331$, and extends out to $v_{\rm blue}^{\rm max} \simeq -500\,{\rm km\ s}^{-1}$ (see Figure 4.4). In their recent analysis of outflows in low redshift starburst galaxies, Martin & Bouché (2009) associate the velocity of maximum apparent optical depth with the speed of a shell of swept-up, interstellar gas at the time of blowout from the disk of the galaxy, at a few pressure scale heights. In their picture, gas at higher negative velocities is located further away from the disk (and is therefore accelerating), and exhibits lower apparent optical depths as a result of geometrical dilution. If this scenario also applies to the Cosmic Eye, we would conclude that rotation, velocity dispersion, and outflow speed of swept-up interstellar matter at blowout are all of comparable magnitude. However, it is still far from clear how all these motions fit into one coherent picture.

It is interesting that the outflow speeds in the Cosmic Eye are lower than the values measured in most other LBGs. The value $v_{\rm blue} \simeq -70\,{\rm km\ s}^{-1}$ is only about half the mean blueshift of the strongest interstellar lines in the composite spectrum of 811 LBGs constructed by Shapley et al. (2003), and lower than $v_{\rm blue} \simeq -150\,{\rm km\ s}^{-1}$ and $v_{\rm blue} \simeq -255\,{\rm km\ s}^{-1}$ measured in the Cosmic Horseshoe (Quider et al. 2009) and MS 1512-cB58 (Pettini et al. 2002) respectively. The maximum blueshift at which absorption is detected, $v_{\rm blue}^{\rm max} \simeq -500\,{\rm km\ s}^{-1}$ is also lower than $v_{\rm blue}^{\rm max} \simeq -750\,{\rm km\ s}^{-1}$ in both the Horseshoe and cB58. However, this limit may simply be an observational one, determined by the decrease in covering factor with distance from the central starburst, and there may be gas at higher negative velocities which is too diluted to produce detectable absorption (Martin & Bouché 2009). While there are indications at both low ($z \sim 0$, Martin 2005; Rupke et al. 2005) and intermediate ($z \simeq 1.4$, Weiner et al. 2009) redshifts that 'superwind' speeds scale with galactic mass and star formation rate, there is sufficient scatter in these relations to accommodate the differences we have uncovered between the three strongly lensed high-$z$ galaxies, even though they are thought to have comparable masses and star formation rates.

Finally we note that, alongside rotation, random motions, and outflows, our UV spectrum has shown the presence of high column density, neutral gas apparently moving *towards* the OB stars in the Cosmic Eye, further complicating the kinematic picture of this galaxy. With the available data, we cannot arrive at definite conclusions concerning the nature and location of this gas. One possibility is that it may be a chance superposition of another galaxy (or damped Ly$\alpha$ system) along the line of sight. Alternatively, it may be dynamically related to the Cosmic Eye. For example, it may be gas ejected from the

---

[4]These estimates refers to the inner regions ($\sim 2\,$kpc) of the galaxy; larger motions may well be found if one were able to probe baryons over the full virial radius of the galaxy.

galaxy by a previous episode of star formation and now falling back onto it, or we may be viewing a merger along a favourable sightline, although in both cases the $350\,\mathrm{km\,s^{-1}}$ velocity offset from $z_\mathrm{sys}$ seems very high, given that the Cosmic Eye does not appear to be a very massive galaxy [e.g. $M_\mathrm{stars+gas} \leq 1 \times 10^{10} M_\odot$ (Coppin et al 2007), and $v_\mathrm{rot}\sin i = 55\,\mathrm{km\,s^{-1}}$ (Stark et al. 2008)]. The lensing model of Dye et al. (2007) does include a second, separate clump of UV light in the source plane, which could indicate a merger, or a foreground galaxy. However, Coppin et al. (2007) reported a redshift $z_\mathrm{CO} = 3.0740 \pm 0.0002$ for the CO emission which they found to be peaked at the position of this second source; the small velocity difference $\Delta v = 50 \pm 20\,\mathrm{km\,s^{-1}}$ from the systemic redshft $z_\mathrm{sys} = 3.07331 \pm 0.00024$ (Section 4.3.1) makes it unlikely that the absorbing gas we have found with $v_\mathrm{red} \simeq +350\,\mathrm{km\,s^{-1}}$ is associated with the CO emitting clump.

Additional kinematic data on strongly lensed galaxies spanning a range of physical properties are clearly needed in order to explore how outflows (and in some cases presumably inflows) tie into the other motions within a galaxy, as well as the galaxy's intrinsic characteristics.

### 4.6.3 Metallicity and stellar populations

The C IV P Cygni profile encodes information about the metallicity of the O stars, as well as the relative numbers of massive stars in the Cosmic Eye. Here we consider each in turn.

Up to now, the degree of metal enrichment attained by high redshift star-forming galaxies has been determined primarily from the analysis of the most prominent nebular lines emitted from their H II regions (e.g. Pettini et al. 2001; Shapley et al. 2004; Erb et al. 2006a; Maiolino et al. 2008). Strongly lensed galaxies give us the opportunity to conduct a complementary metallicity measurement based on UV spectral features due to massive stars. Young stars and H II regions are expected to have intrinsically the same chemical composition, since the former have only recently formed out of the gas which they ionize into the latter; thus a comparison between stellar and nebular abundances is essentially a consistency check which may reveal systematic offsets between different metallicity indicators. In the case of the Cosmic Eye, Stark et al. (2008) deduced a metallicity $Z_\mathrm{H\,II} \simeq 0.9 Z_\odot$ assuming that the upper-branch solution of the R23 method first introduced by Pagel et al. (1979) applies. On the other hand, we showed in Section 4.4 that at solar metallicities the C IV P Cygni profile would be stronger than observed, and that a metallicity $Z_\mathrm{LMC/SMC} \approx 0.4 Z_\odot$ gives a better match to the data. Discrepancies by factors of $\sim 2$ between different metallicity indicators in high redshifts galaxies are probably to be expected (Pettini 2006). On the other hand, in our earlier study of the Cosmic Horseshoe (Quider et al. 2009), we did find the metallicity deduced from the R23 index to be the odd one out (in the sense of being a factor of $\sim 3$ higher) among several stellar and nebular measures. At lower redshifts too, methods relying on the R23 index result in metallicities towards the upper end of the range spanned by different indicators (see, for example, Figure 2 of Kewley & Ellison 2008). In light of these considerations, the apparent difference between nebular and stellar metallicity in the Cosmic Eye is not surprising.

As mentioned in Section 4.4, the C IV P Cygni profiles of the Cosmic Eye, Cosmic Horseshoe, and MS 1512-cB58 are all remarkably similar. While initially this may seem

to be an odd coincidence, considering that these three galaxies were randomly selected by gravitational lensing, on further reflection this result is perhaps to be expected. The key issue here is continuous star formation. When considering the composite spectrum of an entire galaxy,[5] it is exceedingly unlikely that we would pick out a special time in its stellar evolution. While in individual regions star formation is likely to proceed in bursts, a succession of such bursts on a galaxy-wide scale will approximate a continuous process of star formation. Under such circumstances, the contrast of the C IV (and other) wind lines over the underlying OB photospheric continuum will stabilize after $\sim 50\,\mathrm{Myr}$ from the onset of star formation, corresponding to the lifetime of the lowest mass stars contributing to the light at $1550\,\mathrm{\AA}$. Since this time interval is comparable to the dynamical timescale of most LBGs (e.g. Erb et al. 2006c), only a fairly exceptional star-formation history would produce significant changes in the integrated UV stellar spectrum.

As discussed above, the stellar metallicity is also an important factor in determining the strengths of the P Cygni lines, but on this basis too we would not expect marked differences between the Cosmic Eye, the Cosmic Horseshoe and MS 1512-cB58, given that the three galaxies have similar metallicity, $Z \simeq 0.4 Z_\odot$. Such a uniform degree of metal enrichment is in turn not as surprising as it may seem, since the three objects are of comparable luminosities, reflecting the fact that most strongly lensed galaxies targeted for detailed analyses so far are intrinsically luminous, with $L \sim L^*$. A test of these ideas would be provided by observations of highly magnified galaxies of lower intrinsic luminosity (and presumably metallicity) than the few examples studied up to now.

## 4.7  Summary and Conclusions

Strong gravitational lensing of a $z = 3.07331$ star-forming [SFR $\simeq 50\,M_\odot\,\mathrm{yr}^{-1}$ for a Chabrier (2003) IMF] galaxy magnifies it by a factor of $\sim 25$ and distorts its image into two $3''$ long arcs which have been collectively named the 'Cosmic Eye' by their discoverers, Smail et al. (2007). The high magnification has allowed us to use the ESI spectrograph on the Keck II telescope to record the galaxy's rest-frame UV spectrum with high resolution and S/N ratio. By analyzing these data together with existing observations of the Cosmic Eye at other wavelengths, we have reached the following main conclusions.

(i) The interstellar absorption lines exhibit two components, of approximately equal strength, which are respectively blueshifted by $-70\,\mathrm{km\,s^{-1}}$ and redshifted by $+350\,\mathrm{km\,s^{-1}}$ relative to the stars and H II regions. While these values apply to the gas with the highest apparent optical depths, both components include absorption spanning several hundred km s$^{-1}$. We associate the blueshifted component with a galaxy-wide outflow similar to, but possibly weaker than, those seen in most star-forming galaxies at $z = 2$–3. The redshifted absorption is very unusual, and may represent gas ejected by a previous episode of star formation and now falling back onto the galaxy, or a merger viewed along a favourable line of sight. Alternatively, it may just be a chance superposition of another galaxy along the line of sight.

(ii) Both components of the metal absorption lines show indications that they do not fully cover the OB stars against which they are being viewed; we estimate covering

---

[5]The UV luminosity of an $L^*$ $z = 3$ LBG is equivalent to the integrated output of $\sim 2.5 \times 10^5$ O7 stars (Pettini et al. 1998b).

fractions of $\sim 70\%$ and $\sim 85\%$ for the blueshifted and redshifted component respectively. There must also be more pervasive diffuse gas, because the strong damped Ly$\alpha$ line, corresponding to a column density $N(\mathrm{H\,I}) = (3.0 \pm 0.8) \times 10^{21}\,\mathrm{cm}^{-2}$, covers at least 95% of the UV stellar continuum. We tentatively associate this high column density of H I with the redshifted component of the metal lines, where absorption from ionized species is weak or missing altogether, and propose that it provides the 'foreground screen' of dust responsible for the lower-than-expected far-infrared luminosity of the Cosmic Eye found by Siana et al. (2009) with the *Spitzer Space Telescope*.

(iii) The internal kinematics of the galaxy lensed into the Cosmic Eye are very complex, our data now adding outflow, and possibly even inflow, to the rotation and velocity dispersion already known from the integral field spectroscopy with adaptive optics by Stark et al. (2008). Ordered rotation, chaotic motions, and outflow all seem to be of comparable magnitude, with $v_{\mathrm{rot}} \sin i \approx \sigma_0 \approx v_{\mathrm{blue}} \simeq 50$–$70\,\mathrm{km\,s}^{-1}$. However, we do not have a model yet of how these different motions fit together into one coherent kinematic picture.

(iv) Turning to the stellar spectrum, we find that the C IV P Cygni profile is well fit by a *Starburst99* stellar population model spectrum having continous star formation with a Salpeter IMF, stellar masses from 5 to $100\,M_\odot$, and a LMC/SMC metallicity of $Z \sim 0.4\,Z_\odot$. The P Cygni profiles of the Cosmic Eye, the Cosmic Horseshoe, and MS 1512-cB58, three high redshift star-forming galaxies studied at high spectral resolution, are all nearly identical. This is not unexpected, however, when we consider that in each case we see the integrated light of several hundred thousand O-type stars, and that these three galaxies have similar metallicities and dynamical timescales over which star formation is taking place.

(v) The metallicity $Z \simeq 0.4 Z_\odot$ deduced for the O stars in the Cosmic Eye is lower by a factor of $\sim 2$ than the value derived from the analysis of the strong nebular lines from its H II regions using the R23 index. We consider this apparent discrepancy to reflect systematic offsets between different abundance estimators, rather than intrinsic inhomogeneities in the chemical composition of stars and ionized gas.

(vi) The interpretation of both interstellar and stellar features in the UV spectrum of the Cosmic Eye is complicated by the presence of numerous intervening absorption lines associated with eight absorption systems at redshifts $z_{\mathrm{abs}} = 2.4563$–$3.0528$. These narrow features are not resolved in existing low-resolution data, highlighting the caution that should be exercised in interpreting the spectra that are typically available for unlensed LBGs.

In closing, the new data presented here further emphasize the complexity of the physical conditions which prevailed in actively star-forming galaxies at redshifts $z = 2$–3. It is remarkable that the three strongly-lensed galaxies targeted by our ESI observations, while showing very similar young stellar populations, are all different in the detailed properties of their interstellar media. Whether such variety is simply the result of different geometries and viewing angles, or has its roots in more fundamental physical reasons remains to be established. Fortunately, with the increasing attention being given to detailed studies of gravitationally lensed galaxies, we can look forward with optimism to a more comprehensive empirical picture of galaxy formation coming together in the years ahead.

# 5

# Outflows in Absorption and Emission from Galaxies at $1 < z < 2$

## 5.1  Introduction

Outflows are a phenomenon regularly seen in star-forming galaxies at low (e.g. Heckman et al. 2000; Martin 2005) as well as high (e.g. Pettini et al. 2001; Shapley et al. 2003; Steidel et al. 2010; Vanzella et al. 2009) redshifts. They are commonly thought to be driven by the kinetic energy deposited by supernovae and the winds of massive stars (Pettini et al. 2001). Simulations rely on feedback for the suppression of star formation, and galactic winds are a major component of mechanical feedback (Davé, Oppenheimer & Finlator 2011). Beyond constraining galaxy models, outflows have been shown to have a significant impact on the intergalactic medium and a strong connection to the stellar mass-metallicity relation (Adelberger et al. 2003, Finlator & Davé 2008, Steidel et al. 2010).

Despite its importance in the development of structure in the Universe, the redshift range $1 < z < 2$ is not well covered by current studies of outflows. Much of a galaxy's stellar mass assembled during this period (Hopkins & Beacom 2006) and, due to hierarchical structure formation, galaxies from this epoch are the building blocks for the structures we see today. Therefore, an understanding of the outflow properties of these galaxies is essential for filling in our picture of galaxy evolution.

Absorption lines caused by the illumination of a galaxy's interstellar medium by the stars are the features typically used for characterizing outflows. These features are easily identified in spectra because they are often deep (near or at saturation), blueshifted with respect to the systemic velocity, and span up to $\Delta v \sim 1000 \, \mathrm{km \, s^{-1}}$ (Quider et al. 2010 and references therein). In the rest-frame far-UV spectrum of a star-forming galaxy, numerous such absorption features from a range of elemental species can be seen, making these features readily available for study. Information such as the velocity extent, covering factor, and metallicity of the outflow can be measured and nearly all that we know about

outflows in high redshift galaxies comes from absorption line studies (see Chapter 1).

To this picture is added emission from Fe II and the P-Cygni profile of Mg II in the rest-frame near-UV spectrum of galaxies. Rubin et al. (2011) propose that the blue component of the non-resonant Fe II* emission lines comes from the same gas seen in absorption. However, redshifted portion of this emission arises in the entirety of the outflow. Finally, the redshifted Mg II emission and resonant Fe II emission arise in photon scattering from the receding portion of the outflow. Prochaska et al. (2011) adopt this mechanism and model its impact on the emergent absorption and emission line profiles for Fe II and Mg II.

One of the main consequences of their work is that emission from resonance transitions can be superposed upon absorption located at the systemic redshift. The effect of this is to diminish the strength of the affected absorption line by diminishing the absorption strength near the systemic redshift. This shifts the absorption line's centroid further blueward than the outflow velocity's actual value. This process is referred to as line-filling or emission filling of absorption lines. Quantifying the effect of line-filling on interstellar absorption lines is essential for correct interpretation of these spectral features.

An introduction to the Fe II features explored in this work is useful for context. Figure 5.1 shows the energy level diagrams for the Fe II UV1, UV2, and UV3 multiplets. Numerous Fe II resonant absorption (upward arrows) and Fe II* fine-structure emission (downward arrows) transitions are identified by their rest wavelengths (Å) and Einstein A-coefficients ($s^{-1}$). These transitions, as well as the other features observed in the spectra of galaxies in our sample, are reported in Table 5.1. Fe II* emission can result from UV pumping by Fe II resonance absorption when Fe II is optically thick. In addition to fine-structure emission, the resonant Fe II transitions are susceptible to resonant emission at the absorption wavelengths shown in the diagram. The strength of the resonant emission is determined by the energetic pathways available to electrons which are energetically descending back to the ground state. The transition least likely to experience resonant emission (and therefore least likely to exhibit line-filling) is Fe II $\lambda$2374. As can be seen in Figure 5.1, electrons excited by Fe II $\lambda$2374 absorption can descend back to the ground state by either resonant emission at 2374 Å or fine-structure emission at 2396 Å. The most likely path to the ground state will be Fe II* $\lambda$2396 emission because its A-value is considerably higher than the A-value of the 2374 Å resonant transition. Therefore, it is very unlikely that Fe II $\lambda$2374 will undergo resonant emission because a more favorable path is available to the electrons for de-excitation. On the other hand, the Fe II $\lambda$2382 transition must exhibit resonant emission because that is the only pathway available for electrons that are de-exciting back to the ground state. Fe II $\lambda$2382 is the only absorption transition which does not have an associated Fe II* emission pathway for electron de-excitation. As a consequence, Fe II $\lambda$2382 is the Fe II transition most affected by resonant emission and, therefore, line-filling.

In this Chapter we examine the rest-frame near-UV spectra of a sample of 96 star-forming galaxies with $1 < z < 2$. Our purpose is to look for evidence of emission filling and, if found, to estimate its prevalence. We report, for the first time, a large sample of high redshift galaxies with Fe II* emission and Mg II emission and look for trends with stellar mass and reddening among these galaxies. The origin of Fe II* emission is also considered.

# FeII UV1

z $^6D^0_{3/2}$

5/2

7/2

9/2

$3d^64p$

λ2600 2.35e8 λ2626 3.41e7 λ2586 8.94e7 λ2612 1.23e8 λ2632 6.21e7

a $^6D_{1/2}$

3/2

5/2

7/2

9/2

$3d^64s$

# FeII UV2

z $^6F^0_{7/2}$

9/2

11/2

$3d^64p$

λ2382 3.13e8 λ2374 4.25e7 λ2396 2.67e8

a $^6D_{1/2}$

3/2

5/2

7/2

9/2

$3d^64s$

# FeII UV3

z $^6P^0_{3/2}$

4/2

7/2

$3d^64p$

λ2344 1.73e8 λ2365 5.90e7

a $^6D_{1/2}$

3/2

5/2

7/2

9/2

$3d^64s$
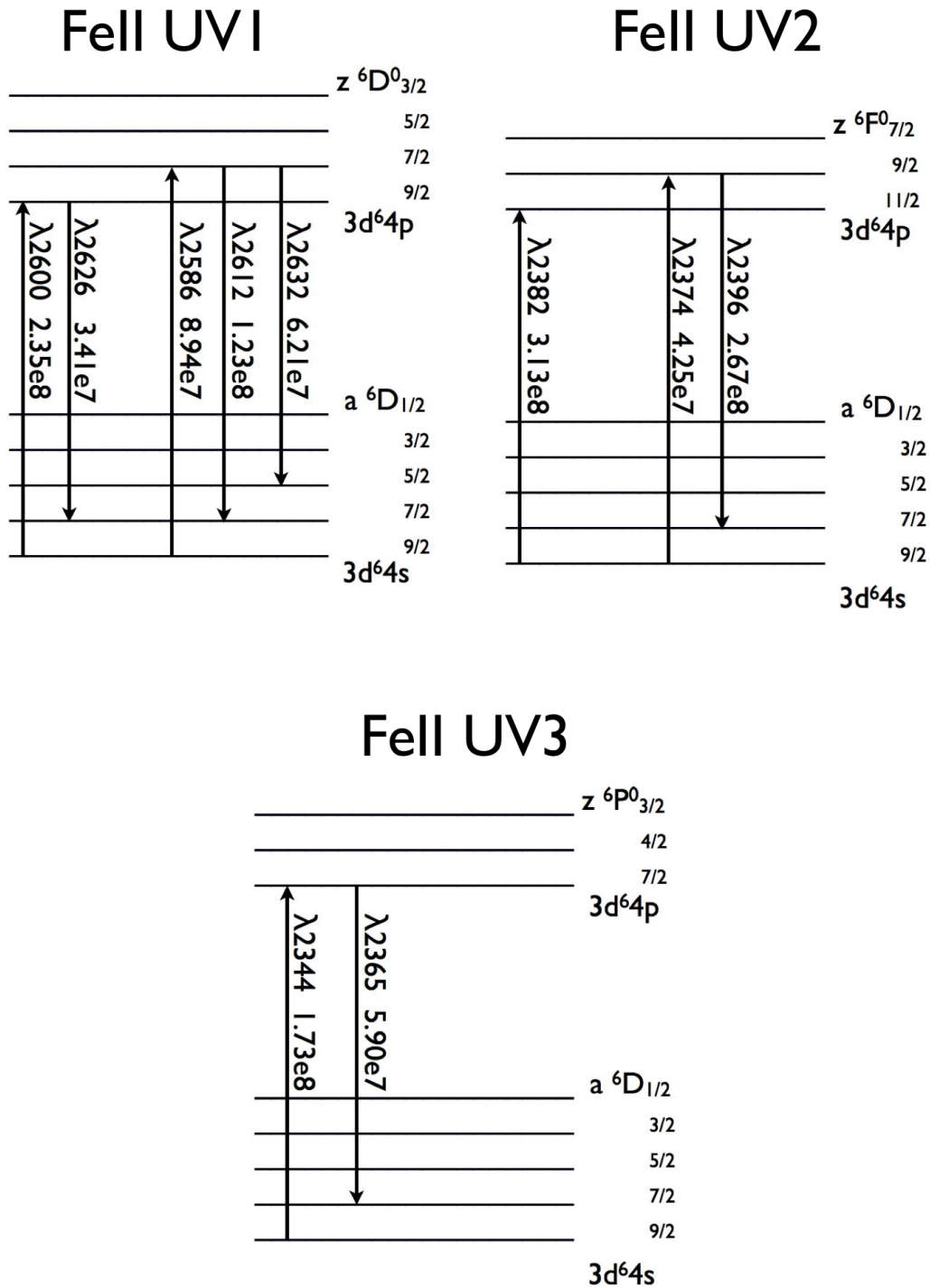
Figure 5.1 The energy level diagrams for selected transitions of the Fe II atom (based on Figure 7 of Hartigan et al. (1999) and Figure 1 of Prochaska et al. (2011)). Each transition is labeled with its rest wavelength (Å) and Einstein A-coefficient (s$^{-1}$), as reported in Table 5.1. Upward arrows indicate resonance absorption (absorption from the ground state). The fine-structure splitting of the energy levels in the Fe II atom allows for fine-structure emission. The downward arrows show the Fe II* (fine-structure) emission that is energetically tied to the resonance absorption transitions. Other Fe II* emission is possible but it is not shown in the diagrams because it is not linked to the resonant absorption transitions.

## 5.2 Observations and Data Reduction

The observations and data reduction for this sample were described in detail in Chapter 2. For immediate reference, however, here is a summary of the salient points. We obtained Keck/DEIMOS spectra of 147 BX/BM galaxies drawn from the spectroscopic survey of Steidel et al. (2004). The final spectra have $\sim 60\,\mathrm{km\,s^{-1}}$ $\mathrm{pixel^{-1}}$ and $\sim 30\,\%$ of spectra have S/N $\geq 5$.

## 5.3 Systemic Redshift Determination

### 5.3.1 Method

An accurately determined systemic redshift is essential for this study. The systemic redshift serves as the velocity zero-point for studying the kinematics of galactic gas. Further, it is used for properly aligning galaxies while making stacks to study average spectral features.

Determining the systemic redshift of a high redshift star-forming galaxy is not trivial. There are three main sets of spectroscopic features which can be used. The most reliable systemic redshift comes from measuring the wavelength of strong emission lines from H II regions. These nebular emission lines are many times brighter than the continuum level and they are Gaussian-shaped, making them easily identified and measured. Unfortunately, the strongest lines tend to be redshifted into the infrared. The next best measurement comes from the centers of stellar photospheric absorption lines. While they are located at accessible wavelengths, these features are broad and shallow so they are hard to identify at the S/N of most high redshift galaxy spectra. Lastly, the interstellar absorption lines can be used to estimate the systemic redshift of a galaxy.

Because of the redshifting of the rest-UV spectrum of high redshift sources into the easily accessible optical band where multi-object spectrographs are operational, use of interstellar absorption lines to infer a galaxy's systemic redshift is often the only option. It is well-documented that these features are blue-shifted with respect to the systemic redshift (Shapley et al. 2003) and that the degree of blue-shifting varies for individual galaxies (Steidel et al. 2010). These absorption lines have non-Gaussian profiles (Pettini et al. 2002, Quider et al. 2009, 2010) which can introduce ambiguity and difficulty into the measurement process. Finally, some of these absorption features may have emission lines superposed on them, affecting their morphology and line centers (Prochaska et al. 2011). These factors make interstellar absorption lines the least reliable indicator of the systemic redshift.

We use strong [O II] $\lambda\lambda\,3727,3729$ emission to measure the systemic redshift for 55 galaxies in our sample. The [O II] emission line is a doublet which originates in the H II regions surrounding the hot OB stars. It is a common feature in star-forming galaxy spectra and we detect this doublet in every galaxy whose redshift and S/N permit it. Our spectra are of sufficient quality to resolve both members of the doublet in most cases. We performed a constrained double Gaussian fit to the [O II] complex. We fixed the separation between Gaussian centers, required that the Gaussians have the same width, and permitted the area of each Gaussian to vary. Fits were performed on the

spectra prior to rebinning because the lower S/N of the un-rebinned spectra does not inhibit our ability to fit these features. Three of these galaxies were at $z < 1$, causing Mg II to fall outside of the spectral window, so they were not included in the remainder of the analysis. This leaves us with 52 galaxies in our [O II] emission sample and they have an average redshift $< z > = 1.39656 \pm 0.20$.

In the remaining cases, interstellar absorption lines were used to estimate systemic redshifts. To do this, we follow the technique presented by Steidel et al. (2010). These authors found that, on average, the interstellar absorption lines for LBGs at $z \sim 2.2$ are offset from the systemic redshift by $-166 \pm 130$ km s$^{-1}$. They analyzed a sample of galaxies which have both interstellar absorption lines and systemic redshifts defined by H$\alpha$ emission. The absorption transitions they used depended upon what was most visible in the spectrum; usually the strongest features, such as Si II $\lambda$1260 and C II $\lambda$1334, were used. With this in mind, we derive rules for relating the nebular and interstellar absorption features for our own galaxies.

In order to derive these rules, we used a subset of our sample which has both [O II] nebular emission and Fe II $\lambda$2374 absorption to define the average blueshift for interstellar absorption lines. Fe II $\lambda$2374 should be the absorption line least affected by Fe II emission (see §5.1 and Martin, Shapley, Kornei, & Coil 2011, in prep.). Therefore, of the available Fe II transitions, the 2374 Å transition's profile center and morphology should be most representative of the kinematics of the outflow. The coarse resolution of our spectra, combined with the often low S/N, means that the interstellar absorption lines are generally well fit by a single Gaussian function. We fit each Fe II $\lambda$2374 absorption line and used the fit's center wavelength to determine the absorption velocity offset from the [O II]-defined systemic redshift. As [O II] and this Fe II transition are at opposite ends of the accessible wavelength range, we only had 20 systems whose spectra included both features with reasonable measurement errors ($\sigma \leq 100$ km s$^{-1}$ for measurements of the absorption line center). The relationship between the [O II]-defined systemic redshift and the redshift of the interstellar absorption is found to be

$$z_{\mathrm{sys}} = z_{\mathrm{abs}} + 85 \pm 87 \, \mathrm{km \, s^{-1}} \tag{5.1}$$

where 85 km s$^{-1}$ is the average velocity offset and 87 km s$^{-1}$ is the standard deviation of all 20 offsets. There is substantial scatter in this relationship, indicative of the variations among the galaxies in our sample. This level of scatter is consistent with Steidel et al. (2010) who used a larger galaxy sample.

For the remaining 44 galaxies in our sample, we calculated the systemic redshift using eq. (5.1) and an absorption redshift measured from the interstellar absorption lines. Where possible, we used Fe II $\lambda$2374 to define the absorption redshift. When that feature was unavailable, we used Fe II $\lambda$2586 as this transition should also be less affected by Fe II emission (as can be deduced from an inspection of Figure 5.1). In the 14 galaxies where these two features were not detected, the UV absorption redshift from Keck/LRIS spectroscopy was substituted for $z_{\mathrm{abs}}$. In later sections, we will measure velocity offsets from systemic for an array of absorption and emission features in our spectra. While we are introducing a velocity offset in order to obtain the systemic redshift in the first place, this method has been shown to work for the sample on average, thereby giving us an overall assessment of the velocity offsets for the sample as a whole. This procedure is the only way to compare the Doppler shifts of different absorption lines so, while not ideal,

we proceed with such measurements. The galaxies with redshifts determined using the redshift of UV absorption lines and eq. (5.1) have $< z > = 1.836 \pm 0.160$.

The flow chart in Figure 5.2 summarizes the number of galaxies in the main samples considered in this work. It shows how the sample of 147 galaxies we originally observed with DEIMOS evolved into the sample of 96 galaxies considered in this work.

### 5.3.2 Assessment of systemic redshift

The success of eq. (5.1) can be evaluated using composite spectra. If this relation is correct, the spectroscopic features of the [O II]-defined systemic redshift sample (the [O II] galaxies) and the absorption-defined systemic redshift sample (the absorption galaxies) should align in rest-wavelength, keeping in mind there may be physical differences between the two samples. Figure 5.3 compares a rest-frame stack of the 52 [O II] galaxies to a stack of the 44 absorption galaxies; the details of the method used to create these composite spectra are given in Section 5.4. Focusing on the centers of the absorption and emission lines, there seems overall to be a close alignment between the two stacks. The morphological and line strength differences between the two samples will be discussed in Section 5.4.5.

A close-up view of two spectral regions of interest is shown in Figure 5.4. The top panel shows the C II] $\lambda 2326$ nebular emission line. This line originates from the same region as [O II] emission, making it a good marker of the systemic redshift. Both the [O II] and absorption galaxy composites have C II] emission line profiles that are consistent with a Gaussian centered at 2326.00 Å, the vacuum rest wavelength of C II]. This is a good indication that eq. (5.1) works.

The bottom panel shows the Fe II $\lambda\lambda 2374,2382$ absorption transitions for both samples. Recall that eq. (5.1) was constructed using the Fe II $\lambda 2374$ absorption line for a subset of the [O II] galaxies. Somewhat curiously, the absorption line galaxies seem to have gas at a slightly higher velocity than the [O II] galaxies. Despite this small offset, which will be explored in Section 5.4.5, these two samples seem to have absorption profiles which are consistent, within the measured scatter of the velocity offset used in eq. (5.1).

## 5.4 Composite Spectra

The spectra of high redshift star-forming galaxies, such as those in our sample, are generally noisy. This low S/N limits the amount of information that can be gleaned from an individual spectrum. However, stacking $N$ low quality spectra creates a single spectrum with a signal-to-noise ratio that is $\sim \sqrt{(N)}$ higher than that of an individual spectrum. Features which were previously hidden in the noise become apparent. Creating stacks using samples sorted into bins based on their physical properties allows for the study of the relationship between average spectral characteristics and galaxy properties (e.g., Shapley et al. 2003; Weiner et al. 2009; Rubin et al. 2011).

### 5.4.1 Construction of stacked spectra

Constructing stacked spectra requires continuum normalizing each galaxy spectrum. After the systemic redshift for a galaxy was determined, a continuum was fit using the
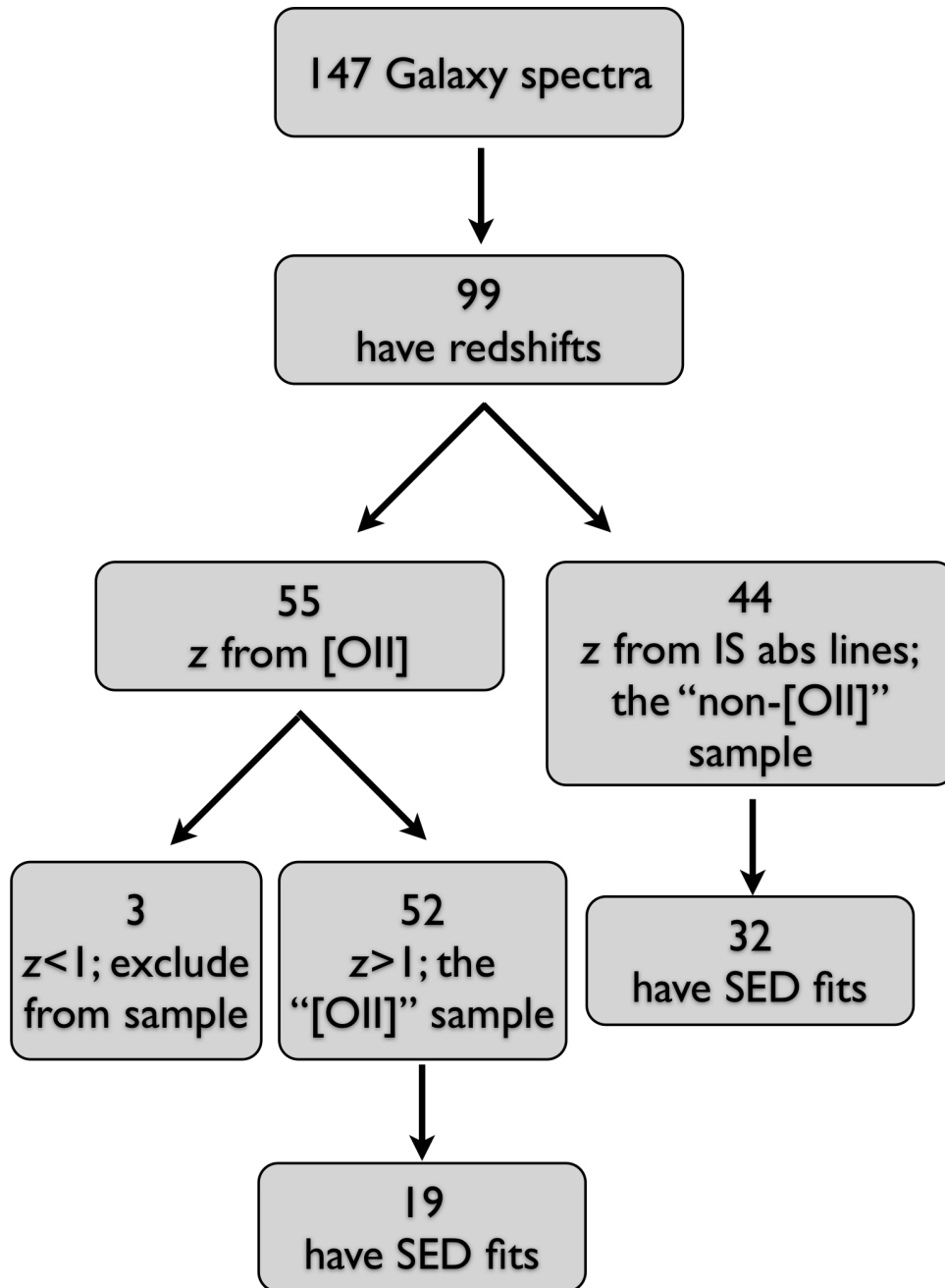
Figure 5.2 A flow chart summarizing the number of galaxies in the main samples considered in this work. Numbers in the boxes refer to the number of BX/BM galaxies which fall into the category indicated by the location of the box in the flow chart as well as the description within the box.
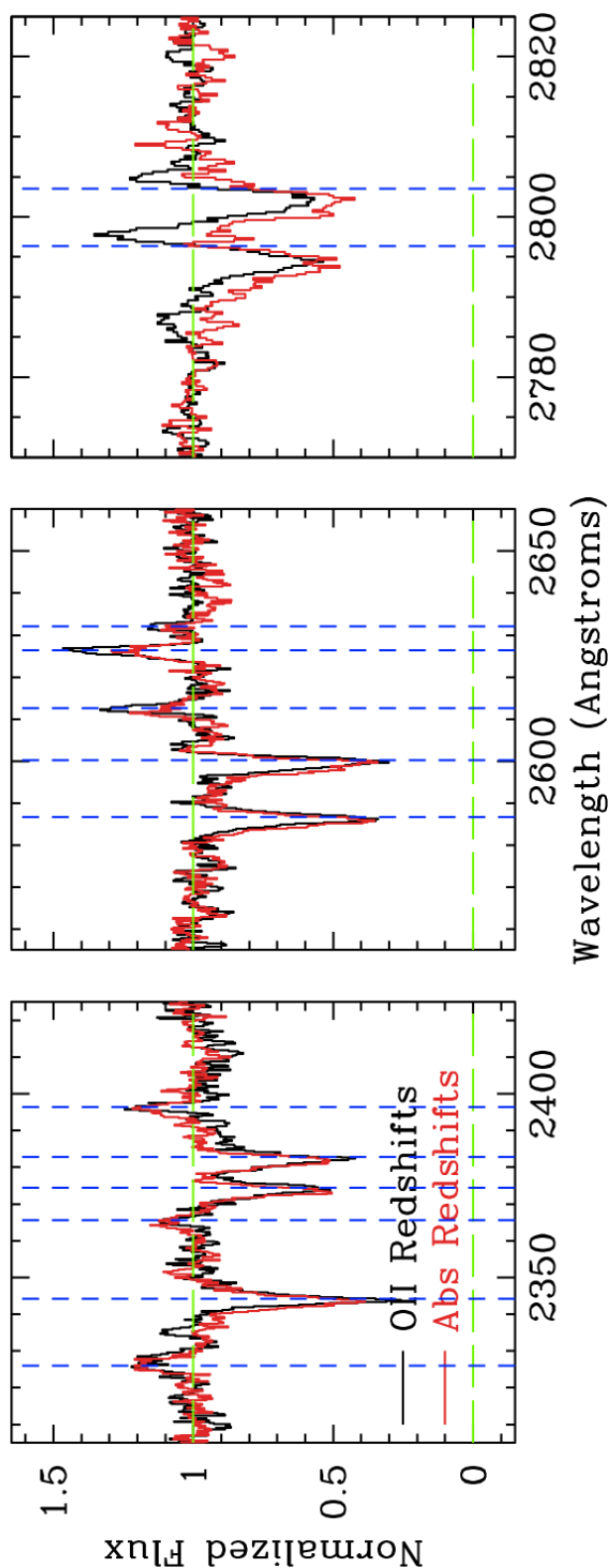
Figure 5.3 A comparison of the stack of 52 galaxies with redshifts determined by [O II] emission (black line) and a stack of 44 galaxies with systemic redshifts determined using eq. (5.1) (red line). The features of these two stacks should align. The morphological and line strength differences between these two composites are explored in Section 5.4.5.
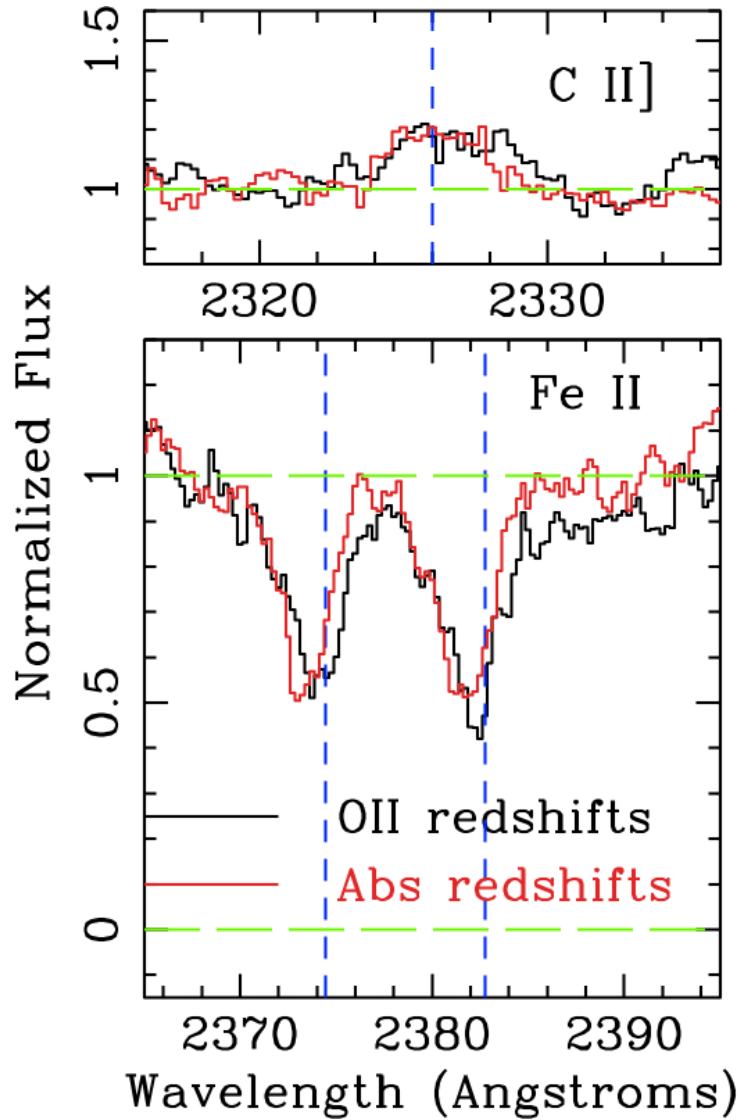
Figure 5.4 A zoom-in on two regions of interest from Figure 5.3. The blue dashed lines mark the rest wavelength for the transitions shown. *top*: C II] $\lambda 2326$ nebular emission which should lie at the systemic redshift of a galaxy. The two galaxy composites have a Gaussian-shaped emission feature centered on the C II] rest wavelength of 2326.00 Å. *bottom*: Fe II $\lambda\lambda 2374,2382$ absorption lines which are known to have a negative velocity with respect to the systemic redshift. While these two absorption features are aligned overall, there is a non-trivial offset which is addressed in Section 5.4.5.

Table 5.1 OBSERVED ABSORPTION AND EMISSION FEATURES

| Ion | $\lambda_{\text{lab}}$<sup>a</sup> (Å) | A<sup>a</sup>(s$^{-1}$) | $f$<sup>a</sup> | Notes |
|---|---|---|---|---|
| C II] | 2326.00 | 4.43E+01 | ... | Emission; blended with [O III] $\lambda\lambda$2321,2331 emission |
| [O II] | 2470.97 | 2.12E-02 | ... | Emission; blended with [O II] $\lambda$2471 |
| | 2471.09 | 5.22E-02 | ... | Emission; blended with [O II] $\lambda$2470 |
| Mg I | 2852.96 | 4.91E+08 | 1.83 | Absorption |
| Mg II | 2796.35 | 2.60E+08 | 0.6155 | Absorption and Emission |
| | 2803.53 | 2.57E+08 | 0.3058 | Absorption and Emission |
| Fe II | 2249.88 | ... | 0.00182 | Absorption |
| | 2260.78 | ... | 0.00244 | Absorption |
| | 2344.21 | 1.73E+08 | 0.114 | Absorption |
| | 2365.55 | 5.90E+07 | .0495 | Emission |
| | 2374.46 | 4.25E+07 | 0.0313 | Absorption |
| | 2382.76 | 3.13E+08 | 0.320 | Absorption |
| | 2396.36 | 2.67E+08 | 0.279 | Emission |
| | 2586.65 | 8.94E+07 | 0.0691 | Absorption |
| | 2600.17 | 2.35E+08 | 0.239 | Absorption |
| | 2612.11 | 1.23E+08 | 0.122 | Emission |
| | 2626.45 | 3.41E+07 | 0.0455 | Emission |
| | 2632.11 | 6.21E+07 | 0.087 | Emission |

<sup>a</sup> Vacuum wavelength, A-values, and oscillator strengths are from Morton (2003) when available and from the NIST Atomic Spectra Database otherwise.

procedure outlined in Rix et al. (2004). We identified regions of the spectrum which contained flux solely from the continuum and fit a spline curve to both the mean wavelength and mean flux values within these defined continuum windows. The same windows were used for each galaxy with adjusting on an individual basis to avoid the chip gap (see Chapter 2 for clarification) or noise spikes. The error in the continuum fits was calculated and found to be $\sim \pm 5\,\%$ for most galaxies. Each galaxy spectrum was then divided by the spline fit to its continuum. These continuum normalized spectra were used for the remainder of the analysis.

Our stacked spectra are created with $3\sigma$ rejection. The standard deviation of the flux values at a given wavelength step was calculated and pixels with flux values $\geq 3\sigma$ were rejected. The mean flux value of the remaining pixels was output. This was done for each pixel so the individual spectra contributing to the mean flux at a given pixel varies. The error spectrum for a stack was computed by adding in quadrature the error spectra for the individual galaxies contributing to the mean flux at each wavelength step. The final stacked spectra have $0.25\,\text{Å}$ per pixel in the rest frame.

## 5.4.2 Composite of all galaxies

Presented in Figure 5.5 is the stack of all 96 galaxies in our sample. We identify 19 distinct absorption and emission features from Mg, Fe, C, and O. These are indicated by the short vertical lines along the bottom of the Figure and listed in Table 5.1. These
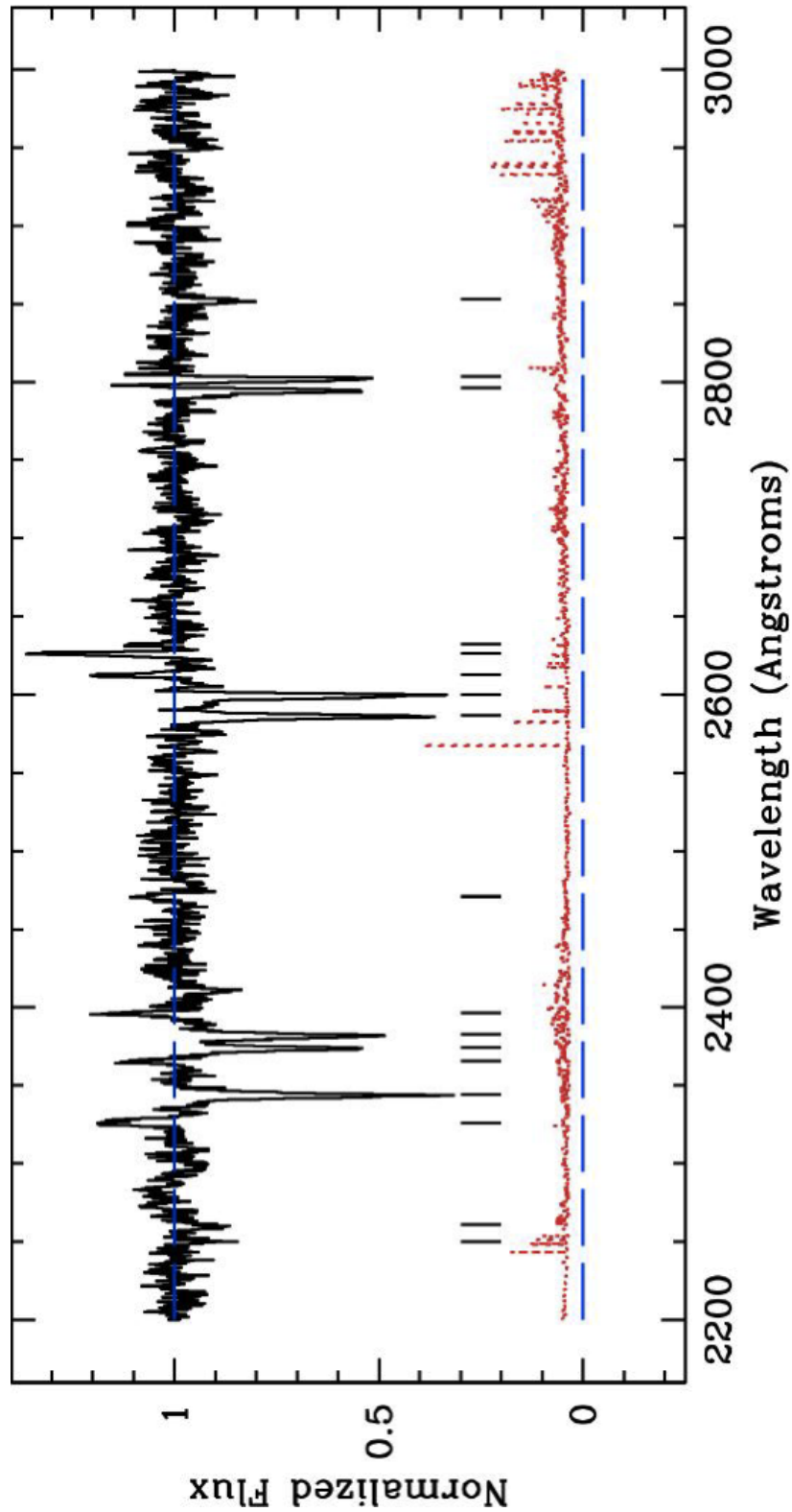
Figure 5.5 A mean stack of 96 galaxies with $3\sigma$ rejection at each pixel. The galaxy composite is shown in black while the $1\sigma$ error spectrum is shown in red. Absorption and emission features are indicated by vertical lines and they are listed in Table 5.1.

Table 5.2 MEASURED ABSORPTION FEATURES IN COMPOSITE SPECTRA

| | All Galaxies | High Mass | Low Mass | High Dust | Low Dust | No [O II] Emission | [O II] Emission |
|---|---|---|---|---|---|---|---|
| $N$ | 96 | 17 | 17 | 17 | 17 | 44 | 52 |
| $W_{\mathrm{MgI},2582}$ | 0.97±0.11 | 1.09±0.22 | ⋯ | 0.37±0.24 | 0.64±0.17 | 0.75±0.21 | 0.51±0.12 |
| $W_{\mathrm{MgII},2796}$ | 1.58±0.11 | 3.07±0.53 | 1.69±0.24 | 2.54±0.56 | 1.18±0.40 | 2.06±0.19 | 1.20±0.11 |
| $W_{\mathrm{MgII},2803}$ | 1.53±0.07 | 3.36±0.43 | 1.30±0.22 | 2.59±0.54 | 1.55±0.10 | 2.31±0.41 | 1.20±0.08 |
| $W_{\mathrm{FeII},2260}$ | 0.39±0.14 | 0.55±0.20 | 0.69±0.21 | 0.76±0.25 | 0.47±0.14 | 0.46±0.19 | 0.34±0.14 |
| $W_{\mathrm{FeII},2344}$ | 2.33±0.09 | 2.55±0.15 | 1.89±0.12 | 2.11±0.11 | 2.46±0.13 | 2.19±0.11 | 2.17±0.11 |
| $W_{\mathrm{FeII},2374}$ | 1.55±0.09 | 1.36±0.11 | 1.49±0.15 | 1.30±0.15 | 1.74±0.12 | 1.44±0.12 | 1.71±0.13 |
| $W_{\mathrm{FeII},2382}$ | 1.92±0.08 | 1.85±0.12 | 1.35±0.16 | 1.33±0.14 | 2.00±0.13 | 1.70±0.15 | 2.04±0.16 |
| $W_{\mathrm{FeII},2586}$ | 2.19±0.10 | 2.82±0.20 | 1.86±0.13 | 2.31±0.15 | 2.22±0.11 | 2.17±0.13 | 2.15±0.10 |
| $W_{\mathrm{FeII},2600}$ | 2.26±0.07 | 2.78±0.14 | 2.81±0.28 | 2.97±0.17 | 2.60±0.16 | 2.61±0.16 | 2.14±0.07 |
| $v_{\mathrm{MgI},2582}$ | −116 ± 64 | −46 ± 44 | ⋯ | −124 ± 69 | −160 ± 47 | −178 ± 67 | −116 ± 54 |
| $v_{\mathrm{MgII},2796}$ | −298 ± 21 | −288 ± 60 | −341 ± 48 | −258 ± 92 | −318 ± 80 | −339 ± 34 | −240 ± 18 |
| $v_{\mathrm{MgII},2803}$ | −208 ± 7 | −154 ± 47 | −216 ± 32 | −128 ± 88 | −208 ± 9 | −241 ± 75 | −192 ± 9 |
| $v_{\mathrm{FeII},2260}$ | −145 ± 105 | −161 ± 101 | −119 ± 97 | 68 ± 126 | −174 ± 72 | −186 ± 119 | +9 ± 88 |
| $v_{\mathrm{FeII},2344}$ | −67 ± 14 | −82 ± 18 | −79 ± 16 | −83 ± 13 | −106 ± 17 | −112 ± 15 | −38 ± 16 |
| $v_{\mathrm{FeII},2374}$ | −113 ± 16 | −113 ± 15 | −104 ± 26 | −99 ± 28 | −133 ± 18 | −141 ± 19 | −60 ± 23 |
| $v_{\mathrm{FeII},2382}$ | −141 ± 13 | −115 ± 15 | −162 ± 30 | −73 ± 26 | −224 ± 22 | −164 ± 24 | −122 ± 26 |
| $v_{\mathrm{FeII},2586}$ | −86 ± 15 | −159 ± 53 | −70 ± 13 | −82 ± 16 | −76 ± 10 | −132 ± 17 | −57 ± 13 |
| $v_{\mathrm{FeII},2600}$ | −118 ± 9 | −124 ± 15 | −170 ± 33 | −153 ± 19 | −154 ± 14 | −182 ± 21 | −93 ± 7 |

*Notes* Rest-frame equivalent widths ($W$) are measured in Å and positive values indicate absorption. Velocities ($v$) refer to the feature's centroid and are measured in km s$^{-1}$ from the systemic velocity.

Table 5.3 MEASURED EMISSION FEATURES IN COMPOSITE SPECTRA

| | All Galaxies | High Mass | Low Mass | High Dust | Low Dust | No [O II] Emission | [O II] Emission |
|---|---|---|---|---|---|---|---|
| $N$ | 96 | 17 | 17 | 17 | 17 | 44 | 52 |
| $W_{\text{CII}],2326}$ | $-0.75 \pm 0.07$ | ... | $-1.44 \pm 0.15$ | $-0.72 \pm 0.19$ | $-1.07 \pm 0.09$ | $-0.71 \pm 0.11$ | $-0.98 \pm 0.20$ |
| $W_{\text{MgII},2796}$ | $-0.15 \pm 0.05$ | ... | $-0.55 \pm 0.13$ | ... | $-0.95 \pm 0.23$ | ... | $-0.51 \pm 0.07$ |
| $W_{\text{MgII},2803}$ | $-0.13 \pm 0.05$ | ... | $-0.21 \pm 0.06$ | ... | $-0.15 \pm 0.07$ | ... | $-0.34 \pm 0.09$ |
| $W_{\text{FeII},2365}$ | $-0.25 \pm 0.08$ | ... | $-0.28 \pm 0.11$ | $-0.40 \pm 0.14$ | $-0.32 \pm 0.07$ | $-0.36 \pm 0.12$ | $-0.20 \pm 0.07$ |
| $W_{\text{FeII},2396}$ | $-0.42 \pm 0.05$ | $-0.90 \pm 0.18$ | $-0.81 \pm 0.10$ | $-0.90 \pm 0.14$ | $-0.47 \pm 0.07$ | $-0.58 \pm 0.11$ | $-0.43 \pm 0.05$ |
| $W_{\text{FeII},2612}$ | $-0.49 \pm 0.05$ | ... | $-0.71 \pm 0.12$ | $-0.59 \pm 0.13$ | $-0.44 \pm 0.15$ | $-0.41 \pm 0.11$ | $-0.62 \pm 0.05$ |
| $W_{\text{FeII},2626}$ | $-0.90 \pm 0.05$ | $-0.92 \pm 0.18$ | $-1.14 \pm 0.13$ | $-0.90 \pm 0.14$ | $-1.38 \pm 0.14$ | $-0.73 \pm 0.13$ | $-1.07 \pm 0.06$ |
| $W_{\text{FeII},2632}$ | $-0.21 \pm 0.05$ | $-0.25 \pm 0.13$ | $-0.76 \pm 0.21$ | $-0.15 \pm 0.08$ | $-0.56 \pm 0.21$ | ... | $-0.31 \pm 0.07$ |
| $v_{\text{CII}],2326}$ | $59 \pm 26$ | ... | $49 \pm 42$ | $92 \pm 84$ | $66 \pm 24$ | $11 \pm 35$ | $60 \pm 77$ |
| $v_{\text{MgII},2796}$ | $147 \pm 27$ | ... | $141 \pm 26$ | ... | $93 \pm 42$ | ... | $150 \pm 12$ |
| $v_{\text{MgII},2803}$ | $153 \pm 25$ | ... | $130 \pm 16$ | ... | $184 \pm 37$ | ... | $183 \pm 26$ |
| $v_{\text{FeII},2365}$ | $-41 \pm 49$ | ... | $-92 \pm 47$ | $37 \pm 65$ | $-87 \pm 27$ | $-108 \pm 71$ | $-40 \pm 35$ |
| $v_{\text{FeII},2396}$ | $-42 \pm 25$ | $-45 \pm 61$ | $-108 \pm 25$ | $-112 \pm 39$ | $1 \pm 21$ | $-88 \pm 42$ | $-5 \pm 14$ |
| $v_{\text{FeII},2612}$ | $-10 \pm 15$ | ... | $-6 \pm 28$ | $-64 \pm 41$ | $-98 \pm 48$ | $-59 \pm 51$ | $-5 \pm 11$ |
| $v_{\text{FeII},2626}$ | $-48 \pm 8$ | $37 \pm 49$ | $-56 \pm 21$ | $-37 \pm 28$ | $-30 \pm 29$ | $-55 \pm 33$ | $-43 \pm 9$ |
| $v_{\text{FeII},2632}$ | $-23 \pm 27$ | $10 \pm 48$ | $164 \pm 69$ | $-26 \pm 50$ | $21 \pm 74$ | ... | $18 \pm 30$ |

*Notes* Rest-frame equivalent widths ($W$) are measured in Å and positive values indicate absorption. Velocities ($v$) refer to the feature's centroid and are measured in km s$^{-1}$ from the systemic velocity.

features have both interstellar absorption (Fe and Mg) and nebular emission (C and O). The majority of these lines are commonly seen in the spectra of star-forming galaxies at low and high redshift. Surprisingly, we record uncommonly seen Fe II fine structure emission and Mg II emission (Martin et al. 2005; Heckman et al. 2001; Leitherer et al. 2011; Weiner et al. 2009; Rubin et al. 2010, 2011).

Table 5.2 and Table 5.3 contain the rest equivalent width ($W_0$) and velocity centroid measurements for the absorption and emission profiles, respectively, seen in this and the other composite spectra (to be discussed later in this section). The Fe II $\lambda 2249$ and [O II] $\lambda\lambda 2470, 2471$ features are not listed in the Tables because they are not detected in any stack except that of the complete sample.

The rest equivalent width was calculated through direct integration of the flux in absorption or emission, as appropriate. Features were integrated within the bounds of where the flux first meets the continuum on the blue and red sides of a feature's rest wavelength. To calculate the $1\sigma$ uncertainties on the equivalent width and velocity measurements, we used a Monte Carlo realization of the composite spectrum. Random numbers were drawn from Gaussian distributions whose standard deviations were the $1\sigma$ composite error spectrum value for each pixel. This random number vector was multiplied by the $1\sigma$ error spectrum and added to the composite at each pixel. Rest equivalent width values and velocity centroids were measured for the modified composite spectrum. We repeated this procedure 5000 times. The errors listed for $W_0$ and velocity are the standard deviation of the 5000 measurements of these values made for each feature. This procedure was repeated for each composite spectrum.

Now we turn briefly to a consideration of the overall absorption and emission properties of this particular stacked spectrum of all 96 galaxies.

## Absorption Features

Nearly all of the absorption lines have negative velocity centroids measured with a high degree of significance. This is commonly interpreted as evidence of large-scale galactic outflows. With the exception of Mg II the velocities listed in the "All Galaxies" column of Table 5.2 are consistent with, yet systematically lower than, the $\Delta v = -150 \pm 60$ km s$^{-1}$ and $\Delta v = -165$ km s$^{-1}$ velocity offsets from the systemic redshift for the low ionization absorption lines seen in the stacked spectra of $z \sim 3$ and $z \sim 3.7$ LBGs, respectively (Shapley et al. 2003; Vanzella et al. 2009). At lower redshift, Steidel et al. (2004) find that the interstellar absorption lines in their sample of 27 BX/BM galaxies are offset from the systemic velocity by $\Delta v = -175 \pm 25$ km s$^{-1}$. Looking at these studies in the light of our measurements suggest that the average velocity of galaxy-wide outflows may decrease from $z \sim 3.7$ down to $z \sim 1.6$, the average redshift of our sample. Nevertheless, it is important to keep in mind that studies of interstellar absorption lines for individual galaxies in low resolution (Steidel et al. 2004, 2010) and high resolution (e.g., Dessauges-Zavadsky et al. 2010, Pettini et al. 2002, Quider et al. 2009, 2010) show that there is a large degree of variation, on the order of a few hundred km s$^{-1}$, among the outflow velocities for individual galaxies. Indeed, some galaxies even seem to host *inflows*; in the case of the Cosmic Eye (discussed in Chapter 4), the positive velocity component of the interstellar absorption lines had a greater rest-equivalent width and a greater velocity than the outflow component. Studying composite spectra allows us to smooth out these

individual variations and focus on the average properties of a galaxy sample. In this, composite spectra provide useful information for the study of a galaxy population as a whole.

The Mg II absorption profiles are at a velocity that is nearly $2-3\times$ higher than the other interstellar absorption lines. The topmost panel of Figure 5.6 shows a detailed view of the Mg II region. The terminal velocity of the outflow and its $1\sigma$ error are $v_{max} = -708 \pm 96$, as indicated in the Figure. Mg II outflow velocities of $200-300\,\mathrm{km\,s^{-1}}$, the range covered by these features in our composite, are commonly seen in star-forming galaxies over a wide range of redshifts (Martin & Bouché 2009, Weiner et al. 2009, Rubin et al. 2010). Detecting outflows out to higher velocities is more challenging because there is less absorbing material moving at such great speed. However, the terminal velocity seen here is consistent with that measured for individual lensed galaxies, as discussed in Chapters 3 and 4. The Mg II atoms which are absorbing light at 2796 Å and 2803 Å are expected to be co-spatial with the other low ionization atoms (Fe, in the case of our spectra, and other elements such as C, Si, O in the case of other studies) that are considered when determining average interstellar absorption line velocities. Therefore, the velocity offset between Mg II absorption and the other low ionizaiton lines is curious. Prochaska et al. (2011) and Rubin et al. (2011) propose that the Mg II profiles, and the more blue velocity centroids for Mg II absorption, can be attributed to resonant scattering. We will return to this point in Section 5.6.1.

The strengths of absorption lines are dictated by their oscillator strengths ($f$-values), which are listed in Table 5.1. In the optically thin, unsaturated limit, the ratio of $W_0$ for two absorption lines should be the ratio of their $f$-values. As the gas becomes optically thick and the absorption lines become saturated, the $W_0$ ratio becomes one. Line ratios which deviate from these theoretical limits indicate that there is something more than basic atomic physics affecting line profile strength. In the case of the Fe II absorption lines seen in this composite, the line ratios are in good agreement with theory. They are all about the same strength ($W_0 \sim 2\,\text{Å}$), indicating that these transitions are saturated. The Fe II lines with the lowest oscillator strengths (those at $\lambda = 2260$ and 2374 Å) are weaker than the other lines yet still within their theoretical rest equivalent width ratio limits. The Mg II doublet also appears saturated, as both lines have equivalent widths which are the same within the errors.

**Emission Features**

Of particular note is the prevalence of emission features. Fe II* fine-structure emission lines are not commonly seen in the spectra of high redshift star-forming galaxies. In our composite of all 96 galaxies, we record five Fe II* emission lines which are consistently at a negative velocity $2-3\times$ less than the average Fe II outflow velocity. Shapley et al. (2003) observe fine structure emission from Si II in their composite of $z \sim 3$ LBGs but are unable to conclusively determine its origin. They speculate that it could arise in the outflow because they were unable to reproduce the observed emission strength using CLOUDY photoionization modeling (Ferland et al. 1998), as would be possible if the Si II emission originated in H II regions. Most recently, Rubin et al. (2011) observe Fe II* emission in the spectrum of a starburst galaxy at $z = 0.69$. They observe all of the Fe II* emission transitions seen in our composite and propose that it results from the
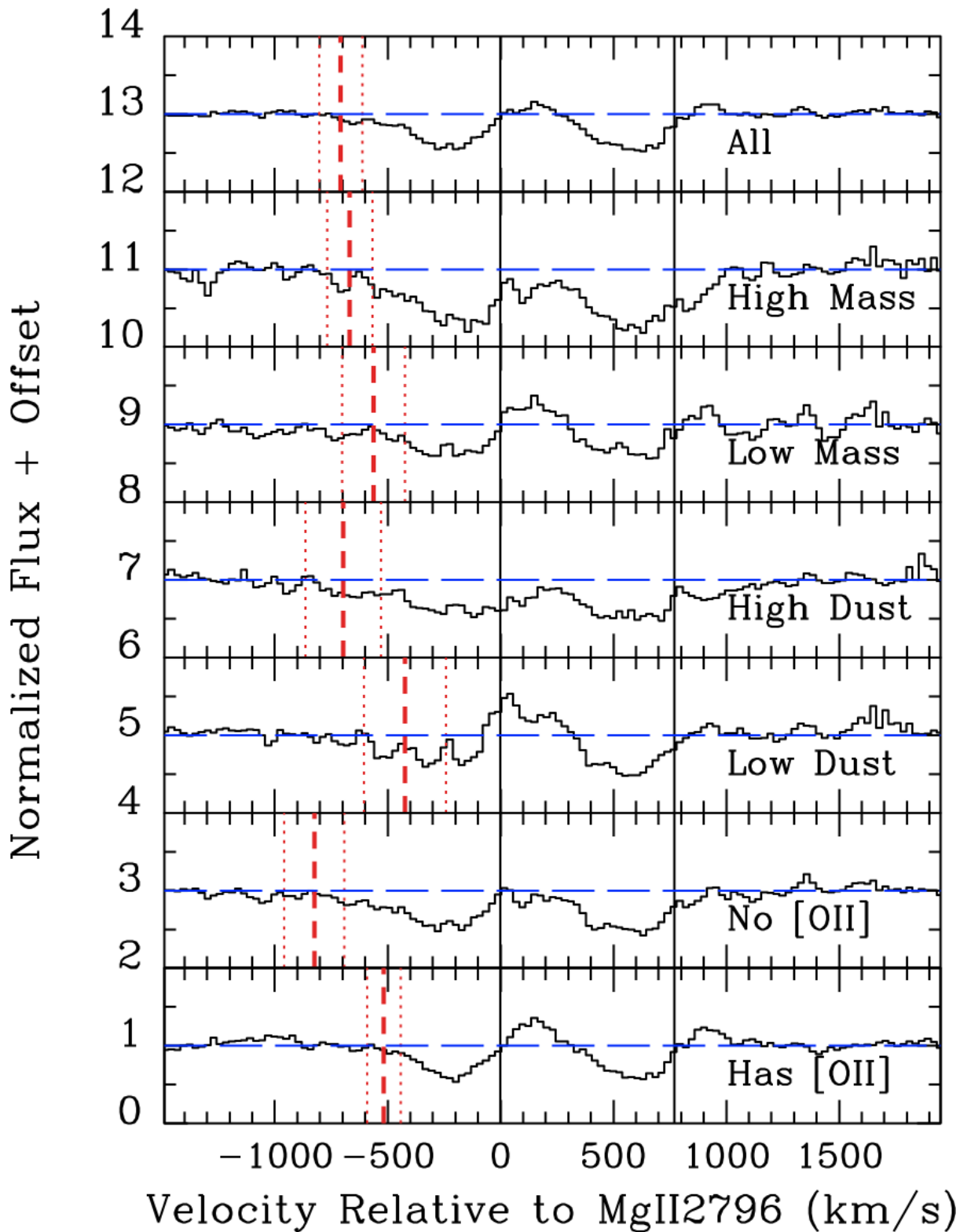
Figure 5.6 The Mg II region for each composite spectrum listed in Table 5.2 and Table 5.3. Red dashed lines indicate the terminal velocity of the Mg II $\lambda2796$ absorption profile and dotted red lines indicate the $1\sigma$ error on the terminal velocity.

outflow. Prochaska et al. (2011) also propose that Fe II* fine-structure emission results from photon scattering within the outflow. We will return to the origin of this emission in a later section.

Also present is weak yet statistically significant Mg II emission from both the 2796 Å and 2803 Å transitions. The positive velocity of these features is also likely to result from resonant scattering, a theory that will be explored in Section 5.6.1. Finally, a substantial emission feature from nebular C II] is seen at a relatively small positive velocity. This feature can be seen in a composite of low metallicity ($12 + \log (O/H) < 8.2$) local starburst and star-forming galaxies (Leitherer et al. 2011) but it is not apparent in their composite of high metallicity ($12 + \log (O/H) > 8.7$) galaxies. The physical conditions and galaxy properties giving rise to the visibility and morphology of these emission lines are not well understood (Weiner et al. 2009; Prochaska et al. 2011; Rubin et al. 2011). Therefore, it is of great importance to explore these features over a wide range of galaxy properties. This work is the first large-scale study of Fe II fine structure emission and Mg II emission.

## SED Fit Parameters

The remainder of Section 5.4 seeks to probe the interplay between emergent line profiles and galaxy properties. Spectral energy distribution (SED) modeling yielded stellar mass, reddening, age, and star formation rate information for 51 galaxies in our sample (see Figure 5.2). We were unable to complete SED fits for all of the 96 galaxies in our main sample because not all galaxies have been imaged at red wavelengths (such as the K band or IRAC 3.6 or 4.5 micron imaging) and such imaging data are necessary for completing SED fits. We do not believe that the galaxies without SED fits are systematically different from those with SED fits; the galaxies without SED fits simply were not imaged at long wavelengths but we expect that they would be detected if imaging similar to that conducted for the galaxies with SED fits were executed.

The range in galaxy properties obtained through SED fitting is shown using histograms in Figure 5.7. We refer the reader to Shapley et al. (2005) for details of the SED fitting but we highlight a few essential points here. Continuous star formation and a Chabrier initial mass function (IMF) were assumed. There are considerable degeneracies between the fit parameters. Taking this into account, the most reliable fit parameter is the stellar mass because the degeneracies between age and reddening effectively cancel out when determining this parameter. We divide our sample of 51 galaxies into thirds by mass and reddening to assess the effect these properties have on the emergent line profiles. We apply these insights to understanding the differences between the [O II] galaxies and the absorption galaxies.

The SED parameters for each composite are given in Table 5.4. Unfortunately, SED fits were not available for all 96 galaxies. Therefore, the values listed in Table 5.4 for the composites of all galaxies, those with [O II] emission, and those without [O II] emission are for only the subset of galaxies which have SED fits. While these values are made from incomplete information, they provide an essential context for interpreting the composite spectra in relation to each other and the range of galaxy properties.
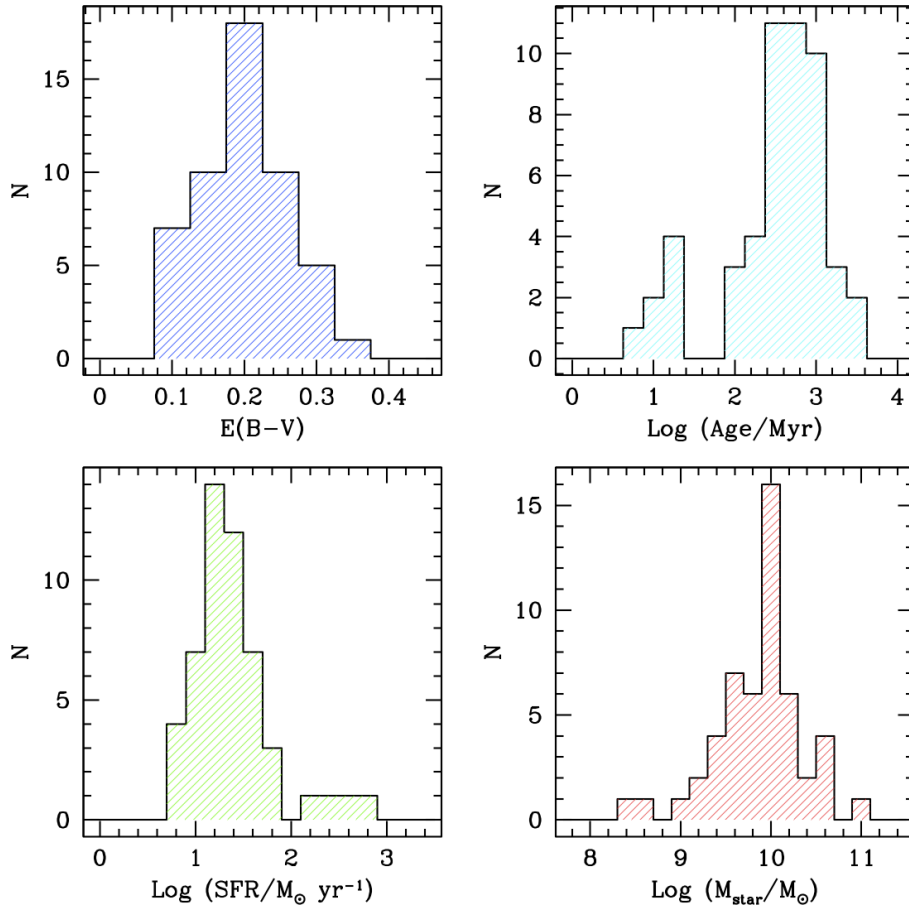
Figure 5.7 These four panels show the distribution of SED fit parameters (clockwise from top left: reddening, age, stellar mass, and star formation rate) for 51 galaxies in our sample which had imaging sufficient for SED fitting. A Chabrier IMF and continuous star formation were assumed.

Table 5.4 MEAN SED FIT PARAMETERS FOR COMPOSITE SPECTRA

| | $N$ | $M_*$ ($10^{10}\,M_\odot$) | $E(B-V)$ | $SFR$ ($M_\odot\mathrm{yr}^{-1}$) | Age (Myr) | $<z>$ |
|---|---|---|---|---|---|---|
| All Galaxies[a] | 51 | $1.28 \pm 1.7$ | $0.199 \pm 0.065$ | $47 \pm 106$ | $660 \pm 770$ | $1.739 \pm 0.230$ |
| With [O II][b] | 19 | $0.74 \pm 0.54$ | $0.214 \pm 0.048$ | $23 \pm 28$ | $496 \pm 363$ | $1.522 \pm 0.164$ |
| Without [O II][c] | 32 | $1.32 \pm 1.86$ | $0.195 \pm 0.068$ | $68 \pm 141$ | $716 \pm 787$ | $1.868 \pm 0.154$ |
| High Mass | 17 | $2.57 \pm 2.14$ | $0.201 \pm 0.052$ | $26 \pm 15$ | $1176 \pm 862$ | $1.868 \pm 0.212$ |
| Low Mass | 17 | $0.33 \pm 0.17$ | $0.202 \pm 0.077$ | $70 \pm 133$ | $216 \pm 232$ | $1.694 \pm 0.216$ |
| High Dust | 17 | $1.82 \pm 2.40$ | $0.268 \pm 0.038$ | $114 \pm 184$ | $612 \pm 831$ | $1.746 \pm 0.153$ |
| Low Dust | 17 | $0.87 \pm 0.45$ | $0.134 \pm 0.023$ | $16 \pm 9$ | $688 \pm 526$ | $1.804 \pm 0.207$ |

*Notes* Reported errors are the standard deviation ($\sigma$).
[a] The composite is made of 96 galaxies with $<z> = 1.597 \pm 0.288$. SED fit parameters are available for a subset of these galaxies.
[b] The composite is made of 52 galaxies with $<z> = 1.397 \pm 0.20$. SED fit parameters are available for a subset of these galaxies.
[c] The composite is made of 44 galaxies with $<z> = 1.836 \pm 0.160$. SED fit parameters are available for a subset of these galaxies.

### 5.4.3 Composites by stellar mass

Stellar mass is the most reliable galaxy property to come from SED fitting (Shapley et al. 2005). We divided our sample of 51 galaxies into three bins by galaxy mass. There were 17 galaxies in each bin. The highest mass bin has an average stellar mass of $M_* = (2.57 \pm 2.14) \times 10^{10} M_\odot$ and the lowest mass bin has an average stellar mass of $M_* = (0.33 \pm 0.17) \times 10^{10} M_\odot$. Considering the number of objects with SED fits and the range of stellar masses probed by these objects, the sample division we have adopted affords us a good balance between signal-to-noise ratio in the composite spectra and dynamic range. The two composite spectra by stellar mass are shown together in Figure 5.8.

A qualitative inspection of Figure 5.8 is instructive for interpreting the measurements in Tables 5.2 and 5.3. As we saw for the composite of all galaxies, it is immediately clear that all of the Fe II absorption as well as the Mg II absorption profiles are blueshifted with respect to the rest frame (which is indicated by the blue dashed line in the Figure for each transition). The low mass stack appears to have stronger emission in both Fe II* and Mg II; indeed, the high mass composite completely lacks any discernible Mg II emission. The Fe II emission in either spectrum is not strikingly offset from the rest frame but the Mg II emission in the low mass composite has a distinct positive velocity.

#### Mg II Features

The Mg II region for these two composites, shown in Figures 5.8 and 5.6, differ in their absorption and emission properties. The low mass stack has Mg II $\lambda 2796$ emission that is $\sim 3.6 \times$ stronger and MgII $\lambda 2803$ emission that is $\sim 1.6 \times$ stronger than such emission in the composite of all galaxies. This trend of decreasing Mg II emission strength with increasing stellar mass is consistent with other studies at slightly lower redshifts $1 < z < 1.4$ (Weiner et al. 2009; Rubin et al. 2010). In contrast to these studies, the average redshift of our two mass composites is higher: $< z >= 1.694$ and $< z >= 1.868$ for the low and high mass composites, respectively.

The distribution of gas in a galaxy depends upon its mass. An inspection of Figure 5.6 shows that there is substantial absorption at positive velocity with respect to systemic for MgII $\lambda 2803$ (i.e. to the right of the rightmost vertical black line in the Figure) for the high mass sample. Weiner et al. (2009) interpret this absorption as gas at the systemic velocity. There appears to be no gas at the systemic velocity for the low mass composite. This trend is consistent with that seen by Weiner et al. and Rubin et al. (2010).

#### Fe II Absorption

A consideration of the Fe II features can provide some insight into the processes at work in these galaxies. The Fe II $\lambda 2382$ feature should be the strongest Fe II absorption line by a factor of a few to over a hundred, based on $f$-value ratios. However, in both the low and high mass composites, its rest equivalent width is actually lower than nearly every other Fe II absorption line, taking into account measurement uncertainty. Deviations from the theoretical limits on line ratios have been interpreted as reflecting the covering fraction of outflowing gas in front of the continuum-producing stars (Quider et al. 2008, Martin & Bouché 2009). However, Prochaska et al. (2011) suggest that in the case of Fe II,
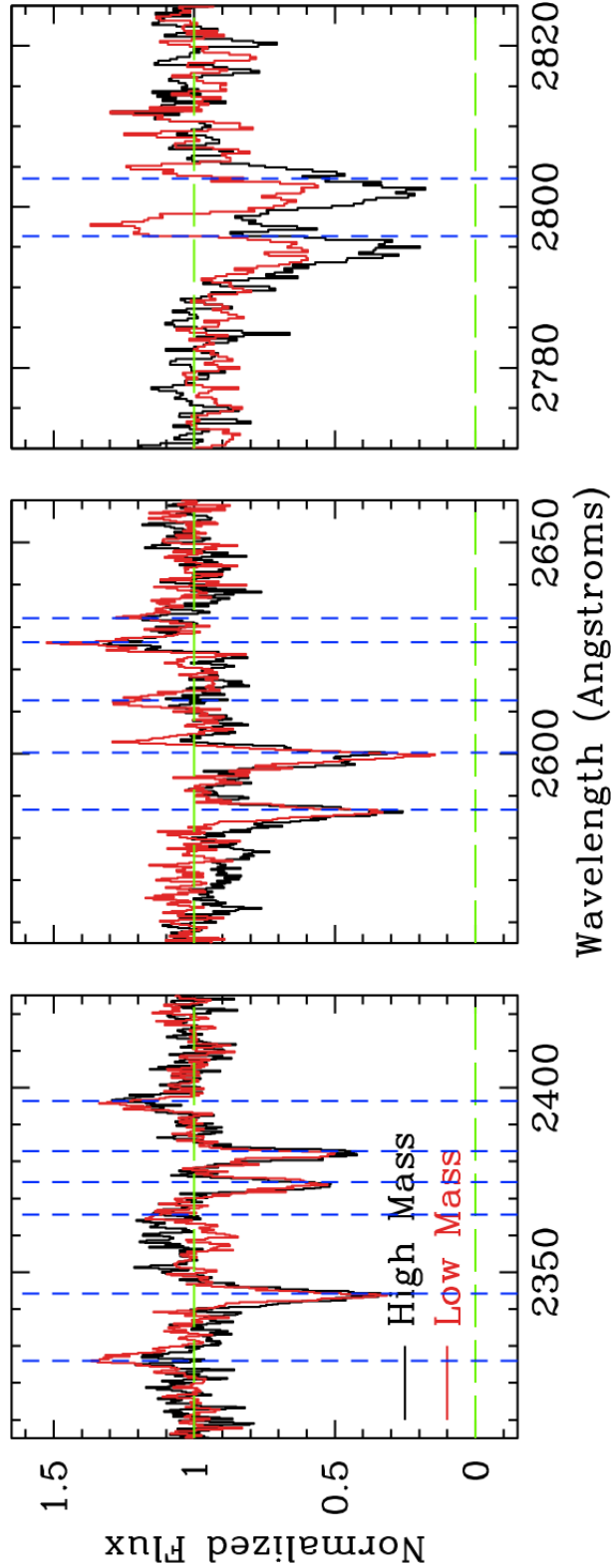
Figure 5.8 Both of the composites shown here are a mean stack of 17 galaxies with $3\sigma$ rejection. The composite spectrum of high mass galaxies is shown in black and has an average stellar mass of $M_* = (2.57 \pm 2.14) \times 10^{10} M_\odot$. The low mass composite galaxy spectrum is in red has an average stellar mass of $M_* = (0.33 \pm 0.17) \times 10^{10} M_\odot$. The first two panels show the Fe II spectral regions while the rightmost panel shows the Mg II feature. Blue dashed lines show the rest wavelength for each feature.

resonant and fine structure emission lines are present near the systemic velocity of the Fe II absorption lines which can "fill-in" the absorption. The observational consequences of this are that absorption line equivalent widths can be reduced by up to 50% and absorption line centroids can be shifted blueward by tens of km s$^{-1}$.

The Fe II absorption lines in the high mass composite have line ratios which are consistent with emission filling. As with the composite of all galaxies, the Fe II transitions at 2344Å, 2586Å, and 2600Å are saturated while the two weakest transitions are not. Therefore, we expect Fe II $\lambda$2382 to be as strong as the saturated transitions but its equivalent width only 68% that of the average equivalent width for the three saturated transitions. The velocity offsets for the Fe II lines are less suggestive of emission filling. The velocity offset for Fe II $\lambda$2382 is consistent with the outflow velocity of the other Fe II transitions. The models of Prochaska et al. (2011) predict that the velocity centroid of emission filled absorption lines should be blueshifted.

A stronger case for emission filling of Fe II absorption can be made from the low mass composite spectrum. In this case, the Fe II absorption lines are clearly not saturated. $W_{\mathrm{FeII,2382}}/W_{\mathrm{FeII,2374}} = 10$ in the unsaturated limit. Despite this, Fe II $\lambda$2382 has an equivalent width which is consistent with that of Fe II $\lambda$2374. Additional evidence can be seen in the velocity offsets for the Fe II transitions. The absorption feature that is least affected by Fe II emission is Fe II $\lambda$2374 (see §5.1 and Martin et al. 2011, in prep.) so its velocity centroid should be most representative of the wind outflow velocity. The velocity centroid for Fe II $\lambda$2382 is $\sim 60$ km s$^{-1}$ faster than that of Fe II $\lambda$2374, a value that is consistent with the predictions of emission filling. Interestingly, Fe II $\lambda$2600 also has a centroid velocity that is similarly faster than the outflow as traced by Fe II $\lambda$2374. This suggests that Fe II $\lambda$2600 may also be affected by emission filling, even though the equivalent width of this feature is not diminished to any discernible degree.

Emission filling has implications for interpreting the Fe II absorption lines and therefore the study of winds from these galaxies. This is the first time a strong case for emission filling has been made for high redshift star-forming galaxies.

### 5.4.4  Composites by dust reddening

Dust is expected to be found in cool gas clouds with metals. A consideration of the influence of dust on the emergent Mg II profile is motivated by studies of Ly$\alpha$, another strong resonance transition. The absorption of photons by dust has been shown in models to affect the emergent line profile for the Ly$\alpha$ feature in star-forming galaxies (Verhamme et al. 2006). Resonant photons have a much longer path length for escaping a galaxy compared to non-resonant photons and dust further adds to the attenuation. Dust has the observational consequence of suppressing Ly$\alpha$ emission. In their sample of $z \sim 3$ LBGs, Shapley et al. (2003) found that the quartile of galaxies with the strongest Ly$\alpha$ emission also had an average $E(B-V)$ that was only half that of the quartile with the strongest Ly$\alpha$ absorption and no emission. Prochaska et al. (2011) have modeled the effect of dust on the emergent Mg II absorption and emission profiles. Increasing the amount of dust in the outflow has the effect, as with Ly$\alpha$, of suppressing emission. In most scenarios they consider, dust does not substantially change the Mg II absorption depth; only in the dustiest scenario does Mg II absorption increase compared to the fiducial, dust-free model.

Stacks of the 17 galaxies with the highest and lowest $E(B-V)$ values—0.268 and 0.134 on average, respectively—are shown in Figure 5.9. Most apparently, they differ in their Mg II emission properties. The low dust composite has the strongest MgII $\lambda 2796$ of all the stacked spectra while the high dust stack has no Mg II emission. The absorption depth of the Mg II profiles is nearly identical for the two stacks. These two observations agree well with the predictions of Prochaska et al. (2011).

Unfortunately, these two samples do not have the same stellar mass. As discussed in Section 5.4.3, stellar mass influences the emergent Mg II profile so some consideration of mass trends within these dust-selected composites is prudent. Note that the spectra stacks by stellar mass used in the previous section have nearly identical $E(B-V)$ values. Therefore, the trends seen in those mass-selected stacks are most likely representative of trends with mass rather than trends with reddening. The low dust galaxies have an average stellar mass which is only about half that of the high dust sample. It has long been known that more massive galaxies are dustier so it is not surprising that the high dust composite has a higher mass than the low dust stack.

An inspection of Figure 5.6 is instructive for disentangling the mass trends that must also be convolved with dust trends in our stacks of dust-selected galaxies. The high (low) dust Mg II profile follows the trend of the high (low) mass profile with regards to presence of gas at the systemic velocity and the terminal velocity of the outflow.

An interpretation of the Fe II transitions is less clear-cut. The models of Prochaska et al. (2011) predict that the presence of dust will suppress the red side of the Fe II* emission lines. This has the effect of blueshifting the centroid of the Fe II* emission lines. The predicted shifts are $\sim -50\,\mathrm{km\,s^{-1}}$ which is approximately the scatter in the Fe II* emission line centers for our dust composites so we are unable to test this prediction. Turning to the Fe II absorption lines, we can compare the line ratios and the velocity offsets for these transitions to see if they conform to the trends seen with galaxy mass. The rest equivalent width measurements for both dust composites suggest line filling. In contrast to the trend found with mass, the low dust composite seems to be less afflicted by line-filling than the high dust composite when considering $W_{\mathrm{FeII,2382}}$ and its ratio with other transitions. However, the 2382 Å absorption is considerably blueshifted for the low dust sample, nearly $3\times$ the velocity of the same transition in the high dust sample. This suggests that there is significant line-filling in the low dust sample, which would be more in line with the trends seen in the mass-selected stacks.

In summary, the dust-selected galaxy stacks illustrate the difficulty inherent in disentangling the influence of a particular galactic property on the emergent line profiles for Mg II and Fe II.

## 5.4.5  Composites by presence of [O II] emission

An inspection of Figure 5.3 and Figure 5.4 immediately reveals line strength and velocity offset differences between the spectroscopic features in the [O II] galaxy sample and the absorption galaxy sample. Every star-forming galaxy should exhibit [O II] emission. In principle, the [O II] galaxy sample should have properties very similar to the non-[O II] galaxy sample because the only reason we did not detect [O II] in those galaxies is their higher redshift and/or their low S/N in the extreme red end of the spectrum. In light of this, the differences between these two samples are curious and warrant investigation.
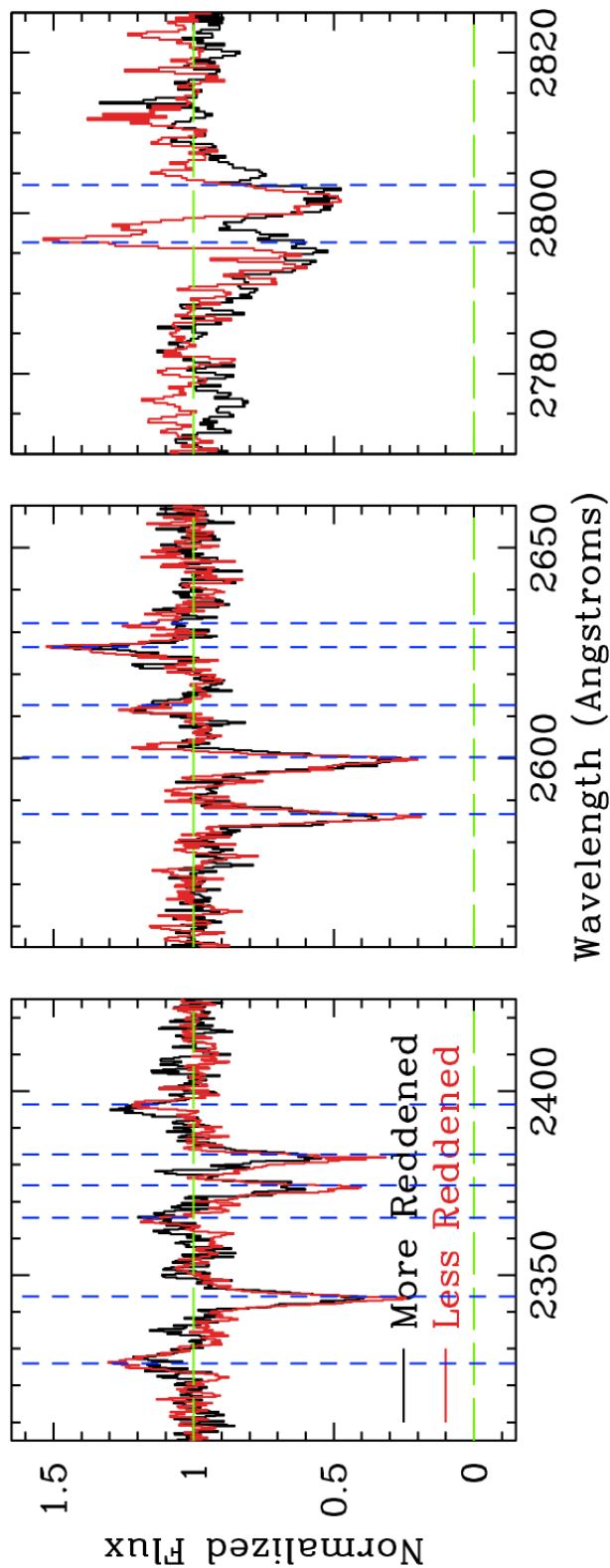
Figure 5.9 Both of the composites shown here are a mean stack of 17 galaxies with $3\sigma$ rejection. The high reddening composite galaxy spectrum is shown in black while the low reddening composite galaxy spectrum is in red. The first two panels show the Fe II spectral regions while the rightmost panel shows the Mg II feature. Blue dashed lines show the rest wavelength for each feature.

Exploring the influence of stellar mass and dust reddening on the emergent line profiles in the previous two sections informs our interpretation of these two composite spectra. Of the 51 galaxies with SED fits, 19 galaxies have [O II] emission while 32 do not. Note that the [O II]-selected composites were composed of more galaxies than just those with SED fits so the galactic parameters listed in Table 5.4 for these two samples are not reflective of all galaxies in each composite. The galaxies without [O II] emission are nearly twice as massive as those with detected [O II]. In contrast to the trends seen with mass and reddening, the [O II] emission galaxies are more dusty on average than the non-[O II] galaxies, but we note that these values are consistent with each other within the scatter.

The trends in the Mg II features resemble those seen in the mass-selected stacks. Perhaps this is not surprising, though, because 7 of the least massive galaxies are [O II] emission galaxies while only 3 of them are among the most massive. Therefore, we expect the [O II]-selected composites to reflect the trends found in the mass-selected composites. Galaxies with [O II] emission have strong Mg II emission and a lower terminal velocity while those without [O II] have no Mg II emission and a higher terminal velocity, as expected.

The trends in Fe II absorption strength do not resemble those of either the mass-selected or the dust-selected samples. The [O II] galaxies, as the less massive and dustier galaxies, should be most affected by line-filling. However, their Fe II absorption line rest equivalent widths do not show evidence of line-filling. In contrast to this, the more massive and less reddened non-[O II] galaxies have Fe II absorption line strengths which are consistent with line-filing. The velocity offsets for the Fe II absorption transitions are suggestive of line-filling for each composite.

In addition to the complication posed by different masses and reddening, the influence of redshift on the emergent line profiles also needs to be considered. The [O II] emission galaxies have an average redshift of $< z >= 1.397$ while the non-[O II] sample has $< z >= 1.836$. The redshift differences between the two samples may explain why the [O II] galaxies are less massive. Galaxies of the same luminosity but located at the average redshift of the two samples will have apparent magnitudes that differ by 0.75 mag, with the lower redshift galaxies appearing brighter. Less massive galaxies tend to be less luminous so we could simply be missing the fainter lower mass galaxies at higher redshifts while simultaneously identifying more lower mass galaxies at lower redshifts, where they will appear brighter. Alternatively, these two samples could be reflective of evolutionary trends for galaxy outflow and emission properties with redshift.

## 5.5 Individual Galaxies

One advantage of our dataset is that numerous of our spectra are of sufficient quality for measuring absorption and emission features in individual galaxies. This is not often the case for this type of study so making measurements from individual objects is a good check on the results derived from stacked spectra. Measuring features from individual galaxies also allows us to probe the range of properties exhibited by the objects in our sample.

Here we consider the velocity offsets and rest equivalent widths for individual galaxies. Unlike measurements of the composite spectra, these were made by fitting a single

Gaussian profile to each absorption and emission feature. While some of the profiles in the composite spectra exhibit asymmetry, and this is particularly true of the Mg II features, the low signal-to-noise ratio of the individual spectra causes most features in most spectra to be well fit by a Gaussian profile. The velocities we measure refer to the center and the rest equivalent widths refer to the area of the fits.

### 5.5.1 Velocity of outflows

Recall from Section 5.3 that we use two methods for determining the systemic redshift of our sample. The preferred method is measuring the systemic redshift from the [O II] emission features. When [O II] is not available we use the absorption line redshift and eq. (5.1) to calculate the systemic redshift. The second method yields systemic redshifts on average (Steidel et al. 2010) but on an individual basis it does not yield systemic redshifts as accurate as those obtained from [O II] emission. Therefore, we explore the issue of velocity offsets using only the sample of 52 galaxies with systemic redshifts determined from [O II] emission.

The velocity offsets between Fe II absorption lines can indicate emission filling of an Fe II absorption trough by Fe II* emission. The transition least affected by emission filling is Fe II $\lambda$2374 so its velocity should most accurately portray the galaxy's outflow velocity (Martin et al. 2011, in prep.). In Figure 5.10 we compare the velocity of absorption due to Fe II $\lambda$2382, Fe II $\lambda$2600, Mg II $\lambda$2796 and emission due to Fe II $\lambda$2326 to the velocity of Fe II $\lambda$2374. We only include points with $\sigma < 100\,\mathrm{km\,s^{-1}}$, as indicated by the error bars on each point.

An inspection of this plot confirms the overall absorption velocity trends seen in the composite spectra. Nearly all of the absorption lines have velocity offsets greater than Fe II $\lambda$2374. These are the locus of points lying to the right of the dashed line in the Figure. Among the Fe II absorption lines, Fe II $\lambda$2382 is consistently offset to a greater degree than Fe II $\lambda$2600 from the velocity of Fe II $\lambda$2374. On average, Fe II $\lambda$2382 is blueshifted by 53 km s$^{-1}$ and Fe II $\lambda$2600 is blueshifted by 12 km s$^{-1}$ with respect to Fe II $\lambda$2374. This is suggestive of line-filling shifting blueward the center of these absorption lines. Indeed, with the exception of one very uncertain point, $v_{2374} < 200\,\mathrm{km\,s^{-1}}$ but velocities out to 300 km s$^{-1}$ are measured for the 2382 Å transition.

In contrast to the composites, Mg II $\lambda$2796 does not seem to have a velocity offset that is consistently greater than the other absorption lines. One explanation for this is that the velocities measured from the composites are centroid velocities while the velocities in this section are for the center of a Gaussian fit to the feature. The Mg II absorption profile is the profile most likely to exhibit asymmetric line structure. If the Gaussian is fit to the gas of greatest optical depth, it will measure a velocity lower than the centroid velocity for asymmetric Mg II profiles. As can be seen in the stacked spectra, the Fe II absorption and emission profiles are much less asymmetric than Mg II so the center of a single Gaussian fit to one of the Fe II features will not be much different from the centroid velocity of the line.

Nearly all of the Fe II $\lambda$2326 emission has a velocity that is less than that of Fe II $\lambda$2374, with their values lying to the left of the dashed line. Over half of the emission line velocities are at $v \geq 0$ with the balance of those points consistent with $v = 0$. Rubin et al. (2011) studied the same Fe II* emission line from a starburst galaxy at $z = 0.69$
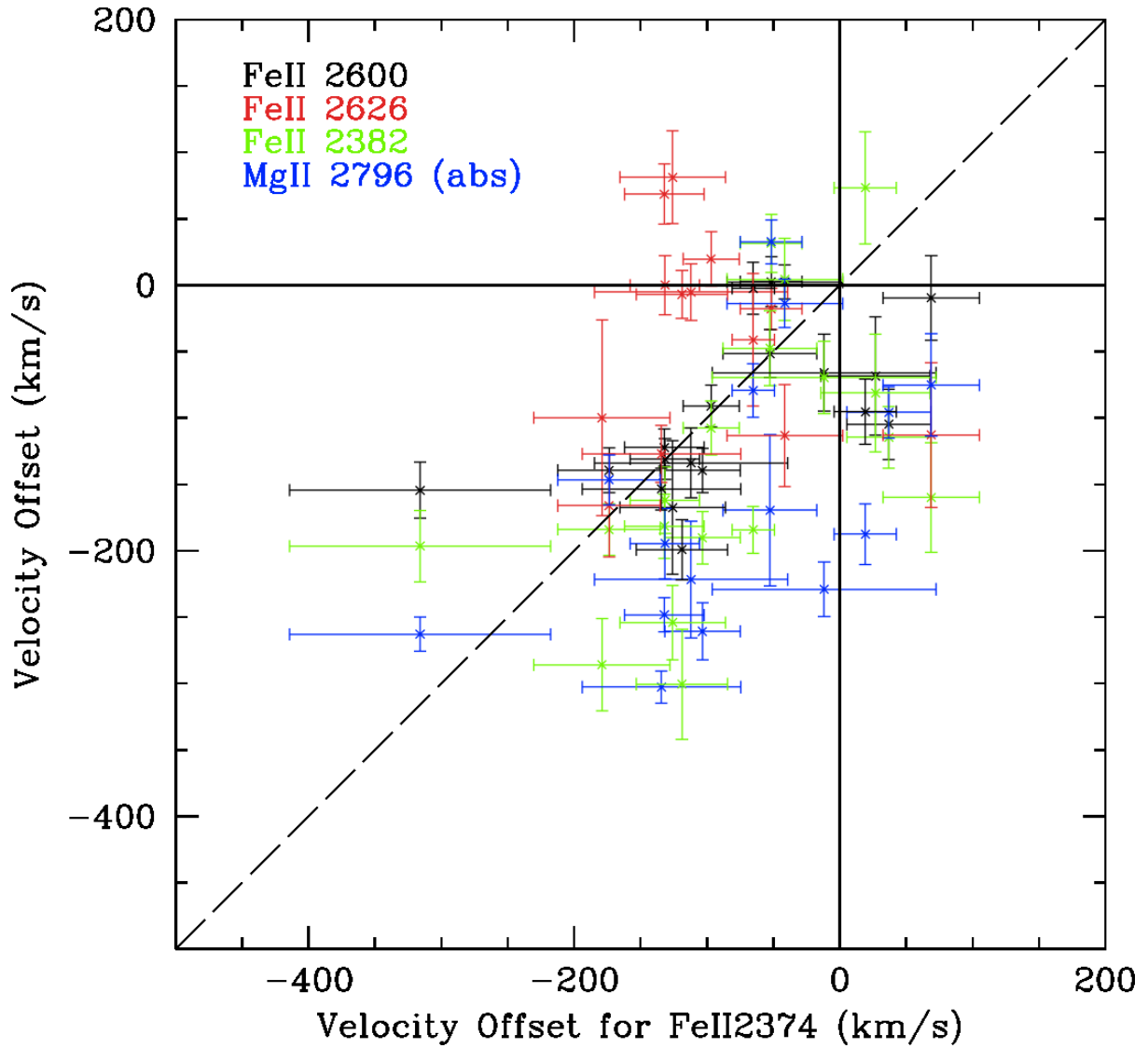
Figure 5.10 Velocity offsets from systemic for individual galaxies. Only galaxies with [O II] redshifts and $\sigma_{vel} < 100\,\mathrm{km\,s^{-1}}$ are included. The dashed line denotes when the outflow velocities of Fe II $\lambda2374$ and the other transitions (identifiable by the color-coded key in the upper left corner) are the same. $1\sigma$ error bars are shown.

and found its velocity center to be $v_{cen} = -28\,\mathrm{km\,s^{-1}}$, consistent with numerous of the measurements for individual galaxies shown in Figure 5.10 as well as the velocity offsets measured for this emission line in the composite spectra.

## 5.5.2 Fe II absorption line strength

Precision in the systemic redshift of a galaxy is less important when considering the rest equivalent width of a feature. The primary concern is that the features are correctly identified, which is the case for galaxies whose redshifts were determined using both methods. Therefore, we include all 96 galaxies in our consideration of the feature rest equivalent widths. We focus on the Fe II $\lambda\lambda$2374,2382 transitions for two reasons. Their oscillator strengths differ by a factor of 10 so their line ratio is a clear-cut test for line-filling and saturation. Secondly, Fe II $\lambda$2374 is the transition least affected by line-filling and Fe II $\lambda$2382 is the feature expected to be most affected by line-filling (see §5.1 and Martin et al. 2011, in prep.). Comparing these two features maximizes our ability to detect the signature of line-filling.

Figure 5.11 shows the rest equivalent width measurements for all galaxies where it is measured for Fe II $\lambda\lambda$2374,2382 at $> 2\sigma$ significance. The theoretical limits for the ratio of line strengths for these two features are shown as well. The oscillator strengths of these two transitions put the theoretical bounds on their relative strengths such that $1 \leq W_{2382}/W_{2374} \leq 10$.

The majority of the galaxies shown here have line ratios which fall within the theoretical limits, within the error on these measurements. Most systems are situated near the saturated limit of a unity line ratio. This is consistent with the Fe II line saturation seen in numerous of the composite spectra, including the composite of all galaxies.

We identify a handful of galaxies with the statistically significant line ratio $W_{2382}/W_{2374} < 1$, putting them beyond the regime of explanation solely looking at the absorption transitions themselves. These galaxies are candidates for emission filling. The four candidates identified with colored dots in Figure 5.11 are shown in Figure 5.12. These spectra represent a range of line strengths and spectra quality. They exhibit a range of Mg II morphology, from strong emission with little absorption to strong absorption with no emission, as well as a cross-section of Fe II* emission strengths.

Two of the galaxies in Figure 5.12 have SED fits. The galaxy Q2343-BX111 ($z = 1.92296$) is the most massive galaxy in our sample with $M_* = 17.5 \times 10^{10} M_\odot$. It is also one of the oldest galaxies with an age of $3250\,\mathrm{Myr}$. Its reddening of $E(B - V) = 0.240$ also puts it in the top third of galaxies for reddening. The least remarkable parameter for this galaxy is its star formation rate of SFR=$54\,M_\odot\,\mathrm{yr^{-1}}$ which is a value typical of our sample. An inspection of this spectrum shows that it qualitatively adheres to the high mass composite more so than the high dust composite, particularly in its lack of Fe II* emission and depth of Mg II absorption profiles.

The galaxy Q1623-BM109 ($z = 1.54996$) also has SED fit parameters. Its mass is in the middle third of our sample ($M_* = 1.6 \times 10^{10} M_\odot$) but it is in the upper third for reddening with $E(B - V) = 0.235$. Its age and star formation rate are typical of our sample: $508\,\mathrm{Myr}$ and $31\,M_\odot\,\mathrm{yr^{-1}}$, respectively. This spectrum resembles that of the high dust composite in that it has weak Fe II* emission, Mg II absorption lines which do not extend to zero flux, and no Mg II emission.
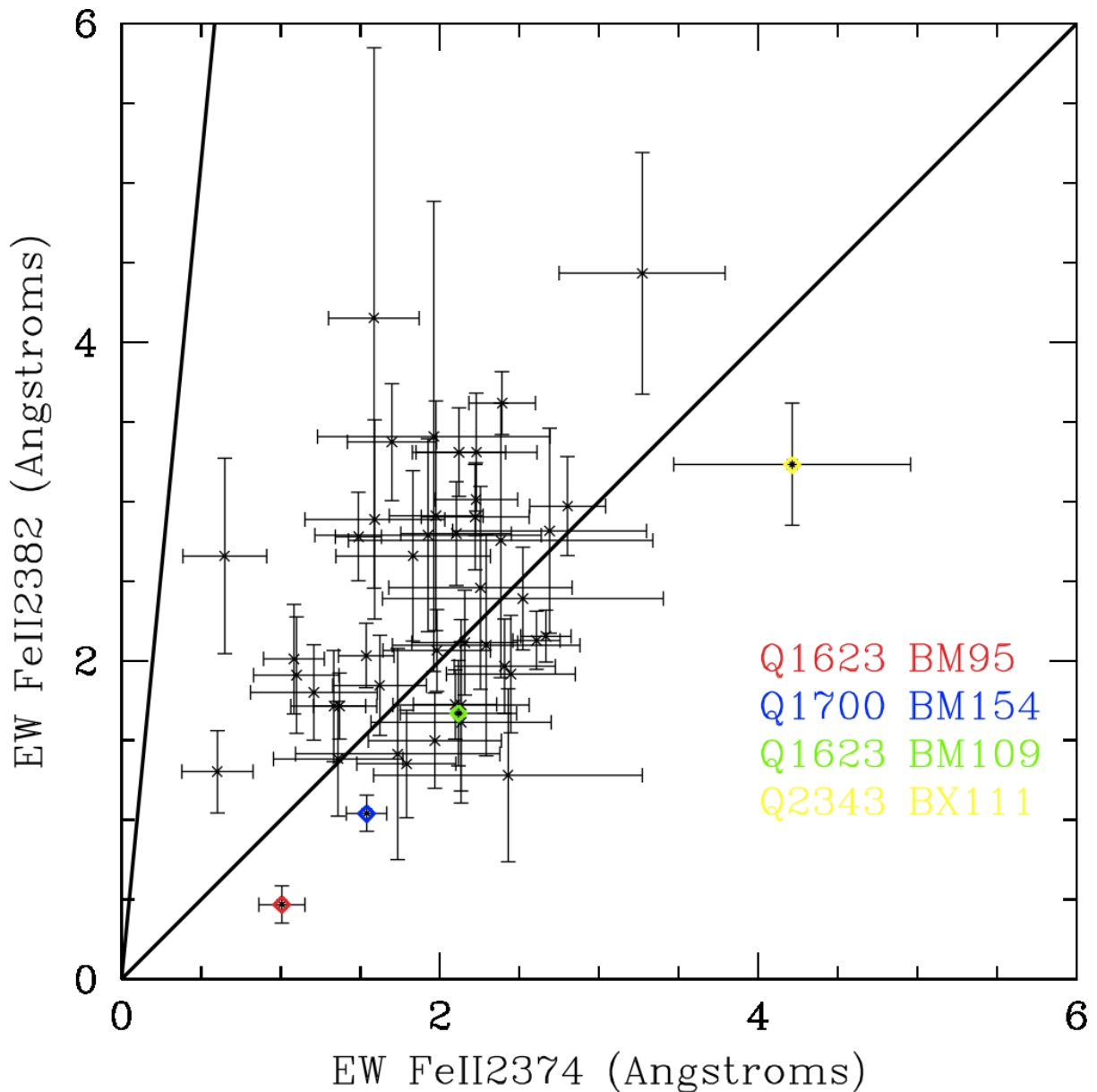
Figure 5.11 Rest equivalent width measurements for the Fe II λ2374 and Fe II λ2382 absorption lines in individual galaxies. All galaxies with measurements $> 2\sigma$ significance are shown with $1\sigma$ error bars. These values are plotted against the theoretically expected ratio for these two absorption lines. Galaxies whose ratio falls below the wedge defined by these theoretical limits are candidates for line-filling. Colored dots represent the four galaxies shown in Figure 5.12, which are named in the color-coded key in the lower right corner.
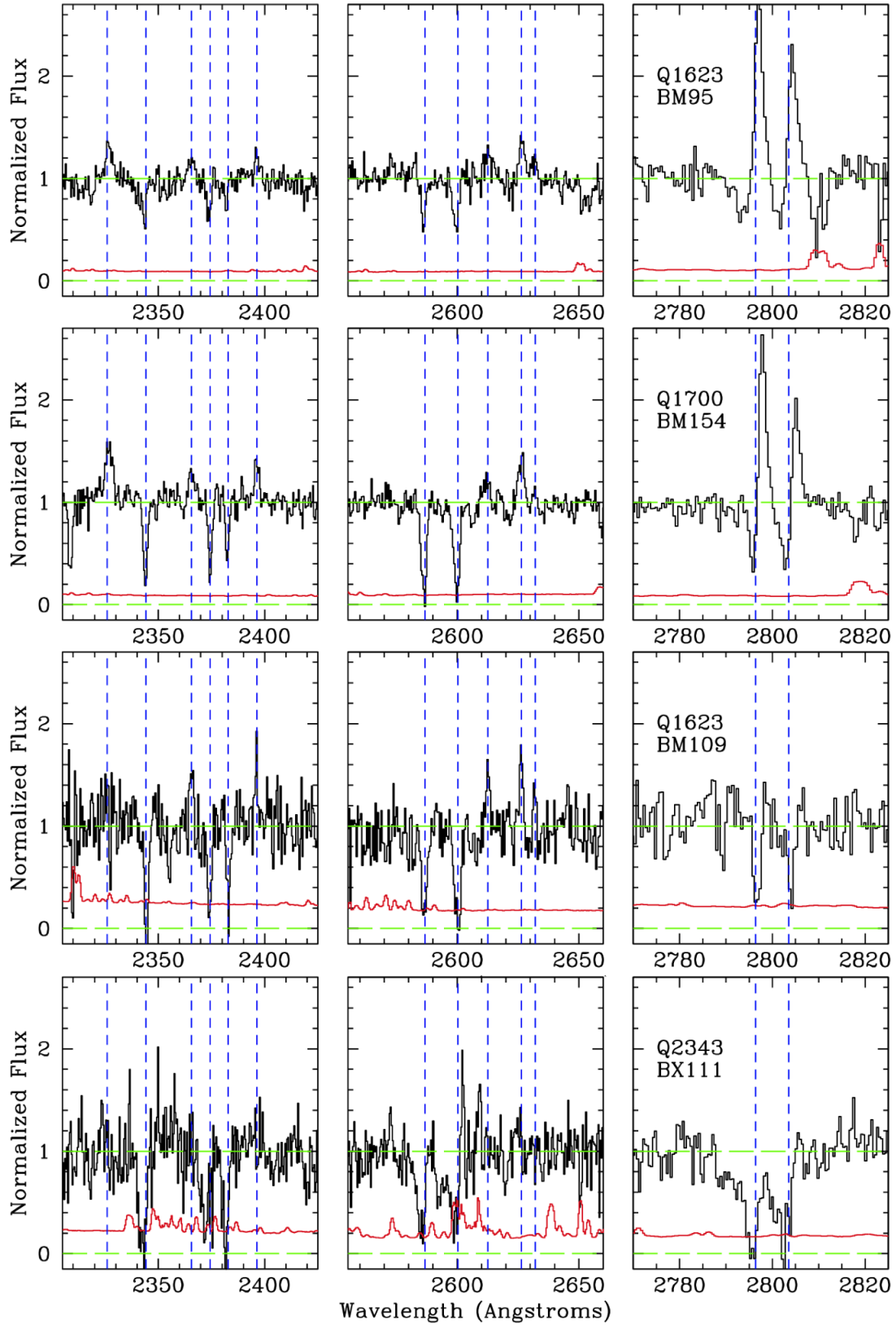
Figure 5.12 Spectra of the four galaxies highlighted in Figure 5.11 as candidates for emission filling of the Fe II λ2382 absorption line. The galaxy spectrum is shown in black and the 1σ error spectrum is in red. Their redshifts are, from top to bottom, $z = 1.57806, 1.54996, 1.57025$, and $1.92296$.

While the remaining two galaxies, Q1623-BM95 ($z = 1.57806$) and Q1700-BM154 ($z = 1.54996$), do not have SED fit parameters, a comparison to our composite spectra is instructive for gauging their mass and dust properties. These two galaxies have very strong Mg II emission. Indeed, their Mg II emission has nearly twice the peak flux of the Mg II emission seen in any of the composites. Based on their Mg II emission alone, it unlikely that they are among the high mass, high dust galaxies. It would be worthwhile to follow up on these strong Mg II emitters to see how their properties compare to those of the galaxies in the composites.

We have looked for evidence of line-filling in other line ratios. These results are inconclusive. There are two reasons for this. Firstly, the unsaturated limit in the line ratio between Fe II $\lambda2374$ and other transitions is not as large as it is for the 2382 Å transition. Secondly, the degree of line-filling for other transitions is less than that for the 2382 Å transition (Martin et al. 2011, in prep). Both of these factors translate into the signature of line-filling being hard to distinguish from the measurement uncertainty.

To summarize this section, we measure absorption line rest equivalent width ratios which are outside of the theoretically possible limit of $1 \leq W_{2382}/W_{2374} \leq 10$. One interpretation of this result is that Fe II fine structure emission is filling in the Fe II absorption at 2382 Å. The spectra of several galaxies with $W_{2382}/W_{2374} < 1$ at a statistically significant level are examined and found to have a range of Mg II absorption and emission strengths as well as different Fe II* emission strengths. These absorption and emission properties imply that these galaxies have a wide range of stellar mass and dust values. While this is only a small sample of galaxies, it appears as though emission filling is not ubiquitous in high redshift star-forming galaxies. However, when it does occur, it seems to affect galaxies across a wide range of masses and reddening.

## 5.6 Discussion

For the first time we present the spectra of 96 star-forming galaxies in the redshift range $1 < z < 2$ which exhibit a suite of Fe II and Mg II absorption and emission lines. We consider the implications of this study for the understanding of high redshift star-forming galaxies.

### 5.6.1 The origin of Fe II* and Mg II emission

In the previous sections we note the prevalence of Fe II* and Mg II emission in our galaxy sample. This work is unique in that it identifies, for the first time, a large sample of high redshift star-forming galaxies with Fe II* emission as well as Mg II emission.

Rubin et al. (2011) propose that photon scattering within the outflow is responsible for both Fe II* and Mg II emission. There are three possible origins for this emission: in recombination regions (Kinney et al. 1993), in active galactic nuclei (AGN; Vestergaard & Wilkes 2001), and in outflows (Rubin et al. 2011). Spatial information on the extent of the outflow coupled with velocity information for the outflow and nebular components of a galaxy can be used to identify the origin of the outflow. In the case of the galaxy investigated in Rubin et al. (2011), they find that emission is detected out to $\sim 7$ kpc which puts it beyond the range of AGN activity. They also find that the Fe II* emission

lines are systematically offset in velocity from the H II region emission lines so this makes it unlikely that they originate in the same spatial location. These authors interpret this evidence as indicating that the Fe II* and Mg II emission in this galaxy originate in the outflow.

We can apply the same line of investigation to our sample. The C II] emission in our sample originates in H II regions. Table 5.3 lists velocity centroid measurements for C II] and Fe II* emission in all of our composite spectra. While the velocities measured for each feature have uncertainties which make them roughly consistent with zero offset from systemic, the C II] is systematically positively offset while the Fe II* emission velocity is consistently negative. The absolute value of these sets of offsets are approximately the same. This finding mirrors that of Rubin et al. (2011); therefore, we, too, find a nebular origin of these emission lines to be unlikely. It is worthwhile to note that Shapley et al. (2003) also ruled out a nebular origin of the Si II* emission seen in their composite of $z \sim 3$ LBGs. They modeled this transition using the CLOUDY photoionization code and found that emission from H II regions is not strong enough to account for the emission seen in their composite.

While the spatial extent of the emission in our sample is not presented here, it is explored in Quider et al. (2011, in prep.) as a complement to this work. This study looks at 2D spectra to characterize the origin and extent of the emission reported in the present study. In several cases, including the galaxy Q1700-BM154 discussed in Section 5.5.2, we find that Mg II emission is offset from the continuum emission. This contrasts with the position of [O II] emission, which is centered on the continuum. This result makes it unlikely that the origin of this emission is either an AGN or H II regions.

If this emission originates in galaxy-wide outflows, it is not surprising that this emission is so prevalent in our composites and individual galaxies. All of our galaxy composites exhibit outflow signatures in absorption so we are confident that large-scale, high velocity outflows are common in rapidly star-forming galaxies at $1 < z < 2$.

The question that remains to be answered is why Fe II* emission has been rarely seen until now. This may simply be a case of the observational constraints of other studies. The only other studies of galaxies with comparable redshift range and galactic properties were not tuned to detecting Fe II* emission. The spectra in Weiner et al. (2009) do not cover the wavelength range of the Fe II* emission lines so their study could not investigate its prevalence in these galaxies. The spectra in Rubin et al. (2010) were only one hour exposures on Keck/ DEIMOS. In contrast, Table 2.1 shows that our spectra are $7.5 - 11\,\mathrm{h}$ exposures for similar galaxies. Their co-added spectra have a signal-to-noise ratio of $\sim 3 - 9$ pixel$^{-1}$ while about one-third of our individual galaxy spectra have S/N $> 3$ pixel$^{-1}$. An inspection of Tables 5.2 and 5.3 shows that the Fe II* emission lines we detect are nearly all weaker than the absorption lines by a factor of a few. Therefore, our sample is simply just more sensitive to weak emission features than that of Rubin et al. (2010).

It may also be the case that Fe II emission is more diffuse and extended than the light captured by a typical spectroscopic slit. Steidel et al. (2011) recently showed that Ly$\alpha$ emission extends out to many times a galaxy's radius as determined by the stellar continuum emission. Perhaps Fe II emission is present in all high redshift star-forming galaxies with outflows but it is just not adequately captured by a spectroscopic slit, typically about 1" wide. This still is a somewhat dissatisfying explanation for the lack

of Fe II in previous studies because there does not seem to be anything remarkable about our observing setup or source selection that would make us more able to detect faint extended emission.

Less clear-cut is why Mg II emission has been rarely seen in individual galaxy spectra. Weiner et al. (2009) identify Mg II emission in only 4% of their sample of $\sim 1400$ spectra at $z \sim 1.4$ and Rubin et al. (2010) identify only four individual galaxies with Mg II emission in their sample of 468 galaxies. In contrast, we detect Mg II emission at the $> 1.5\sigma$ level for $\sim 30\%$ of our 96 galaxies. This, too, could be a consequence of differing achieved signal-to-noise ratios among these studies. This is the most likely explanation because the composites by stellar mass in this work and in these other studies exhibit similar trends with Mg II absorption and emission. Such trends would not emerge if the individual galaxies did not possess these properties themselves.

We propose that Fe II* emission should be detected in other similar galaxies when observed with sufficient signal-to-noise ratio. It is curious that fine structure emission from other transitions accessible in the far-UV have not been observed in detailed individual galaxy studies (e.g., Pettini et al. 2002; Quider et al. 2009, 2010). It would be interesting to observe these galaxies in the near-UV to see if these Fe II* emission features are present. If they are not, perhaps this suggests some redshift dependence for these features, as the majority of detailed studies of individual galaxies to date have been conducted on galaxies with $z > 2$. However, one very interesting case is CSWA20 (Pettini et al. 2011), a lensed star-forming galaxy at $z = 1.433$. Its interstellar medium appears to be evacuated along the line of sight so a view of its stars and H II regions is unobscured. This galaxy exhibits narrow Mg II emission which, the authors conclude, arises in the H II regions. To date, Fe II* emission has not been detected in this galaxy but there are poor constraints on these emission lines. An understanding of how this galaxy compares to those in this study as well as at higher redshift could improve our interpretation of the origin of these emission lines.

## 5.6.2 The link between absorption and emission profiles

Blueshifted absorption lines in star-forming galaxies with $z > 1$ are routinely interpreted as tracing a large-scale outflow from the galaxy's star-forming regions (e.g., Rubin et al. 2010; Shapley et al. 2003; Steidel et al. 2004; Weiner et al. 2009; and references therein). These absorption lines arise in the outflowing material oriented along the observer's line of sight. Outflows can be seen in absorption out to nearly $1000\,\mathrm{km\,s^{-1}}$ (Quider et al. 2010 and references therein).

To this picture we now add emission from Fe II* and the P-Cygni profile of Mg II. Rubin et al. (2011) propose that the blue component of the Fe II* emission lines comes from the same gas seen in absorption. However, redshifted Fe II* emission arises in the entirety of the outflow. Finally, the redshifted Mg II emission arises in photon scattering from the receding portion of the outflow. Prochaska et al. (2011) adopt this mechanism and model its impact on the emergent line profiles.

**Emergent Mg II profiles**

One of the main results of Prochaska et al. (2011) is that emergent Mg II profiles can be P-Cygni in nature. When the outflow becomes optically thick to Mg II λλ2796,2803 photons, they can become resonantly trapped. The only way they can escape is when redshifted to a degree that makes the portion of the outflow moving towards the observer transparent to photons of that energy. This occurs by re-emission of Mg II photons by the receding portion of the outflow. The P-Cygni nature of the Mg II profiles is confirmed upon inspection of Figure 5.6, Figure 5.12 (Q1623-BM95 and Q1700-BM154), and the measured offsets for the emission and absorption components.

The mechanism giving rise to the profile morphology of Mg II has been well studied in Lyα, also a resonance transition. The effects of resonant scattering on the emergent Lyα profile were discussed in Chapter 3 and many of the same considerations apply to Mg II. We have shown here that Mg II profile morphology is related to the stellar mass and reddening of a galaxy. While we believe these trends to be real, in the spirit of studies of Lyα, we caution over-interpreting the Mg II line profile. In Chapter 3, Section 8.3, we compare cB58 and the Cosmic Horseshoe. These two lensed LBGs have very similar dynamical masses and star formation rates but exhibit Lyα profile morphologies at the extremes of absorption and emission strength for the entire known LBG population. The lesson to learn from Lyα is that geometry and orientation are two key elements in determining the observed profile of a resonance transition. We advise caution in interpreting the link between galaxy properties and emergent Mg II profiles.

**Emission filling of absorption lines**

Another of the main results of Prochaska et al. (2011) is that emission from resonance transitions can be superposed upon absorption located at the systemic redshift. The effect of this is to diminish the strength of the affected absorption line by diminishing the absorption strength near the systemic redshift, thereby shifting the absorption line's centroid further blueward. This process is referred to as line-filling or emission filling of absorption lines. We have found evidence of this effect in both the composite and individual galaxies. There are several consequences of this phenomenon relating to both the line strength and blueshifting. We examine each in turn.

The first question to ask is whether there is reason to believe that our spectra could exhibit Fe II resonance emission. We record emission from numerous Fe II* transitions, as listed in Table 5.1. These emission lines originate in energy levels of the Fe II atom which are reached by resonant absorption in Fe II λλ2586,2600. Therefore, we know that the necessary energy levels are populated and de-exciting through emission. Prochaska et al. (2011) find that non-resonant Fe II* emission is present when resonant Fe II emission occurs. Therefore, we conclude that it is not unreasonable to suspect that emission filling is possible in our sample.

We present evidence of non-physical absorption line ratios for the Fe II λλ2374,2382 transitions in both composite and individual spectra. After looking at the strength of the other Fe II absorption features, we conclude that emission filling is a likely explanation for this result. A common use of line ratios is to constrain the covering fraction of the continuum emitting stars by the gas seen in absorption (e.g., Martin & Bouché 2009; Quider et al. 2009; and references therein). Discrepancies in the theoretical line ratio

among different transitions of the same element and ionization state can be interpreted as due to continuum leakage. Different Fe II transitions are susceptible to varying degrees of line-filling (Prochaska et al. 2011; Martin et al. 2011, in prep.). This can influence conclusions drawn about partial coverage, optical depth, and other parameters for which line strengths are important.

The blueshifting of absorption line centers that results from line-filling can complicate measurements of outflow velocities. We measure systematically bluer velocities for the Fe II $\lambda 2382$ and Mg II $\lambda 2796$ compared to most other transitions and compared to Fe II $\lambda 2374$ in particular. This velocity offset is most pronounced for Mg II, which, as discussed above, clearly suffers resonant line-filling as evidenced by its P-Cygni profile morphology. Velocity offsets of up to $100\,\mathrm{km\ s^{-1}}$ are seen within the Fe II absorption transitions. These offsets are seen in the composite spectra as well as in individual galaxy spectra. Oftentimes, out of necessity, the strongest absorption lines are used for determining the absorption redshift of high redshift galaxies (Shapley et al. 2003; Steidel et al. 2004, 2010; and references therein). The velocity differences among Fe II lines found in this study suggest that line-filling should be taken into consideration when measuring absorption line redshifts. On the other hand, we compare a suite of interstellar absorption lines for two galaxies in Chapters 3 and 4 (see Figure 3.5 and Figure 4.4). We find these transitions to be remarkably consistent in their velocity centers and extent. Clearly more work needs to be done to assess the extent of blueshifting caused by emission filling.

The combination of reduced absorption equivalent width and line center blueshifting can reduce the signature of gas absorption at the systemic redshift. We tentatively concluded that there is less gas at $v = 0$ in the low mass and low dust samples compared to the high mass and high dust samples. However, Mg II emission in the low mass/dust samples is strong so this may be swamping the absorption line at $v = 0$. The velocity centroids of the low mass/dust Mg II $\lambda\lambda 2796,2803$ absorption lines are bluer than those of the high mass/dust sample by $\sim 60\,\mathrm{km\ s^{-1}}$, which is suggestive of emission filling in the low mass/dust samples.

## 5.7  Conclusions

We have analyzed Keck/DEIMOS rest-frame near-UV spectra of 96 star-forming galaxies in the redshift range $1 < z < 2$. The coverage of a suite of Fe II and Mg II absorption and emission features, as well as their relatively high S/N ratio (S/N$> 5$ for $\sim 30$ galaxies), make this sample uniquely suited to studying absorption and emission from the outflowing cool gas in high redshift star-forming galaxies. The dependence of spectroscopic features on stellar mass and reddening are assessed using stacked spectra. Individual galaxies are also analyzed to probe the range of absorption and emission properties spanned by our sample. Our main conclusions are as follows.

(i) Fe II* emission is ubiquitous in these galaxies. Significant detections of up to 5 non-resonant Fe II* emission lines are made in individual galaxies as well as the composite spectra. These emission lines are of similar strength and velocity offset from systemic for all of the composites. This is the first detection of Fe II* in a large sample of high redshift galaxies showing that this is a common phenomenon, rather than a peculiarity of the few galaxies in which it had been detected prior to this work.

(ii) The Fe II and Mg II absorption and emission features are determined to originate in the galaxy-wide outflow from the star-forming regions.

(iii) Mg II emission is seen in $\sim 30$ individual galaxies at the $> 1.5\sigma$ level as well as in the low mass and low reddening stacked spectra. The high mass and high dust composites have significantly greater Mg II absorption equivalent width and greater outflow terminal velocities than the low mass and low dust samples. The profile morphology of Mg II appears to be a P-Cygni profile. This is consistent with the resonant scattering of Mg II photons within the outflow.

(iv) We find evidence for emission filling of the Fe II $\lambda 2382$ absorption transition. Firstly, the velocity of the Fe II $\lambda 2382$ is systematically blueward of the Fe II $\lambda 2374$ velocity in individual galaxies as well as the composite spectra. Secondly, the line ratio $W_{2382}/W_{2374} \leq 1$, where unity is the theoretical saturation limit, is measured for several individual galaxies and composite spectra. These trends are explained by the line-filling of Fe II $\lambda 2382$ by resonant Fe II emission. Line-filling is identified as existing across a wide range of galaxy properties and, therefore, spectral feature strengths and morphologies.

The results of this work open a new avenue for studying cool gas outflows from high redshift star-forming galaxies. This study provides guidance on the observing conditions and galaxy properties which allow for the detection of Fe II and Mg II emission and it will help to grow the sample of high redshift galaxies with these emission features. Such a sample would allow for tighter constraints on the outflow properties of high redshift galaxies.

# 6

# The Pittsburgh SDSS Mg II Quasar Absorption-Line Survey Catalog

## 6.1 Introduction

Quasar absorption line (QAL) surveys form the basis for selecting and studying large numbers of cosmologically-distant galaxies via their gas cross sections. Of particular usefulness among QALs is the Mg II $\lambda\lambda$2796,2803 resonance doublet. $Mg^+$ is a dominant ionization stage in gas having a large neutral hydrogen fraction, and the Mg II $\lambda\lambda$2796,2803 transitions have particularly strong oscillator strengths, making the doublet an excellent tracer of low-ionization and neutral gas. Additionally, in comparison to other UV absorption lines commonly found in quasar spectra, the relatively long rest wavelength of the doublet permits its identification with ground-based optical spectroscopy down to fairly low redshift ($z \lesssim 0.14$; e.g., Nestor, Turnshek, & Rao 2006).

The utility of Mg II absorbers for the study of galaxies has prompted several QAL surveys in past decades. Initial studies were usually made at moderate spectral resolution and signal-to-noise ratio, and this generally resulted in the detection of absorption systems with moderate to strong rest equivalent widths, $W_0^{\lambda 2796} \lesssim 0.3$ Å. The first surveys (e.g., Weymann et al. 1979; Lanzetta, Turnshek, & Wolfe 1987; Tytler et al. 1987; Sargent, Steidel, & Boksenberg 1988; Caulet 1989) contained a few to a few dozen systems. The survey of Steidel & Sargent (1992), which identified more than 100 Mg II absorption systems, was the largest statistical sample of Mg II systems for more than a decade. Imaging surveys along quasar sightlines demonstrate that the bulk of the Mg II absorbers are associated with galaxies (e.g., Bergeron & Boissé 1991; Steidel, Dickinson, & Persson 1994; Kacprzak et al. 2010; Chen et al. 2010; Rao et al. 2011). Thus, the Mg II absorption-line catalogs have been used by various authors to study subsamples of systems with the aim of investigating the properties of the low-ionization and neutral gas regions associated with galaxies. These Mg II-based studies have the potential to reveal information on galactic halos/disks (e.g., Charlton & Churchill 1996), outflows induced

by star formation and supernovae (e.g., Norman et al. 1996; Bond et al. 2001; Nestor et al. 2011), accreting protogalactic gas (Mo & Miralda-Escude 1996), merger-induced activity and tidal debris (e.g., Sargent & Steidel 1990; Maller et al. 2001; Kacprzak et al. 2007), dwarf galaxies (e.g., LeBrun et al. 1993), low surface brightness galaxies (e.g., Phillips, Disney, & Davis 1993), and even the extended environments of other quasars (e.g., Bowen et al. 2006). High-resolution spectroscopy is generally required to resolve the kinematic "component" structure of the absorbing gas; this component structure provides important detailed information on the velocity field of the gas associated with an absorbing galaxy (e.g., Churchill et al. 2000; Churchill & Vogt 2001; Steidel et al. 2002). It turns out that a significant fraction of strong Mg II systems ($W_0^{\lambda 2796} \geq 0.5$ Å) are damped Ly$\alpha$ (DLA) absorbers with neutral gas column densities $N_{HI} \geq 2 \times 10^{20}$ atoms cm$^{-2}$, and weaker Mg II systems are not DLAs (e.g., Rao, Turnshek, & Briggs 1995; Rao & Turnshek 2000; Rao, Turnshek, & Nestor 2006). Thus, Mg II-based surveys are particularly effective and important for preselecting systems to be used in DLA surveys at redshifts $z \lesssim 1.65$, when the Ly$\alpha$ line falls in the UV and is unobservable from the ground. For example, follow-up imaging of DLA galaxies shows that DLAs trace the neutral gas phase of a mixed population of galaxy types (e.g., Rao et al. 2003; Chen & Lanzetta 2003; Rao et al. 2011).

More recently, moderate resolution spectroscopy from the Sloan Digital Sky Survey (SDSS; York et al. 2000) has led to a huge increase in the number of quasar spectra available for QAL surveys. This has advanced the study of intervening absorption systems, moving sample sizes into the realm of high statistical significance. The survey of Nestor, Turnshek, & Rao (2005, hereafter NTR05) utilized $\sim 3400$ quasar spectra from the SDSS early data release (EDR). *This present contribution is a continuation of the work begun in NTR05, and the reader is referred to NTR05 for additional details on the methods used here.* From the spectra analyzed by NTR05, a statistical sample of over 1300 Mg II systems having $W_0^{\lambda 2796} \geq 0.3$Å was derived. In addition to providing a firm basis for the statistics of Mg II absorbers, that sample has also been used for follow-up studies, such as the first identification of a correlation between gas-phase metals and absorbing gas velocity spread (Nestor et al. 2003), an investigation of the mean spatial extent and photometric properties of Mg II absorbing galaxies (Zibetti et al. 2005), and an expanded investigation of DLAs at $z < 1.65$ (Rao et al. 2006). The Mg II EDR statistics have also been compared with Mg II statistics derived from a radio-selected sample of quasars in order to place an upper limit on the number of Mg II absorbers missed in optical surveys due to the dimming of background quasars by dust in the intervening absorbers (Ellison et al. 2004; 2009). In the past few years, much larger Mg II absorber catalogs have been developed from subsequent data releases of the SDSS (e.g., Prochter, Prochaska, & Burles 2006; this contribution). Our present catalog has already been used to study the statistical properties of the absorbing gas and associated galaxies in order to take advantage of the high precision inherent in such large surveys. These studies include an expanded investigation of the correlation between metals and absorbing gas velocity spread (Turnshek et al. 2005), an expanded investigation of the mean spatial extent and photometric properties of the absorbing galaxies (Zibetti et al. 2007), investigations of the sightline velocity clustering of the absorbers and the transverse spatial clustering of bright galaxies along the sightlines passing through them (Rimoldini 2007), an investigation of the dust extinction and gravitational lensing effects that the absorbers induce on

background quasars (Ménard et al. 2008), and a sensitive search for emission associated with the absorbing galaxies (Ménard et al. 2009). In addition, follow-up imaging to search for galaxies associated with the rarest and strongest Mg II systems has taken place (Nestor et al. 2007; 2010).

In this chapter we present the current state of our SDSS Mg II absorber catalog, which is presently complete through SDSS Data Release Four (DR4). As noted above, this contribution represents a continuation of the work presented by NTR05 in that we used the method of NTR05; however, we did not use their measurements of the EDR Mg II absorbers.[1] It contains $\sim 16,700$ absorbers in the redshift interval $0.36 \lesssim z \lesssim 2.28$ identified in $\sim 44,600$ SDSS quasar spectra. The catalog, along with other information (§6.4), is now publicly available at http://enki.phyast.pitt.edu/PittSDSSMgIIcat.php. Searches of more recent SDSS quasar spectra are underway, and in the future we hope to extend the catalog to include additional Mg II absorbers beyond DR4. However, future extensions will only be announced and made available on the website. The combination of size and well understood statistics makes the catalog ideal for: (1) statistical studies of, for example, the properties and evolution of the low-ionization and neutral gas regions of galaxies, (2) identifying rare systems, which are readily identified only in very large surveys, and (3) selecting well-defined samples for follow-up studies. In a subsequent paper we will present and discuss the statistical properties of the absorbers in the present catalog (Nestor et al., in preparation).

## 6.2 Quasar Selection Criteria

The quasar spectra used to build the Mg II absorber catalog are a subset of the SDSS data releases through DR4. The searches for Mg II absorption doublets were generally performed on the initially released versions of the spectra. However, spectra have been re-extracted and re-calibrated in subsequent SDSS data releases (Adelman-McCarthy 2008; Abazajian et al 2009). Therefore, for example, a quasar spectrum taken from DR7 may not be identical to the one we analyzed to form the catalog. However, since the nature of measuring an absorption-line equivalent width involves fitting a continuum and making a measurement over a small wavelength interval, the re-extraction and re-calibration of spectra will generally have no effect on the statistical properties of the absorbers in the catalog.

The quasar spectra to be searched for Mg II absorbers were isolated using an SQL query of the public SDSS DR4 database (available at http://cas.sdss.org/astrodr4/). All of the spectroscopic and photometric data in the SDSS is contained in two master tables: `SpecObjAll`, for spectroscopic data, and `PhotoObjAll`, for photometric data. The data in these two tables are organized into numerous "views" by imposing an array of selection criteria on the master tables. We used a `SpecPhoto` view to generate the quasar sample to be searched. The view we used was intended to eliminate all spectra of poor quality, sky spectra, duplicate observations (those spectra labeled as SECONDARY), and all data outside the primary DR4 survey area. In addition, `SpecPhoto` contains all of the spectroscopic information and the most accurate photometric information at the time of

---

[1]The current version of the catalog does not include all EDR quasars. It only includes those quasars which meet our catalog's selection criteria (see §6.2).

the data release (those observations labeled as BEST) for each included object.

We used four criteria to define the quasar sample: (1) a spectral classification of 3 or 4, which indicates a QSO or a HIZ-QSO, respectively, (2) $z > 0.36$ to ensure visibility of the Mg II $\lambda\lambda2796,2803$ doublet at the SDSS low wavelength limit of 3820 Å, (3) $zstatus > 1$ to eliminate missing or failed redshift measurements, and (4) $i < 20$ for the fiber magnitude. Incorporating these criteria into an SQL query of the `SpecPhoto` view yielded $\sim 44,600$ quasars. These quasars form the basis for the Mg II absorber catalog. The quasars that meet our redshift, magnitude, and zstatus selection criteria represent $\sim 72\%$ of all objects in SDSS DR4 which are spectroscopically classified as a QSO or HIZ-QSO. Alternatively stated, $\sim 28\%$ of SDSS DR4 quasars were unsuitable for inclusion in the catalog because of emission redshifts that were too low or poorly constrained, or magnitudes that were too faint for recording spectra of sufficient quality.

## 6.3 Construction of the Catalog

There were three main steps which led to the construction of the Mg II catalog: (1) automated processing of the quasar spectra, (2) visual inspection of the automatically identified Mg II candidate doublets to eliminate systems judged to be unreliable, and (3) measurement of the confirmed Mg II doublets. NTR05 developed this procedure and applied it to the SDSS EDR data. In this section we briefly review these steps, referring the reader to NTR05 for more detail. When we generically refer to an absorption line's wavelength ($\lambda_0$), rest equivalent width ($W_0$), or error in rest equivalent width ($\sigma_{W_0}$), this applies to the particular line in question (e.g., see Table 1).

### 6.3.1 Automated processing of quasar spectra

The automated processing of the quasar spectra is comprised of two distinct phases: normalization of the spectra and identification of Mg II doublet candidates.

To maximize computation and storage efficiency, the data were abridged to exclude spectral regions not in the range to be searched for Mg II systems. This included the spectral regions shortward of the quasars' Ly$\alpha$ emission lines, in order to avoid the confusion and inaccuracy associated with searching in the Ly$\alpha$ forest, and longward of Mg II $\lambda2800$ broad emission lines, where intervening Mg II absorption would be absent. A combination of cubic splines and Gaussians were employed to fit the spectra, including the true continua and broad emission and broad absorption features. These continua fits, or pseudo-continua fits (i.e., continua that fit broad emission or absorption features and not just true continua), were used to normalize the spectral fluxes and flux uncertainties. The continuum-fitting process was successful for the vast majority ($\gg 99\%$) of spectra. The software only failed to derive satisfactory continua for a small number of quasars having rare spectra, such as extreme broad absorption line (BAL) quasars; these spectra were excluded from the sample. Occasionally the automated software produced a poor fit in a localized spectral region. Such occurrences were very infrequent in comparison to the overall size of the survey, and always produced false candidates (rather than missing true systems) when present. These cases had no measurable effect on the overall properties of the catalog. In the uncommon circumstance (i.e., in $< 1\%$ of the cases) of a poor

continuum fit being coincident with a Mg II absorption doublet, the fit was interactively re-fit to produce a satisfactory continuum before final equivalent width measurements were performed (see §6.3.3).

All normalized spectra were run though a routine that flags possible Mg II doublets. In order to isolate a sample of absorbers that were primarily intervening, systems with measured absorption redshifts within 3000 km s$^{-1}$ of the SDSS quasar emission redshift were not included in the catalog. Therefore, biases that might arise due to over-densities of absorbers in quasar environments will be minimized or avoided in any statistical study based on the catalog. This same software also determines the $\lambda 2796$ rest equivalent width detection limit, $W_0^{lim}$ (see §6.3.3), as a function of redshift or observed wavelength, $(1 + z) = \lambda_{obs}/2796.352$, for the range of Mg II redshifts corresponding to a searched spectral region. This $W_0^{lim}$ information was recorded for each wavelength in each searched spectral region so that it could be integrated over all sightlines to determine the total number of redshift intervals surveyed as a function of $W_0^{lim}$ and redshift (e.g., see figure 8 in NTR05).

The Mg II doublet finding routine is conservative by design to ensure that all possible doublets are located in this initial step. A total of $\sim 44,600$ quasar spectra were searched for the Mg II absorption doublet. The conservative nature of our automated doublet finder led to a large number of flagged candidates: on average, more than two Mg II candidates were flagged for each quasar.

## 6.3.2   Visual inspection of candidate Mg II doublets

All candidate Mg II doublets were individually inspected by eye to determine their validity. As the candidate-flagging routine was designed to be conservative, this resulted in the rejection of approximately 85% of all candidates during visual inspection.[2] The most common false-positives were due to: (1) absorption in a BAL trough, (2) multiple identifications of a candidate Mg II doublet (this sometimes occurred within strong Mg II absorption profiles; we selected the apparent best absorption redshift and rejected redundant identifications), (3) non-Mg II absorption lines, or (4) coincidentally aligned noise spikes.

Consistent with previous QAL surveys (§6.1), our experience with the SDSS spectra has shown that isolated absorption features measured with a significance $\geq 5\sigma_{W_T}$ are what the eye determines to be confident detections. Here $\sigma_{W_T}$ is the theoretical error in rest equivalent width used to calculate the detectability limit, $W_0^{lim}$, of a Mg II doublet (see §6.3.3). When combined with additional information, such as the confident detection of a doublet partner, significances $\geq 3\sigma_{W_T}$ tend to be consistent with confident-by-eye detections. Candidate doublets identified with significances close to these thresholds would often be difficult to categorize as real or spurious based on quick visual inspection. Such candidates were generally retained at this stage by default. However, after final measurements were available (see §6.3.3) we used visual inspection to reject suspicious candidates. This included candidates with doublet ratios significantly different from the physically allowed range of $1.0 \leq W_0^{\lambda 2796}/W_0^{\lambda 2803} \leq 2.0$. We also examined each spectrum to assess the possibility that a candidate Mg II system was flagged due to the presence

---

[2] The high rate of visual rejection may have unfortunately resulted in the accidental rejection of some clearly significant candidates (see §6.4.2).

of a QAL system at another redshift, and candidates which were not convincingly Mg II were rejected.

### 6.3.3 Measurements of Mg II doublets

The reported measurements of the redshifts and rest equivalent widths of all accepted systems were finalized interactively when necessary. A pair of Gaussian line profiles separated in wavelength by the redshifted doublet separation were fitted to each accepted candidate's profile. The location of these fitted profiles defined the observed redshift and were used to perform an optimal extraction (see NTR05) of each line's rest equivalent width, $W_0$, and its associated error, $\sigma_{W_0}$. This is the optimal procedure when the observed profile is well described by the chosen function. We draw particular attention to equations 1 and 2 from NTR05:

$$(1+z)\,W_0 = \frac{\sum_i P(\lambda_i - \lambda_0)\,(1 - f_i)}{\sum_i P^2(\lambda_i - \lambda_0)}\,\Delta\lambda, \tag{6.1}$$

$$(1+z)\,\sigma_{W_0} = \frac{\sqrt{\sum_i P^2(\lambda_i - \lambda_0)\,\sigma_{f_i}^2}}{\sum_i P^2(\lambda_i - \lambda_0)}\,\Delta\lambda, \tag{6.2}$$

where $P(\lambda_i - \lambda_0)$, $\lambda_i$, $f_i$, and $\sigma_{f_i}$ represent the line profile centered at $\lambda_0$, the wavelength, the normalized flux, and flux uncertainty as a function of pixel. The sum is performed over an integer number of pixels that cover at least $\pm 3$ characteristic Gaussian widths. For systems with clearly saturated or resolved profiles, two pairs of Gaussians were used to fit the absorption system, and this proved to be almost always successful at accurately reproducing the observed profiles. In these cases the reported redshift is the rest-equivalent-width-weighted redshift. For weaker and/or unresolved systems, the additional degrees of freedom afforded by a double-Gaussian did not generally give different values for $W_0^{\lambda 2796}$ and $W_0^{\lambda 2803}$. In over 95% of the cases doublet members were fit with single Gaussian profiles. Upon careful inspection of the systems retained in the catalog after measurement, it was found that systems stronger than $W_0^{\lambda 2796} \lesssim 3$ Å frequently had their strengths slightly ($< 1\sigma_{W_0}$) but systematically over-estimated when using a single Gaussian profile fit. Therefore, the $\sim 700$ strongest systems were re-inspected and re-measured using double-Gaussians when appropriate. The centroids of each Gaussian were left free during the fit.

Consistent with experience (§6.3.2), the values for the $\lambda 2796$ rest equivalent width detection limit, $W_0^{lim}$, as a function of redshift or observed wavelength, $(1+z) = \lambda_{obs}/2796.352$, were calculated by requiring $W_0^{\lambda 2796} \geq 5\sigma_{W_T}$ and $W_0^{\lambda 2803} \geq 3\sigma_{W_T}$. Thus, to compute $W_0^{lim}$ for each spectrum we did the following. We started by determining the $1\sigma$ rest equivalent width error, $\sigma_{W_0}$ (equation 2), for a theoretical, unresolved line near the location of each doublet member and set $\sigma_{W_T} = \sigma_{W_0}$. We then took the value of $W_0^{lim}$ to be the larger of five times this error ($5\sigma_{W_T}$) at the location of the $\lambda 2796$ line or six times this error ($2 \times 3\sigma_{W_T}$) at the location of the $\lambda 2803$ line. The factor of two avoids introducing a detection bias caused by the Mg II doublet ratio, which has a theoretical range of approximately 1.0 (completely saturated) to 2.0 (completely unsaturated). Systems with measured $W_0^{\lambda 2796} < W_0^{lim}$ were excluded from the catalog. This eliminated the vast majority of suspicious systems that were not rejected during visual inspection. At this

point, a total of $\sim 16,700$ Mg II doublets were considered real and successfully measured. Whenever possible, systems close in redshift were measured as separate systems. It is important to note that the redshift difference for which this was possible was *not* constant, because it depended on both redshift and the widths of the features, and therefore on $W_0^{\lambda 2796}$ and $W_0^{\lambda 2803}$. We retained such systems as separate in the catalog, and note that they can always be combined *ex post facto* for statistical purposes, when necessary. This is a deviation from the policy of NTR05, where systems with separations less than 500 km s$^{-1}$ were always measured as a single system.

### 6.3.4 Measurements of adjacent Mn II, Fe II, and Mg I absorption lines in cataloged Mg II systems

In addition to the measurements of Mg II $\lambda\lambda2796,2803$ doublets, we also made rest equivalent width measurements at the predicted locations of six additional absorption lines (Fe II $\lambda\lambda2586, 2600$, Mn II $\lambda\lambda2576, 2594, 2606$, and Mg I $\lambda2852$) for all of the systems in the catalog, when possible. Since these lines are not too far displaced from the Mg II doublet, it was usually possible to make measurements at their predicted locations. There are many significant detections. For example, for Mg II systems in the redshift interval $0.36 \leq z \leq 2.28$ in SDSS spectra, the Mn II $\lambda2576$ transition is usually covered when $z > 0.48$ and the Mg I $\lambda2852$ transition is usually covered when $z < 2.22$. Including nondetections caused by lack of coverage, the $2\sigma$ and $3\sigma$ detection fractions for these six absorption transitions are as follows: Fe II $\lambda2586$ (53.7% and 43.6%), Fe II $\lambda2600$ (73.5% and 64.1%), Mn II $\lambda2576$ (10.9% and 4.9%), Mn II $\lambda2594$ (8.1% and 3.3%), Mn II $\lambda2606$ (7.0% and 2.7%), and Mg I $\lambda2852$ (40.6% and 27.9%).

One motivation for making these additional measurements is to facilitate future use of this catalog to identify candidate DLA systems. For example, as discussed by Rao et al. (2006), it appears that measurements of Fe II $\lambda2600$, Mg II $\lambda2796$, and Mg I $\lambda2852$ can be used together to isolate a subset of Mg II systems that will contain a complete sample of DLA systems, but with a higher DLA fraction than previously achieved. For example, follow-up UV spectroscopy to measure $N_{HI}$ in a properly selected subset of Mg II systems (see Rao et al. 2006) indicate that the sample will be complete and $\sim 42\%$ will be DLAs.

Figure 6.1 shows two regions of a spectrum containing one of the Mg II absorption-line systems in the catalog. The absorption system is in the spectrum of quasar SDSS J085244.74+343540.4 ($z_{em} = 1.655$) and the absorption redshift is $z = 1.310$. The figure shows the Mg II doublet and the six additional metal-line absorption transitions that have been measured for this system. Table 6.1 presents the metal line measurements for this system as an example of information that may be found in the catalog.

## 6.4 The Catalog Characteristics

### 6.4.1 The catalog format

The Pittsburgh SDSS Mg II Quasar Absorption-Line Survey Catalog is available for public use at http://enki.phyast.pitt.edu/PittSDSSMgIIcat.php. It includes information about
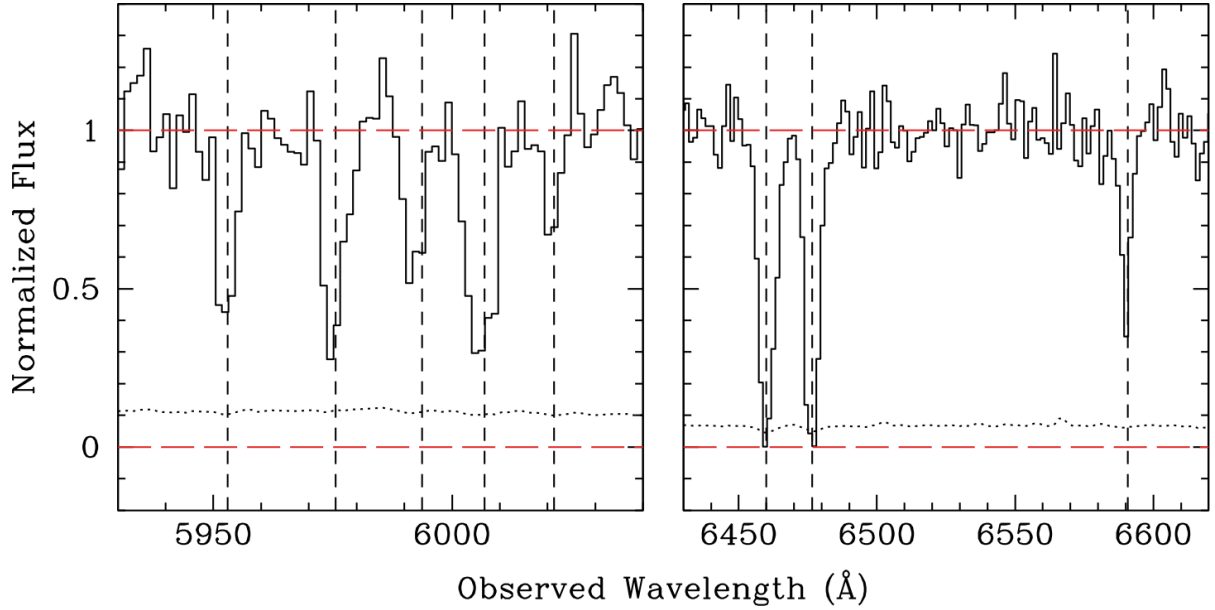
Figure 6.1 Two regions of the normalized spectrum of SDSS quasar J085244.74+343540.4 showing eight metal absorption line transitions at $z = 1.3102$ (Mn II$\lambda$2576, Fe II$\lambda$2586, Mn II$\lambda$2594, Fe II$\lambda$2600, Mn II$\lambda$2606, Mg II $\lambda\lambda$2796,2803, and Mg I$\lambda$2852). The lower dotted curve is the $1\sigma$ error in normalized flux.

Table 6.1 METAL-LINE MEASUREMENTS FOR
J085244.74+343540.4 ($z_{em} = 1.655$)

| Transition | $\lambda_0$ | $W_0^1 \pm \sigma_{W_0}$ |
|---|---|---|
| | (Å) | (Å) |
| Mg II | 2796.35 | $3.046^2 \pm 0.083$ |
| Mg II | 2803.53 | $2.930 \pm 0.085$ |
| Fe II | 2586.65 | $1.567 \pm 0.159$ |
| Fe II | 2600.17 | $2.189 \pm 0.166$ |
| Mn II | 2576.88 | $1.261 \pm 0.138$ |
| Mn II | 2594.50 | $1.034 \pm 0.179$ |
| Mn II | 2606.46 | $0.583 \pm 0.165$ |
| Mg I | 2852.96 | $1.150 \pm 0.087$ |

[1] $z_{abs} = 1.3102$
[2] $W_0^{lim} = 0.372$ Å (see Section 6.3.3 for a discussion of $W_0^{lim}$).

Table 6.2 Catalog Values for SDSS DR4
Quasars Searched for Mg ii

| Column | Description |
|:---:|:---|
| 1 | J2000 name |
| 2 | SDSS Modified Julian Date (MJD) |
| 3 | SDSS Plate Number |
| 4 | SDSS Fiber Number |
| 5 | Right Ascension (J2000) |
| 6 | Declination (J2000) |
| 7 | $z_{em}$ |
| 8 | Error in $z_{em}$ |
| 9 | BEST fiber $u$ magnitude |
| 10 | BEST fiber $g$ magnitude |
| 11 | BEST fiber $r$ magnitude |
| 12 | BEST fiber $i$ magnitude |
| 13 | BEST fiber $z$ magnitude |
| 14 | Error in BEST fiber $u$ magnitude |
| 15 | Error in BEST fiber $g$ magnitude |
| 16 | Error in BEST fiber $r$ magnitude |
| 17 | Error in BEST fiber $i$ magnitude |
| 18 | Error in BEST fiber $z$ magnitude |

the quasars that were searched for Mg ii doublets, the measurements of the Mg ii doublets (§6.3.3), the measurements of up to six additional metal absorption lines (§6.3.4), and the quasar spectral files in text format. Values of $W_0^{lim}$ (§6.3.3) have been merged with the quasar spectral files, so the available quasar spectral files contain flux, flux uncertainty, pseudo-continuum fit, and $W_0^{lim}$, all as a function of wavelength. The quasar properties in Table 6.2 are available for each quasar that was searched for Mg ii. The variable names given in Table 6.2 are drawn from DR4, and we refer the reader to http://www.sdss.org/dr4 for further explanation of the values given in the Table.

In summary, quasar spectra files and DR4 quasar properties are made available for $\sim 44,600$ quasars, and absorption system information is available for $\sim 16,700$ Mg ii doublets.

## 6.4.2 Missed systems

We have attempted to quantify our incidence of missed Mg ii absorption doublets which are real, clearly significant, and located within our searched quasar sample. There are two possible steps during the construction of the catalog where one might think a Mg ii system could be missed or lost: (1) the automated Mg ii identification routine and (2) the interactive inspection and/or measurement of a candidate Mg ii system which often results in removing a system for the reasons given in §6.3.2 and §6.3.3. As the Mg ii identification software has been robustly tested and conservatively written (see NTR05), we

are confident that the first possibility is an exceedingly small source of missed Mg II absorbers when compared to the second possibility, which includes the potential for human error.

To quantify our incidence of missed Mg II absorption systems, we randomly selected 500 quasars from our catalog. Two of us (AMQ and DBN) then visually inspected 200 separate spectra and 100 common spectra (for a total of 500 spectra) to search for Mg II absorbers. As explained in §6.3.2, our formal detection/rejection threshold is such that the human eye seems to be generally capable of identifying Mg II absorbers to slightly better than the sensitivity limit ($W_0^{lim}$) adopted for the construction of the catalog. Therefore, manually re-inspecting the spectra for Mg II absorption doublets in a slow and careful manner allows us to account not only for software errors, but also human errors made during the initial laborious process of manually accepting/rejecting candidates from the extremely large master list. In the entire sample of 500 spectra, we discovered five significant missed systems with $W_0^{\lambda 2796} - W_0^{lim} > \sigma_{W_0}$. Therefore, we conclude that human error caused the rejection of some systems. We estimate that for every 100 searched spectra approximately one Mg II absorber unambiguously above our detection threshold has been missed. This is a systematic human error that appears not to be correlated with any Mg II system property.

### 6.4.3 Quasar properties

Figure 6.2 shows the distribution of SDSS emission redshifts for all quasars in the catalog along with the distribution of absorption redshifts for all Mg II systems in the catalog. The distribution of emission redshifts is similar to the one derived from the DR5 quasar catalog (Schneider et al. 2007).[3] Schneider et al. (2007) note that the dips in the emission redshift distribution near $z = 2.7$ and $z = 3.5$ are due to the SDSS quasar selection algorithm. Figure 6.3 shows the SDSS $i$ magnitude (left panel) and $g$ magnitude (right panel) distributions for all quasars in the catalog (red dotted line) and for those quasars with at least one intervening Mg II absorption system (black solid line). The $i$ magnitude distribution is similar to the one published by Schneider et al. (2007) for DR5 quasars. The bottom panels of Figure 6.3 show the corresponding fractions of quasars with one or more Mg II systems as a function of magnitude, without regard to quasar redshift. As expected, the brighter quasars have a higher probability of exhibiting Mg II absorption since the high signal-to-noise ratio of their spectra permits the detection of weaker Mg II systems, which have a higher incidence than stronger systems (e.g., NTR05).

### 6.4.4 Mg II absorber properties

A thorough treatment of the Mg II absorber statistics from the catalog will be presented in a subsequent paper (Nestor et al., in preparation). Here, we present the raw properties of the Mg II doublets in the catalog to illustrate the properties of the catalog itself.

Returning to Figure 6.2, the black histogram shows the distribution of absorber redshifts for Mg II doublets in the catalog. The redshift distribution of the Mg II absorbers is constrained to lie between $0.36 \lesssim z \lesssim 2.28$ because of the wavelength coverage of the SDSS spectrograph. As mentioned in NTR05, the dip at $z \approx 1.1$ is due to the ubiquitous

---

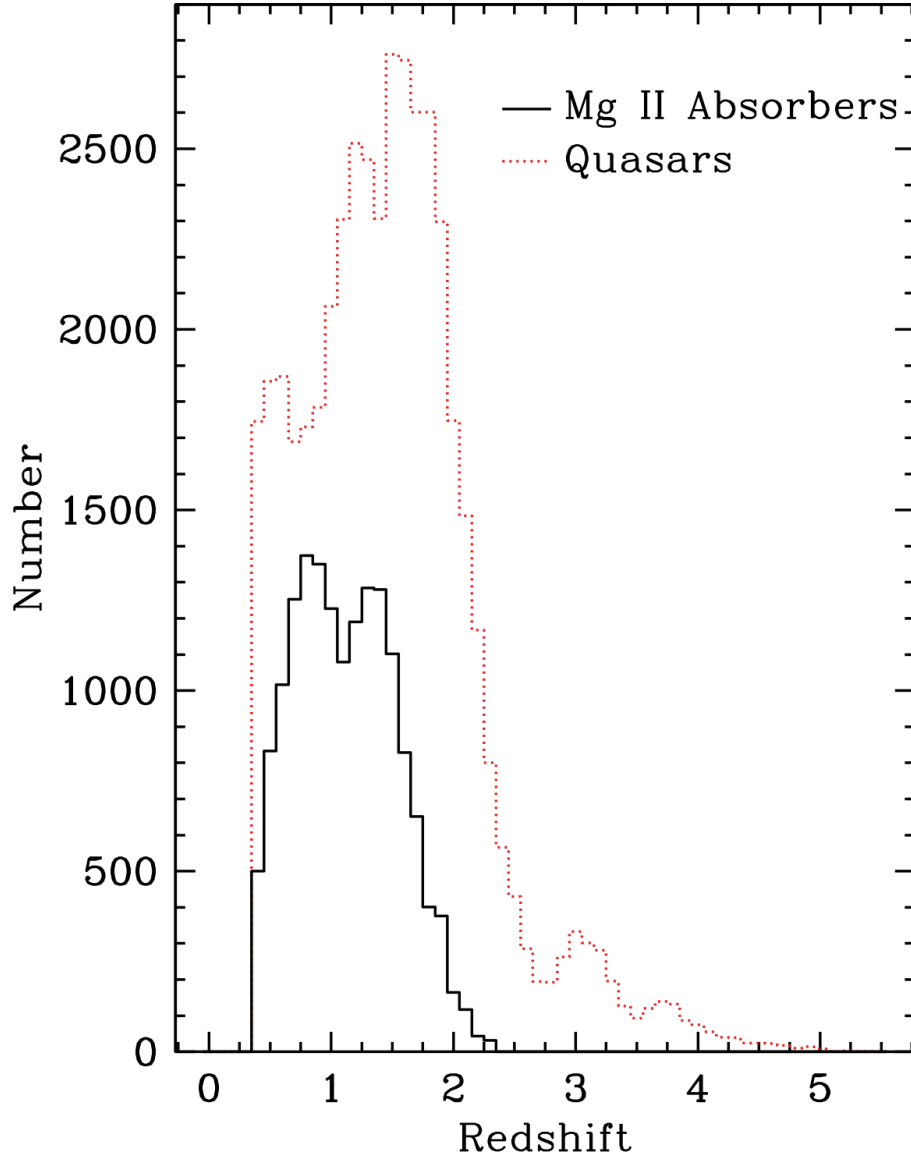[3] A DR4 quasar catalog was not published.

Figure 6.2 The emission redshift distribution for all quasars in the catalog (red dotted line) and the absorption redshift distribution for all Mg II systems in the catalog (black solid line). The redshift bin width for both distributions is 0.1. Only quasars with emission redshift $z_{em} > 0.36$ were searched for Mg II (see §6.2). The absorption redshift range of the Mg II systems is determined by the wavelength coverage of SDSS spectra, namely $0.36 \lesssim z_{abs} \lesssim 2.28$. The drop in the number of absorption systems near $z \approx 1.1$ is due to a decrease in SDSS spectrograph sensitivity in the transition region from the blue-side to red-side cameras.
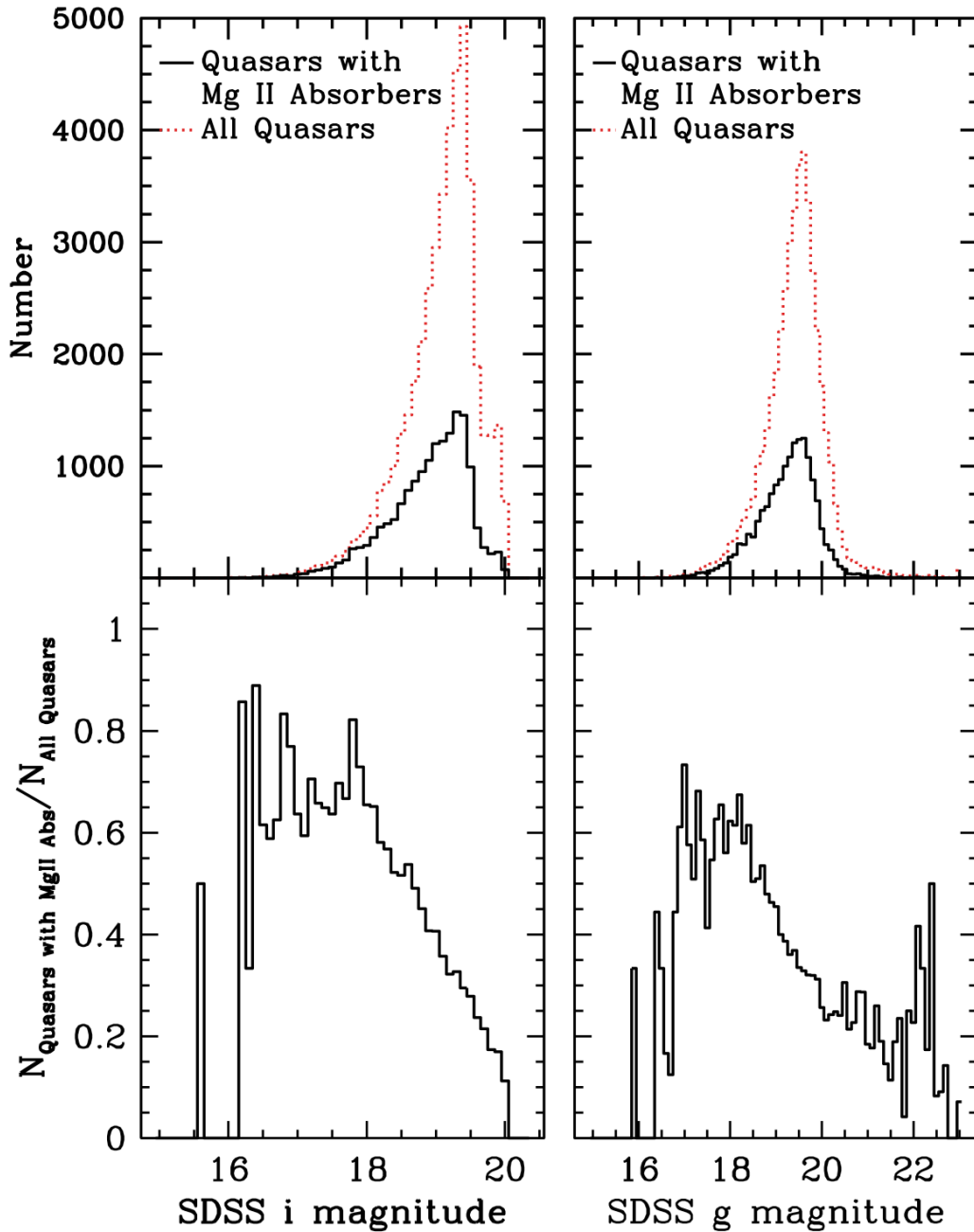
Figure 6.3 The top panels show the *i* (*left*) and *g* (*right*) magnitude distributions for all quasars in the catalog (red dotted line) and for those quasars with one or more Mg II absorbers (black solid line). The magnitude bin width is 0.1. The bottom panels show the corresponding fractions of quasars with one or more Mg II systems as a function of magnitude, without regard to quasar redshift. As expected, the brighter quasars have a higher probability of exhibiting Mg II absorption since the high S/N of their spectra permits the detection of weaker Mg II systems, which have a higher incidence than stronger systems.
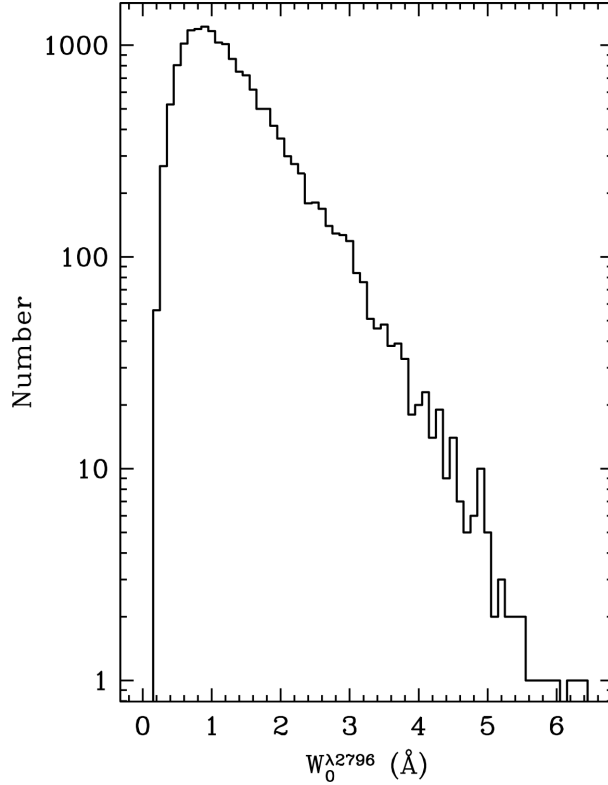
Figure 6.4 The observed $\lambda 2796$ rest equivalent width, $W_0^{\lambda 2796}$, distribution for the Mg II absorbers in the catalog. The bin width is 0.1 Å.

decrease in signal-to-noise ratio at the wavelength corresponding to the split between the blue-side and red-side cameras by the dichroic. The black histograms in the top panels of Figure 6.3 show the distribution of $i$ and $g$ magnitudes for quasars having at least one Mg II absorber in its spectrum. As noted in §6.4.3, the bottom panels indicate that a higher fraction of Mg II systems have been detected in brighter quasars. This is due to the fact that the higher signal-to-noise ratios of the brighter quasars permit the detection of weaker Mg II systems, which have a higher incidence that stronger Mg II systems.

The observed $W_0^{\lambda 2796}$ distribution is presented in Figure 6.4. Nearly 50% of the absorbers have $0.6 < W_0^{\lambda 2796} < 1.2$ Å. We identify 9,783 Mg II absorbers with $W_0^{\lambda 2796} > 1.0$ Å. For comparison, Prochter et al. (2006) compiled 7,421 Mg II absorbers with $W_0^{\lambda 2796} > 1.0$ Å in their SDSS DR3 catalog. A large fraction of the absorbers in our catalog have high rest equivalent width, with 15.8% having $W_0^{\lambda 2796} > 2.0$ Å.

Figures 6.5 and 6.6 show the measured relationship between $W_0^{\lambda 2796}$ and $W_0^{\lambda 2803}$. The diagonal lines on Figure 6.5 represent the theoretical limits for completely saturated ($W_0^{\lambda 2796}/W_0^{\lambda 2803} = 1.0$) and unsaturated ($W_0^{\lambda 2796}/W_0^{\lambda 2803} = 2.0$) absorption. The error bars along the horizontal axis represent the average measured $\sigma_{W_0}$ for various rest equivalent width regions. Figure 6.6 illustrates the relationship between the doublet ratio and the value of $W_0^{\lambda 2796}$.

The vast majority of the Mg II absorbers in the catalog have doublet ratios that lie within the theoretical limits, and deviations from these limits can be attributed to noise and line blending. In some instances, for example, systems that are clearly real, exhibiting
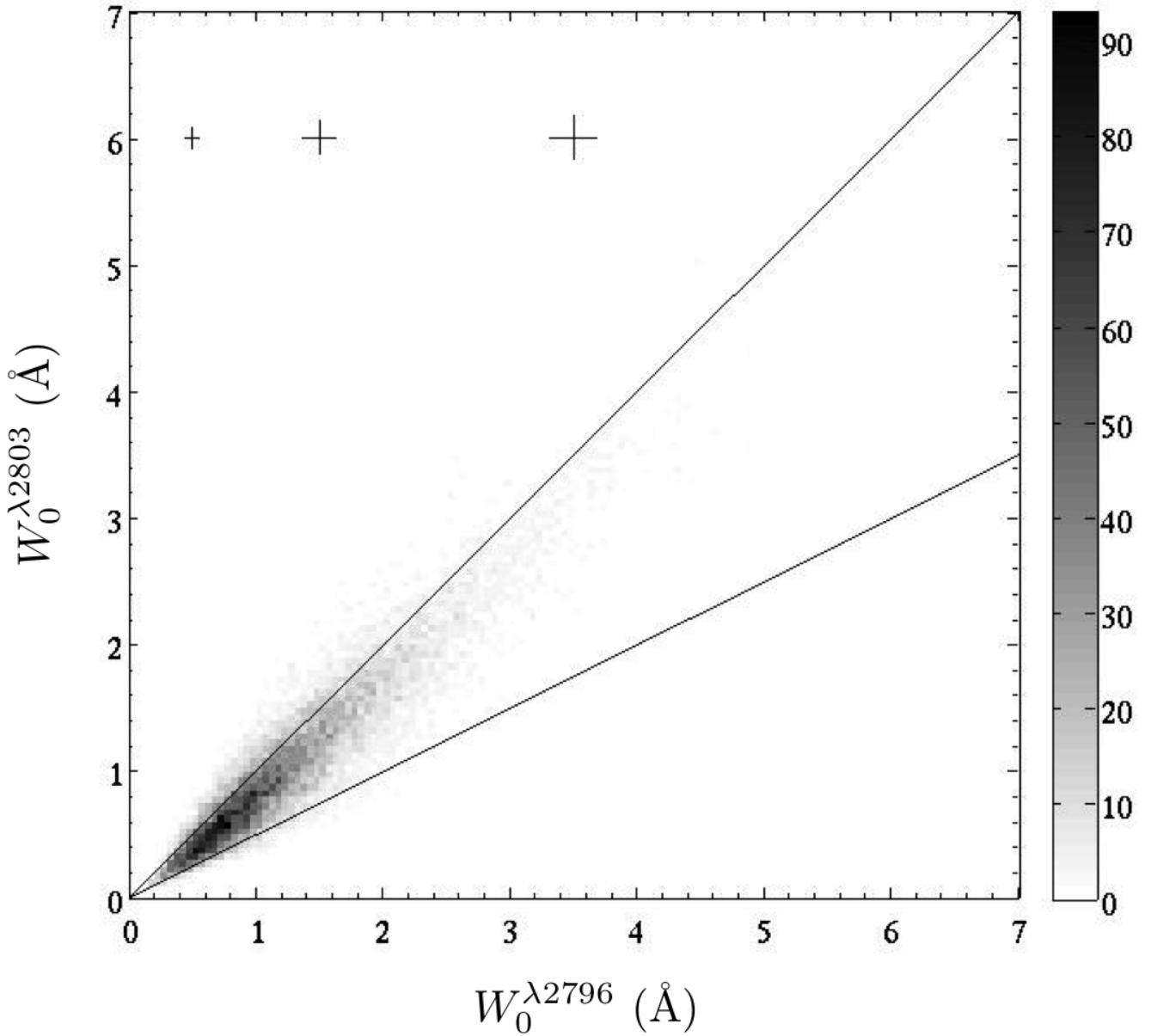
Figure 6.5 A plot of $W_0^{\lambda 2796}$ versus $W_0^{\lambda 2803}$ for absorbers in the catalog is shown. The two diagonal lines represent the theoretical boundaries for the Mg II doublet ratios in a hypothetical error-free data set (i.e., $1 \leq W_0^{\lambda 2796} / W_0^{\lambda 2803} \leq 2$). The vast majority of doublets in the catalog have doublet ratios that fall within the theoretical boundaries. Those that fall outside the theoretical boundaries can be attributed to errors associated with noise and/or line blending. The crosses in the upper left corner represent the average $\pm 1\sigma_{W_0}$ errors in the $W_0^{\lambda 2796}$ and $W_0^{\lambda 2803}$ measurements for $W_0^{\lambda 2796} = W_0^{\lambda 2803} \approx 0.5$ Å, 1.5 Å, and 3.5 Å, respectively. The grey-scale bar on the right hand side provides information on the frequency distribution of doublet ratios.
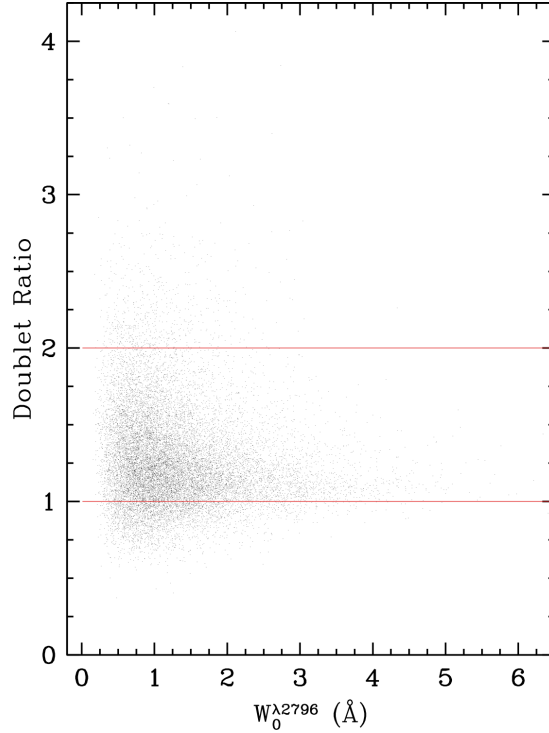
Figure 6.6 A plot of $W_0^{\lambda 2796} / W_0^{\lambda 2803}$ versus $W_0^{\lambda 2796}$ for the Mg II absorption doublets in the catalog. This is a different rendering of the same data shown in Figure 6.5.

high-significance metal lines from other species at the same absorption redshift, will have poorly-measured $W_0^{\lambda 2803}$ values due to contamination from a line in another absorption system. Such systems may have measured doublet-ratios well outside of the theoretical range. Most of our effort has been given to obtaining the best possible measurements of $W_0^{\lambda 2796}$ in identified systems. Therefore, these values can generally be used with more confidence. Of course, we also attempt to measure an accurate value for $W_0^{\lambda 2803}$, but less effort and no testing has been devoted to determining possible problems with these measurements. Therefore, more caution should be exercised if the desire is to use the $W_0^{\lambda 2803}$ values in high-precision studies.

## 6.5 Summary

We have presented the Pittsburgh SDSS Mg II Quasar Absorption-Line Survey Catalog — a well-characterized catalog of Mg II absorption doublets found in the spectra of quasars up through SDSS DR4, along with supporting information. We have combined automated and manual techniques to search the spectra of $\sim 44,600$ quasars to arrive at a catalog of $\sim 16,700$ Mg II $\lambda\lambda 2796,2803$ absorption doublets which we now make available for public use. The available information includes the Mg II absorber catalog itself, with measurements of the absorbers and associated errors, measurements of up to six nearby metal absorption lines (Mn II, Fe II, and Mg I), and information on the quasar catalog which was searched, including wavelength-dependent spectral files (flux, flux uncertainty, pseudo-continuum fit, and $\lambda 2796$ rest equivalent width detection limit) for each quasar.

The results contain the information necessary for statistical studies. We estimate that for every 100 searched spectra approximately one Mg II absorber unambiguously above our detection threshold has been missed. A complete analysis of the statistics of the catalog will be given in a subsequent paper (Nestor et al., in preparation).

We make the catalog available to the community with the hope that its very large size and documented statistical characteristics will lead to future innovative investigations at low to moderate redshift.

# 7

# Proposed Studies of Star-Forming Galaxies in the High Redshift Universe

U NDERSTANDING the nature of star-forming galaxies at intermediate and high redshift is essential to our theory of galaxy formation and evolution. The work presented in Chapters 3, 4, and 5 investigates the nature of star-forming galaxies in the redshift range $1 < z < 3$. Chapter 6 presents a catalog of $\sim 16\,700$ Mg II absorption systems in the redshift range $0.36 < z < 2.28$, many of which are likely associated with star-forming galaxies. Chapters 3, 4, and 5 collectively explore many of the defining characteristics of star-forming galaxies, including gas motions (outflow and inflow with respect to the star-forming regions), geometric configuration of the stars and gas along the line of sight, metallicity of the interstellar medium and stars, and their stellar populations. Chapter 5 also investigates a complication in the use of absorption lines for determining the aforementioned galaxy characteristics.

The introduction to Chapter 3 highlights several outstanding questions in the field of galaxy formation and evolution. They are:

(i) To what extent do different metallicity indicators, based on stellar photospheric lines, wind lines from the most massive stars, interstellar absorption lines, and emission lines from H II regions, give consistent answers? This is an important issue, not only to explore the degree of chemical homogeneity of galaxies undergoing rapid star-formation, but also to clarify the sources of the systematic offsets between different H II region metallicity calibrators, and possibly bring them into better internal agreement (see, for example, the discussions by Pettini 2006, and Kewley & Ellison 2008). Metallicity indicators are also important for characterizing the mass-metallicity relation and its evolution with redshift. Current determinations often use different metallicity indicators at different redshifts.

(ii) What do the profiles of the interstellar absorption lines tell us about large-scale outflows in actively star-forming galaxies and about the inflow of gas fueling star formation? Can we see any evidence of the leakage of hydrogen ionizing photons from the sites of star formation into the intergalactic medium (IGM) which has proved so difficult to

145

detect directly (e.g. Shapley et al. 2006; Iwata et al. 2009) and yet seems to be required by a number of indirect lines of evidence (e.g. Faucher-Giguère et al. 2008)?

(iii) Can we place limits on possible variations of the stellar initial mass function (IMF) at $z = 2$–3? Claims to this effect have certainly been put forward (e.g. Wilkins et al. 2008 and references therein), but the evidence is still controversial (e.g. Reddy & Steidel 2009).

(iv) What are the factors affecting the wide variety of spectral morphologies of the Ly$\alpha$ line, from strong narrow emission to damped absorption (e.g. Mas-Hesse et al. 2003; Verhamme, Schaerer, & Maselli 2006), and what can we learn about the relationship of the so called 'Ly$\alpha$ emitters' to the more general LBG population?

Identifying the range of answers to these questions which are possible for individual galaxies as well as the population of star-forming galaxies as a whole has been the driving force behind this thesis. Answers to these fundamental questions are far from comprehensive and complete, however, so much of the foreseeable work in the study of high redshift galaxies will continue to be motivated by these, and similar, considerations. In the remainder of this Chapter, we suggest avenues for continuing investigations which will expand upon and deepen the work presented in this thesis.

# 7.1  Probing Down the Luminosity Function

The detailed studies presented in Chapters 3 and 4 highlight the complexity and range of the physical conditions which prevailed in actively star-forming galaxies at redshifts $z = 2 - 3$. While the OB stellar populations of these galaxies appear very similar, they have widely different interstellar media, as seen in Figure 7.1. Here I show a small sample of the interstellar lines I have examined, along with line profiles from MS 1512–cB58 (called cB58 for short), the 'prototypical' lensed LBG. Clearly, there is a high degree of variability in the interstellar absorption features of these galaxies. All of the galaxies exhibit large-scale outflows of interstellar matter, with velocities reaching several hundred km s$^{-1}$ relative to the OB stars and H II regions, as evidenced by the net blueshift of the interstellar lines. Additionally, the Cosmic Eye exhibits an unusual high velocity *inflow* of gas.

The detailed studies presented in Chapters 3 and 4 require that a high-$z$ galaxy have a flux boost from the magnification due to gravitational lensing. To date, only bright ($L \geq L_*$) galaxies with similar dynamical masses and star formation rates have been studied simply because these are the galaxies that happen to have been found.

One fruitful avenue for future work is to probe down the luminosity function and conduct spectroscopic studies of the more numerous yet less observationally accessible galaxies with $L < L_*$. These faint galaxies are typically beyond the capability of current 8 to 10 meter class telescopes but the flux boost from gravitational lensing can put them within reach. Such studies would offer more insight into all of the questions outlined in the beginning of this Chapter but address them in the context of the more numerous galaxies at $1 < z < 3$. Further, an increased sample size with a greater dynamic range in galaxy properties may reveal, or at least point to, trends that are more nuanced than those presented in Chapter 5. Larger samples of gravitationally lensed galaxies are being found using targeted searches of the Sloan Digital Sky Survey and Hubble Space Telescope
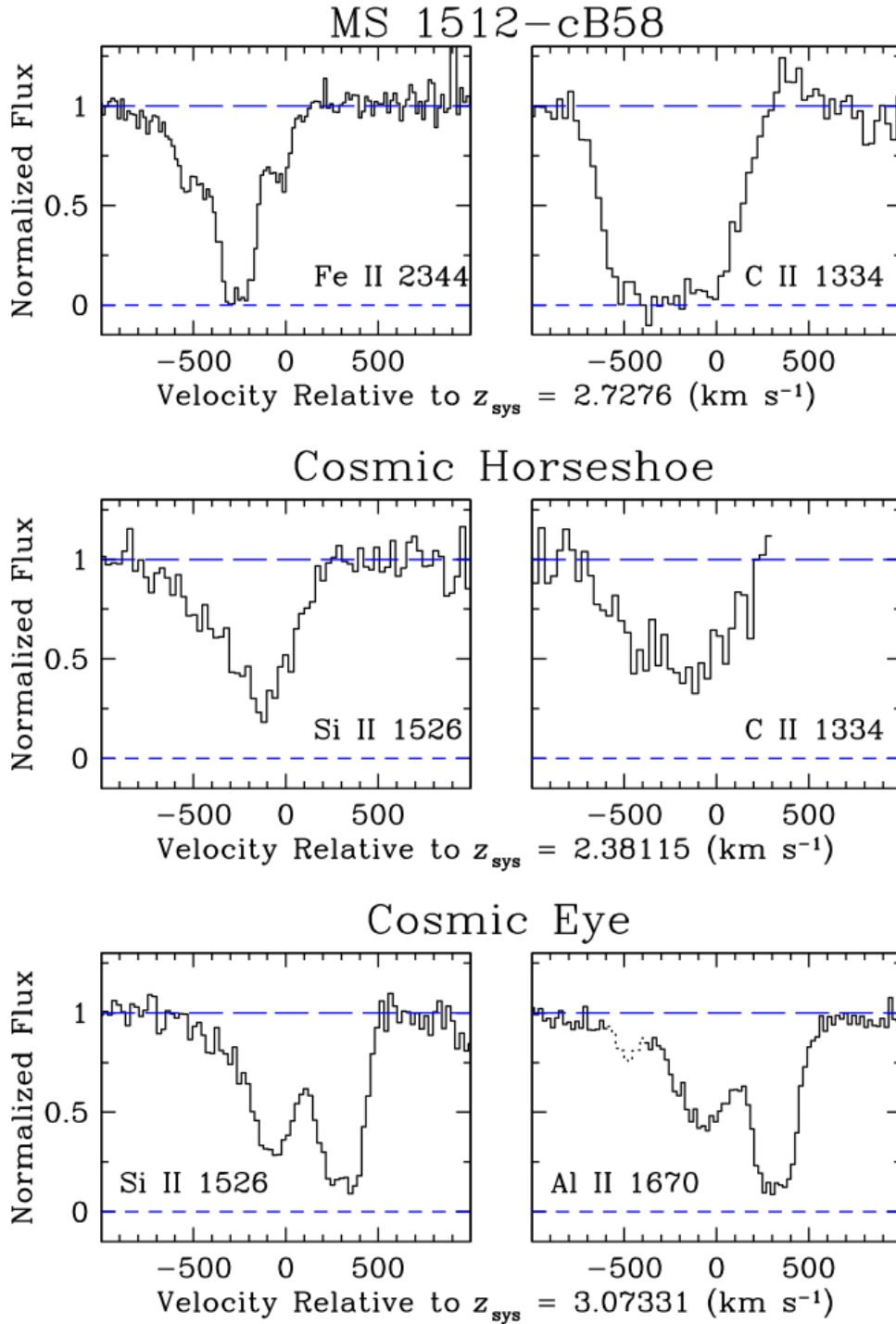
Figure 7.1 A small sampling of the interstellar absorption lines prominent in the rest-frame UV spectra of three strongly lensed high-$z$ galaxies recorded at $R \sim 4000$ and S/N$\sim 10 - 30$. The Cosmic Horseshoe is presented in Chapter 3 and the Cosmic Eye is presented in Chapter 4. In the Cosmic Horseshoe, the C II $\lambda 1334$ absorption line (middle row, right-hand panel) falls immediately blueward of a detector defect which was excluded from the plot for clarity. Dotted lines indicate regions of absorption which are not related to the identified transition.

images of galaxy clusters (see Chapter 1, Section 4.1) so studies of low luminosity galaxies are a very real possibility in the near future.

## 7.2  Galaxy Contributions to Reionization

One of the main results of Chapter 3 is that, for the first time, the ISM of a high redshift star-forming galaxy is conclusively shown to incompletely cover the OB stars. Partial coverage appears to be the case in the Cosmic Eye as well, although to a lesser degree. The depth of the line profiles in Figure 7.1 illustrates this. The line cores in cB58 reach to zero residual intensity, indicating that the stars are fully covered by the interstellar gas, while the line cores of these saturated transitions do not reach zero flux for the other two galaxies. Incomplete coverage of the stars by the ISM is a prerequisite for the escape of Lyman continuum (LyC) photons from star-forming galaxies.

One of the outstanding problems in cosmology is understanding the process of reionizing the intergalactic medium (IGM) by $z \sim 6$. Far-UV LyC emission from the short-lived O stars in young star-forming galaxies is thought to drive this reionization (Bolton & Haehnelt 2007; Ryan-Weber et al. 2009). Confirming this basic picture of reionization has proved particularly challenging. Standard practice is to search for LyC photons escaping from galaxies at $z \sim 1-3$ as their relative proximity allows for superior galaxy characterization (see Chapters 3 and 4); further, decreased IGM opacity permits the transmission of a higher percentage of escaping LyC photons. Armed with detailed knowledge of LyC emitting galaxies, we can seek answers to *how* LyC emission occurs in some galaxies and not others. If we understand the conditions which enable a large percentage of LyC photons to exit a galaxy at $z \sim 1-3$, we are well positioned to extrapolate these conditions to galaxies at $z > 6$ which allows us to predict the LyC escape fraction in these higher redshift galaxies. Ultimately, the goal is to construct a physical picture that explains the contribution of high redshift star-forming galaxies to reionizing the IGM.

To date, there have been very few detections of LyC photons from galaxies, all at $z \sim 3$ (Steidel et al. 2001; Shapley et al. 2006; Iwata et al. 2009). Repeated attempts to record LyC emission at $z \sim 1$ have not yielded any detections (Siana et al. 2007, 2010; Cowie et al. 2009). One proposed area of future work is to search for LyC from lensed galaxies which have LyC escape routes through the ISM, like the Cosmic Horseshoe. Lensed galaxies are bright so LyC emission can be detected at sensitivities over an order of magnitude better than unlensed galaxies. Further, the properties of lensed galaxies can be pinned down to an unprecedented degree compared to unlensed galaxies from similar epochs. Studying galaxies at $z = 1-3$ is our only way to understand LyC emission from star-forming galaxies at higher redshifts and lensed galaxies can point toward the physical processes within a galaxy which allow it contribute to the reionization of the IGM.

## 7.3  Spatially Resolved Star-Forming Regions

Studies of unlensed galaxies in the high redshift universe do not have the resolution necessary to distinguish between different regions of star formation within a galaxy. Therefore,
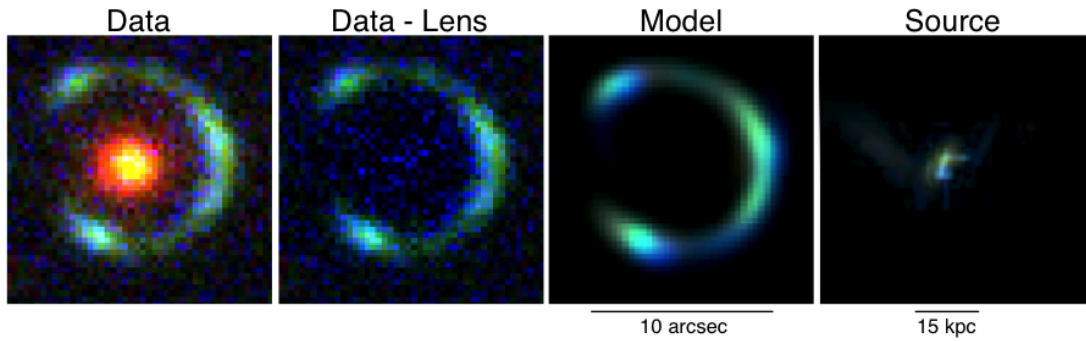
Figure 7.2 *Left*: Color composite view of the Cosmic Horseshoe made with $u, g, i$ band images obtained using the Isaac Newton Telescope. Please note that the pixel size is 0.33" and the median seeing is 1.7". The blue arc is the galaxy studied in Chapter 3 and the centrally located red galaxy is the lens. *Middle left*: The light from the lensing galaxy is subtracted in each band. *Middle right*: Reconstructed source lensed by the most probable lens model (Brewer et al. 2011, in prep. but also see Dye et al. 2008). *Right*: Source reconstruction showing details in the lensed galaxy on the scale of a few kpc. Higher resolution imaging, such as that from the Hubble Space Telescope, will allow for the study of regions within the source galaxy down to a size of $\sim 100\,\mathrm{pc}$.

the characteristics related to the stars and star formation (e.g., metallicity, outflow velocity and geometry, stellar populations) are reduced to a single number for each galaxy. In actuality, we expect spatial inhomogeneities within a galaxy, at a minimum in the geometry of star-forming regions along the line of sight to our telescopes but most likely in numerous other properties as well. Information on the range of properties found *within* an individual galaxy would go a long way towards answering the guiding questions posed at the beginning of this Chapter and provide novel constraints for galaxy formation models. Further, this information may help to explain some of the general trends among galaxy properties, such as those found in Chapter 5. Lensed galaxies are the only way to study small-scale spatial variability in high redshift galaxies.

I looked for variations among the spectra collected from different portions of the Cosmic Horseshoe and the Cosmic Eye (Chapters 3 and 4) but did not find any. It is most likely that this reflects an insufficient signal-to-noise ratio for the individual spectra of the different regions rather than a lack of variation. Indeed, Hainline et al. (2009) find inconsistencies among the rest-frame optical spectra of the Cosmic Horseshoe. Further, integral field unit (IFU) spectroscopy of the Cosmic Eye has shown that it does, in fact, have spatial variation across the galaxy (Stark et al. 2008). The source galaxy for the Cosmic Eye has a rotation curve with $V_{\mathrm{rot}} = 50\,\mathrm{km\,s^{-1}}$ over $\pm 2\,\mathrm{kpc}$, finely sampled on $\sim 100\,\mathrm{pc}$ scales—an order of magnitude improvement on the spatial resolution achievable for unlensed galaxies. One favorable aspect of gravitational lensing is that the resolution of the reconstructed source is not uniform, with highly magnified emission in the vicinity of critical lines providing stronger constraints on small scale structure in the source.

This is a fertile area for future imaging studies. High resolution imaging of a lensed galaxy coupled with accurate lens modeling are necessary to probe structures down to $\sim 100\,\mathrm{pc}$ in the source galaxy. Both of these factors work in conjunction to create an accurate mapping between the lensed galaxy image and spatial locations in the source.

A reconstruction of the source galaxy for the Cosmic Horseshoe using low resolution imaging is shown in the rightmost panel of Figure 7.2. Structures that are $\sim 10\times$ smaller than those shown in the Figure can be resolved with high resolution imaging from space-based telescopes, such as *HST*. In addition to improving lens models, detailed images are useful for visually identifying emission from star-forming regions, particularly when studying variation across lenses that are too faint for IFU spectroscopy. Such imaging is also important for studying spatial variation in emission that is in a waveband beyond the range of ground-based IFUs (such as LyC emission from galaxies with $z < 3$).

IFU spectroscopy provides another avenue of investigation. This type of spectroscopy is well-matched to studying lensed galaxies. IFUs can take advantage of the spatial distortions caused by gravitational lensing and map variations across a source. IFUs are not limited to using a single spectrograph slit, as is the case for standard spectrographs (such as ESI used in Chapters 3 and 4). Lensed galaxies are often distorted into extended arcs that are traceable by IFUs.

## 7.4 Galaxy Outflows in Emission

Studies of galactic outflows in absorption have yielded a wealth of information. Matters such as the kinematics, geometry, extent, composition, and mass of the outflow have been explored with absorption lines (e.g., Chapters 3, 4, and 5; Pettini et al. 2002; Martin & Bouché 2009; Steidel et al. 2010; Weiner et al. 2009; Rubin et al. 2010). I confirmed the existence of emission from cool galactic outflows in Chapter 5. This emission has the potential to place more stringent constraints on the morphology, extent, and physical properties of outflows (Rubin et al. 2011). Uniting the information gleaned from absorption and emission studies will lead to more complete physical models of galactic outflows and a better understanding of their role in the evolution of galaxies and the IGM.

Future work in this area requires larger samples of galaxies with emission in Fe II and Mg II. One way to find such galaxies is to target objects that are already known to have a large-scale outflows. The strongest Mg II absorption systems have been shown to correspond to such galaxies (Nestor et al. 2011). Catalogs of Mg II absorbers, such as the one I present in Chapter 6, can be used to identify galaxies with outflows for follow-up spectroscopy to search for emission from the outflow. If identified, IFU spectroscopy can then be used to map the morphology of outflows from the center of the galaxy to its outer edges.

The strongest Mg II absorbers (i.e., those with $W_0^{\lambda 2796} > 3$ Å) are rare (see Figure 6.4). Therefore, large numbers of quasars need to be culled to find these systems. Work is underway to extend my catalog of Mg II absorbers to encompass the quasars in the Sloan Digital Sky Survey beyond Data Release 4 (Monier et al. 2011, in prep.). Future surveys, such as that to be conducted by the Large Synoptic Survey Telescope, will be critical to finding more of these rare systems.

# Bibliography

[1] Abazajian, K. N., et al. 2009, ApJS, 182, 543

[2] Adelberger, K. L., Steidel, C. C., Shapley, A. E., Hunt, M. P., Erb, D. K., Reddy, N. A., & Pettini, M. 2004, ApJ, 607, 226

[3] Adelberger, K. L., Steidel, C. C., Shapley, A. E., & Pettini, M. 2003, ApJ, 584, 45

[4] Adelman-McCarthy, J.K., et al. 2008, ApJS, 175, 297

[5] Ajiki, M., et al. 2002, ApJL, 576, L25

[6] Asplund, M., Grevesse, N, & Sauval, A. J. 2005, in Barnes T. G. III, & Bash, F. N. eds., ASP Conf. Ser. Vol. 336, Cosmic Abundances as Records of Stellar Evolution and Nucleosynthesis. Astron. Soc. Pac., San Francisco, p. 25

[7] Baker, A. J., Lutz, D., Genzel, R., Tacconi, L. J., & Lehnert, M. D. 2001, A&A, 372, L37

[8] Baker, A. J., Tacconi, L. J., Genzel, R., Lehnert, M. D., & Lutz, D. 2004, ApJ, 604, 125

[9] Belokurov, V., et al. 2007, ApJL, 671, L9

[10] Belokurov, V., Evans, N. W., Hewett, P. C., Moiseev, A., McMahon, R. G., Sanchez, S. F., & King, L. J. 2009, MNRAS, 392, 104

[11] Bergeron, J., & Boissé, P. 1991, A&A, 243, 344

[12] Blain, A. W., Kneib, J.-P., Ivison, R. J., & Smail, I. 1999, ApJL, 512, L87

[13] Blain, A. W., Smail, I., Ivison, R. J., Kneib, J.-P., & Frayer, D. T. 2002, Phys. Rep., 369, 111

[14] Bolton, A. S., Burles, S., Koopmans, L. V. E., Treu, T., & Moustakas, L. A. 2006, ApJ, 638, 703

[15] Bolton, J. S., & Haehnelt, M. G. 2007, MNRAS, 382, 325

[16] Bond, N.A., Churchill, C.W., Charlton, J.C., & Vogt, S.S. 2001, ApJ, 562, 641

[17] Bowen, D.V., et al. 2006, ApJL, 645, L105

[18] Brinchmann, J., Pettini, M., & Charlot, S. 2008, MNRAS, 385, 769

[19] Bullock, J. S., Kolatt, T. S., Sigad, Y., Somerville, R. S., Kravtsov, A. V., Klypin, A. A., Primack, J. R., & Dekel, A. 2001, MNRAS, 321, 559

[20] Cabanac, R. A., Valls-Gabaud, D., & Lidman, C. 2008, MNRAS, 386, 2065

[21] Calzetti, D., Armus, L., Bohlin, R. C., Kinney, A. L., Koornneef, J., & Storchi-Bergmann, T. 2000, ApJ, 533, 682

[22] Caulet, A. 1989, ApJ, 340, 90

[23] Chabrier, G. 2003, PASP, 115, 763

[24] Chandar, R., Leitherer, C., Tremonti, C. A., Calzetti, D., Aloisi, A., Meurer, G. R., & de Mello, D. 2005, ApJ, 628, 210

[25] Chapman, S. C., et al. 2000, MNRAS, 319, 318

[26] Charlton, J.C., & Churchill, C.W. 1996, ApJ, 465, 631

[27] Chen, H.-W., & Lanzetta, K.M. 2003, ApJ, 597, 706

[28] Chen, H.-W., Helsby, J.E., Gauthier, J.-R., Shectman, S.A., Thompson, I.B., & Tinker, J.L. 2010, ApJ, 714, 1521

[29] Churchill, C. W., & Charlton, J. C. 1999, AJ, 118, 59

[30] Churchill, C.W., Mellon, R.R., Charlton, J.C., Jannuzi, B.T., Krihakos, S., Steidel, C.C., & Schneider, D.P. 2000, ApJ, 543, 577

[31] Churchill, C.W., & Vogt, S.S. 2001, AJ, 122, 679

[32] Coppin, K. E. K., et al. 2007, ApJ, 665, 936

[33] Cowie, L. L., Barger, A. J., & Trouille, L. 2009, ApJ, 692, 1476

[34] Crowther, P. A., Prinja, R. K., Pettini, M., & Steidel, C. C. 2006, MNRAS, 368, 895

[35] Daddi, E., Cimatti, A., Renzini, A., Fontana, A., Mignoli, M., Pozzetti, L., Tozzi, P., & Zamorani, G. 2004, ApJ, 617, 746

[36] Davé, R., Oppenheimer, B. D., & Finlator, K. 2011, arXiv:1103.3528

[37] Dessauges-Zavadsky, M., D'Odorico, S., Schaerer, D., Modigliani, A., Tapken, C., & Vernet, J. 2010, A&A, 510, A26

[38] Djorgovski, Thompson, and Smith 1992

[39] Dye, S., Evans, N. W., Belokurov, V., Warren, S. J., & Hewett, P. 2008, MNRAS, 388, 384

[40] Dye, S., Smail, I., Swinbank, A. M., Ebeling, H., & Edge, A. C. 2007, MNRAS, 379, 308

[41] Ellingson, E., Yee, H. K. C., Bechtold, J., & Elston, R. 1996, ApJL, 466, L71

[42] Ellison, S.L., Churchill, C.W., Rix, S.A., & Pettini, M. 2004, ApJ, 615, 118

[43] Ellison, S.L., & Lopez, S. 2009, MNRAS, 397, 467

[44] Erb, D. K., Shapley, A. E., Pettini, M., Steidel, C. C., Reddy, N. A., & Adelberger, K. L. 2006a, ApJ, 644, 813

[45] Erb, D. K., Steidel, C. C., Shapley, A. E., Pettini, M., Reddy, N. A., & Adelberger, K. L. 2006b, ApJ, 646, 107

[46] Erb, D. K., Steidel, C. C., Shapley, A. E., Pettini, M., Reddy, N. A., & Adelberger, K. L. 2006c, ApJ, 647, 128

[47] Estrada, J., et al. 2007, ApJ, 660, 1176

[48] Faucher-Giguère, C.-A., Lidz, A., Hernquist, L., & Zaldarriaga, M. 2008, ApJL, 682, L9

[49] Ferland, G. J., Korista, K. T., Verner, D. A., Ferguson, J. W., Kingdon, J. B., & Verner, E. M. 1998, PASP, 110, 761

[50] Finkelstein, S. L., Papovich, C., Rudnick, G., Egami, E., LeFloc'h, E., Rieke, M. J., Rigby, J. R., & Willmer, C. N. A. 2009, ApJ, 700, 376

[51] Finlator, K., & Davé, R. 2008, MNRAS, 385, 2181

[52] Förster Schreiber, N. M., et al. 2009, ApJ, 706, 1364

[53] Grimes, J. P., et al. 2009, ApJS, 181, 272

[54] Hainline, K. N., Shapley, A. E., Kornei, K. A., Pettini, M., Buckley-Geer, E., Allam, S. S., & Tucker, D. L. 2009, ApJ, 701, 52

[55] Halliday, C., et al. 2008, A&A, 479, 417

[56] Hansen, M., & Oh, S. P. 2006, MNRAS, 367, 979

[57] Hartigan, P., Morse, J. A., Tumlinson, J., Raymond, J., & Heathcote, S. 1999, ApJ, 512, 901

[58] Heckman, T. M., et al. 2005, ApJL, 619, L35

[59] Heckman, T. M., Lehnert, M. D., Strickland, D. K., & Armus, L. 2000, ApJS, 129, 493

[60] Heckman, T. M., Sembach, K. R., Meurer, G. R., Leitherer, C., Calzetti, D., & Martin, C. L. 2001, ApJ, 558, 56

[61] Hopkins, A. M., & Beacom, J. F. 2006, ApJ, 651, 142

[62] Hu, E. M., Cowie, L. L., & McMahon, R. G. 1998, ApJL, 502, L99

[63] Iwata, I., et al. 2009, ApJ, 692, 1287

[64] Jenkins, E. B. 1971, ApJ, 169, 25

[65] Jenkins, E. B., & Tripp, T. M. 2006, ApJ, 637, 548

[66] Kacprzak, G.G., Churchill, C.W., Ceverion, D., Steidel, C.C., Klypin, A., & Murphy, M.T. 2010, ApJ, 711, 533

[67] Kacprzak, G. G., Churchill, C. W., Evans, J. L., Murphy, M. T., & Steidel, C. C. 2011, arXiv:1106.3068

[68] Kacprzak, G.G., Churchill, C.W., Steidel, C.C., Murphy, M.T., & Evans, J.L. 2007, ApJ, 662, 909

[69] Kauffmann, G., White, S. D. M., & Guiderdoni, B. 1993, MNRAS, 264, 201

[70] Kennicutt, R. C., Jr. 1998, ARA&A, 36, 189

[71] Kennicutt, R. C., Jr., Bresolin, F., & Garnett, D. R. 2003, ApJ, 591, 801

[72] Kewley, L. J., & Ellison, S. L. 2008, ApJ, 681, 1183

[73] Kinney, A. L., Bohlin, R. C., Calzetti, D., Panagia, N., & Wyse, R. F. G. 1993, ApJS, 86, 5

[74] Kobulnicky, H. A., & Kewley, L. J. 2004, ApJ, 617, 240

[75] Komatsu, E., et al. 2011, ApJS, 192, 18

[76] Kornei, K. A., Shapley, A. E., Erb, D. K., Steidel, C. C., Reddy, N. A., Pettini, M., & Bogosavljević, M. 2009, ApJ, submitted

[77] Kubo, J. M., et al. 2010, ApJL, 724, L137

[78] Kubo, J. M., Allam, S. S., Annis, J., Buckley-Geer, E. J., Diehl, H. T., Kubik, D., Lin, H., & Tucker, D. 2009, ApJL, 696, L61

[79] Kudritzki, R.-P., & Puls, J. 2000, ARA&A, 38, 613

[80] Lanzetta, K.M., Turnshek, D.A., & Wolfe, A.M. 1987, ApJ, 322, 739

[81] Law, D. R., Steidel, C. C., Erb, D. K., Larkin, J. E., Pettini, M., Shapley, A. E., & Wright, S. A. 2009, ApJ, 697, 2057

[82] Law, D. R., Steidel, C. C., Erb, D. K., Pettini, M., Reddy, N. A., Shapley, A. E., Adelberger, K. L., & Simenc, D. J. 2007, ApJ, 656, 1

[83] LeBrun, V., Bergeron, J., Boisse, P., & Christian, C. 1993, A&A, 279, 33

[84] Leitherer, C. 2008, in Hunt, K. L., Madden, S., & Schneider, R., eds., IAU Symp. 255, Low-Metallicity Star Formation: From the First Stars to Dwarf Galaxies. Cambridge Univ. Press, Cambridge, p. 305

[85] Leitherer, C., et al. 1999, ApJS, 123, 3

[86] Leitherer, C., Calzetti, D., & Martins, L. P. 2002, ApJ, 574, 114

[87] Leitherer, C., Leão, J. R. S., Heckman, T. M., Lennon, D. J., Pettini, M., & Robert, C. 2001, ApJ, 550, 724

[88] Lemoine-Busserolle, M., Contini, T., Pelló, R., Le Borgne, J.-F., Kneib, J.-P., & Lidman, C. 2003, A&A, 397, 839

[89] Lin, H., et al. 2009, ApJ, 699, 1242

[90] Liu, X., Shapley, A. E., Coil, A. L., Brinchmann, J., & Ma, C.-P. 2008, ApJ, 678, 758

[91] Madau, P., Pozzetti, L., & Dickinson, M. 1998, ApJ, 498, 106

[92] Maiolino, R., et al. 2008, A&A, 488, 463

[93] Maller, A., Prochaska, J.X., Somerville, R.S, & Primack, J.R. 2001, MNRAS, 326, 1475

[94] Mar, D. P., & Bailey, G. 1995, Publications of the Astronomical Society of Australia, 12, 239

[95] Martin, C. L. 2005, ApJ, 621, 227

[96] Martin, C. L., & Bouché, N. 2009, ApJ, 703, 1394

[97] Mas-Hesse, J. M., Kunth, D., Tenorio-Tagle, G., Leitherer, C., Terlevich, R. J., & Terlevich, E. 2003, ApJ, 598, 858

[98] Ménard, B., Nestor, D., Turnshek, D., Quider, A., Richards, G., Chelouche, D., & Rao, S. 2008, MNRAS, 385, 1053

[99] Ménard, B., Wild, V., Nestor, D. B., Quider, A., Rao, S., Turnshek, D. A. 2010, arXiv:0912.3263

[100] Meurer, G. R., Heckman, T. M., & Calzetti, D. 1999, ApJ, 521, 64

[101] Mo, H.J., & Miralda-Escude, J. 1996, ApJ, 469, 58

[102] Morton, D. C. 2003, ApJS, 149, 205

[103] Nestor, D. B., Johnson, B. D., Wild, V., Ménard, B., Turnshek, D. A., Rao, S., & Pettini, M. 2011, MNRAS, 412, 1559

[104] Nestor, D.B., Rao, S.M., Turnshek, D.A., & Vanden Berk, D. 2003, ApJL, 595, L5

[105] Nestor, D.B., Turnshek, D.A., & Rao, S.M. 2005, ApJ, 628, 637 (NTR05)

[106] Nestor, D.B., Turnshek, D.A., & Rao, S.M. 2006, ApJ, 643, 75

[107] Nestor, D.B., Turnshek, D.A., Rao, S.M., & Quider, A.M. 2007, ApJ, 658, 185

[108] Neufeld, D. A. 1991, ApJL, 370, L85

[109] Norman, C.A., Bowen, D.V., Heckman, T., Blades, C., & Danly, L. 1996, ApJ, 472, 73

[110] Noterdaeme, P., Petitjean, P., Ledoux, C., & Srianand, R. 2009, A&A, 505, 1087

[111] Ofek, E. O., Seitz, S., & Klein, F. 2008, MNRAS, 389, 311

[112] Pagel, B. E. J. 2003, in Charbonnel, C., Schaerer, D., & Meynet, G., eds., CNO Abundances in Dwarf and Spiral Galaxies, Astronomical Society of the Pacific Conference Series, San Francisco, 304, p. 187

[113] Pagel, B. E. J., Edmunds, M. G., Blackwell, D. E., Chun, M. S., & Smith, G. 1979, MNRAS, 189, 95

[114] Papovich, C., Dickinson, M., & Ferguson, H. C. 2001, ApJ, 559, 620

[115] Partridge, R. B., & Peebles, P. J. E. 1967, ApJ, 147, 868

[116] Pentericci, L., Grazian, A., Fontana, A., Castellano, M., Giallongo, E., Salimbeni, S., & Santini, P. 2009, A&A, 494, 553

[117] Pettini, M. 2004, Cosmochemistry. The melting pot of the elements, 257

[118] Pettini, M. 2006 in LeBrun V., Mazure A., Arnouts S. & Burgarella D., eds., The Fabulous Destiny of Galaxies: Bridging Past and Present. Frontier Group, Paris, p. 319 (astro-ph/0603066).

[119] Pettini, M., et al. 2007, Nuovo Cimento B Serie, 122, 1043

[120] Pettini, M., et al. 2010, MNRAS, 402, 2335

[121] Pettini, M., Kellogg, M., Steidel, C. C., Dickinson, M., Adelberger, K. L., & Giavalisco, M. 1998a, ApJ, 508, 539

[122] Pettini, M., & Pagel, B. E. J. 2004, MNRAS, 348, L59

[123] Pettini, M., Rix, S. A., Steidel, C. C., Adelberger, K. L., Hunt, M. P., & Shapley, A. E. 2002, ApJ, 569, 742

[124] Pettini, M., Shapley, A. E., Steidel, C. C., Cuby, J.-G., Dickinson, M., Moorwood, A. F. M., Adelberger, K. L., & Giavalisco, M. 2001, ApJ, 554, 981

[125] Pettini, M., Steidel, C. C., Adelberger, K. L., Dickinson, M., & Giavalisco, M. 2000, ApJ, 528, 96

[126] Pettini, M., Steidel, C. C., Adelberger, K. L., Kellogg, M., Dickinson, M., & Giavalisco, M. 1998b, in Woodward, C. E., Shull, J. M., Thronson, H. A., eds., ASP Conf. Ser. Vol. 148, Origins, Astron. Soc. Pac., San Francisco, p. 67

[127] Phillips, S, Disney, M.J., & Davis, J.I. 1993, MNRAS, 260, 453

[128] Pontzen, A. et al. 2010, MNRAS, submitted

[129] Prochaska, J. X., Kasen, D., & Rubin, K. 2011, arXiv:1102.3444

[130] Prochter, G.E., Prochaska, J.X., & Burles, S.M. 2006, ApJ, 639, 766

[131] Quider, A. M., Nestor, D. B., Turnshek, D. A., Rao, S. M., Monier, E. M., Weyant, A. N., & Busche, J. R. 2011, AJ, 141, 137

[132] Quider, A. M., Pettini, M., Shapley, A. E., & Steidel, C. C. 2009, MNRAS, 398, 1263

[133] Quider, A. M., Shapley, A. E., Pettini, M., Steidel, C. C., & Stark, D. P. 2010, MNRAS, 402, 1467

[134] Rao, S. M., Belfort-Mihalyi, M., Turnshek, D. A., Monier, E. M., Nestor, D. B., & Quider, A. M. 2011, arXiv:1103.4047

[135] Rao, S.M., Nestor, D.B., Turnshek, D.A., Lane, W.M., Monier, E.M., & Bergeron, J. 2003, ApJ, 595, 94

[136] Rao, S.M., Turnshek, D.A., & Briggs, F.H. 1995, ApJ, 449, 488

[137] Rao, S.M., & Turnshek, D.A. 2000, ApJS, 130, 1

[138] Rao, S.M., Turnshek, D.A., & Nestor, D.B. 2006, ApJ, 636, 610

[139] Reddy, N. A., Erb, D. K., Steidel, C. C., Shapley, A. E., Adelberger, K. L., & Pettini, M. 2005, ApJ, 633, 748

[140] Reddy, N. A., & Steidel, C. C. 2009, ApJ, 692, 778

[141] Reddy, N. A., Steidel, C. C., Fadda, D., Yan, L., Pettini, M., Shapley, A. E., Erb, D. K., & Adelberger, K. L. 2006, ApJ, 644, 792

[142] Reddy, N. A., Steidel, C. C., Pettini, M., Adelberger, K. L., Shapley, A. E., Erb, D. K., & Dickinson, M. 2008, ApJS, 175, 48

[143] Rhoads, J. E., Malhotra, S., Dey, A., Stern, D., Spinrad, H., & Jannuzi, B. T. 2000, ApJL, 545, L85

[144] Richard, J., Jones, T., Ellis, R., Stark, D. P., Livermore, R., & Swinbank, M. 2011, MNRAS, 126

[145] Rigby, J. R., Charlton, J. C., & Churchill, C. W. 2001, Gas and Galaxy Evolution, 240, 58

[146] Rimoldini, L. 2007, PhD Thesis (University of Pittsburgh), Proquest Dissertations and Theses, UMI Number: 3284615

[147] Rix, S. A., Pettini, M., Leitherer, C., Bresolin, F., Kudritzki, R.-P., & Steidel, C. C. 2004, ApJ, 615, 98

[148] Rubin, K. H. R., Prochaska, J. X., Ménard, B., Murray, N., Kasen, D., Koo, D. C., & Phillips, A. C. 2011, ApJ, 728, 55

[149] Rubin, K. H. R., Weiner, B. J., Koo, D. C., Martin, C. L., Prochaska, J. X., Coil, A. L., & Newman, J. A. 2010, ApJ, 719, 1503

[150] Rupke, D. S., Veilleux,S., & Sanders, D. B. 2005, ApJS, 160, 115

[151] Ryan-Weber, E. V., Pettini, M., Madau, P., & Zych, B. J. 2009, MNRAS, 395, 1476

[152] Saito, T., Shimasaku, K., Okamura, S., Ouchi, M., Akiyama, M., & Yoshida, M. 2006, ApJ, 648, 54

[153] Salpeter, E. E. 1955, ApJ, 121, 161

[154] Sargent, W.L.W., Steidel, C.C., & Boksenberg, A. 1988, ApJ, 334, 22

[155] Sargent, W.L.W., & Steidel, C.C. 1990, ApJL, 359, L37

[156] Savage, B. D. & Sembach, K. R. 1991, ApJ, 379, 245

[157] Savaglio, S., Panagia, N., & Padovani, P. 2002, ApJ, 567, 702

[158] Sawicki, M. 2001, AJ, 121, 2405

[159] Schaerer, D. 2007, in Cepa, J. ed, The Emission Line Universe, Cambridge Univ. Press, Cambridge, in press (arXiv:0706.0139 )

[160] Schneider, D.P., et al. 2007, AJ, 134, 102

[161] Seitz, S., Saglia, R. P., Bender, R., Hopp, U., Belloni, P., & Ziegler, B. 1998, MNRAS, 298, 945

[162] Shapley, A. E., Erb, D. K., Pettini, M., Steidel, C. C., & Adelberger, K. L. 2004, ApJ, 612, 108

[163] Shapley, A. E., Steidel, C. C., Adelberger, K. L., Dickinson, M., Giavalisco, M., & Pettini, M. 2001, ApJ, 562, 95

[164] Shapley, A. E., Steidel, C. C., Erb, D. K., Reddy, N. A., Adelberger, K. L., Pettini, M., Barmby, P., & Huang, J. 2005, ApJ, 626, 698

[165] Shapley, A. E., Steidel, C. C., Pettini, M., & Adelberger, K. L. 2003, ApJ, 588, 65

[166] Shapley, A. E., Steidel, C. C., Pettini, M., Adelberger, K. L., & Erb, D. K. 2006, ApJ, 651, 688

[167] Sheinis, A. I., Miller, J. S., Bolte, M., & Sutin, B. M. 2000, Proc. SPIE, 4008, 522

[168] Shin, M.-S., Strauss, M. A., Oguri, M., Inada, N., Falco, E. E., Broadhurst, T., & Gunn, J. E. 2008, AJ, 136, 44

[169] Siana, B., et al. 2007, ApJ, 668, 62

[170] Siana, B., et al. 2009, ApJ, 698, 1273

[171] Siana, B., et al. 2010, ApJ, 723, 241

[172] Siana, B., Teplitz, H. I., Chary, R.-R., Colbert, J., & Frayer, D. T. 2008, ApJ, 689, 59

[173] Smail, I., et al. 2007, ApJ, 654, L33

[174] Spergel, D. N., et al. 2003, ApJS, 148, 175

[175] Stark, D. P., Swinbank, A. M., Ellis, R. S., Dye, S., Smail, I. R., & Richard, J. 2008, Nature, 455, 775

[176] Steidel, C. C. 1990, ApJS, 72, 1

[177] Steidel, C. C., Adelberger, K. L., Giavalisco, M., Dickinson, M., & Pettini, M. 1999, ApJ, 519, 1

[178] Steidel, C. C., Adelberger, K. L., Shapley, A. E., Pettini, M., Dickinson, M., & Giavalisco, M. 2003, ApJ, 592, 728

[179] Steidel, C. C., Bogosavljević, M., Shapley, A. E., Kollmeier, J. A., Reddy, N. A., Erb, D. K., & Pettini, M. 2011, arXiv:1101.2204

[180] Steidel, C.C., Dickinson, M., & Persson, S.E. 1994, ApJL, 437, L75

[181] Steidel, C. C., Erb, D. K., Shapley, A. E., Pettini, M., Reddy, N., Bogosavljević, M., Rudie, G. C., & Rakic, O. 2010, ApJ, 717, 289

[182] Steidel, C.C., Kollmeier, J.A., Shapley, A.E., Churchill, C.W., Dickinson, M., & Pettini, M. 2002, ApJ, 570, 526

[183] Steidel, C. C., Pettini, M., & Adelberger, K. L. 2001, ApJ, 546, 665

[184] Steidel, C. C., Giavalisco, M., Pettini, M., Dickinson, M., & Adelberger, K. L. 1996, ApJL, 462, L17

[185] Steidel, C.C., & Sargent, W.L.W. 1992, ApJS, 80, 1

[186] Steidel, C. C., Shapley, A. E., Pettini, M., Adelberger, K. L., Erb, D. K., Reddy, N. A., & Hunt, M. P. 2004, ApJ, 604, 534

[187] Swinbank, A. M., Bower, R. G., Smith, G. P., Wilman, R. J., Smail, I., Ellis, R. S., Morris, S. L., & Kneib, J.-P. 2007, MNRAS, 376, 479

[188] Swinbank, A. M., et al. 2009, MNRAS, 400, 1121

[189] Tapken, C., Appenzeller, I., Noll, S., Richling, S., Heidt, J., Meinköhn, E., & Mehlert, D. 2007, A&A, 467, 63

[190] Teplitz, H. I., et al. 2000, ApJL, 533, L65

[191] Tremonti, C. A., et al. 2004, ApJ, 613, 898

[192] Turnshek, D.A., Rao, S.M., Nestor, D.B., Belfort-Mihalyi, M., & Quider, A.M. 2005, IAU Colloq. 199: Probing Galaxies through Quasar Absorption Lines, 104

[193] Tytler, D., Boksenberg, A., Sargent, W.L.W., Young, P., & Kunth, D. 1987, ApJS, 64, 667

[194] Vanzella, E., et al. 2009, ApJ, 695, 1163

[195] Verhamme, A., Schaerer, D., & Maselli, A. 2006, A&A, 460, 397

[196] Verhamme, A., Schaerer, D., Atek, H., & Tapken, C. 2008, A&A, 491, 89

[197] Vestergaard, M., & Wilkes, B. J. 2001, ApJS, 134, 1

[198] Weiner, B. J., et al. 2009, ApJ, 692, 187

[199] Wen, Z.-L., Han, J.-L., Xu, X.-Y., Jiang, Y.-Y., Guo, Z.-Q., Wang, P.-F., & Liu, F.-S. 2009, Research in Astronomy and Astrophysics, 9, 5

[200] Weymann, R.J., Williams, R.E., Peterson, B.M., & Turnshek, D.A. 1979, ApJ, 234, 33

[201] Wilkins, S. M., Hopkins, A. M., Trentham, N., & Tojeiro, R. 2008, MNRAS, 391, 363

[202] Yee, H. K. C., Ellingson, E., Bechtold, J., Carlberg, R. G., & Cuillandre, J.-C. 1996, AJ, 111, 1783

[203] York, D.G., et al. 2000, AJ, 120, 1579

[204] Yuan, T.-T., & Kewley, L. J. 2009, ApJL, 699, L161

[205] Zibetti, S., Ménard, B., Nestor, D.B., & Turnshek, D.A. 2005, ApJ, 631, L105

[206] Zibetti, S., Ménard, B., Nestor, D.B., Quider, A.M., Rao, S.M., & Turnshek, D.A. 2007, ApJ, 658, 161